Patient-specific biomechanical simulation for deep brain stimulation

Alexandre Bilger

Université de Lille 1 SCIENCES ET TECHNOLOGIES

Inria INVENTEURS DU MONDE NUMÉRIQUE

Région Nord-Pas de Calais

Document soumis pour obtenir
le titre de Docteur de l'Université
des Sciences et Technologies de Lille

EDSPI: Section Informatique

Alexandre BILGER Equipe INRIA SHACRA

PATIENT-SPECIFIC BIOMECHANICAL SIMULATION FOR DEEP BRAIN STIMULATION

Defended on the **16th of December 2014**

JURY

Advisors:	**Stéphane Cotin** Research Director at Inria Lille and Strasbourg, France
	Christian Duriez Research Director at Inria Lille, France
Reviewers:	**Adam Wittek** Professor at University of Western Australia, Perth, Australia
	François Faure Professor at University Joseph Fourier, Grenoble, France
Examiners:	**Ingerid Reinertsen** Research Scientist at SINTEF, Trondheim, Norway
	Laurent Thines Staff neurosurgeon, CHRU Lille, France
President:	**Jérôme Yelnik** Research Director at Inserm, Paris, France

Abstract

Deep brain stimulation is a neurosurgical treatment involving the permanent implantation of electrodes in the brain, to stimulate a specific deep structure. Electrical stimulation of some brain structures treats symptoms of motor or affective neurological disorders. The success of the operation relies on the electrode placement precision, which the goal is to maximize the therapeutic outcomes, and minimize the adverse effects. To do that, a pre-operative planning step determine the target coordinates to stimulate, as well as the electrode trajectory to reach it, thanks to a combination of medical images of the patient and numerical tools. However, intra-operative brain deformation, called *brain shift*, might invalidate the planning.

The contributions of this thesis rely on a biomechanical model of *brain shift* which comprises a mechanical model for deformation, as well as a model of cerebrospinal fluid leak. We present a pre-operative tool, based on our model, in order to provide to the surgeon an information on the deformation risks, that he could use to select a safe trajectory for the patient, even in the case of *brain shift*. Moreover, we propose an intra-operative registration method based on our biomechanical model, in order to compute the new location of anatomical structures. Finally, thanks to a model of insertion of the electrode and its interaction with brain tissue, we reproduce the operating protocol in order to compute the electrode curvature due to *brain shift*.

Keywords: Deep brain stimuation, brain shift, simulation, pre-operative planning, intra-operative registration, SOFA framework

Resumé en français

La stimulation cérébrale profonde est un traitement chirurgical impliquant l'implantation permanante d'électrodes dans le cerveau, afin de stimuler une zone spécifique. La stimulation électrique continue de certaines structures cérébrales traite des symptomes de troubles neurologiques moteurs ou affectifs. Le succès de l'opération repose sur la précision du placement de l'électrode dont le but est de maximiser les bénéfices thérapeutiques, et de minimiser les effets secondaires. Pour cela, une phase de plannification pre-opératoire détermine les coordonnées de la cible à stimuler, ainsi que la trajectoire de l'électrode pour atteindre la cible, à l'aide d'une combinaison d'images médicales du patient et d'outils numériques. Cependant, la déformation intra-opératoire du cerveau, appelée *brain shift*, peut rendre la plannification invalide.

Les contributions de cette thèse s'appuient sur un modèle biomécanique du *brain shift* qui comprend un modèle de déformation mécanique, ainsi qu'une modélisation de la fuite de liquide cérébro-spinal. Nous présentons un outil pré-opératoire, basé sur notre modèle, afin de fournir au chirurgien une information sur les risques de déformation, qu'il utilise pour sélectionner une trajectoire sécurisée pour le patient, même en cas de *brain shift*. Dans un deuxième temps, nous proposons une méthode de recalage intra-opératoire basée sur notre modèle biomécanique, afin de calculer la nouvelle position des structures anatomiques. Enfin, grâce à un modèle d'insertion de l'électrode et de son interaction avec les tissus cérébraux, nous reproduisons le protocole opératoire afin de calculer la déflexion de l'électrode due au *brain shift*.

Mots-clés: Stimulation cérébrale profonde, brain shift, simulation, plannification pre-opératoire, recalage intra-opératoire, SOFA framework

Contents

List of publications

- Bilger, A., Dequidt, J., Duriez, C., and Cotin, S. (2011). Biomechanical simulation of electrode migration for deep brain stimulation. *Proc. Medical Image Computing and Computer-Assisted Intervention (2011)*, 14(1):339--346
- Bilger, A., Essert, C., Duriez, C., and Cotin, S. (2012). Brain-shift aware risk map for Deep Brain Stimulation Planning. In *DBSMC - MICCAI 2012 Workshop on Deep Brain Stimulation Methodological Challenges*, Nice, France
- Bilger, A., Duriez, C., and Cotin, S. (2014c). Computation and visualization of risk assessment in deep brain stimulation planning. *Studies in health technology and informatics*, 196:29--35
- Bilger, A., Bardinet, E., Fernandez-Vidal, S., Duriez, C., Jannin, P., and Cotin, S. (2014b). Intra-operative Registration for Stereotactic Procedures driven by a combined Biomechanical Brain and CSF Model. In *ISBMS-International Symposium on Biomedical Simulation*, Strasbourg, France
- Bilger, A., Bardinet, E., Fernandez-Vidal, S., Duriez, C., Jannin, P., and Cotin, S. (2014a). Intra-operative Registration for Deep Brain Stimulation Procedures based on a Full Physics Head Model. In *MICCAI 2014 Workshop on Deep Brain Stimulation Methodological Challenges-2nd edition*, Boston, USA

Acronyms

AC Anterior Commissure. 24, 34, 85, 86

CSF Cerebro-Spinal Fluid. 26, 37, 38, 59, 61, 62, 65, 66, 69, 71, 74, 75, 77, 80, 93, 95, 98--100, 102, 105, 108, 109, 111, 115, 117--120, 128, 129, 131, 134, 137, 138, 141, 142

CT Computed Tomography. 19, 33--36, 64, 69, 85, 90, 93, 115, 116, 118--121, 128, 129

DBS Deep Brain Stimulation. 15--19, 26, 32, 33, 36, 37, 39, 61, 62, 80, 83, 85, 86, 89, 115--117, 128, 131, 133, 141, 143

FDA Federal Food and Drug Administration. 15

FEM Finite Element Method. 39, 40, 51, 52, 54, 58, 61, 62, 64, 66, 67, 76, 117, 128, 134, 138, 141

GPi Globus Pallidus interna. 17

GPU Graphics Processing Unit. 81

ICP Intracranial Pressure. 26, 37

iMRI Intraoperative Magnetic Resonance Imaging. 115, 116

MDD Major Depressive Disorder. 17

MRE Magnetic resonance elastography. 57, 58

MRI Magnetic resonance imaging. 19, 32, 34, 36, 57, 58, 64, 69, 85, 86, 88, 90, 93, 98, 115--121, 128, 129, 143

PC Posterior Commissure. 24, 34, 85, 86

PD Parkinson's Decease. 16--18, 26, 143

STN Subthalamic Nucleus. 15, 17, 26, 85, 86, 90, 124

TRD Treatment-Resistant Depression. 17

TS Tourette Syndrome. 17, 18

VIM Ventrointermediate nucleus. 15, 17, 124

VTA Volume of Tissue Activated. 90, 143

Introduction

Chapter 1

Abstract

This chapter introduces the thesis by presenting the medical context and the associated problems. First, deep brain stimulation is introduced with details: the goals, the treated pathologies and a description of the surgical procedure. Follows a presentation of the neuroanatomy involved with deep brain stimulation. Then, the operating protocol is precisely explained before a description of the encountered problems. To end this chapter, a description of our contributions are given.

Contents

1.1 Medical context

1.1.1 Description of Deep Brain Stimulation

Deep Brain Stimulation (DBS) has been first proposed by a French medical team in 1987[Benabid et al., 1987] to treat movement disorders by electrically stimulating the Ventrointermediate nucleus (VIM), a structure located deep in the brain tissue. The same group showed the effect of the electrical stimulation on the Subthalamic Nucleus (STN), another brain structure, in 1992 on a patient suffering from Parkinson's disease [Pollak et al., 1992], then on three patients in 1995 [Limousin et al., 1995]. In 1998, the group published a 1-year follow-up study on 20 patients [Limousin and Krack, 1998]. The efficiency of this method became famous and spread worldwide. DBS has been approved by the Federal Food and Drug Administration (FDA) for the treatment of several symptoms, starting by the approval of the treatment of tremor in 1997. Despite a 20 years old technique, we will see that some DBS mechanisms are not well understood, and the surgery still needs improvements.

(a) Neurostimulator Activa RC (b) Lead (c) Extension

Figure 1.1 – *Examples of DBS components (Medtronic). Images from www.medtronic.com/.*

DBS is the electrical stimulation of a specific area located deep into the brain tissue, but also refers to the surgery resulting to the stimulation. Two surgeries are necessary to implant the complete DBS system, which consists of three components:

1. The stimulating electrode (Fig. 1.1(b)) is a metallic interface between the targeted brain tissue and the rest of the electrical system. Usually, four electrodes are aligned on an insulated wire, each measuring 1.5 mm. The physician may choose different models of lead: one to spread the four electrodes over 10.5 mm (each electrodes are separated by 1.5 mm), or another spread over 7.5 mm (separated by 0.5 mm). The distal tip distance is also 1.5 mm and the diameter of the lead is 1.27 mm.
2. A neurostimulator (Fig. 1.1(a)) sends the electrical pulses and is powered by a battery. The device is usually implanted under the skin, just below the collarbone or in the abdominal area.
3. An extension (Fig. 1.1(c)) connects the electrodes and the neurostimulator.

The complete system is fully implanted with no exposed parts (outside the skin). The neurosurgical procedure consists in implanting the stimulating electrodes in the brain. The electrodes remain in the brain after the surgery and continuously deliver electrical impulses to targeted areas. The neurostimulator is usually implanted during a second surgery, where it is connected to the implanted electrodes. Figure 1.2 represents the DBS system implanted on a patient.

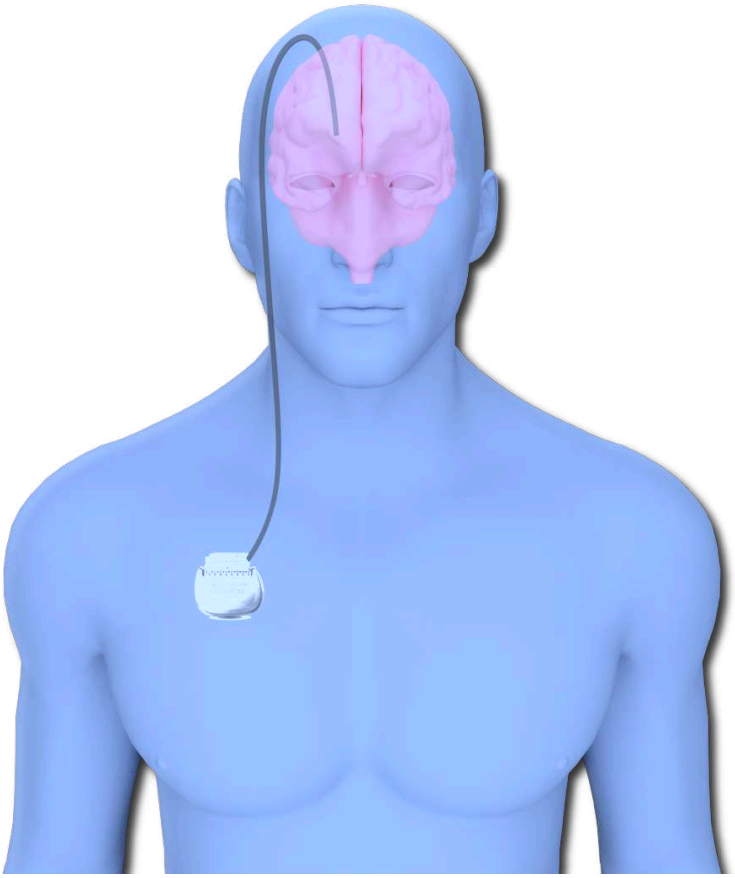

Figure 1.2 – *3D model representing a unilateral DBS system in a patient, with the three components (neurostimulator, extension and electrode)*

Bilaterality or unilaterality Both brain hemispheres are symmetrical in terms of anatomical structures, that is why the targeted structure in DBS is stimulated in both sides. In this case, two stimulating electrodes are implanted, one in each hemisphere.

However it has been observed that a number of patients have experienced a benefit from a single stimulation [Kumar et al., 1998]. Still, bilateral DBS is widely used compared to unilateral: 74% of the DBS procedures [Abosch et al., 2013].

1.1.2 The therapeutic effects of Deep Brain Stimulation

The electrical stimulation of a specific part of the brain can treat different diseases such as movement and affective disorders.

Parkinson's disease

Parkinson's Decease (PD) is a movement disorder. The main motor symptoms are:

1. Tremor: involuntary shaking or oscillating movement of part(s) of the body (hands, arms, legs, jaw or face). It is the most noticeable sign of the disease.

2. Bradykinesia: slowness of movement. The consequences are the appearance of an abnormal stillness, a decrease in facial expressivity and a difficulty to perform everyday movements.
3. Rigidity: stiffness and resistance of the limbs, neck and trunk.
4. Postural instability: a tendency to be unstable when standing upright.

Some other symptoms, non related to movements and coordination such as loss of sense of smell, depression, constipation, mood disorders, sleep disturbances etc, often appear during the disease. The disease usually starts between 45 and 70 years old. The study [Hirtz et al., 2007] estimated the incidence rate of the disease in developed countries at 14 per 100,000 person-years.

The disease is due to the death of dopamine-generating cells in the substantia nigra. There is no cure for PD. However, medications can slow down the disease progression or decrease the symptoms. For instance, Levodop is widely used to fill the lack of dopamine in the substantia nigra in order to diminish the motor symptoms. PD symptoms continue and worsen over time. When symptoms cannot be controlled with medications, physicians can envisage a DBS system implantation. It has been observed [Pollak et al., 1992] that the electrical stimulation of the STN induced akinesia[1] alleviation. Other structures can be targeted such as the globus pallidus interna (Globus Pallidus interna (GPi)) and the VIM. According to [Abosch et al., 2013], 94% of the DBS treating PD targeted the subthalamic nucleus, 3% the GPi and 3% the VIM. The disease is not cured by DBS, but it can remove or diminish the symptoms and greatly improve the patient's quality of life. 70% of the DBS surgeries aim at treating PD [Abosch et al., 2013].

Chronic pain

According to [Debono et al., 2013], chronic pain is "defined as pain that persists for longer than 3 to 6 months with persistence beyond “normal healing time” of an injury". 56 patients were treated by DBS for different forms of chronic pain in [Rasche et al., 2006]. In the study, the authors conclude that DBS could be a treatment for carefully selected patients. The structures targeted were the lateral somatosensory thalamus and the periventricular gray region.

Major depression

According to [Fava, 2003], 50% to 60% of the patients suffering from Major Depressive Disorder (MDD) do not response adequately to antidepressant treatment. When at least two trials with antidepressants from different phramacologic classes fail to achieve significant improvement, the depression is considered resistant. In addition to phramacotherapy, other treatments, such as electroconvulsive therapy, transcranial magnetic stimulation, vagal nerve stimulation and ablative neurosurgery, fail to achieve clinical improvement of Treatment-Resistant Depression (TRD) without serious adverse effects. In 2005, Mayberg et al. run a trial of DBS for treating TRD on six patients, stimulating the subgenual cingulate white matter, a brain structure in the *Brodman area 25* observed to be overactive in TRD. They conclude on the efficiency appearance of the stimulation despite the limitations of the study. In 2012, the review by Anderson et al. on TRD treated by DBS in clinical trials since 2005 [Mayberg et al., 2005] highlights the difficulty to select an optimal target to stimulate and the small patient number treated, despite encouraging results.

Tourette syndrome / Tic disorders

Tics are involuntary, sudden and repeated sounds or movements. The symptoms (motor or phonic or both) are considered persistent after one year. Tourette Syndrome (TS) is a persistent tic disorder with motor and vocal tics, usually beginning before age 18.

[1] absence, poverty, or loss of control of voluntary muscle movements.

Like major depression, severe treatment resistant tic disorders have been studied to be treated by DBS, but the treatment is still experimental. However the number of patient treated (in 2014 more than 100 TS patients from different studies since 1999 [Visser-Vandewalle et al., 2014]) experienced reduction of tics. In TS, nine different brain structures have been targeted for a potential stimulation spot [Visser-Vandewalle et al., 2014] in the following areas: thalamus, globus pallidus internus (postoventrolateral and anteromedial part), globus pallidus externus, internal capsule and nucleus accumbens.

Other clinical applications

DBS is also considered to treat other medication resistant disorders such as epilepsy, schizophrenia, obesity etc.

Conclusion

Although most of the DBS surgeries are performed to treat PD, the procedure has proved its efficiency for other disorders such as chronic pain, major depression or Tourette syndrome. With improved knowledge, some experimental trials tends to treat other disorders such as epilepsy, schizophrenia or obesity. The advances in DBS enable to better understand the brain functions. Moreover, more complex hardware is in development to offer more possibilities to the electrical pattern for instance. Regarding the growing number of publications per year (Figure 1.3) DBS remains a challenge in research.Among the 106 articles relating to clinical neurosurgery with more than 400 citations, six are about DBS [Ponce and Lozano, 2014].

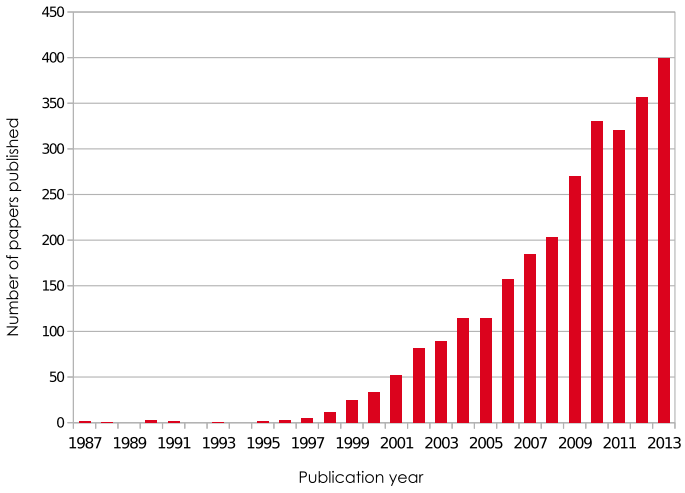

Figure 1.3 – *Number of publications containing "Deep brain stimulation" in the title in PubMed.*

1.2 Neuroanatomy

This section describes parts of the anatomy of the central nervous system and the surrounding structures. All of these structures cannot be exhaustively described in this manuscript, but the reader can learn more in the book [Thines et al., 2008], as most of the anatomical description of this section are based on this neuroanatomical atlas. The structures mentioned here are useful for the understanding of the problems

and methods presented thereafter. Some of them appear in the model presented in Chapter 2. In addition to the anatomical description, we provide information about the visibility of the structures in different imaging modalities.

This section is illustrated with 3D models of the anatomical structures, as well as contours of the structures segmented on images (CT and MRI) of DBS patients. Post-mortem photographs are available in [Thines et al., 2008].

1.2.1 Neuroimaging

Neurosurgeons need a representation of the interior of the patient's head to prepare the intervention or to check the placement of the electrodes. Medical imaging reveals the internal structures in the body. In this section, we focus only on the two main techniques used in DBS.

Computed Tomography (CT) and Magnetic resonance imaging (MRI) used in DBS provide 3D images in which each voxel intensity (greyscale images) gives a physical information of the corresponding tissue area.

Computed Tomography

CT uses X-rays emitted to the head of the patient. A X-ray sensor is placed on the other side and measure the amount of absorption of the x-rays. An algorithm converts the raw data into a cross-sectional image. The figure 1.5 shows an example of three sections of a CT image.

The voxel intensity measures the X-ray attenuation of the corresponding tissue volume. Air and fluid, which do not attenuate X-ray, appear darker than brain or bone.

Magnetic Resonance Imaging

MRI uses a magnetic field around the head of the patient. The hydrogen atoms in the tissue are excited and emit a radio frequency which is then detected. An algorithm converts the detected signal into a 3D image.

The resolution of the image depends on the magnet strength. It is measured in tesla (T). While most of the MRI scanners use a 1.5 T magnet, the more powerful scanner uses a 11.75 T (in 2014).

The intensities and contrasts of the image depends on imaging parameters. The main sequences are T1 weighted, T2 weighted and PD weighted. An example of T1-weighted MRI is depicted in Figure 1.9.

CT vs MRI

There is no point to compare CT and MRI images as it does not show the same things. As an example, the bones in a CT are easily visible, but not in a MRI. In opposite, internal brain structures, such as the targeted structure, can be seen with more contrast in a MRI. However, both techniques have other pros and cons. For instance, a MRI scan is not compatible with metallic objects. The stereotactic frame is not compatible with MRI, whereas it is clearly visible in a CT. In the other hand, CT emit radiations, which is harmful for the patient (and medical staff). For these reasons, both techniques are used for the procedure, and the images can be fused. The fusion takes advantage of both imaging methods. The visibility of the different relevant structures in images will be discussed in the following sections.

1.2.2 Skin / Scalp

The skin is the outer organ covering almost the whole body. It is composed of multiple layers and is between 2-3 mm thick. The scalp is the skin on the head excluding the face and is usually covered by hairs.

1.2.3 Skull

The skull is a bony structure enclosing and protecting the brain. Jaws are supported by the skull. A 3D representation of the skull is depicted in the figure 1.4.

The skull is composed of two parts (in the adult):

1. the neurocranium is a cavity surrounding the brain and brainstem. The neurocranium itself is composed of:
   a) the endocranium is the inner part of the neurocranium (see figure 1.5).
   b) the calvaria is the upper part of the neurocranium.
2. the viscerocranium is made of facial bones

The skull has multiple orifices through which blood vessels and nerves enter and exit.

The cranial bones can reach 2000 Hounsfield units (measure the radiodensity), whereas the brain has an X-ray attenuation of less than 100 HU[Boris et al., 1987]. This high difference allows us to clearly visualize the difference between both materials in a CT scan. The figure 1.5 shows the contour of the segmented skull. We notice the high contrast between the skull and the brain tissue. On the contrary, bones are difficult to visualize in a MR image due to a weak signal [Wang et al., 2009].

Due to its role to protect the brain, the skull is very stiff. The Young's modulus of the skull is approximately 10^{10} Pa [van Essen et al., 2005].

1.2.4 Meninges

Between the endocranium and the brain, the meninges surround the central nervous system. They consist of 3 layers: the dura mater, the arachnoid and the pia mater. The arachnoid and the pia mater together compose the leptomeninges. The order of these layers is depicted in the figure 1.6.

Dura Mater

This layer is the outer layer and cover the inner part of the endocranium. It is a very stiff and thick membrane. The dura mater consists of two types of layers: the endosteal, which is in contact with the endocranium, and the inner meningeal with four folds:

- the falx cerebri (more details in section 1.2.6)
- the tentorium cerebelli
- the falx cerebelli
- the diaphragma sellae

Most of the endosteal dura is vascular.

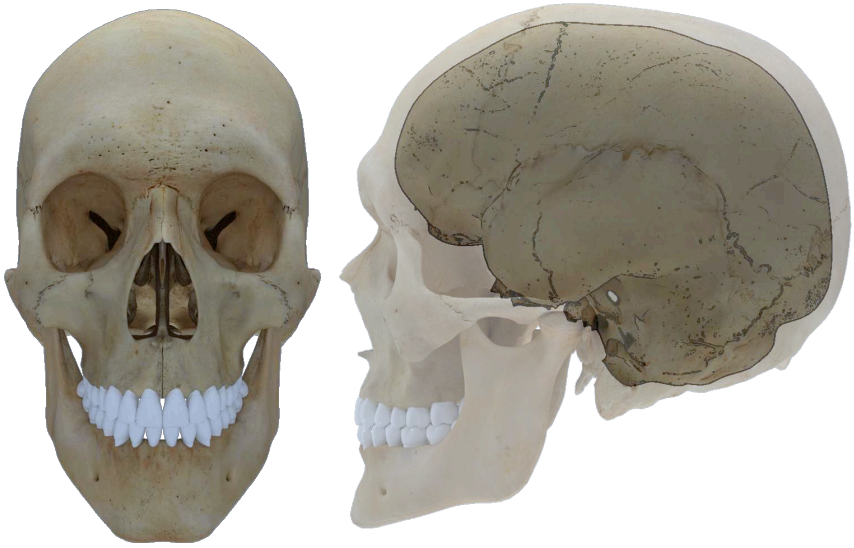

Figure 1.4 – *3D model representing a human skull. Frontal view on the left and sagittal view on the right. The sagittal view shows the exterior of the skull in transparent and the endocranium in solid colors with highlighted edges.*

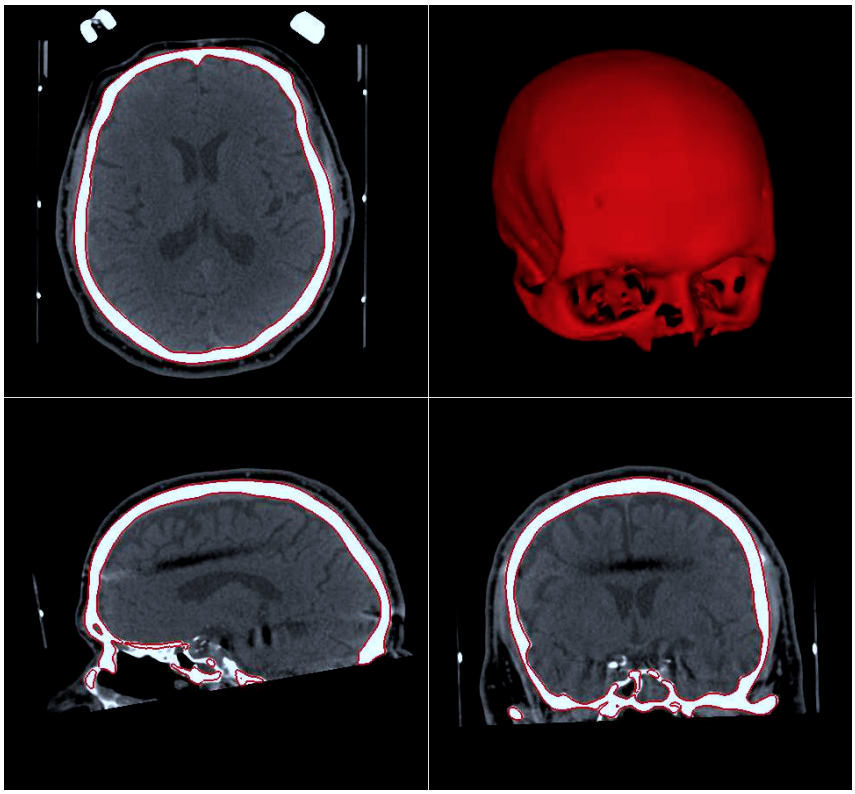

Figure 1.5 – *Pre-operative CT scan of a DBS patient in four views: transverse (top left), sagittal (bottom left), coronal (bottom right) and 3D view (top right). The contour in red is the segmentation of the skull (the stereotactic frame is already fixed on the skull in this image).*

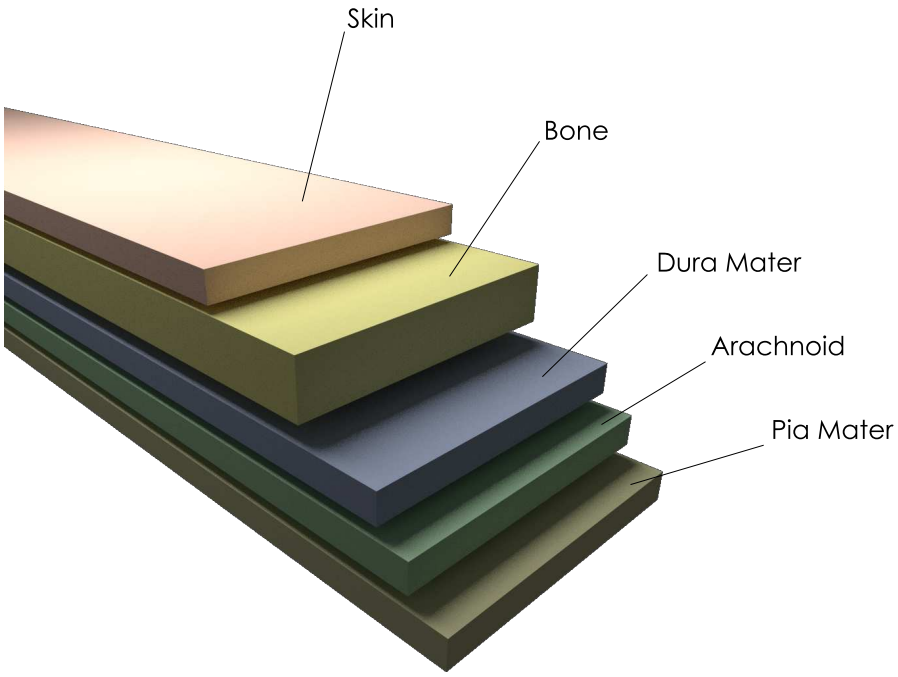

Figure 1.6 – *3D model representing the different layers between the skin and the brain.*

Arachnoid Mater

Arachnoid is the layer between the dura mater and the pia mater. This layer is not vascularized. Arachnoid does not follow the folds of the brain.

Pia mater

The surrounding membrane of the brain. Pia mater follows the convolution of the brain, contrary to the arachnoid. The layer contains the cortical blood vessels.

Spaces between Meninges

Subarachnoid Space Because the pia mater follows the brain sulci, and the arachnoid does not, spaces exist between both layers. It is called subarachnoid space and is filled with cerebrospinal fluid (see section 1.2.8). The subarachnoid space is visible in CT scans since the differences of density between fluid and brain tissue and bone.

Extradural Space Space between the endocranium and the dura mater. This space appears only in some pathologies.

Subdural Space Space between the dura mater and the arachnoid. This space appears only in some pathologies.

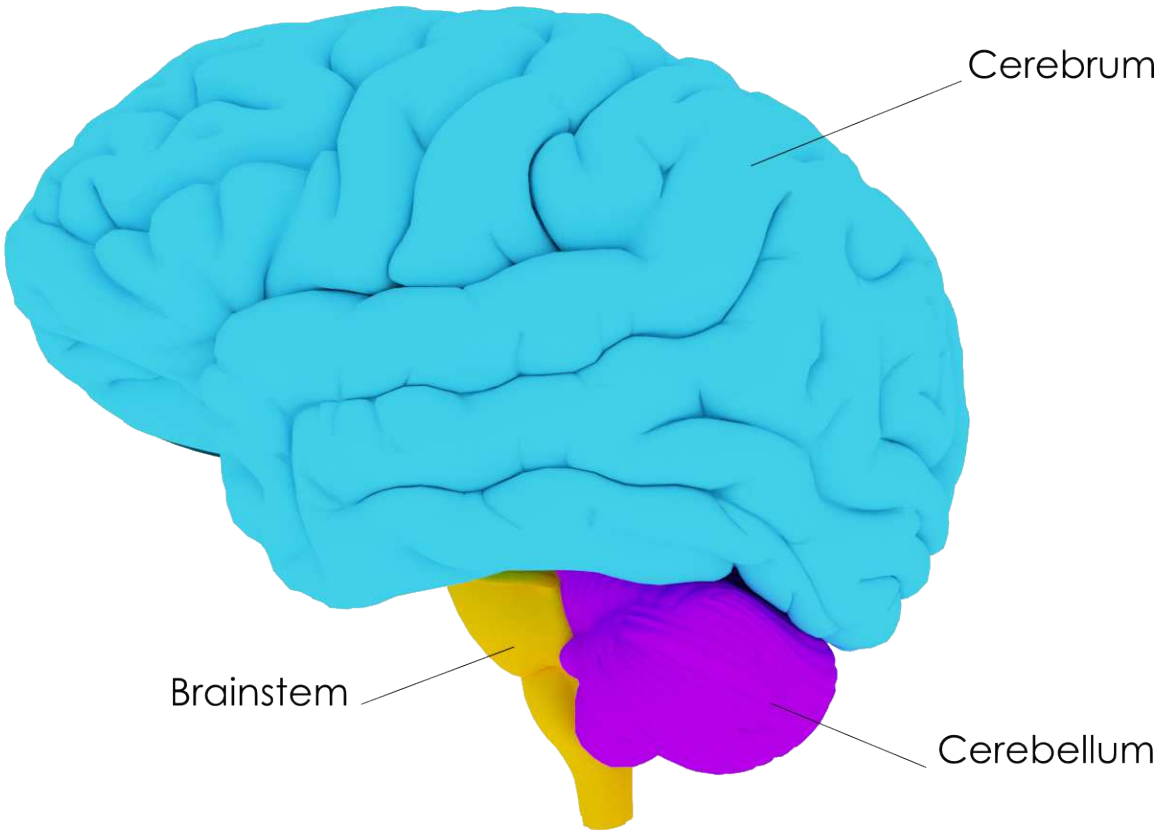

Figure 1.7 – *3D model representing the brain in sagittal view. The three main parts (cerebrum, cerebellum and brainstem) are represented with a different color.*

1.2.5 Brain

The brain is contained in the cranial vault. This organ is the center of the central nervous system and controls the rest of the body through the spinal cord. It is covered by pia mater and floats in cerebrospinal fluid (see section 1.2.8).

The three different parts of the brain (depicted in the figure 1.7) are:

- the cerebrum: largest and superior-most part. It is divided into two cerebral hemispheres.
- the brainstem: posterior part of the brain, linked to the spinal cord.
- the cerebellum: located at the rear of the brain, beneath the cerebrum, behind the brainstem. Like the cerebrum, the cerebellum is divided into two cerebellar hemispheres.

Inner meningeal dura mater separates the different parts:

- the cerebellum and the cerebrum is separated by the tentorium cerebelli.
- the falx cerebri separates the two cerebral hemispheres
- the falx cerebelli seperates the two cerebellar hemispheres

The cerebral cortex is the outermost layer of the cerebrum. It is composed of neural tissue (neurons and neuroglia), called grey matter. This layer is folded to expand its surface[Toro et al., 2008]. A depression in

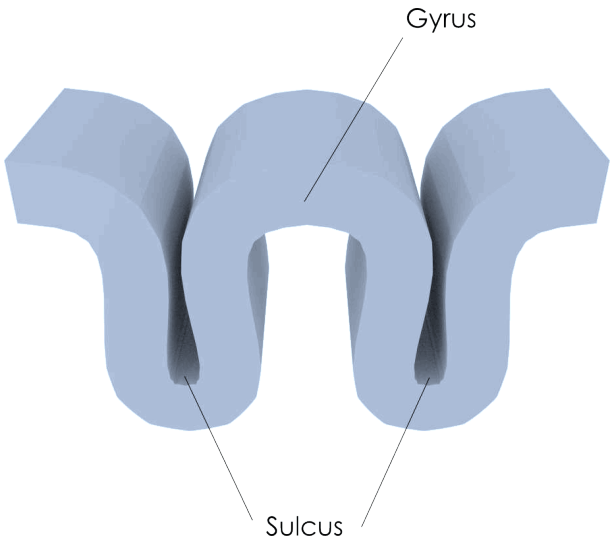

Figure 1.8 – *3D model representing the convoluted surface of the cortex.*

the convoluted is called sulcus (plural sulci) and a ridge is called a gyrus (plural gyri) (see figure 1.8). Most of pial blood vessels are found in the sulci [Duvernoy et al., 1981]. Information about the sulci are therefore hints on the vessels location.

The cerebral cortex is nearly symmetrical in both cerebral hemispheres. It is divided into four lobes: the frontal lobe, the parietal lobe, the occipital lobe and the temporal lobe. The functions of the brain are also symmetric but the left hemisphere interacts with the right side of the body and vice versa.

Beneath the cortex, white matter transmit signals from one region of the cerebrum to another. White matter consist of nerve fibers and myelin.

Located in the central part of the cerebrum, a pair of symmetrical lateral ventricles contains cerebrospinal fluid. The ventricular system is also composed of the third and fourth ventricles. The ventricular system is detailed in Section 1.2.9.

The Anterior Commissure (AC) and the Posterior Commissure (PC) are white matter tracts connecting the two cerebral hemispheres across the midline. The Talairach coordinate system [Talairach and Tournoux, 1988] uses these two landmarks to locate others brain structures.

Mechanical properties We have seen the brain is composed of several types of tissue: white and grey matter. This means also different mechanical properties for each type of tissue [Kaster et al., 2011; Kruse et al., 2008; Mehdizadeh et al., 2008]. We will see later that a part of the ventricular system is included in the brain. It is mainly composed fluid, which adds more heterogeneity in the brain behavior. In addition, the tissue are composed of fibers, which adds anisotropy in the tissue structure. However, the mechanical anisotropy has not been comprehensively established [Bilston, 2011].

1.2.6 Falx cerebri

The falx cerebri is dura mater (see section 1.2.4) separating both cerebral hemispheres. The figure 1.10 represents the falx cerebri in three different views of the cerebrum and the lateral ventricles.

Mechanical properties As falx cerebri is composed of dura mater, the structure is deformable but very strong. Dura mater is a strong membrane that has been used for artificial heart valves [Noort et al., 1981].

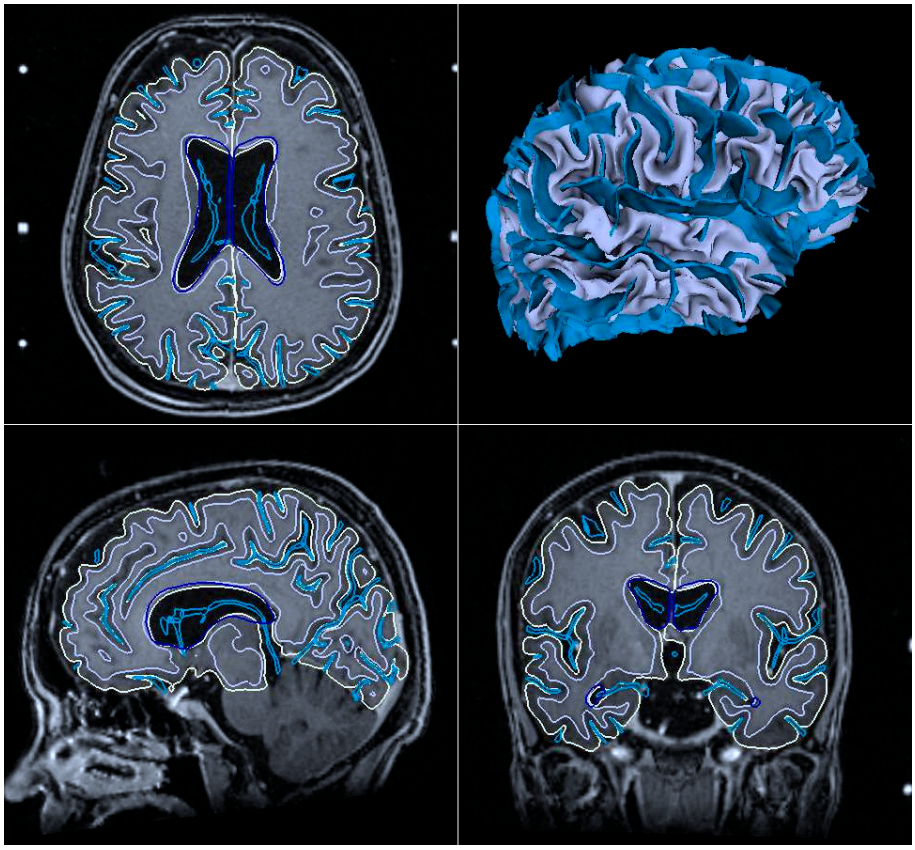

Figure 1.9 – *Brain MRI in transverse (top left), sagittal (bottom left), coronal (bottom right) and 3D view (top right). The following structures and interfaces has been segmented:*
- *Pia mater*
- *Sulci contour*
- *Gray matter/White matter interface*
- *Lateral ventricles contour*

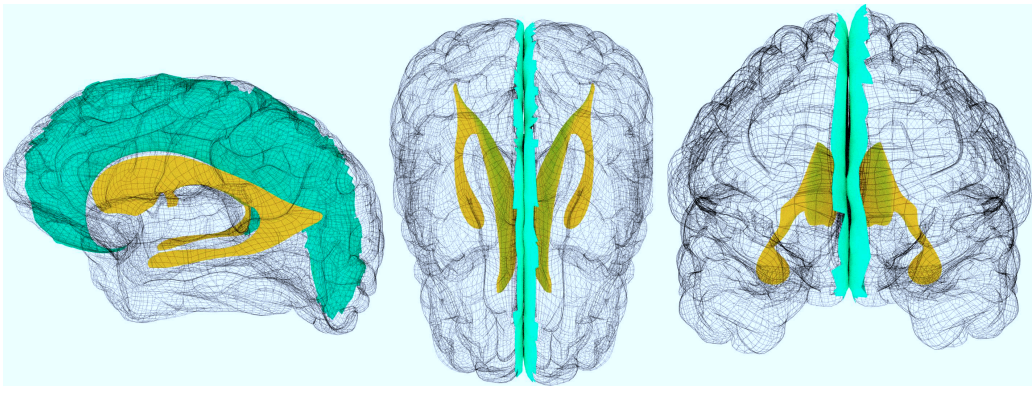

Figure 1.10 – *Sagittal view on the left, axial view on the middle and coronal view on the right showing the falx cerebri and the lateral ventricles. The cerebrum is rendered in wireframe and the falx cerebri and ventricles in different solid colors:*
- *Lateral ventricles*
- *Falx cerebri*
- *Cerebrum (wireframe)*

Falx cerebri can be deformed when the surgeon directly manipulates it in open surgery, but in minimally invasive surgery, such as DBS, the structure does not deform.

1.2.7 Blood vessels / Sulci

Blood vessels are a network of hollow tubes transporting blood through the body. Arteries are vessels transporting blood from the heart, and veins transport blood to the heart.

The brain is also supplied by blood through vessels. Oxygen, glucose and nutriments are provided by arteries, while veins carry deoxygenated blood back to the heart.

The figures 1.11, 1.12 and 1.13 represent the blood vessels network in the whole head. The figure 1.14 only shows the blood vessels on the surface of the brain.

1.2.8 Cerebrospinal fluid

Cerebro-Spinal Fluid (CSF) is a liquid surrounding the central nervous system (brain and spinal cord). In the brain, CSF is found in the subarachnoid space (see section 1.2.4) as well as in the ventricular system (section 1.2.9). Its global volume is about 150 mL (125 mL in the subarachnoid spaces including in the spinal cord and 25 mL in the ventricles). CSF is continuously produced by the choroid plexus, a nerve complex in the ventricles. The production is about 500 mL a day. CSF is absorbed by the dural venous sinuses, and in small quantity by the lymphatic channels. It circulates from the lateral ventricles to the third ventricle then to the fourth ventricle. From the fourth ventricle, the CSF can reach the subarachnoid space. The liquid is essentially composed of water, but also small quantities of glucose and proteins.

The CSF acts as mechanical protection of the brain. When the brain deforms violently (e.g. due to a car accident), the liquid cushions the impact onto the bone structures. It also supports the central nervous system at rest. The volume of CSF can be modified depending of the Intracranial Pressure (ICP): if a mass lesion grows, CSF is absorbed more rapidly to allow more space of the mass lesion, and the ICP is maintained.

1.2.9 Ventricular System

The ventricular system has already been mentioned in Section 1.2.5 and 1.2.8. It is composed of the lateral ventricles, the third ventricle and the fourth ventricle. It contains CSF. The ventricular system is depicted in the figure 1.15.

1.2.10 Basal ganglia

Basal ganglia are a set of nuclei located in the base of the cerebrum, deep in the white mater. They comprise the caudate nucleus, the putamen and the pallidum. Other nuclei are associated with the basal ganglia such as the STN or the substantia nigra. These structures are represented in the figure 1.16. The STN is the structure targeted in 94% of the DBS treating PD. It is a lens-shaped structure measuring 10 mm x 8 mm x 3 mm. Three functional territories have been observed from tracing experiments in the monkey [Karachi et al., 2002]. The sensorimotor territory, the associative territory and the limbic territory are depicted in the figure 1.17. All neurons with movement-related activity are located in the sensorimotor region [Baltuch and Stern, 2007].

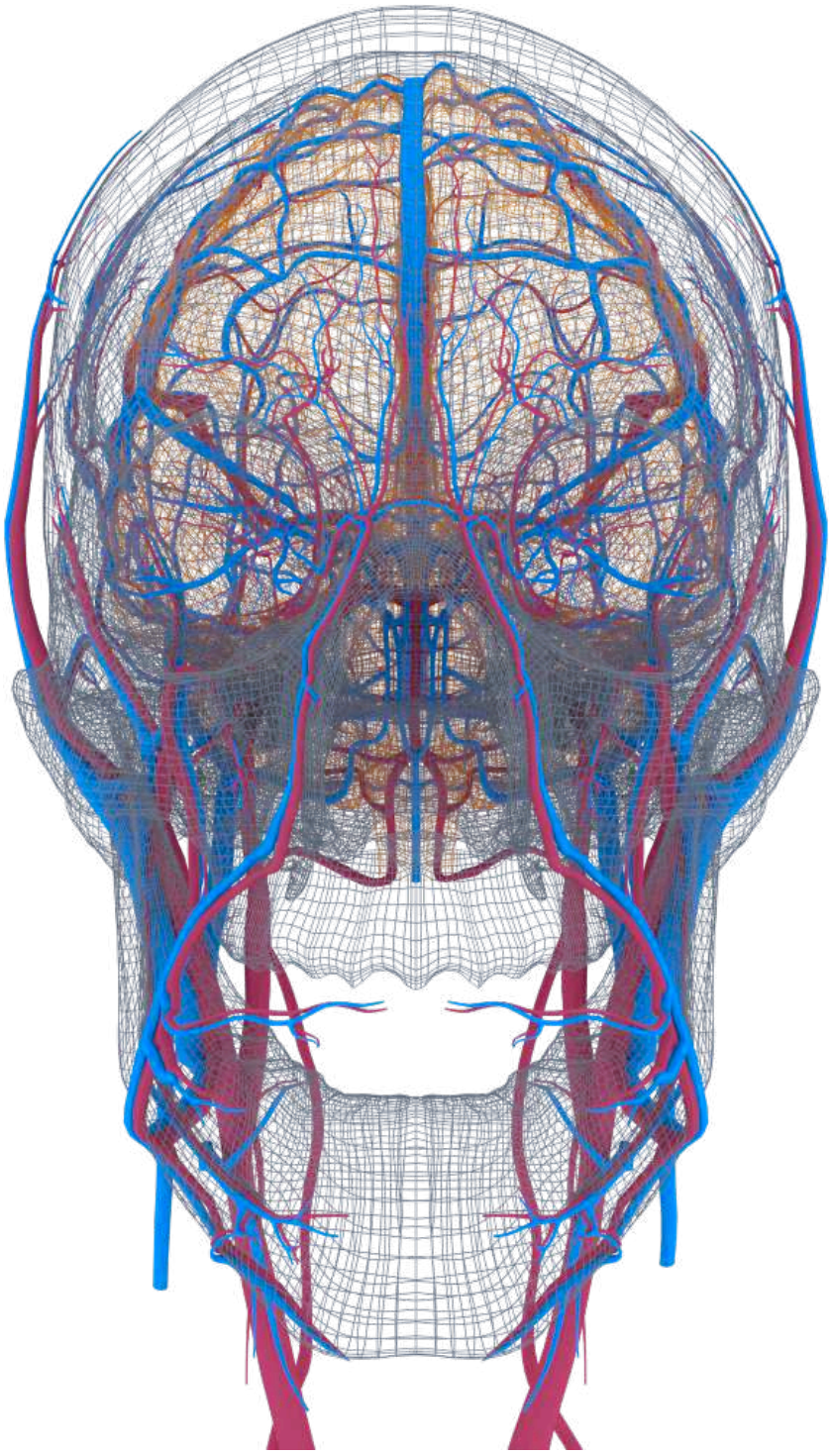

Figure 1.11 – *Blood vessels network in the head. The following structures are depicted:*
- *Arteries*
- *Veins*
- *Pia mater (wireframe)*
- *Cranial bones surface (wireframe)*

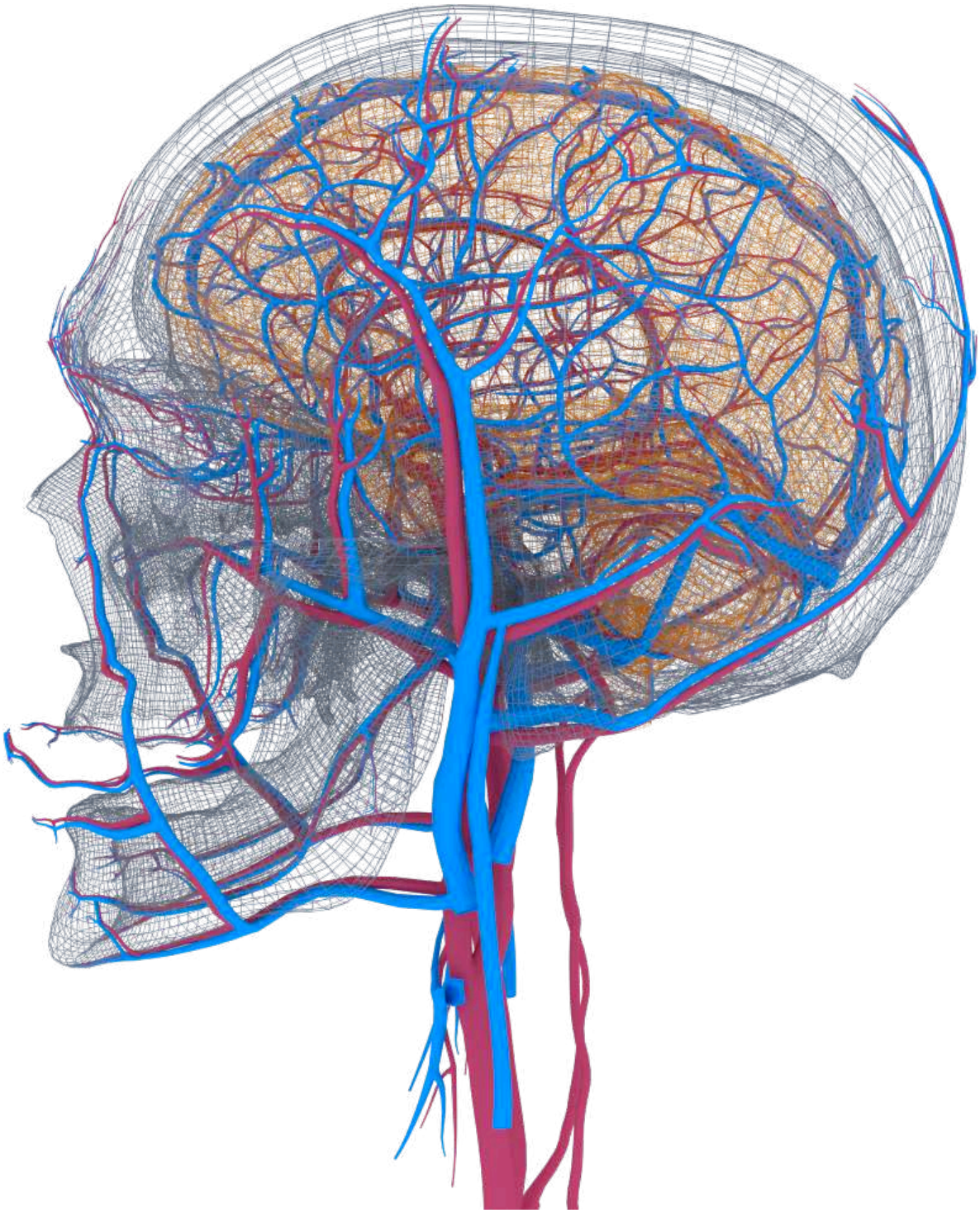

Figure 1.12 – *Blood vessels network in the head. The following structures are depicted:*
- *Arteries*
- *Veins*
- *Pia mater (wireframe)*
- *Cranial bones surface (wireframe)*

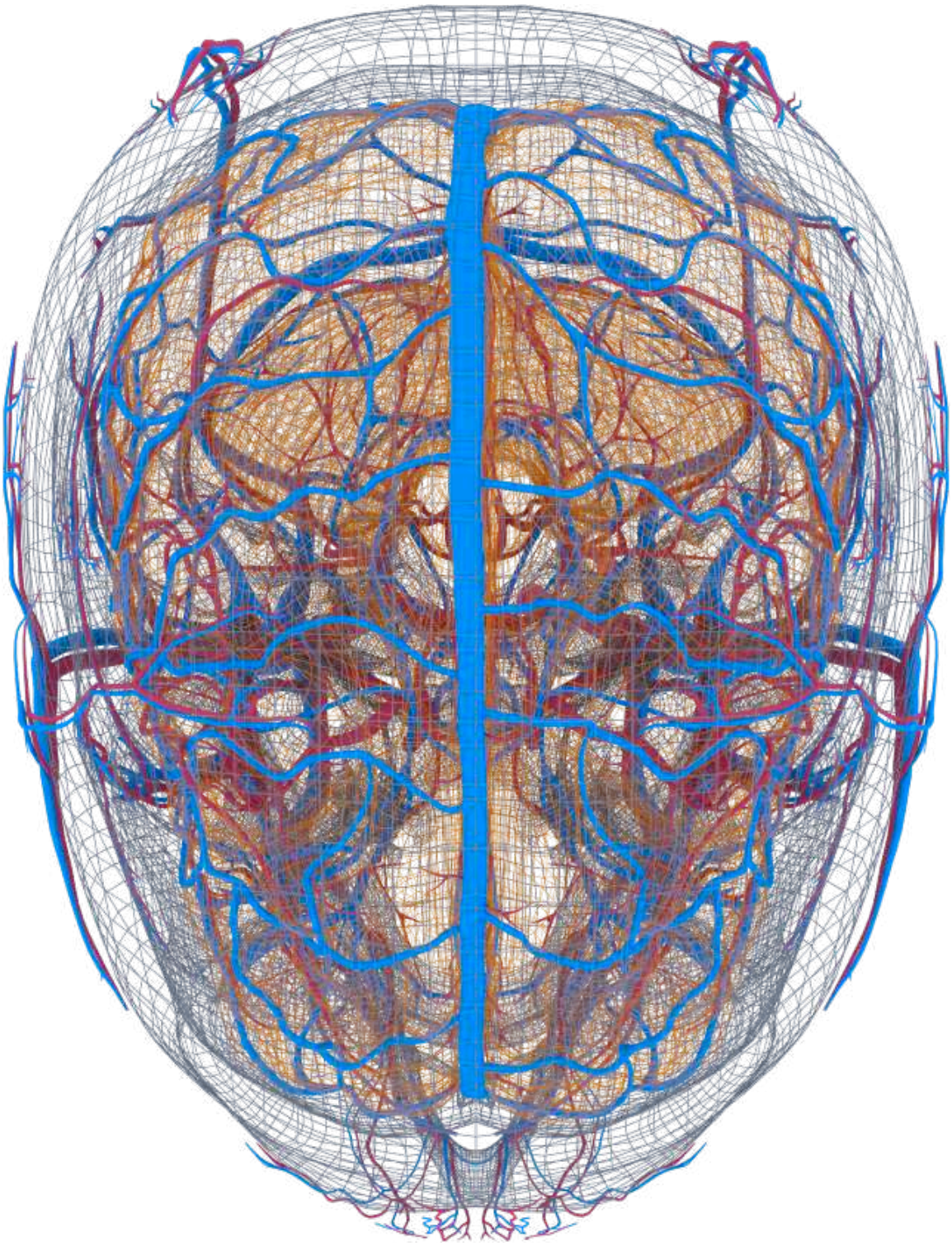

Figure 1.13 – *Blood vessels network in the head. The following structures are depicted:*
- *Arteries*
- *Veins*
- *Pia mater (wireframe)*
- *Cranial bones surface (wireframe)*

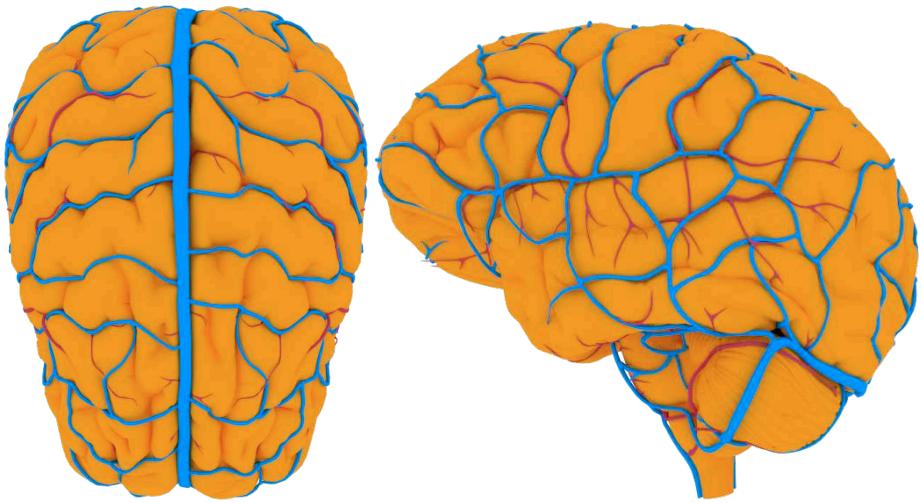

Figure 1.14 – *Vascular anatomy in the brain. The following structures are depicted:*
- *Arteries*
- *Veins*
- *Pia mater*

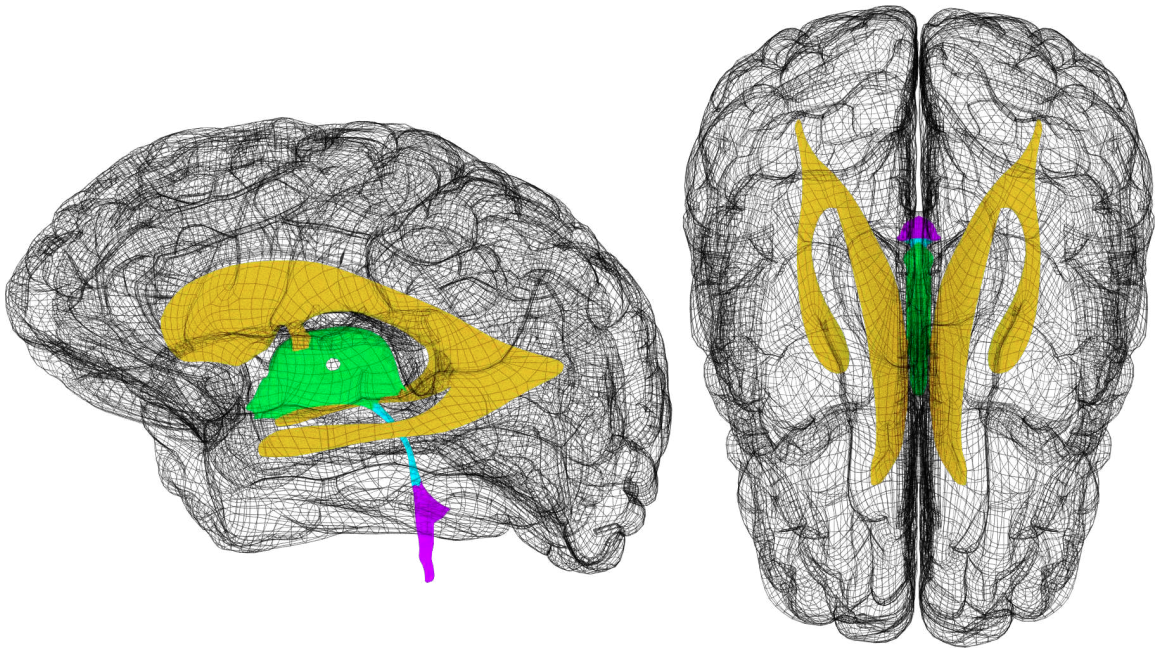

Figure 1.15 – *3D model representing the ventricular system (sagittal view on the left and axial view on the right). The cerebrum is rendered in wireframe and the ventricular system in different solid colors:*
- *Lateral ventricles*
- *Thrid ventricle*
- *Fourth ventricle*
- *Cerebral aquaduct*
- *Cerebrum (wireframe)*

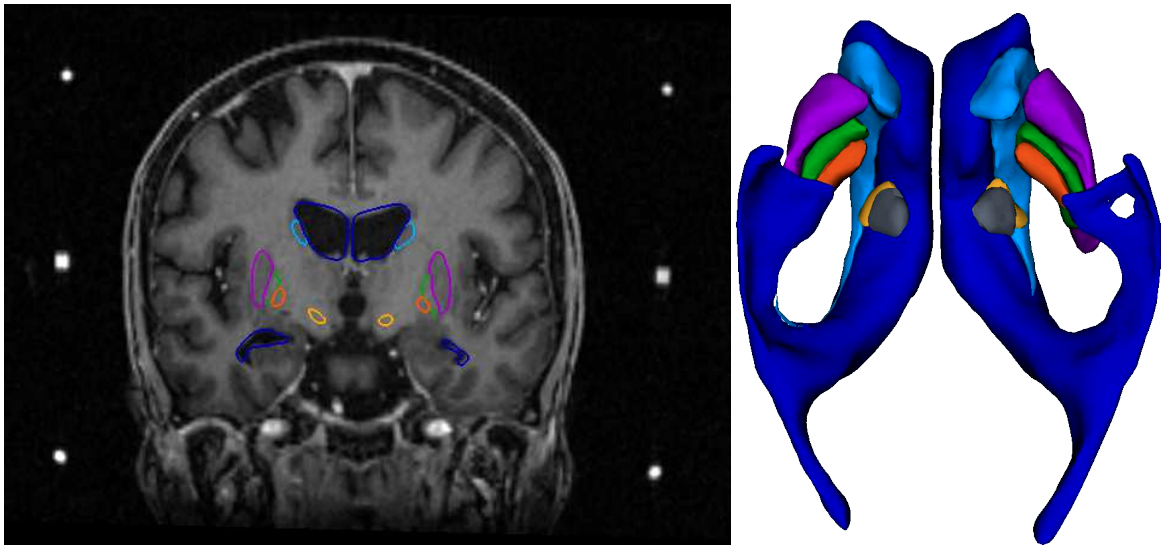

Figure 1.16 – *Basal Ganglia: MRI coronal view (left) and 3D view from the bottom (left).*
- *Lateral ventricles*
- *STN*
- *Substantia nigra*
- *Putamen*
- *GPi*
- *GPe*
- *Caudate nucleus*

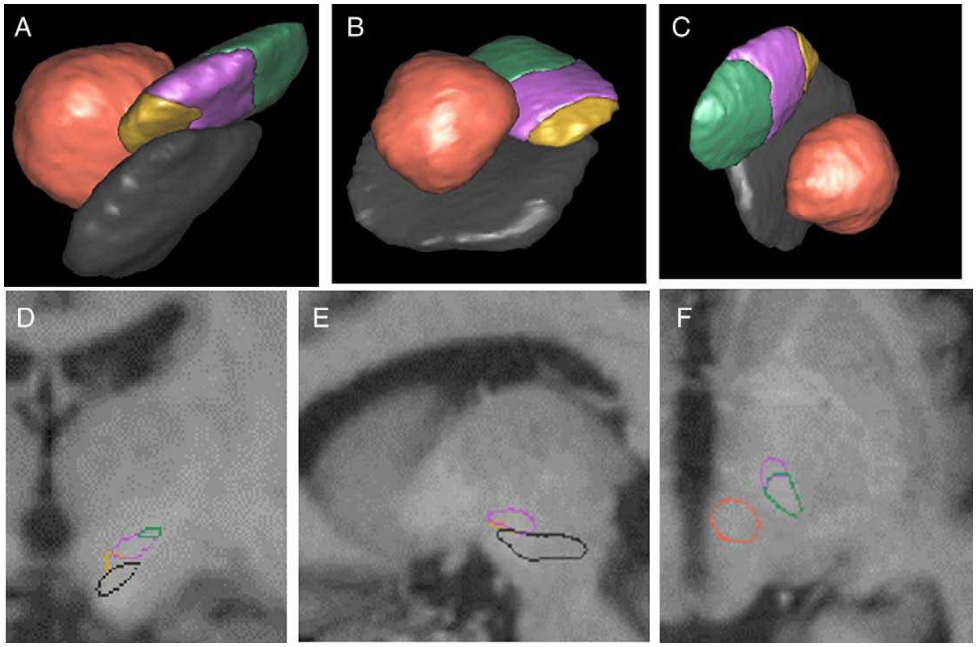

Figure 1.17 – *The three functional territories of the subthalamic nucleus as inferred from tracing experiments in the monkey [Karachi et al., 2002]. The sensorimotor territory is in green, the associative territory in purple, and the limbic territory in yellow. Anterior view (A), lateral view (B) and superior view (C) with the red nucleus (in orange) and substantia nigra (in grey). Frontal (D), sagittal (D) and horizontal (E) sections of the same structures after fusion with the T1 MRI. Courtesy of [Yelnik et al., 2007]*

1.3 Operating protocol

This section describes the procedural steps involved in DBS surgery. In an international survey over 143 DBS centers,[Abosch et al., 2013] identified 19 steps which they grouped into three phases: before (pre-operative), during (intra-operative) and after (post-operative) the surgery. Figure 1.18 summarizes the procedural steps during the three phases. The manuscript follows the same scheme, but voluntary omitting steps not related to the work of this thesis or the understanding of the problem. The sterilization, the anesthesia concerns and the continuous follow-up of the patient are not treated here. The description of the procedural steps is based on the operating protocol in effect in the DBS centers of Rennes (Hôpital Ponchaillou) and of Paris (Hôpital Pitié-Salpêtrière).

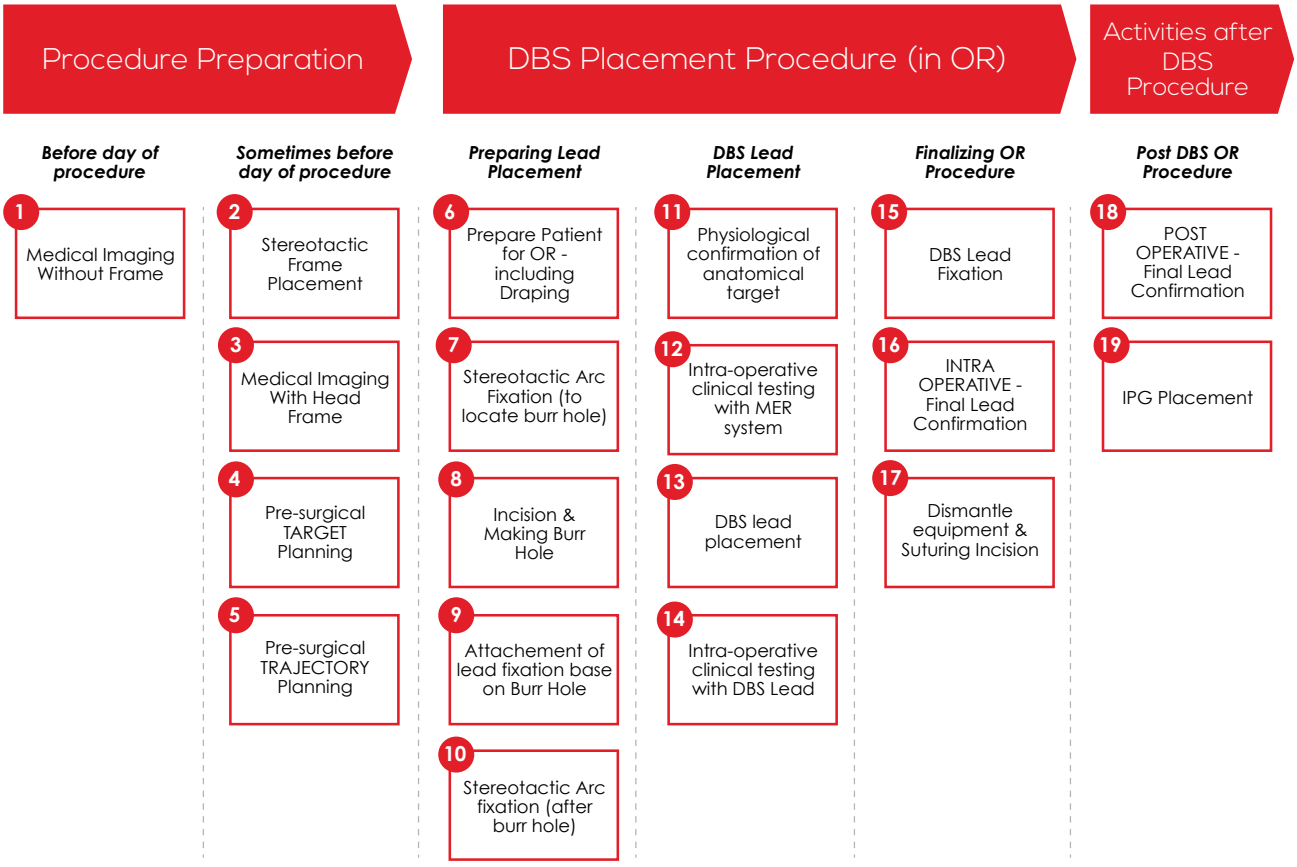

Figure 1.18 – *Procedural steps in DBS surgery (from [Abosch et al., 2013]). The chronological order of the surgery is from left to right and from top to down.*

1.3.1 Pre-operative procedural steps

Inclusion acquisition

The first step involved in the DBS procedure is to acquire a medical image of the patient, without any frame. The modality of the image is mostly an MRI (83% [Abosch et al., 2013]) because of its high contrast

on the brain structures. This image can be used to determine the eligibility of the patient for the treatment of the symptoms by DBS. A patient could be not eligible because of structural anomalies such as severa atrophy, leukoencephalopathy and multiple lacunae [Dormont et al., 2010] or difficulties to find safe solutions to implant the electrodes. Note that the pre-operative MRI can be used later, during the pre-operative planning.

Stereotactic Frame Placement

The day before the surgery (Hôpital Pitié-Salpêtrière), or the same day (Hôpital Ponchaillou), a stereotactic frame is placed on the patient's head. The frame is fixed to the skull under local anesthesia with four screws not to allow any relative movement between the frame and the skull during the surgery. It acts as a 3D frame to locate very precisely a target in the brain by setting two angles and a translation. An example of stereotactic frame is visible in the figure 1.19.

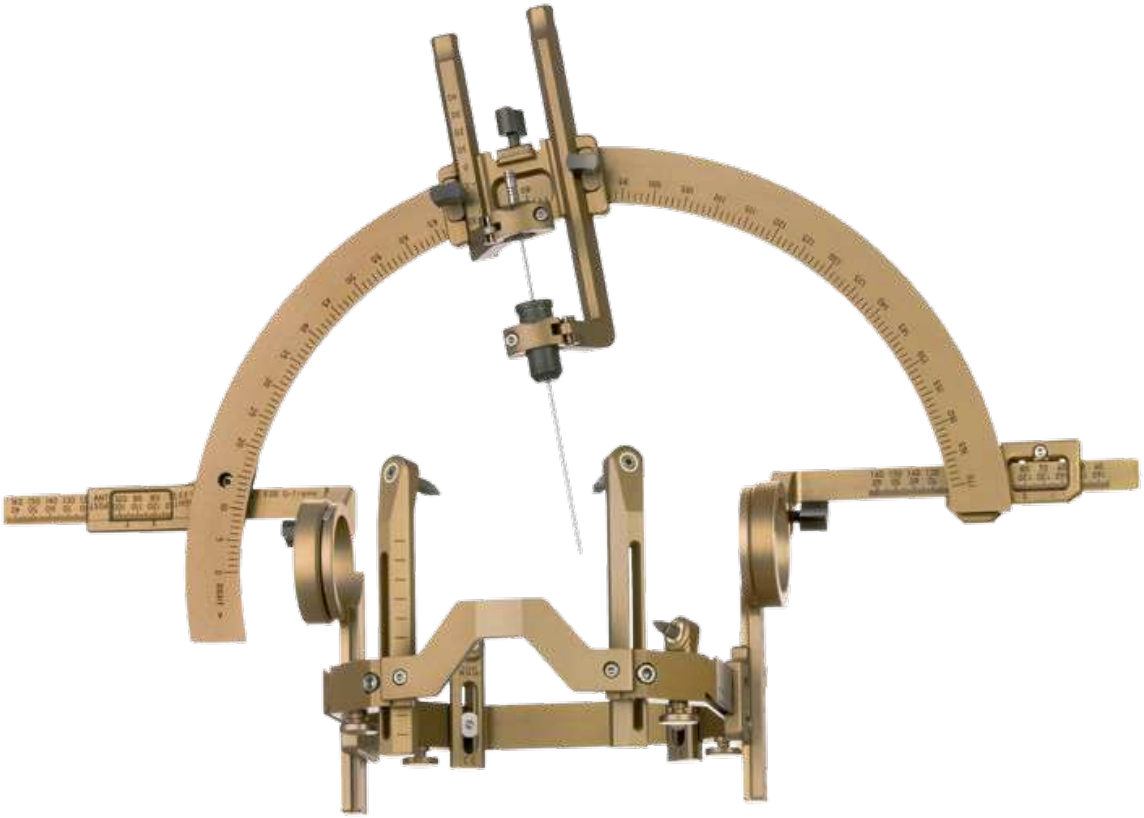

Figure 1.19 – *Photograph of a stereotactic frame (Leksell Electa)*

Pre-operative CT scan

Another medical image is acquired once the frame is setup. In 69% of the cases, it is a CT scan because the frame is incompatible with an MRI device. Moreover, CT scans show clearly the metal parts in the image. In the figure 1.5, we can observe the artefacts of the frame in a pre-operative CT scan. This image will be a reference to identify anatomical location according to the frame.

Pre-operative planning: target

Just before the surgery, the combination of two pre-operative images (usually MRI without frame and CT with frame) is used to determine the coordinates of the target to stimulate in the stereotactic frame. Because the structures targeted in stereotactic surgery are usually not clearly visible in the common medical images, indirect methods exist to determine the target coordinates. For instance, the company Leksell provides a software, SurgiPlan, which computes the coordinates based on formulas using the AC-PC line. However, in this thesis, we rely on a histological atlas of the basal ganglia [Yelnik et al., 2007]: a registration of this atlas on the patient provides the targeted structure location. The selection of the target coordinates is treated in details in Chapter [Brain Shift Risk during pre-operative Planning].

Pre-operative planning: trajectory

After having determined the target coordinates, the surgeon selects a trajectory to reach the target with the stimulating electrode. The trajectory is defined as a linear segment between a point on the scalp, and the target coordinates. The goal of this procedural step is to determine the optimal entry point on the scalp meeting the following constraints (the complete list is given in [Essert et al., 2011]):

- The trajectory must not intersect any vital structure such as blood vessels (or ventricles).
- A trajectory is safer if the distance to the risky structures is maximal
- The trajectory length is restricted (to 90 mm according to [Essert et al., 2011]).
- The entry point should be in the hairy scalp area for aesthetic reasons.

Again, several methods exist to determine an optimal trajectory:

- Based on the average trajectory, the surgeon decides on the safety of the trajectory by manually checking whether the trajectory intersect vital structures directly in the 3D image.
- Optimization software automatically computes the optimal electrode trajectory (for instance [Essert et al., 2011]).

The selection of the trajectory is addressed in details in Chapter [Brain Shift Risk during pre-operative Planning].

1.3.2 Intra-operative procedural steps

The following procedural steps take place in the operating room.

Stereotactic Frame

When the patient is ready in the operating room, the last pieces (the arc) of the stereotactic frame are setup. Then, the surgeons adjust the frame angles corresponding to the selected trajectory and target coordinates.

Making Burr Hole

Once the stereotactic frame is adjusted, the surgeon knows where to incise the skin. The arc is removed to free the operating space and not to obstruct the following surgical gestures. Under local anesthesia, the skin is incised around the entry point, determined pre-operatively. After the incision in the skin, the

surgeon drill a burr hole in the skull (about 14 mm diameter). The lead fixation base is attached to the burr hole. The arc of the stereotactic frame is placed again for the following steps.

Microdrive

A microdrive robot is placed on the stereotactic frame. This robot allows to insert electrodes in the brain with high precision. The microdrive is fixed to the frame that has been adjust with the selected angles so that the movement of the electrode is constraint to only one dimension. The resolution of the Elekta MicroDrive is 0.05 mm. Up to five electrodes can be implanted in parallel following the pattern in the figure 1.20(a).

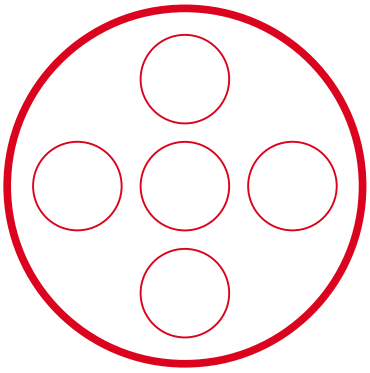

(a) Microdrive pattern holder: one central channel surrounded by four peripheral channels separated by 2mm.

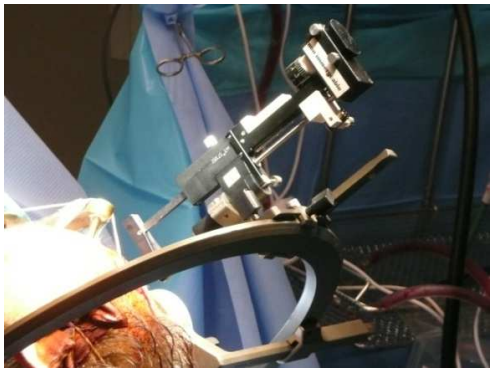

(b) Photograph of a Microdrive fixed to the stereotactic frame during a surgery

Figure 1.20 – *Microdrive pattern holde and photograph.*

Electrophysiological confirmation

One or several (up to five) micro-electrodes are inserted with the microdrive robot. This type of electrode allows to record electrophysilogical signals in the brain tissue due to the electrical activity of neurons. Each structure has its own electrophysiological signature, allowing neurologists to identify the structure crossed by the recording micro-electrode. This is a test to confirm the target coordinates of the pre-operative planning. Once the target location is confirmed, the micro-electrode(s) is(are) removed.

Macro Stimulation

An additional test is performed with a macro-electrode. This electrode has low impedance with a larger tip (between 1 and 1.4 mm) [Gross et al., 2006]. With this electrode, recording and stimulation can be performed. Macrostimulation tests enable to determine if the electrode is located in an area where the stimulation provide sufficient therapeutic effects and no significant negative adverse effects. The macro-electrode is removed after the tests.

Permanent Electrode Implantation

Finally, the permanent stimulating electrode is inserted, usually using a guiding rigid cannula (a tube to force a path to a needle in living tissue). The electrode is fixed to the skull with the fixation. Intra-operative images can be acquired (X-ray or CT) to confirm the placement of the electrodes.

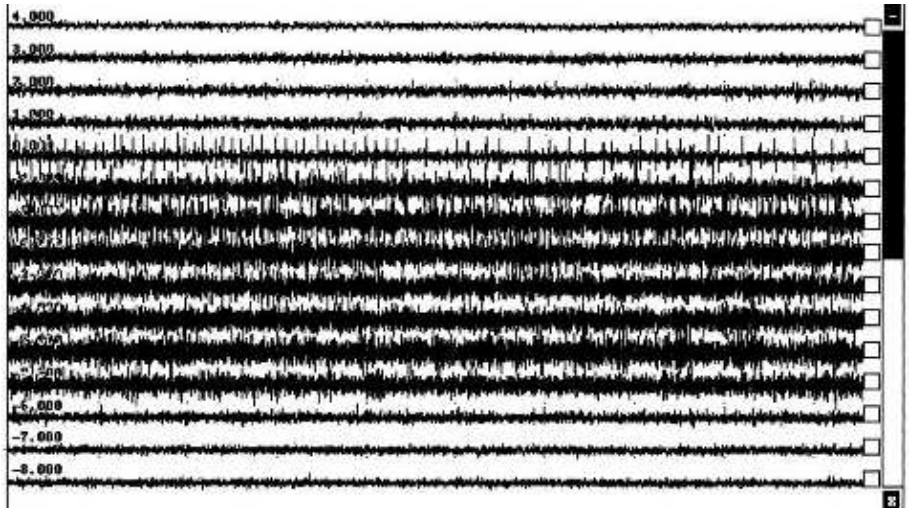

Figure 1.21 – *An example of electrophysiological recording of the STN. Courtesy of [Hamid et al., 2005]*

Comments

Bilateral DBS involves two implantations. For this reason, the procedural steps are not necessarily sequential from the first implantation to the second. For example, the second burr hole can be performed just after the first one before the first electrode implantation. This can have an impact on the duration the skull remains opened.

1.3.3 Post-operative procedural steps

Post-operative Image

A post-operative image is acquired when the electrode(s) are implanted to verify the placement of the electrodes. The electrode creates an artifact in the MR image, therefore [Pollo et al., 2004] proposed a solution to identify the real position of the electrode. Note that some recommendations on the MRI acquisition characteristics has been made due to the interaction between the magnetic field and the electrode. For example, the power of the MRI is limited to 1.5 T. On the other hand, [Hemm et al., 2009] proposed the identification of the electrode in the artifacts of a CT scan. Because of security reasons, a CT scan is generally preferred, rather than a MRI. However, as we already mentioned, a CT scan cannot show enough contrast in the brain tissue to identify the anatomy of the electrode vicinity, therefore a technique to register the pre-operative MRI on the post-operative CT is required.

Neurostimulator Implantation

One or two weeks after the electrodes implantation, the neurostimulator is implanted and linked to the stimulating electrode. As the surgery requires general anesthesia, it takes place after the electrode implantation.

Patient Follow-up

If all the previous steps have been a success, the patient is ready to be continuously stimulated. However, the DBS system requires to adjust some parameters, such as the voltage, frequency or the stimulating electrode(s). A neurologist is in charge of the adjustment. Several visits per year are necessary as changes could appear, such as brain shift leading to a change of stimulating electrodes, or even a re-implantation in another location due to a lack of efficiency.

1.4 Brain Shift and Adverse Effects

1.4.1 Description of Brain Shift

According to [Slotty et al., 2012], the term brain shift describes movement and deformation of the brain in terms of its anatomical and physiological position in the skull. Brain shift can be observed after a head injury or during a neurosurgery.

Brain Shift as a symptom

The brain is a deformable medium. For this reason, it is protected by several layers such as the skull, dura mater and cerebrospinal fluid. In healthy patients and daily life, this protection does not allow any movement or deformation. However, a head injury can lead to brain deformation, such as a midline shift and a brain herniation.

Midline Shift A severe head injury (e.g. car accident) can lead the brain to shift beyond the center line of the brain. Other events such has a tumor growth can be the source of a midline shift. A midline shift indicates an increase of the ICP. The symptoms of a midline shift can be movement difficulties with a side of the body and vision problem.

Brain Herniation Brain herniation occurs when the ICP is very high. Several types of herniation exist such as subfalcine herniation (midline shift), transalar herniation (accross the sphenoid wing), transtentorial herniation (across the tentorium) or tonsillar herniation (lower part of the brain compression). Brain herniation is due to an expending mass less such as tumor, hematomas, infarctions, infection or haemorrhage.

Brain Shift in Neurosurgery

In the previous section (1.4.1), we have seen the brain could deform inside the skull, outside from a surgical context. It is essentially due to a high ICP. However, ICP could change also during a medical procedure. For instance, CSF is collected around the spinal cord in lumbar puncture. This can reduce the intracranial CSF pressure [Grant et al., 1991]. In addition, CSF could leak outside from the skull during a neurosurgery, when the skull and the dura mater are open. The CSF volume decreases, so does the ICP. These changes in ICP during a medical procedure can also lead to a brain shift. This deformation can be problematic regarding to the planned surgery, as the deformation changes the initial hypotheses.

1.4.2 Influence of brain shift on DBS procedure

The implantation of electrodes in DBS involves a stereotactic surgery, including opening of the skull. CSF can leak outside from the skull and that could lead to a brain deformation. But this deformation is never

accounted for during the pre-operative planning in DBS.

Pre-operative planning

The sections 1.3.1 and 1.3.1 describe the goals of the pre-operative planning: basically the definition of the target coordinates and a trajectory to reach it. However, decision making is based on hypotheses that can change during the surgery. Indeed, the surgeon uses various techniques (average position regarding to AC-PC or atlas based) to locate the target. They are based on the pre-operative images of the patient. But the configuration of the brain can be altered during the procedure due to brain shift. The consequence is a displacement/deformation of the targeted structure. This will be discussed later, but the targeted structures being located deep into the brain tissue, the displacement is often very small, and not significant regarding the outcomes of the stimulation.

However, with the deformation of the brain, other structures can also deform and have consequences on the DBS procedure. For instance, the lateral ventricles, but mainly the blood vessels follow the brain deformation. It can have consequences on the safety of the procedure. If a blood vessel shifts on the planned path of the electrode, it could be pierced by the electrode, leading to an intracranial hemorrhage [Nazzaro et al., 2010; Tong et al., 2014].

Post-operative Inverse Brain Shift

CSF is produced continuously in the choroid plexus of the brain at a daily rate of 500 mL, while fluid is constantly absorded into the bloodstream. Therefore, after a surgery involving a CSF leak, CSF is progressively restored and subdural air invasion resolves the days following the procedure. When brain has shifted, the restoration of CSF leads to an "*inverse brain shift*": the deformed brain recovers its original (pre-operative) configuration.

The majority of the brain shift amount occurring in the first moment of the surgery, just after the skull opening, the electrode is implanted while the brain is already deformed. The electrode is inserted according to a linear trajectory, from the entry point to the target coordinates. When the electrode is set in the brain, it is fixed to the skull when the burr hole is closed.

The electrode is flexible to avoid the brain tissue to be damaged when the inverse brain shift occurs. However, the fixation to the skull and the flexibility of the electrode are the causes of its deformation when the inverse brain shift occurs. The electrode are progressively curved according to the brain tissue displacement [van den Munckhof et al., 2010]. As the electrode is fixed to the skull, the curvature produces a displacement of the tip of the electrode [van den Munckhof et al., 2010]. The trajectory is planned to place the tip of the electrode in the targeted structure. However, if the tip of the electrode is displaced, it could create a gap between it and the targeted structure.

Adverse Effects on the Patient

We know from surgeons that, in some cases, the stimulation does not provide improvements to the patient. The surgeon needs to perform the surgery on the patient again, and place the electrode in another location supposed to provide benefits. Although there is no study about the direct influence of brain shift on the absence of outcomes on the patient, we can assume that the electrode migration due to brain shift, or a slight displacement of the target, could be a reason.

Although the reasons are not yet clear, some adverse effects of the stimulation can appear after the operation [Appleby et al., 2007; Tong et al., 2014], while providing the expected outcomes. Usually patients are aware of this, but the outcomes are more important and provide a considerable improvement of the quality of life. Some adverse effects can be observed during the surgery, when neurologists perform stimulation tests to locate the optimal target, and can be avoided. The adverse effects are mainly due

to the electrical stimulation of adjacent brain structures [Breit et al., 2004]. We also can assume that brain shift can also be a reason of a misplacement of the electrode, that still stimulates the target but also non-desired adjacent structures.

1.5 Numerical Simulations in Healthcare

The section 1.4 highlights the problem of brain deformation involved in DBS surgery. This deformation requires to be paid attention during the surgery. In this thesis, we propose solutions based on numerical simulations of the brain deformation. The idea of simulating living tissue in healthcare in not new. It is used either for training of medical students, or to assist a surgery or medical procedure.

1.5.1 Simulations for training

In the twentieth century, the development of mannequin that reproduce human body functions started [Cooper and Taqueti, 2008]. We can cite Resusci-Anne for mouth to mouth ventilation [Winchell and Safar, 1966], Sim One, a computer controlled mannequin including breathing and blood pulses with audio [Denson and Abrahamson, 1969] and Harvey mannequin for cardiology [Gordon, 1974]. Later, the increasing of the computers power enabled to create software based simulators. The computer based simulators can describe virtually phenomenon involved in healthcare with mathematical models. We can cite the works of [Marescaux et al., 1998; Raghupathi et al., 2004; Wang et al., 2006; Clarke et al., 2012; Talbot et al., 2014], who developed computer based simulators for training.

The advantage of simulators in healthcare is to allow the trainee to make errors, without harming a patient. Simulations have been advised in order to reduce the medical errors, which are the third leading cause of death in the United States [Kohn et al., 2000]. The student can be assessed, evaluated on the decision making and the technique in different scenarios (in particular rare scenarios), in order to have an experience before a surgery on a real patient. The challenge of the computer-based simulators for training is to reproduce the patient's behavior in real-time. A simulation requires to compute about 25 images per second in order to give a feeling of interactivity and fluidity to the user. For instance, physics-based simulations, such as Finite Element Method (FEM), requires extensive calculation in order to solve differential equations. Therefore, this type of simulations requires to develop strategies to optimize or approximate solutions in order to compute 25 images per second, while keeping a realistic behavior and appearance.

1.5.2 Computer-Assisted Intervention

On the other hand, computer-based simulation could be used to plan a surgery, to predict a surgical event or to use it to compute locations etc. In this case, it is necessary to achieve a high degree of precision. As approximations or simplifications can alter the precision, one understand the computation time is longer for this type of simulations. Images are not always required, but a succession of simulation steps is still necessary in order to compute the final location of a structure for example. A step can easily take several minutes to compute in order to achieve a high precision, compared to 0.04 seconds required for a real-time simulation. The works presented in this thesis are part of this type of simulation.

1.5.3 SOFA

In order to simulate numerically the brain deformation, we rely on the framework SOFA. SOFA (Simulation Open Framework Architecture) [Sofa, 2014; Faure et al., 2012] is an open source framework dedicated to computer-based medical simulation (although it can run other types of physicals simulations). The main

goal of the framework is to simulate physically rigid or deformable objects in real-time. The framework encompasses different FEM models, time integration and linear system solvers. Moreover, it allows to account for the interactions between objects: collision, needle insertion, etc. The main concept is to create a simulation with modular components. A XML file describes the different components and their relationship in what is called a scene. Note that a scene can also be described with a Python script, which is more convenient in our case. We choose to use this framework for its modularity, and its ease in creating and testing scenes. Moreover, a large amount of properties required by our simulation (collision, deformation, needle insertion etc) are already present in the framework. Almost all the development presented in this thesis has been done in the SOFA environment.

A major aspect of SOFA is the mapping system. It is extensively used in our brain shift simulations. It consists in using different meshes for the different aspects of an object in the simulation, by relying on a mechanism of propagation of forces and displacement between the different models. For instance, one can use a FEM mesh for the mechanical deformation, one surface mesh for the collision and one other surface mesh for the visualization. Distinguishing collision and visual meshes could be crucial for the performances. Indeed, computing collision is very time consuming and depends on the number of elements in the mesh. In opposite, the visual model is only displayed on screen and does not require particular processing. Therefore, the mapping system allows the user to have a nice and detailed mesh for the visualization while keeping good performances with a coarser mesh for the collision.

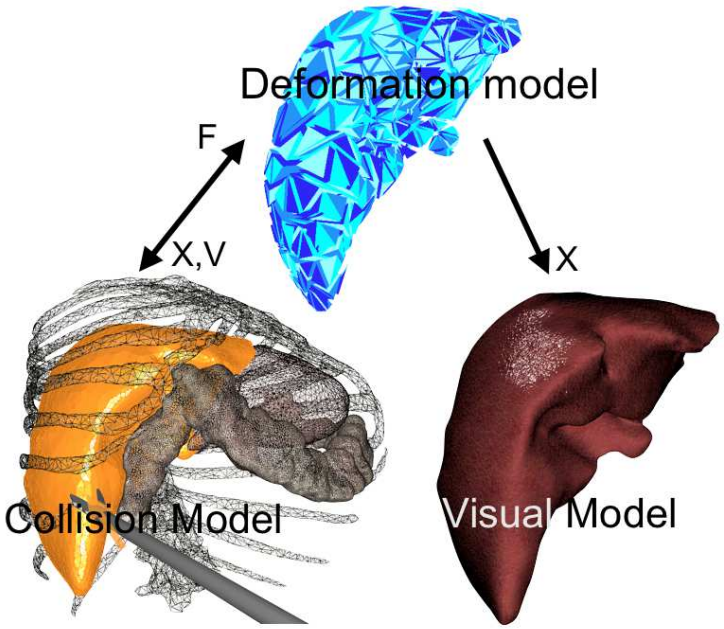

Figure 1.22 – *Mapping system in SOFA*

1.6 Contributions

The previous section 1.4 presented the brain shift phenomenon that can affect the accuracy of a DBS procedure. The objective of this thesis is to develop methods and prototypes of clinical tools with biomechanical simulations of the brain tissue deformation in a DBS surgery context, in order to help surgeons to improve the accuracy and efficiency of the procedure despite the brain deformation. In the following paragraphs, we summarize briefly the contributions in a chronological order regarding to the DBS procedure: applications for pre-operative planning, then for intra-operative surgery and finally for post-operative

evaluation. The three chapters (3, 4 and 5) present the contributions of this thesis using the same chronological order, while the brain deformation physical model common for each contribution is introduced in Chapter 2.

1.6.1 Pre-operative planning

Chapter 3 explains in detail the goals of the planning step in the DBS procedure. Briefly, it consists in defining the targeted structure coordinates and a trajectory to reach it. The brain deformation that can appear intra-operatively changes the configuration of the brain, blood vessels and internal brain structures compared to the planning moment. Depending on the shift amount, it can alter the validity of the planning.

The ideal scenario would be to anticipate exactly the brain deformation. The planning would be based on the deformed brain. Unfortunately, no model exist to predict accurately the amount of brain shift.

Yet, we present two methods to account for the brain shift during the pre-operative planning step. Both methods are based on a notion of risk. The first method has been developed to mimic the current surgeon's technique for defining a safe trajectory. On the contrary, the second technique is more adapted for an automatic computation of electrode trajectories.

1.6.2 Intra-operative registration

With current pre-operative planning methods, brain shift is not taken into account. It means that the brain configuration is different intra-operatively compared to the planning step.

In Chapter 4, we present a method to update the pre-operative configuration of the brain to the intra-operative configuration. This transformation is called a registration. Our method is entirely based on physics and relies on parameters involved in the physical causes of the brain shift.

The methods is based on a pre-operative MRI of the patient and an intra-operative CT scan of the same patient. A simulation is built from the segmentation done in the pre-operative MRI. A minimization process estimates the parameters responsible for the brain shift. Finally, a propagation method applies the displacement field to the internal structures. The surgeon can visualize the displacement of structures of interest and take a decision on the validity of the planned target coordinates and trajectory.

1.6.3 Post-operative electrode curvature

In previous sections, we described the inverse brain shift phenomenon: after a brain shift, the brain recovers its original configuration in the days following the surgery. The implanted electrode being flexible, it is deformed when the brain is deformed.

From the model presented in chapter 2, we add a model of interaction between the brain tissue and the flexible electrode. This will allow us to simulate the surgery protocol, including the insertion of the electrode. When the electrode is inserted, the simulated brain recovers its initial configuration and the model of interaction causes the deformation of the electrode, following the brain deformation. This method is presented in Chapter 5.

Models of Brain Shift

Chapter 2

Abstract

This chapter introduces the model of brain shift developed and used in the contributions presented in the following chapters. In a first part, we present the mathematical background behind most of the models of deformation used in the literature. A basic introduction to the continuum mechanics is followed by a presentation of the Finite Element Method. A state of the art presents the previous models while defining the needs of the biomechanical simulation. We present then the particularity of our brain shift model and how we generate a patient-specific simulation. Later, our model is described and justified.

Contents

2.1 Background

2.1.1 Continuum Mechanics

The deformation of the brain involves the study of its constitutive materials. This science could study the materials at atomic or molecular level (even cells for living tissue), but also at macroscopic level with models that do not account for the atomic/molecular structure of the material. *Continum mechanics* is the branch of physics that study the mechanical behavior of materials, considered as a continuum: no space between particles, the material fills the entire region of space it occupies. The models developed in the theory of continuum mechanics match the experimental tests. In particular, living tissue are often modeled physically and macroscopically thanks to this theory. In this section, we present the basics of continuum mechanics necessary for rest of the manuscript. The interested reader may refer to the book [Reddy, 2007] for a detailed introduction.

Description of Motion

Let $\boldsymbol{B}$ be a deformable body in a three-dimensional Euclidean space. The volume of space occupied by $\boldsymbol{B}$ at a given time t is called a *configuration*. The volume is denoted Ω and its boundary is Γ. A configuration change of the body results in a displacement, which is a combination of a rigid-body displacement and a deformation.

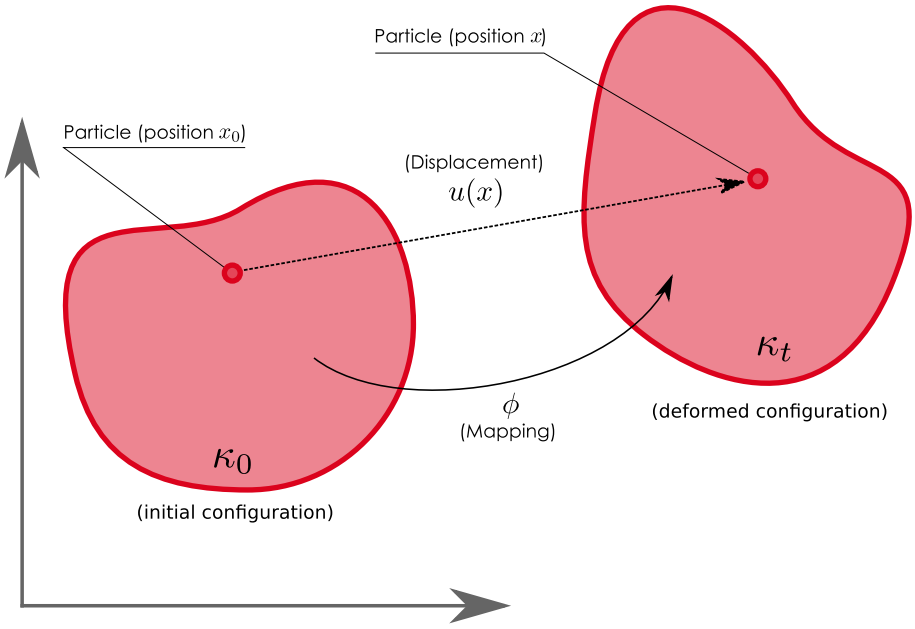

Figure 2.1 – *Illustration of the different definition on the initial configuration and the deformed configuration of a same object.*

Let κ_0 be the initial configuration of the body $\boldsymbol{B}$ and κ_t its configuration at a given time t (see Figure 2.1). In a lagrangian description, a particle having the position $\boldsymbol{x_0}$ in the initial configuration κ_0 is described in the deformed configuration κ_t with a deforming mapping ϕ_t such that

$$\begin{aligned} \phi : \kappa_0 &\longrightarrow \kappa_t \\ \boldsymbol{x_0} &\longmapsto \boldsymbol{x} = \phi(\boldsymbol{x_0}, t) \end{aligned} \tag{2.1}$$

The whole configuration κ_t can be described with all the particles $\boldsymbol{x}$ of the body and the deforming mapping $\boldsymbol{\phi_t}$ acting on all the particles of the initial configuration:

$$\boldsymbol{x} = \boldsymbol{\phi}(\boldsymbol{x_0}, t) \tag{2.2}$$

The displacement $\boldsymbol{u}$ of a particle located at $\boldsymbol{x} \in \kappa_t$ is defined as

$$\boldsymbol{u}(\boldsymbol{x}) = \boldsymbol{x} - \boldsymbol{x_0} = \phi(\boldsymbol{x_0}, t) - \boldsymbol{x_0} \tag{2.3}$$

The displacement field of the body in the deformation field is a vector field of all the displacement vectors for every particle of the body:

$$\boldsymbol{u}(\boldsymbol{x}) = \boldsymbol{x} - \boldsymbol{x_0} = \boldsymbol{\phi}(\boldsymbol{x_0}, t) - \boldsymbol{x_0} \tag{2.4}$$

In the following, we introduce concepts that will be used to describe the deformation of an object. The deformation gradient (second order tensor) of the deformed configuration is defined as

$$\mathbb{F} = \frac{\partial \boldsymbol{\phi}}{\partial \boldsymbol{x}} = \frac{\partial \boldsymbol{u}}{\partial \boldsymbol{x}} + \mathbb{I} = \nabla \boldsymbol{u} + \mathbb{I} \tag{2.5}$$

and its determinant J is called the jacobian:

$$J = \det \mathbb{F} \tag{2.6}$$

The right Cauchy-Green deformation tensor $\mathbb{C}$ (symmetric second order) is defined as:

$$\mathbb{C} = \mathbb{F}^T \mathbb{F} \tag{2.7}$$

and the left Cauchy-Green deformation tensor $\mathbb{B}$ is defined as:

$$\mathbb{B} = \mathbb{F}\mathbb{F}^T \tag{2.8}$$

Strain measure

A strain measure evaluates the deformation part of a displacement. This measure does not account for the rigid-body displacement. Multiple strain measures exist but we focus on the Green-Lagrange strain tensor $\mathbb{E}$ defined as :

$$\mathbb{E} = \frac{1}{2}(\mathbb{C} - \mathbb{I}) \tag{2.9}$$

In cartesian coordinate system, the components $\mathbb{E}_{ij}$ of $\mathbb{E}$ can be expressed as
$\forall\, 1 \leq i, j \leq 3$

$$\mathbb{E}_{i,j} = \frac{1}{2}\left(\frac{\partial u_i}{\partial X_j} + \frac{\partial u_j}{\partial X_i} + \frac{\partial u_i}{\partial X_j}\frac{\partial u_j}{\partial X_i}\right) \tag{2.10}$$

By definition, the Green-Lagrange strain tensor is a symmetric second-order tensor. The coefficient $\mathbb{E}_{11}$, $\mathbb{E}_{22}$ and $\mathbb{E}_{33}$ are called *normal strains* and $\mathbb{E}_{12}$, $\mathbb{E}_{13}$ and $\mathbb{E}_{23}$ are called *shear strains*.

Stress measure

Stress is a measure of the internal forces acting within the body. It is measured in pascal (Pa), that-is-to-say a force expressed by surface unit. Several measures of stress can be defined. If we consider an elementary surface, the stress measures depend on the magnitude of the area, but also on the orientation. The stress vector (measure of stress in a direction $\boldsymbol{n}$) is defined as $\boldsymbol{t}(\boldsymbol{n}) = \lim_{\Delta a \to 0} \frac{\Delta \boldsymbol{f}(\boldsymbol{n})}{\Delta a}$, where $\boldsymbol{f}(\boldsymbol{n})$ is the force on the elementary surface and a is its area. The Cauchy stress tensor is a second-order tensor, such that

$$\forall \hat{\boldsymbol{n}},\ \boldsymbol{t}(\hat{\boldsymbol{n}}) = \hat{\boldsymbol{n}}\boldsymbol{\sigma} \tag{2.11}$$

We give here some of the other stress measures, defined from the Cauchy stress tensor $\boldsymbol{\sigma}$:

First Piola-Kirchhoff stress tensor The first Piola-Kirchhoff stress tensor $\mathbb{P}$ is expressed as

$$\mathbb{P} = J\boldsymbol{\sigma}\mathbb{F}^{-T} \tag{2.12}$$

Second Piola-Kirchhoff stress tensor The second Piola-Kirchhoff stress tensor $\mathbb{S}$ is expressed as

$$\mathbb{S} = \mathbb{F}^{-1}\mathbb{P} = J\mathbb{F}^{-1}\boldsymbol{\sigma}\mathbb{F}^{-T} \tag{2.13}$$

Constitutive Equation

The internal forces of a material result from the deformation of it, therefore we seek to expressed a stress measure depending on a strain measure. The stress-strain relation is called the *constitutive law* and depends on the type of the material of the body.

For elastic materials the stress can be determined by the state of the deformation, on the contrary to plastic materials, where the stress depends also on the history of the deformation.

A material is said *hyperelastic* if it exists a *strain energy density* scalar function W, depending on a strain measure $\boldsymbol{\varepsilon}$ such that

$$W(\boldsymbol{\varepsilon}) = \int_0^{\boldsymbol{\varepsilon}} \boldsymbol{\sigma}\, d\boldsymbol{\varepsilon} \tag{2.14}$$

An elastic material is said to be linear when W is quadratic: the stress-strain relation is therefore linear. A non-linear material is either higher-order polynomial or another non-linear function.

Linear materials The constutive law for linear materials is called the generalised Hooke's law:

$$W(\boldsymbol{\varepsilon}) = C_0 + \sum_{1\leq i,j\leq 3}\left[C_{ij}\varepsilon_{ij} + \sum_{1\leq k,l\leq 3}\frac{1}{2!}C_{ijkl}\varepsilon_{ij}\varepsilon_{kl}\right] \tag{2.15}$$

with C_{ijkl}, C_0 and C_{ij} material constants. By derivation:
$\forall\ 1 \leq i,j \leq 3$

$$\sigma_{ij} = \sum_{1\leq k,l\leq 3} C_{ijkl}\varepsilon_{kl} \tag{2.16}$$

The total number of the C_{ijkl} coefficients is 81 ($= 3^4$), but can be reduced to 21 because of the symmetry of both strain and stress tensors:

$$\begin{bmatrix} \sigma_{11} \\ \sigma_{22} \\ \sigma_{33} \\ \sigma_{23} \\ \sigma_{13} \\ \sigma_{12} \end{bmatrix} = \begin{bmatrix} C_{1111} & C_{1122} & C_{1133} & C_{1123} & C_{1113} & C_{1112} \\ C_{1122} & C_{2222} & C_{2233} & C_{2223} & C_{2213} & C_{2212} \\ C_{1133} & C_{2233} & C_{3333} & C_{3323} & C_{3313} & C_{3312} \\ C_{1123} & C_{2223} & C_{3323} & C_{2323} & C_{2313} & C_{2312} \\ C_{1113} & C_{2213} & C_{3313} & C_{2313} & C_{1313} & C_{1312} \\ C_{1112} & C_{2212} & C_{3312} & C_{2312} & C_{1312} & C_{1212} \end{bmatrix} \begin{bmatrix} \varepsilon_{11} \\ \varepsilon_{22} \\ \varepsilon_{33} \\ 2\,\varepsilon_{23} \\ 2\,\varepsilon_{13} \\ 2\,\varepsilon_{12} \end{bmatrix} \tag{2.17}$$

The matrix $\boldsymbol{\mathcal{C}}$ formed with the reduced stiffness coefficients C_{ijkl} is called the stiffness matrix. In matrix notation, the equation 2.17 becomes:

$$\boldsymbol{\sigma} = \boldsymbol{\mathcal{C}}\boldsymbol{\varepsilon} \tag{2.18}$$

In case of orthotropic materials, the coefficients are reduced to 9:

$$\begin{bmatrix} \sigma_{11} \\ \sigma_{22} \\ \sigma_{33} \\ \sigma_{23} \\ \sigma_{13} \\ \sigma_{12} \end{bmatrix} = \begin{bmatrix} C_{1111} & C_{1122} & C_{1133} & 0 & 0 & 0 \\ C_{1122} & C_{2222} & C_{2233} & 0 & 0 & 0 \\ C_{1133} & C_{2233} & C_{3333} & 0 & 0 & 0 \\ 0 & 0 & 0 & C_{2323} & 0 & 0 \\ 0 & 0 & 0 & 0 & C_{1313} & 0 \\ 0 & 0 & 0 & 0 & 0 & C_{1212} \end{bmatrix} \begin{bmatrix} \varepsilon_{11} \\ \varepsilon_{22} \\ \varepsilon_{33} \\ 2\,\varepsilon_{23} \\ 2\,\varepsilon_{13} \\ 2\,\varepsilon_{12} \end{bmatrix} \tag{2.19}$$

This type of material has three mutually orthogonal directions with independent material properties. The inverse of the stiffness matrix is denoted $\boldsymbol{\mathcal{S}} = \boldsymbol{\mathcal{C}}^{-1}$:

$$\boldsymbol{\mathcal{S}} = \begin{bmatrix} S_{1111} & S_{1122} & S_{1133} & 0 & 0 & 0 \\ S_{1122} & S_{2222} & S_{2233} & 0 & 0 & 0 \\ S_{1133} & S_{2233} & S_{3333} & 0 & 0 & 0 \\ 0 & 0 & 0 & S_{2323} & 0 & 0 \\ 0 & 0 & 0 & 0 & S_{1313} & 0 \\ 0 & 0 & 0 & 0 & 0 & S_{1212} \end{bmatrix} \; 2\;2\;2 \tag{2.20}$$

The Young's modulus E_i, shear modulus μ_{ij} and Poisson's ratio ν_{ij} for the 3 different directions (and their orthogonal plane) are introduced:

$$\boldsymbol{\mathcal{S}} = \begin{bmatrix} \frac{1}{E_1} & -\frac{\nu_{21}}{E_2} & -\frac{\nu_{31}}{E_3} & 0 & 0 & 0 \\ -\frac{\nu_{21}}{E_2} & \frac{1}{E_2} & -\frac{\nu_{32}}{E_3} & 0 & 0 & 0 \\ -\frac{\nu_{31}}{E_3} & -\frac{\nu_{31}}{E_2} & \frac{1}{E_3} & 0 & 0 & 0 \\ 0 & 0 & 0 & \frac{1}{\mu_{23}} & 0 & 0 \\ 0 & 0 & 0 & 0 & \frac{1}{\mu_{13}} & 0 \\ 0 & 0 & 0 & 0 & 0 & \frac{1}{\mu_{12}} \end{bmatrix} \; 2\;2\;2 \tag{2.21}$$

For isotropic materials, the material properties are independent of the directions:

$$\begin{cases} E_1 = E_2 = E_3 = E \\ \mu_{12} = \mu_{13} = \mu_{23} = \mu \\ \nu_{12} = \nu_{13} = \nu_{23} = \nu \end{cases} \tag{2.22}$$

and finally, the constitutive equation of isotropic linear elastic materials becomes
$\forall\ 1 \leq i, j \leq 3$

$$\sigma_{ij} = 2\mu\varepsilon_{ij} + \sum_{k=1}^{3} \lambda\varepsilon_{kk}\delta_{ij} \tag{2.23}$$

where δ_{ij} is the Kronecker delta and λ and μ are the Lamé's constants such that

$$\begin{cases} \lambda = \dfrac{E\nu}{(1+\nu)(1-2\nu)} \\ \mu = \dfrac{E}{2(1+\nu)} \end{cases} \tag{2.24}$$

The inverse relations are:

$$\begin{cases} E = \dfrac{\mu(3\lambda + 2\mu)}{\lambda + \mu} \\ \nu = \dfrac{\lambda}{2(\lambda + \mu)} \end{cases} \tag{2.25}$$

Note that the Young's modulus E is a measure of the stiffness of a linear elastic material. It is also the slope of the linear part of the stress-strain relation, which is a way to determine it experimentally. On the other hand, the Poisson's ratio ν is a measure of the compressibility (change in volume) of a material. The theoretical values range between -1 and 0.5 (see equation 2.24), but most materials have Poisson's ratio values between 0 and 0.5. The value 0.5 is for material perfectly incompressible. Incompressible materials are in fact nearly-incompressible, that is why $\nu = 0.5$ is not possible in equation in equation 2.24. Living tissue consist mostly of cells, themselves made with a majority of water. For this reason, the Poisson's ratio value of living tissue is often near the value 0.5.

Non-linear materials Generally, real materials are more accurately modeled with a non-linear formulation of the constitutive equation. However, Hooke's law (equation 2.18) is a good approximation in most materials for small deformation (see figure 2.2). Beyond the proportionality threshold, a non-linear model is necessary to describe a non-linear material behavior. A large range of constitutive equations have been proposed for non-linear materials. Often, they are expressed as a linear combination of material coefficients (must be determined with experimental tests) and principal invariants of Green-Lagrange strain tensor $\mathbb{E}$, the left Cauchy-Green strain tensor $\mathbb{B}$ and deformation gradient tensor $\mathbb{F}$. This section introduces the invariants of a tensor and its use in an example of a non-linear constitutive equation, the Mooney-Rivlin model.

Invariants of tensor The invariants of a tensor are the coefficients of the characteristic polynomial of the tensor. For a second-order tensor $\mathbb{A}$, the three invariants $I_{\mathbb{A}}$, $II_{\mathbb{A}}$ and $III_{\mathbb{A}}$ are:

$$\begin{cases} I_{\mathbb{A}} = \mathrm{tr}\mathbb{A} \\ II_{\mathbb{A}} = \dfrac{1}{2}\left((\mathrm{tr}\mathbb{A})^2 - \mathrm{tr}(\mathbb{A}\mathbb{A})\right) \\ III_{\mathbb{A}} = \det\mathbb{A} \end{cases} \tag{2.26}$$

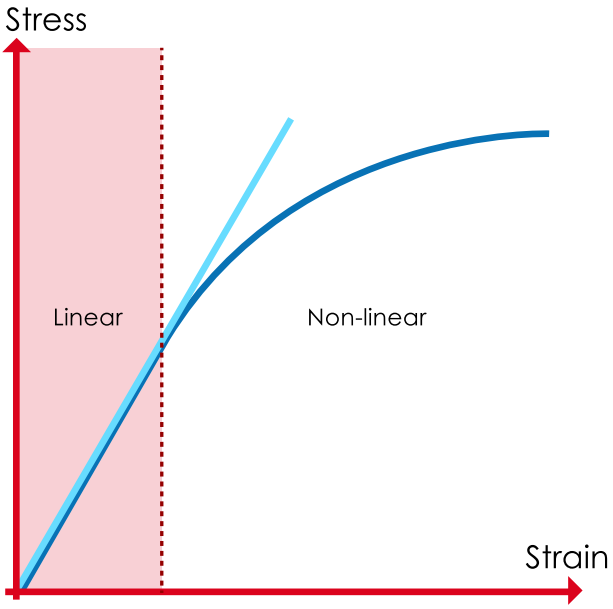

Figure 2.2 – *Example of stress-strain relation: the relation is often non-linear for real materials, but it may be approximated with a linear relation for small deformation.*

Sometimes, the strain energy density of a material is expressed with modified invariants, depending on the jacobian J (Equation 2.6):

$$\begin{cases} \overline{I_{\mathbb{A}}} = J^{-2/3} I_{\mathbb{A}} \\ \overline{II_{\mathbb{A}}} = J^{-4/3} II_{\mathbb{A}} \end{cases} \tag{2.27}$$

Mooney-Rivlin In a Mooney-Rivlin material [Mooney, 1940; Rivlin, 1948], the strain energy density function is expressed as a linear combination of the invariants of the left Cauchy-Green deformation tensor $\mathbb{B}$:

$$W = C_1(\overline{I_{\mathbb{B}}} - 3) + C_2(\overline{II_{\mathbb{B}}} - 3) \tag{2.28}$$

where C_1 and C_2 are material constants, determined by experiments on samples. They do not have any physical meaning and are unitless.

The Mooney-Rivlin model is a special case of the generalized Rivlin model:

$$W = \sum_{i,j=0}^{\infty} C_{ij}(\overline{I_{\mathbb{B}}} - 3)^i(\overline{II_{\mathbb{B}}} - 3)^j \tag{2.29}$$

Other non-linear materials A large number of other constitutive laws exists to characterize various materials, such as rubber-like materials. The simplest hyperelastic material model is the Saint Venant-Kirchhoff model, similar to a linear model but accounting for the non-linearities of the Green-Lagrange strain tensor (more details in Section 2.4.2). We can also cite, among the widely used hyperelastic material models, the Ogden model [Ogden, 1972] and the Arruda-Boyce model [Arruda and Boyce, 1993].

Forces

After having defined a stress-strain relation, our goal is to link the stress to internal forces and positions of the material particles, in order to set a material global equation remaining to solve. We start from the known Newton's law and apply it on an infinitesimal cube of a deformable material. This will lead us to the Cauchy momentum equation.

The second Newton's law describes the relationship between a solid body motion and the forces:

$$\sum \boldsymbol{f} = \begin{cases} 0 & \text{in static problems} \\ m\,\ddot{\boldsymbol{x}} & \text{in dynamic problems} \end{cases} \tag{2.30}$$

where $\ddot{\boldsymbol{x}}$ is the acceleration of the body (second time derivative of the position), m is the mass of the body and $\boldsymbol{f}$ are forces acting on the body. In the following, we continue the development in the case of dynamic problems. For deformable bodies, we apply the second Newton's law on an infinitesimal cube of the material:

$$\rho\,\ddot{\boldsymbol{x}}\,dV = (\boldsymbol{f}_{\text{ext}} + \boldsymbol{f}_{\text{int}})\,dV \tag{2.31}$$

where $\boldsymbol{f}_{\text{ext}}$ is the external forces acting on the infinitesimal cube, and $\boldsymbol{f}_{\text{int}}$ is the internal forces in the material. Both $\boldsymbol{f}_{\text{ext}}$ and $\boldsymbol{f}_{\text{int}}$ can depend on the position, and its derivative (velocity). In the deformable body, we apply the third Newton's law so that internal volume forces cancel each other out. Only boundary constraints $\boldsymbol{t}$ stay. If we sum over the whole volume, we obtain:

$$\int_\Omega \rho\,\ddot{\boldsymbol{x}}\,dV = \int_\Omega \boldsymbol{f}_{\text{ext}}\,dV + \int_\Gamma \boldsymbol{t}\,dS \tag{2.32}$$

From the Ostrogradsky theorem, we have:

$$\int_\Gamma \boldsymbol{t}\,dS = \int_\Omega \text{div}\boldsymbol{\sigma}\,dV \tag{2.33}$$

Therefore,

$$\int_\Omega \rho\,\ddot{\boldsymbol{x}}\,dV = \int_\Omega (\boldsymbol{f}_{\text{ext}} + \text{div}\boldsymbol{\sigma})\,dV \tag{2.34}$$

The equality of the terms in the integrals gives the Cauchy momentum equation:

$$\text{div}\boldsymbol{\sigma} + \boldsymbol{f}_{\text{ext}} = \rho\ddot{\boldsymbol{x}} \tag{2.35}$$

The equation 2.35 is a differential equation to solve if we want to know the evolution of the motion and deformation of a body.

2.1.2 Finite Element Method

Computer simulations aiming at reproducing deformable objects (such as organs) behaviors can be based on the solving of the equations of continuum mechanics. For instance, the equation 2.35 cannot be solved analytically, hence the need of a numerical method to approximate a solution. In this section, the Finite Element Method (FEM), a popular numerical procedure used to approximately solve differential equations, especially in continuum mechanics, is introduced.

Discretization

The basic idea of the FEM is to divide the domain of the equations into smaller simpler subdomains, called *elements*. The continuous domain is discretized into a set of elements. The total set of elements

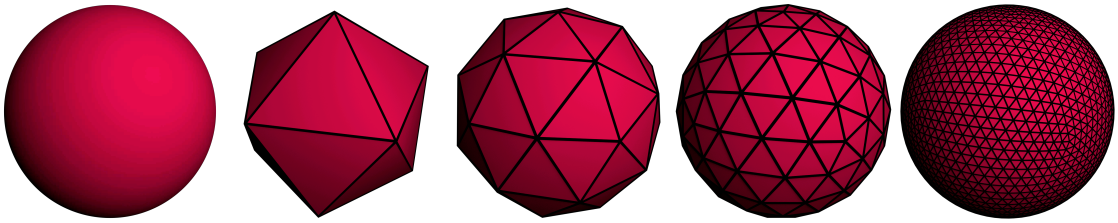

(a) Continuous domain (b) Icosahedron (c) 1 subdivision of (b) (d) 2 subdivisions of (b) (e) 4 subdivisions of (b)

Figure 2.3 – *Different levels of discretization of the same continuous domain. A continuous sphere (a) is approximated with triangles, from less accurate (b) to more accurate (e). A subdivision consists in splitting each triangular face into four triangles, resulting in a more spherical appearance.*

approximates the continuous domain and is called a *mesh*. The differential equations are then solved on each element. The solution over the entire domain is obtain by assembling the contribution of each element. In 2D problems, the mesh could be composed of triangular elements or quadrilateral elements for example. In 3D problems, tetrahedral elements or hexahedral elements can compose the mesh if the domain has a volume, or triangular and quadrilateral elements if the domain is a hollow structure. The elements are composed of *nodes*, which are often on the apexes of the elements. Some particular elements are also composed of extra nodes in addition to the apexes. The segment between two connected nodes is called an *edge*. The discretization of the continuous domain is the first approximation (among others) in the FEM (see different approximations of the same domain in the figure 2.3). Basically, the fidelity of the model depends on the number of elements. Note that the local refinement plays also an important role in the fidelity: for the same number of elements, the resolution of a region can be different and have an influence on the fidelity if the region values varies largely in a small part of space. This is why the meshing process is important for a simulation: usually, if we want material fidelity, we need more elements, meaning more equations to solve and therefore more time is needed to compute them. A trade-off between computational time and fidelity must be found, depending on the application.

Some rules apply when building a mesh in FEM. One element cannot cover its neighbor element. The connection between two neighbor elements is made either by a common node, by a common edge or by a common side. Elements cannot be connected if the common edge or side have a different degree according to the element it belongs to. The degree of an edge depends on the number of nodes it is made of. For instance, a segment (two nodes) is degree 1, while a segment with a node on the middle (three nodes) is degree 2. The degree of an element is defined by the degree of all of its edges. For example, a tetrahedron which every edge is degree two is also degree two. The degree of an element intervenes in the *nodal interpolation*. It is basically the expression of any physical quantity in any point depending only on the values on the nodes. The more nodes in the elements, the more the interpolation will be accurate. A physical quantity u^e is defined in x with the values on the different nodes of the element e:

$$u^e(x) = \begin{pmatrix} \phi_1^e(x) & \phi_2^e(x) & \cdots & \phi_N^e(x) \end{pmatrix} \begin{pmatrix} u_1^e \\ u_2^e \\ \vdots \\ u_N^e \end{pmatrix} = \sum_{i=1}^{N} u_i^e \phi_i^e(x) \tag{2.36}$$

where u_i^e is the value on the node i and N is the total number of nodes in the element e. ϕ_i^e are approximation functions over the element e, and can be linear or higher-order polynomial expressions. They are called *interpolation functions*. The degree of the interpolation functions depends on the number of nodes

in the element. For example, in a triangle, three vertices allow to interpolate linearly (figure 2.5(a)), while three vertices and three mid-edge nodes allow to interpolate with a second-order polynomial (2.5(b)). The interpolation function verify this property: if x_i is the position of the node i in the element e, then

$$\phi_i^e(x_j) = \delta_{ij} \tag{2.37}$$

The interpolation functions are depending on the element shape and has to be determined in order to compute a physical quantity in any location of the domain. These functions are not simple to express in 2D or 3D. That is why, we generally apply a transformation to the real element to result in a *reference element*. The reference element is a simpler and constant element with the same number of nodes than the real element. It is defined in another space of coordinates, where edges are aligned with axis. The location of a point in this space is the coordinate ξ. See an example of a real linear tetrahedron in figure 2.4.

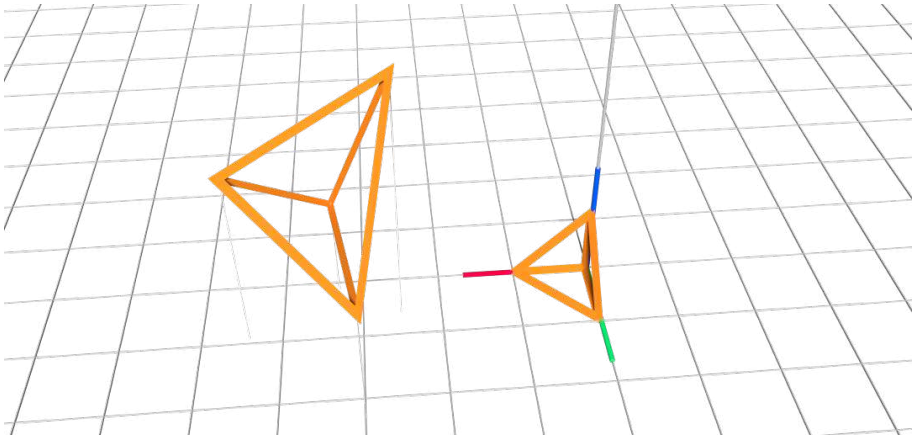

Figure 2.4 – *Reference Element: any tetrahedral element (left) can be transformed to a reference element (right), where computation is easier.*

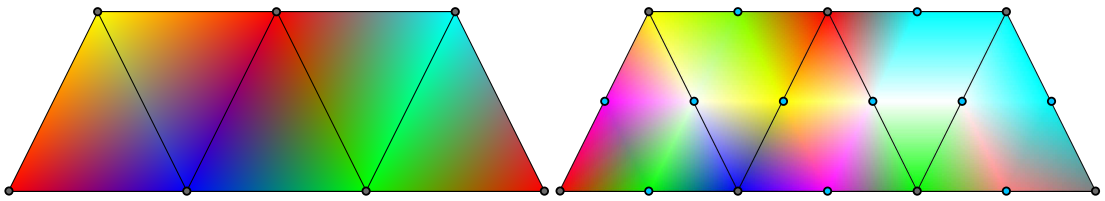

(a) Linear interpolation: the value is interpolated linearly from the three vertices of the triangles

(b) Quadratic interpolation (approximated with two linear interpolations): the value is interpolated from the six nodes of the triangles (three vertices + three mid-edge nodes).

Figure 2.5 – *Comparison of the interpolation on a triangular mesh. The color represents a value interpolated from the nodes of the triangles. In both cases, the colors on the vertices are the same. Only mid-edge nodes are added in (b).*

The relation between x and ξ is bijective, and defined the *shape functions*:

$$x(\xi) = \sum_{i=1}^{N} x_i^e \overline{\phi}_i^e(\xi) \tag{2.38}$$

where x_i are the coordinates of the nodes of the element e. $\overline{\phi}_i^e$ are the *shape functions* of the element. The shape functions depend on the reference element and are well known. In the case of *isoparametric*

elements, we have:

$$\overline{\phi}_i^e = \phi_i^e \tag{2.39}$$

To compute the derivative of a physical value at a point $\boldsymbol{x}$, we also use the shape functions, and its derivative:

$$\frac{\partial u^e(x)}{\partial x} = \sum_{i=1}^{N} \frac{\partial u_i^e}{\partial x} \phi_i^e(x) + u_i^e \frac{\partial \phi_i^e(x)}{\partial x} \tag{2.40}$$

This is how we can compute gradient and divergence.

Global Equation

The differential equation to solve with FEM is the equation 2.35. The residual of this equation is

$$R(\boldsymbol{x}) = \text{div}\boldsymbol{\sigma} + \boldsymbol{f}_{\text{ext}} - \rho\ddot{\boldsymbol{x}} \tag{2.41}$$

The goal is to solve

$$R(\boldsymbol{x}) = 0 \tag{2.42}$$

From this point, a large number of methods exists to solve this equation. In the following, we present only one, which is based on the development of Section 2.1.1.

The equation 2.42 is equivalent to:

$$\int_\Omega R(\boldsymbol{x})\Psi(\boldsymbol{x})d\boldsymbol{x} = 0 \tag{2.43}$$

where the functions Ψ are any test functions.

Using the Galerkin method, the Ψ functions are replaced by the shape functions ϕ:

$$\int_\Omega R(\boldsymbol{x})\phi(\boldsymbol{x})d\boldsymbol{x} = 0 \tag{2.44}$$

which is the strong formulation of the problem. The strong formulation is transformed to the weak formulation through the application of Green formulas. In the weak formulation, a term associated to the boundary conditions appears. The weak formulation corresponds in fact to the virtual work theorem expressed with virtual displacement. The next steps consists in discretizing the integral with a sum over the elements. Then, we replace σ with the constitutive equation of the material. The matrices containing the shape function are used. After this development, we assemble the resulting elementary matrices to get the following global system:

$$\mathbb{M}\ddot{\boldsymbol{x}} + \mathbb{F}(\boldsymbol{x}, \dot{\boldsymbol{x}}) = \boldsymbol{f}_{\text{ext}} \tag{2.45}$$

where

- $\mathbb{M}$ is a constant mass matrix
- $\mathbb{F}$ is a force vector depending on the constitutive equation and on $\boldsymbol{x}$ and $\dot{\boldsymbol{x}}$.

The equation can also be written:

$$\mathbb{M}\ddot{\boldsymbol{x}} = \boldsymbol{f}_{\text{ext}} - \boldsymbol{f}_{\text{int}} \tag{2.46}$$

with

$$\boldsymbol{f}_{\text{int}} = \mathbb{F}(\boldsymbol{x}, \dot{\boldsymbol{x}}) \tag{2.47}$$

Note that for static problems, the equation 2.45 becomes:

$$\mathbb{F}(\boldsymbol{x}, \dot{\boldsymbol{x}}) = \boldsymbol{f}_{\text{ext}} \tag{2.48}$$

To integrate the equation 2.46 in time, we can write the equation 2.46 equivalently as:

$$\begin{cases} \mathbb{M}\dot{\boldsymbol{v}} &= \boldsymbol{f}_{\text{ext}} - \boldsymbol{f}_{\text{int}} \\ \boldsymbol{v} &= \dot{\boldsymbol{x}} \end{cases} \tag{2.49}$$

2.1.3 Time integration

To solve the equation 2.49 in order to calculate the position, velocity and acceleration of the nodes over time, we need to integrate the equation.Let us consider the equation during a time interval $[t_i, t_f]$, with $\Delta t = t_f - t_i$, where the different values of position, velocity and acceleration are known in t_i. If we integer from t_i to t_f, we have:

$$\begin{cases} \mathbb{M}(\boldsymbol{v}_f - \boldsymbol{v}_i) &= \displaystyle\int_{t_i}^{t_f} (\boldsymbol{f}_{\text{ext}} - \boldsymbol{f}_{\text{int}})\, dt \\ \boldsymbol{x}_f &= \boldsymbol{x}_i + \displaystyle\int_{t_i}^{t_f} \boldsymbol{v}\, dt \end{cases} \tag{2.50}$$

The subscript f (respectively i) indicates the value at time t_f (respectively t_i).

The different time integration scheme aim at evaluating the integral from the equation 2.50. In this thesis, we present only the Forward Euler method and the Backward Euler method.

Forward Euler method

The forward Euler method, also called Euler explicit, consists in the evaluation of the integral with the left-hand rectangle method:

$$\begin{cases} \mathbb{M}(\boldsymbol{v}_f - \boldsymbol{v}_i) &= \Delta t \left[\boldsymbol{f}_{\text{ext}} - \boldsymbol{f}_{\text{int}}\right]_i \\ \boldsymbol{x}_f &= \boldsymbol{x}_i + \Delta t\, \boldsymbol{v}_i \end{cases} \tag{2.51}$$

The system 2.51 is simple to solve as the only unknown is $\boldsymbol{v}_f$. The other terms involves only values taken at time t_i.

Explicit methods are only conditionally stable. The Courant criterion is required for stability. It restricts the time step size under a critical time step to ensure stability, and depends on the characteristic length of an element and the dilatational wave speed in the material. Because of this restriction, methods, such as mass scaling[1], have been developed to increase the time step size.

Backward Euler method

The backward Euler method is similar to the forward Euler method but it evaluates the integral with the right-hand rectangle method:

$$\begin{cases} \mathbb{M}(\boldsymbol{v}_f - \boldsymbol{v}_i) &= \Delta t \left[\boldsymbol{f}_{\text{ext}} - \boldsymbol{f}_{\text{int}}\right]_f \\ \boldsymbol{x}_f &= \boldsymbol{x}_i + \Delta t\, \boldsymbol{v}_f \end{cases} \tag{2.52}$$

[1] Increase artificially the mass of the object

The resolution of the system is not as simple as using the Euler explicit. It is due to the fact that terms depends on values taken at time t_f. These values are unknown. For example, $\left[\boldsymbol{f}_{\text{ext}} - \boldsymbol{f}_{\text{int}}\right]_f$ depends on $\boldsymbol{x}_f$ and $\boldsymbol{v}_f$ which are not yet computed. The system becomes non-linear. To solve this non-linear sytem, we can apply the Newton-Raphson algorithm. It consists in iteratively approximate the solution of a non-linear equations thanks to the derivative of the function. Figure 2.6 shows an illustration of the algorithm on a very simple case. For each iteration i of the Newton-Raphson algorithm, the non-linear functions $\boldsymbol{f}_{\text{int}}$ and $\boldsymbol{f}_{\text{ext}}$ are approximated with a first order approximation of a Taylor series expansion:

$$\begin{cases} \boldsymbol{f}_{\text{int}}^{(i)} &= \boldsymbol{f}_{\text{int}}^{(i-1)} + \frac{\partial \boldsymbol{f}_{\text{int}}}{\partial \boldsymbol{x}}^{(i-1)}(\boldsymbol{x}^{(i)} - \boldsymbol{x}^{(i-1)}) + \frac{\partial \boldsymbol{f}_{\text{int}}}{\partial \boldsymbol{v}}^{(i-1)}(\boldsymbol{v}^{(i)} - \boldsymbol{v}^{(i-1)}) \\ \boldsymbol{f}_{\text{ext}}^{(i)} &= \boldsymbol{f}_{\text{ext}}^{(i-1)} + \frac{\partial \boldsymbol{f}_{\text{ext}}}{\partial \boldsymbol{x}}^{(i-1)}(\boldsymbol{x}^{(i)} - \boldsymbol{x}^{(i-1)}) + \frac{\partial \boldsymbol{f}_{\text{ext}}}{\partial \boldsymbol{v}}^{(i-1)}(\boldsymbol{v}^{(i)} - \boldsymbol{v}^{(i-1)}) \end{cases} \tag{2.53}$$

When $i - 1 = 0$, the value is taken at time t_i.

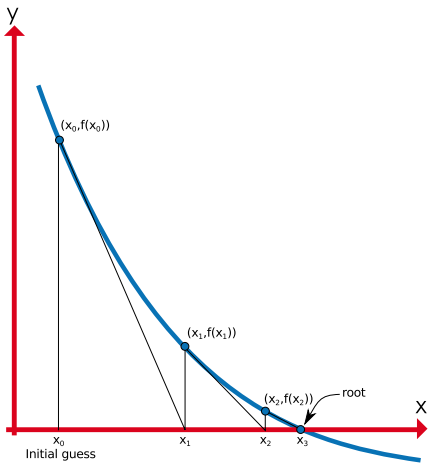

Figure 2.6 – *The Newton-Raphson algorithm applied on a simple 1D function. The initial guess is x_0, the value of the function as well as its derivative is computed at this point in order to compute x_1. This process is iterated until a certain threshold.*

Combining equations 2.53 and 2.52, we obtain:

$$\begin{aligned} \mathbb{M}(\boldsymbol{v}^{(i)} - \boldsymbol{v}^{(i-1)}) = \Delta t \Bigg(& \boldsymbol{f}_{\text{ext}}^{(i-1)} + \frac{\partial \boldsymbol{f}_{\text{ext}}}{\partial \boldsymbol{x}}^{(i-1)}(\boldsymbol{x}^{(i)} - \boldsymbol{x}^{(i-1)}) + \frac{\partial \boldsymbol{f}_{\text{ext}}}{\partial \boldsymbol{v}}^{(i-1)}(\boldsymbol{v}^{(i)} - \boldsymbol{v}^{(i-1)}) \\ & - \boldsymbol{f}_{\text{int}}^{(i-1)} - \frac{\partial \boldsymbol{f}_{\text{int}}}{\partial \boldsymbol{x}}^{(i-1)}(\boldsymbol{x}^{(i)} - \boldsymbol{x}^{(i-1)}) - \frac{\partial \boldsymbol{f}_{\text{int}}}{\partial \boldsymbol{v}}^{(i-1)}(\boldsymbol{v}^{(i)} - \boldsymbol{v}^{(i-1)}) \Bigg) \end{aligned} \tag{2.54}$$

$$\begin{aligned} \Leftrightarrow & \left(\mathbb{M} + \Delta t \underbrace{\left(\frac{\partial \boldsymbol{f}_{\text{int}}}{\partial \boldsymbol{x}}^{(i-1)} - \frac{\partial \boldsymbol{f}_{\text{ext}}}{\partial \boldsymbol{x}}^{(i-1)} \right)}_{\mathbb{B}} + (\Delta t)^2 \underbrace{\left(\frac{\partial \boldsymbol{f}_{\text{int}}}{\partial \boldsymbol{v}}^{(i-1)} - \frac{\partial \boldsymbol{f}_{\text{ext}}}{\partial \boldsymbol{v}}^{(i-1)} \right)}_{\mathbb{K}} \right) \boldsymbol{v}^{(i)} \\ & = \mathbb{M}\boldsymbol{v}^{(i-1)} + \Delta t \left(\boldsymbol{f}_{\text{ext}}^{(i-1)} - \boldsymbol{f}_{\text{int}}^{(i-1)} + \left(\frac{\partial \boldsymbol{f}_{\text{int}}}{\partial \boldsymbol{v}}^{(i-1)} - \frac{\partial \boldsymbol{f}_{\text{ext}}}{\partial \boldsymbol{v}}^{(i-1)} \right) \boldsymbol{v}^{(i-1)} \right) \end{aligned} \tag{2.55}$$

$$\Leftrightarrow \underbrace{\left(\mathbb{M} + \Delta t\, \mathbb{B} + (\Delta t)^2\, \mathbb{K} \right)}_{\mathbb{A}} \underbrace{\boldsymbol{v}^{(i)}}_{\boldsymbol{x}} = \underbrace{\mathbb{M}\boldsymbol{v}^{(i-1)} + \Delta t \left(\boldsymbol{f}_{\text{ext}}^{(i-1)} - \boldsymbol{f}_{\text{int}}^{(i-1)} + \mathbb{K}\, \boldsymbol{v}^{(i-1)} \right)}_{\boldsymbol{b}} \tag{2.56}$$

$$\Leftrightarrow \mathbb{A}\boldsymbol{x} = \boldsymbol{b} \tag{2.57}$$

where

- $\mathbb{B}$ is called the damping matrix
- $\mathbb{K}$ is called the stiffness matrix

The unknown is denoted with $\boldsymbol{x}$, while $\mathbb{A}$ and $\boldsymbol{b}$ are known. The equation 2.57 is a linear system to solve. To solve this system, one can use the large variety of linear solvers. However, a popular method is the conjugate gradient [Hestenes and Stiefel, 1952], which iteratively compute an approximation of the solution until convergence. Note the system can also be pre-conditioned [Courtecuisse et al., 2010]. This choice is popular because of the large size and the sparsity of the matrix.

Each iteration of the Newton-Raphson leads to a linear system to solve. In practice, due to the time required to solve a large linear system, we apply only one iteration, therefore there is one linear system to solve to compute the state at t_f from t_i. A simulation step is the passage from t_i to t_f. A simulation consists in iterations of simulation steps.

2.2 Related works

2.2.1 Mechanical properties

There are several motivations for the study of the mechanical properties of the brain. One can characterize the brain behavior in case of external mechanical load (a car crash for instance) and study its damage in the tissue. One can also develop a computer-based model of the brain to simulate the brain behavior in case of brain diseases where deformation are involved (e.g. hydrocephalus), to train surgery students or to help planning surgical procedures. The first survey about the mechanical properties date back to 1968 [Ommaya, 1968], until the more recent in 2011 [Bilston, 2011]. Another recent survey concentrates on the experimental protocol to obtain the mechanical properties [Chatelin et al., 2010], while [Hrapko et al., 2008] reviewed publications on *in vitro* experimental protocols. Finally, the survey from Bayly et al. focus on the imaging methods used for the validation of biomechanical models [Bayly et al., 2012]. [Bilston, 2011], [Hrapko et al., 2008] and [Chatelin et al., 2010] agree to say an accurate characterization and model of brain tissue is still difficult to obtain nowadays, according to the literature which shows a large number of experimental protocols associated with inconsistent or contradictory data. Among the techniques used, we can found:

1. Rheological experiments on cadaver or animal brain [Miller and Chinzei, 2002; Kaster et al., 2011; Laksari et al., 2012]
2. Magnetic resonance elastography (MRE): developed by [Muthupillai et al., 1995], this non-invasive imaging technique propagates harmonic shear wave, measure the resulting displacement field with a Magnetic resonance imaging (MRI) scanner and deduce the mechanical properties of the biological tissue.
3. Ultrasound: [Lippert et al., 2004] measured ultrasound wave speed through ovin brain samples to estimate the linear viscoelasatic shear modulus
4. Direct observation: in [Pudenz and Shelden, 1946], the top half of a monkey brain was replaced with transparent plastic and filmed
5. Markers implanted in cadaver with X-ray imaging [Hardy et al., 2001]

6. Tagged MRI: this non-invasive technique superimpose grids (variations in brightness) in MRI scan to quantify deformation.

All the techniques have pros and cons. The direct measurement techniques have to use samples from cadaver or animal, which the mechanical parameters differ from *in vivo* tissue. Non-invasive methods based on imaging techniques (such as MRE) are lacking of validation. But the biggest disadvantage of all the study is the inconsistency between them. Bilston advises more rigor in the experiments and the validation of the results. On the opposite, some groups ([Miller and Lu, 2013] for example) try to develop models without patient-specific properties, i.e. with weak sensitivity to the mechanical properties.

To study the mechanical properties of the brain (or other deformable objects), the goal is to first identify the linear viscoelastic limit (see Figure 2.2), then perform tests on larger amplitudes [Bilston, 2011]. Bilston claim this limit is very low, about 0.1-0.3%, according to their previous work [Bilston, 1997]. Although the study is based on bovine brain tissue, other study agree on a low value for the linear viscoelastic limit.

2.2.2 Computational biomechanical models of the brain

According to [Bilston, 2011], "it is unrealistic to expect that one constitutive model will fit all circumstances". The brain model should be selected according to the application such as the analysis of traumatic brain injury mechanisms and tissue thresholds, simulation of brain diseases related to brain deformation, simulation of surgical procedures, or surgical training systems. Despite a disagreement on the choice of the constitutive model of the brain, most of the studies model the brain with FEM, relying on the principles of continuum mechanics. Note that some works ([PAOLIS et al., 2009] for neurosurgy for instance, and many others for other types of applications) relies on mass-spring method, because of its low computational complexity suitable for real-time applications, such as training systems. However, mass-spring system cannot be linked easily to mechanical properties and strongly depends on the mesh topology. In the following, we focus the state of the art on the applications in simulation of surgery-related brain deformation. For example, car crash simulations need to concentrate particularly on the viscosity components of the models due to the high speed impacts. In opposite, the brain shift phenomenon is very slow (compared to a car crash) and viscosity is less important, particularly if we are interested in equilibrium states. We divide the different models of the literature into two types: models relying on a linear formulation, and non-linear models.

Linear constitutive law

Linear models are the simplest. It links the stress and strain via a linear relation. It is valid for all materials for a small deformation. After the linear limit, the stress-strain becomes non-linear (Figure 2.2). Despite its simplicity in the description of materials, a linear constitutive law has the advantage to be simple to implement, stable and fast to compute. Again, it is also valid for small deformation. In addition, the parameters of the constitutive law have a physical meaning (stiffness for example), compared to the coefficients of non-linear law that only fit curves.

[Škrinjar et al., 1998] considers the brain shift phenomenon falls into the range of small displacement. That is why, the authors used a Kelvin-Voigt model, which is an elastic material in parallel to a viscosity property. Very similar to the Kelvin-Voigt model, [Hu et al., 2007] used a Zener formulation [2] to handle the viscosity property of the tissue and accounted for the heterogeneity of the brain tissue. [Ferrant et al., 2002] models the brain as an isotropic linear elastic material to register the brain intra-operatively. In [Paulsen et al., 1999] and [Miga et al., 2000a], the authors introduced an elastic model depending on fluid gradient, which consider the brain as a sponge-like material. It is a part of the consolidation theory (bi-phasic) models, and it models the brain as a porous solid tissue with interstitial fluid. But the model still considers the

[2] modeled with springs

brain to behave linearly. The model is also used in [Miga et al., 1999] in addition to a gravitational effect term. [Castellano-Smith et al., 2001] also used a linear formulation, but distinguished white matter and grey matter mechanical properties and used 10-nodes tetrahedral elements. [Hagemann et al., 1999] also justify the choice of a linear law with small strains. [Clatz et al., 2003, 2004] modeled the brain as as linear material, with Cerebro-Spinal Fluid (CSF) external forces. More recently, [Zhang et al., 2011] used an elastic model in their framework.

Non-linear models

Non-linear materials are often hyperelastic, defined with a strain energy density function, often depending on the invariants of the tensor of deformation. This function is non-unique, hence the large range of existing models.

Most of the models found in the literature are in the following list: 2- and 5-parameter Mooney-Rivlin, 1st, 2nd, and 3rd Ogden. [Schiavone et al., 2009] measured the mechanical parameters of a isotropic homegeneous modified two-parameter Mooney-Rivlin model with an inverse problem using a light aspiration device. The authors concluded that the modified Mooney-Rivlin formulation better fit the results. On the other hand, [Valencia et al., 2012] found the second-order Ogden solid is more adapted for surgery applications.

Miller and his group published a large number of papers on the brain biomechanics. The book chapter [Wittek et al., 2011] presents their works on fully non-linear computational models. In [Miller et al., 2011], the authors argue that bi-phasic models (such as used in [Paulsen et al., 1999] and [Miga et al., 1999])are not consistent with experimental observation. That is why the models developed by the group are only single-phase. In [Miller and Chinzei, 2002], Miller and Chinzei proposed a model based on the combination of an Ogden-like model and a Prony-series relaxation modulus, based on a study on swine brain samples. In this model, the time-dependent behavior can be separated from the non-linear elastic behavior. They also consider the brain incompressible and isotropic. In [Miller and Lu, 2013], Miller and Lu suggest to use the simplest hyperelastic model, the neo-Hookean model, with a term of incompressibility, when known loading is imposed through displacements of the entire boundary, or only a part of the boundary. Indeed, the law and the mechanical parameters have a weak influence in that case.

Summary

The following table (2.1) presents several publications related to the modeling of the brain deformation as well as the constitutive equation and mechanical parameters used.

Table 2.1 – *Constitutive equation and mechanical parameters in the literature*

Publication	Constitutive equation	Mechanical parameters	Application
[Miller and Chinzei, 2002]	Ogden-like model and a Prony-series relaxation modulus	See Table 1 in the publication	Characterization of the brain tissue
[Miller and Lu, 2013]	Neo-Hookean with incompressibility	E=3000 Pa, $\nu = 0.49$	Displacement-zero problem and ...
[Miga et al., 2000a]	Bi-phasic linear model	E=2100 Pa, $\nu = 0.45$	Intra-operative registration

Table 2.1 – *Constitutive equation and mechanical parameters in the literature*

Publication	Constitutive equation	Mechanical parameters	Application
[Clatz et al., 2003]	Linear constitutive law	E=2000 Pa according to [Miller et al., 2002], $\nu = 0.45$	Brain shift modeling
[Ferrant et al., 2001]	Linear constitutive law	E=3000 Pa and $\nu = 0.4$ according to [Miga et al., 2000b]	Intra-operative registration
[Castellano-Smith et al., 2001]	Linear constitutive law with 10-noded tetrahedra	E=4000 Pa for white matter, E=8000 Pa for grey matter according to [Takizawa and Sugiura, 1994] and $\nu = 0.495$	Intra-operative registration
[Chen et al., 2011]	Bi-phasic linear model according to [Paulsen et al., 1999]	E=2100 Pa, $\nu = 0.45$	Intra-operative registration
[Vigneron et al., 2012]	Linear constitutive law	E=3000 Pa and $\nu = 0.45$ according to [Ferrant et al., 2002]	Intra-operative registration
[Hamidian et al., 2008]	Linear elastic model compared to linear solid-mechanic model	E=3000 Pa and $\nu = 0.45$ according to [Ferrant et al., 2002]	Brain shift deformation estimation
[Echegaray et al., 2014]	St. Venant-Kirchhoff material model using total Lagrangian explicit dynamics (TLED)	No data provided	Brain surgery simulator
[Fernandes et al., 2013]	Ogden-based Hyper-viscoelastic constitutive model	See Table 1 in the publication	Estimation of brain shift caused by meningioma
[Yousefi et al., 2013] (similar work than [Fernandes et al., 2013], same group)	Optimized linear law	Parameters are optimized for each patient. $E = 3000 \pm 250$ Pa and $\nu = 0.45 \pm 0.145$	Estimation of brain shift caused by meningioma

Conclusion We have observed a large number of publications in the literature related to the modeling of brain deformation. Some of the result of corresponding studies are even inconsistent or contradictory. There are no consensus on the mechanical properties of the brain. We also agree that the constitutive equation, governing the deformation of the brain, depends on the type of application, and particularly on the velocity involved. Here again, there are no consensus on the constitutive equation within the same type of application.

Despite these facts, modeling the brain deformation has got improved since [Ommaya, 1968]. We know the linear limit is about 0.1-0.3%, which is very low, and the tissue are very soft. Moreover, with the increase of the computational power, we can now simulate complex physics, and particularly brain deformation. In the following, we will present our choices for the model of deformation as well as the

boundary conditions.

2.3 Physical Modeling

2.3.1 Different anatomical components of the model

In Chapter 1, we have introduced the anatomical structures involved in a Deep Brain Stimulation (DBS) procedure, and more particularly during a brain shift. We present here the different structures we account for in our brain shift model, i.e. the ones with a physical influence on the simulation, and how we model them, as well as their interactions.

Obviously, the brain tissue deformation needs to be modeled. We rely on a physics model, based on the resolution of the equations governing the continuum mechanics. As well as the other groups working on brain models, we use the finite element method to solve numerically the differential equations. The details on the brain model are given in the next section.

The brain is included in the endocranium and it floats in CSF. In daily life, the brain does not move or deform, so we can think not to account for the endocranium or the CSF in our model. However, if the brain undergoes a brain shift, the endocranium has an influence on the brain as the brain collides it. We need to detect the collision when it happens and compute the appropriate reaction for the brain, assuming that this interaction will not deform or move the skull. Due to the high stiffness of the skull and the small velocities of the phenomenon, we can also assume the skull is rigid in our simulation. This assumption will allow us to model the endocranium more easily as there is no need to generate an appropriate FEM mesh, and it will speed up the simulation as it does not require to compute a deformation.

As a CSF loss is responsible for the brain shift, it is essential to account for its influence. We propose to model its interaction with the brain, instead of modeling a fluid. In addition to the necessity of a coupling between soft body and fluid, the simulation would behave a lot slower. Finally, a fluid model is not necessary as we are not interested in the fluid state but only on its effects on the brain. The influence of CSF is described in Section 2.3.3 and 1.2.8.

Falx cerebri is another structure that will "stop" the progression of the brain when it deforms. It is located between the two hemispheres, and constraints the lateral movements. That is why we also account for the falx cerebri in our simulation. Due to several order of magnitude between the stiffness of the brain and the falx cerebri, we propose to model dura mater structures as a rigid solid. One can also model the tentorium cerebelli and/or the falx cerebelli similarly to the falx cerebri. However, these structures are located in a brain area with low deformation due to the brain shift. The majority of the deformation takes place near the frontal part. If the brain is almost fixed near the tentorium cerebelli and the falx cerebelli, a model of interaction with the brain will not have any effect other than slowing the simulation. Due to the immobility of the brain in this area, we can add fixed constraints on the nodes of the brain mesh in the same area.

In the following chapter, we discuss on the displacement of the blood vessels due to the brain deformation. One can ask if the blood vessels and the brain tissue have an influence on each other, knowing the work that has been done on the vascularization of the liver [Peterlík et al., 2012]. However, [Cloots et al., 2008] shows the minimal impact of the modeling of the blood vessels in the brain tissue. Following this hypothesis, we do not model physically the blood vessels network. Instead, we compute the displacement of the structure depending only on the deformation of the brain tissue.

2.3.2 Brain deformation model

In order to model the brain deformation, we decided to rely on the finite element method which is a numerical technique to solve the differential equation of continuum mechanics. Our goal is to model

the physical phenomenon of brain shift, that is why mass-spring systems or other technique would not suit our application. In FEM, there are basically two main choices to take: the constitutive equation and the corresponding mechanical properties. After those choices have been made, numerical aspects must be considered. For instance, do we utilize an implicit or explicit time integration scheme? What type of elements do we use? etc The numerical aspects will be discussed in Section 2.4.2.

Constitutive law

Similarly to [Škrinjar et al., 1998], we think the brain shift, in the context of DBS, leads to small deformation. Therefore, a linear formulation of the stress-strain relation is a good approximation. To handle large displacements of the model, we use a numerical technique to account for the geometrical non-linearities (see Section 2.4.2). Moreover, for our application using our brain shift model, the viscosity property has not a big influence, as, most of the time, we rely on equilibrium configurations, In addition, we are not interested in a precise description of the internal stresses, but only on the position of the nodes. Finally, the contribution presented in Chapter 4 takes place in the same context than [Miller and Lu, 2013]. They suggest that the choice of the constitutive equation and the mechanical parameters has a weak influence on the results. It is an additional reason to use a linear formulation. To finish, we think that boundary conditions play a important role (equal or greater than the deformation model) in the modeling of a physical phenomenon. The following describe how we modeled these boundary conditions in the context of brain shift.

2.3.3 Cerebro-spinal Fluid

CSF is a fluid surrounding the brain tissue. As mentioned in Chapter Introduction, a CSF leak is one cause of the brain shift. For this reason, our simulation has to account for the CSF and its interaction with the brain tissue to model physically the brain shift.

To model the action of the fluid on the brain, we consider the forces created by the CSF on the brain. The fluid force $\boldsymbol{df}$ acting on an elementary surface dS is expressed as:

$$\boldsymbol{df} = P\ \boldsymbol{ds} = P\ \boldsymbol{n}_{\text{ext}}\ dS \tag{2.58}$$

where

- P is the pressure of the fluid on dS.
- $\boldsymbol{n}_{\text{ext}}$ is the unit normal vector to the surface dS, oriented to the exterior of the surface.
- $\boldsymbol{ds} = \boldsymbol{n}_{\text{ext}}\ dS$

The total force of pressure $\boldsymbol{f}$ acting on a surface Γ is the sum of all elementary pressure forces:

$$\boldsymbol{f} = \int_{\Gamma} P\boldsymbol{ds} \tag{2.59}$$

Pressure

The pressure is defined as a force divided by an area. The unit is the pascal, which is equal to Newton unit divided by squared meter unit. Let us consider an elementary cube of fluid. The only force acting on the element is the weight of the fluid column above it. Therefore, the fluid pressure p at a point of altitude z is expressed as:

$$p(z) = p(z_0) + \frac{1}{A}\int_{z_0}^{z} dz' \iint_A dx'dy'\rho(z')g(z') \\ = p(z_0) + \int_{z_0}^{z} dz'\rho(z')g(z') \tag{2.60}$$

where

- $p(z)$ is the pressure applying at a point of altitude z
- z_0 is the altitude of a reference point where we know the pressure $p(z_0)$
- ρ is the density of the fluid at a point of altitude z
- g is the gravitational acceleration of the fluid at a point of altitude z
- A is the area of the cube where the fluid creates a pressure

In a homogeneous incompressible fluid, the density remains constant:

$$\forall z,\ \rho(z) = \rho \tag{2.61}$$

We can reasonably consider that the variation of the gravitational acceleration can be neglected:

$$\forall z,\ g(z) = g \tag{2.62}$$

Finally, in a homogeneous incompressible fluid, the pressure is:

$$p(z) = \rho\ g\ h + p(z_0) \tag{2.63}$$

where

- $h = z - z_0$

In addition, from the equations 2.63 and 2.59, the total hydrostatic force $\boldsymbol{f}$ on a submerged planar surface Γ is the pressure of its centroid multiplied by its area:

$$\boldsymbol{f} = (\rho\ g\ h_c + p(z_0))\boldsymbol{a}_\Gamma \tag{2.64}$$

where

- $\boldsymbol{a}_\Gamma$ is the area vector of the surface
- h_c is the altitude of the centroid of the surface located in z_c

2.4 Numerical Methods

The physical models have been described in the previous section. The following focuses on the numerical aspects appearing when the physical models are computerized in to a simulation.

2.4.1 Description of the anatomical models

In this thesis, the methods and simulations have been first applied on high-fidelity anatomical 3D models of the cranial environment. It comprises a large range of anatomical structures, but the structures used in this thesis are:

1. Cortex

2. Falx cerebri
3. Endocranium
4. Lateral ventricles
5. Blood vessels (veins and arteries)

The anatomical models are reconstructed based on Computed Tomography (CT) and MRI scans, photographs of real tissues, and anatomical atlases, in accordance with medical professionals and doctors. The models do not include any idiosyncrasy of a patient.

In a second phase, the simulations are run with patient data, such as segmented images or reconstructed meshes. The process of patient-specific simulation generation is described in Section 2.5.1. The main challenge of simulating patient-specific anatomy is to rely on segmentation methods which have not been developed for this task. As an example, automatic segmentation methods does not account for voxels intersection between two distinct structures when it is used for visualization. However, it is crucial for a simulation that two distinct structures are not in intersection. Therefore, we suggest the investigation of anatomical constrained segmentation methods.

2.4.2 FEM models

FEM has been presented in Section 2.1.2. It is a numerical method to approximately solve the equation of continuum mechanics. As we decided to rely on this method, we described our choices on the numerical aspects of the method.

Co-rotational approach

A linear material is adapted for infinitesimal (or small) deformation. To speed-up a physical simulation, it is also possible to approximate the Green-Lagrange tensor, by neglecting the non-linear term. We call this process a *linearization* of the tensor, i.e. the approximation of the tensor with a linear function. Indeed, the non-linear part of the tensor is negligible compared to the linear part with small deformation. However, when elements undergo a rigid transformation, the non-linear part becomes non-negligible and leads to large errors. Instead of computing the true non-linear part of the tensor, which is very time-consuming, [Felippa and Haugen, 2005] proposes to estimate the rotation matrix of the elements in order to use them to correct the stiffness matrix. Indeed, most of the geometrical non-linearities come from the rotation of the elements. This *co-rotational* approach is a good approximation of the geometrical non-linearities and it enables to simulate large displacement with a linear constitutive law.

It is unclear in most of the papers using a linear formulation whether the tensor of deformation is linearized or not. For instance, [Valencia et al., 2012] present linear models with a linearization of the tensor of deformation. We believe this can cause large errors. Moreover, during our tests, we have observed rotation of some elements that need to be accounted for. That is why we use a co-rotational approach in our model (compared to a linearized Green-Lagrange tensor). The approach benefits from the following advantages:

- Very simple method to account for the geometrical non-linearities, which means it is fast to compute
- Balances the errors due to the linearization of the tensor of deformation
- Allows large displacement, and particularly local rotation of the elements
- Robust and stable

Dynamic Vs Static

The simulation can be either static or dynamic. Mathematically, the difference is visible in the equation 2.30. Assuming constant forces applying on a simulated object, a static approach provides the equilibrium state in one iteration (no integration in time). With more complex forces, the problem becomes quasi-static, and more iterations are necessary until the equilibrium. With the brain, gravity and CSF forces apply. Gravity influence is considered constant, but fluid forces (Section 2.3.3) depend on the position, that is why it is a quasi-static problem.

In our work, the choice of the approach (quasi-static or dynamic) depends on the application. In the contribution of Chapters 3 and 4, we are interested in the equilibrium configuration of the brain. That is why a quasi-static approach is chosen in those cases. However, the contribution of Chapter 5 is related to the insertion of the electrode in the tissue. This type of integration requires time integration, that is why a dynamic approach is chosen for this application.

Type of Elements

We have seen different way of discretizing a continuum in order to perform finite element analysis. For a 3D material, we have the choice of various elements, such as tetrahedra or hexahedra, or a combination of several types of elements. The degree of the element plays also a role in the accuracy of the model. In order to keep reasonable computation times, we focus on linear tetrahedra or hexahedra (no combination).

Our framework (Section 2.5.1) allows the user to select the type of element that will be used in the simulation. We gives the choice to the user to provide a generic framework. However, we are aware of the pros and cons of each type of element [Wang et al., 2004].

Tetrahedral meshes are simpler to generate with automatic methods, compared to hexahedral meshes [Viceconti and Taddei, 2003]. One problem is that tetrahedral elements artificially add stiffness to the object [Benzley et al., 1995; Wang et al., 2004]. In our last publication [Bilger et al., 2014a], we decided to use hexahedra similarly to [Miller et al., 2011], but we still lack of a robust tool to mesh the geometry with fidelity. Meshless methods [Miller et al., 2012] can also be studied in the future.

Time integration

Section 2.1.3 introduced two different types of time integration. Despite a large number of other methods, we focus on these two popular methods. Both have pros and cons: explicit methods are simpler to implement, faster to compute, but require small time steps. On the other hand, implicit method are more complex and require to solve a large linear system. According to [Wittek et al., 2007] both techniques are equivalent in term of accuracy, that is why they selected the fastest method, i.e. an explicit integration, for a real-time purpose. In opposite, the restriction on the time steps encourages us to use a implicit method. In addition, we use the possibility to speed-up the computation in the framework SOFA, for example using a pre-conditionner [Courtecuisse et al., 2010].

2.4.3 Cerebro-spinal fluid

This section presents the numerical model that has been developed, in order to reproduce the action of the fluid on the brain, physically modeled in Section 2.3.3.

Force model

Because we use FEM, the object is discretized into elements defined by the connection of nodes. Therefore, the forces are computed for every surfacic element of the object surface.

$$\boldsymbol{f} = \iint_{S_e} (\rho\, g\, h + p(z_0))\mathbf{ds} \tag{2.65}$$

where

- S_e is the surfacic element

We use only plane element (non-curved), so we can apply the equation 2.64:

$$\boldsymbol{f} = (\rho\, g\, h_C + p(z_0))\boldsymbol{a}_{S_e} \tag{2.66}$$

where h_C is the centroid of the element.

For example, for a triangular element composed of three vertices located in $\boldsymbol{x_1}$, $\boldsymbol{x_2}$ and $\boldsymbol{x_3}$, the hydrostatic force $\boldsymbol{f}$ will be:

$$\boldsymbol{f} = \frac{1}{2}\left(\rho\, g\, h\left(\frac{\boldsymbol{x_1}+\boldsymbol{x_2}+\boldsymbol{x_2}}{3}\right) + p(z_0)\right)(\boldsymbol{x_2}-\boldsymbol{x_1}) \wedge (\boldsymbol{x_3}-\boldsymbol{x_1}) \tag{2.67}$$

If we distribute the forces to the nodes of the triangle, we have:

$\forall\, 1 \leq i \leq 3$

$$\boldsymbol{f_i} = \frac{1}{6}\left(\rho\, g\, h\left(\frac{\boldsymbol{x_1}+\boldsymbol{x_2}+\boldsymbol{x_2}}{3}\right) + p(z_0)\right)(\boldsymbol{x_2}-\boldsymbol{x_1}) \wedge (\boldsymbol{x_3}-\boldsymbol{x_1}) \tag{2.68}$$

So that $\boldsymbol{f_1}+\boldsymbol{f_2}+\boldsymbol{f_3} = \boldsymbol{f}$ This expression of the force on a node has been developed for only one triangle. Actually, the total force on a node is the sum of the contribution of each triangle around the node. This is explicitly taken into account in the expression of the derivative, presented in the following.

As CSF is mainly composed of water, its density is very close to 1000 kg/m³. In our model, we use the value of [Valencia et al., 2012], i.e. 1007 kg/m³.

Derivative

Regarding the equation 2.55, the derivative of the force with respect to the position must be computed. We observe that the expression of the nodal force in the equation 2.68 includes positions of other nodes of the mesh. Because of this property, the derivative of the force at a node i with respect to the position of the node j can be non-null. More precisely, the equation 2.68 includes only nodes which are in the same triangle than the node where the derivative is computed. Therefore, the derivative is non-null when the force is taken at the node i with respect to the position of the nodes around the node i or the node i itself.

Let us define T_i, the set of triangles where the node i is one of vertices. And $T_{i,j}$ is the set of triangles where the nodes i and j are two of the vertices (i and j define an edge of the triangles). If $i = j$, then $T_{i,j} = T_i$. G_t is the center of gravity of the triangle t and n^t is the vector area of the triangle t.

$\forall\, 1 \leq i, j \leq n$, with i, j indices of vertices inside the same triangle (0 otherwise):

$$\frac{\partial \boldsymbol{f_i}(X)}{\partial X_j} = \sum_{t \in T_i} \frac{1}{3}\rho g \left[\left(\frac{\partial G_t}{\partial X_j}\right)\left(\frac{\partial h}{\partial X_j}(G_t)\right)(n_i^t)^T + h(G_t)\left(\frac{\partial n^t}{\partial X_j}\right)\right] \tag{2.69}$$

Because the derivatives with respect to X_j are non-null only if the node j is one of the vertices of the triangle t,

$$\frac{\partial \boldsymbol{f_i}(X)}{\partial X_j} = \sum_{t \in T_{i,j}} \frac{1}{3}\rho g \left[\frac{1}{3}\left(\frac{\partial h}{\partial X_j}(G_t)\right)(n^t)^T + h(G_t)\frac{\partial n^t}{\partial X_j}\right] \tag{2.70}$$

The difficulty is the derivative of the vector area. Let us introduce the anti-symmetric matrix form of a vector:

$\forall \varepsilon \in \mathbb{R}^3$,

$$[\varepsilon]^\times = \begin{bmatrix} 0 & -\varepsilon_z & \varepsilon_y \\ \varepsilon_z & 0 & -\varepsilon_x \\ -\varepsilon_y & \varepsilon_x & 0 \end{bmatrix} \tag{2.71}$$

Therefore, for i,j and k, three nodes in the same triangle t, and l one of the three nodes:

$$\begin{aligned} \frac{\partial n^t(X_i, X_j, X_k)}{\partial X_l} &= \frac{1}{2} \frac{\partial}{\partial X_l} \left((X_j - X_i) \wedge (X_k - X_i) \right) \\ &= \frac{1}{2} \left([X_j - X_i]^\times \frac{\partial (X_k - X_i)}{\partial X_l} - [X_k - X_i]^\times \frac{\partial (X_j - X_i)}{\partial X_l} \right) \\ &= \frac{1}{2} \left([X_j - X_i]^\times (\delta_{lk} - \delta_{li}) \, \mathbb{I} - [X_k - X_i]^\times (\delta_{lj} - \delta_{li}) \, \mathbb{I} \right) \end{aligned} \tag{2.72}$$

Lastly,

$$\frac{\partial h}{\partial x} = \boldsymbol{n_f} = \begin{bmatrix} -\boldsymbol{n_f}_x \\ -\boldsymbol{n_f}_y \\ -\boldsymbol{n_f}_z \end{bmatrix} \tag{2.73}$$

where $\boldsymbol{n_f}$ is the normal vector to the fluid surface, which should be opposite to the gravity vector.

2.4.4 Interactions with bony structures

The global equation to solve in our FEM based approach is the equation 2.45. We have seen how to solve this equation every time step, but this equation is valid only for one object. It is possible to add a second object in the simulation and solve the same equation for this object. However, solving the two equations of motions only computes the new positions of the objects as their are moving alone, without any interactions with the other object. Therefore, any interaction, such as a collision, is not taken into account in the equation 2.45. In this section, we introduce briefly the concepts used to account for the collision between objects in a simulation. We recall that the objective is to take into account the interaction between the brain and the endocranium, and between the brain hemispheres and the falx cerebri.

Collision detection

Collision detection is a important field of computer graphics, and a lot of papers and studies addressed this problem. However, this is a necessary first step before computing the reaction to the collision. To detect a collision between two objects in a simulation, there are *discrete detection* and *continuous detection*. As a simulation is discretized in time, a collision can occur between time steps. A continuous detection consists in extrapolate the movement between time steps and detect precisely the time of the impact [Larsson and Akenine-Möller, 2001; Tang et al., 2009]. These methods are generally time consuming, and are not adapted to real-time simulations. In opposite, discrete detection methods detect collisions for every time steps, no matter what could happen between time steps. The computation is based on the current configuration of the objects. Although the method can miss some contact events, this type of methods are faster and more adapted to real-time simulation.

Independently on the method used, the goal is to detect the elements in collision (or about to collide) with other elements. Note that two elements of the same object can collide. It is a *self-collision* but it is not

necessary in the context of the brain modeling. Multiple detection phases allow to detect the elements (or primitive such as triangles, edges or points) in collision: the *broad-phase* consists in eliminate quickly objects not in collision. The *narrow-phase* determines the primitives close to the collision location. And finally, the *exact-phase* computes exactly the primitives involved in the collision.

Contacts

Once we have detected the primitives in intersection, we need to solve the contact(s), i.e. compute the constraints such that the two objects are no more in intersection. This is formalized by the Signorini's law:

$$0 \leq \delta \perp f \geq 0 \tag{2.74}$$

It expresses that if the distance of interpenetration δ is positive, no contact force f is applied (because objects are not in collision).

One simple and time effective method is to add spring forces to the nodes in intersection. The force $\boldsymbol{f}$ is expressed as

$$\boldsymbol{f} = k\ \delta\ \boldsymbol{n} \tag{2.75}$$

where

1. δ is the distance of interpenetration
2. $\boldsymbol{n}$ is the normal vector to the contact
3. k is the stiffness of the spring

This method is based on *penalty*. Many problems arise from this method, but one big disadvantage is that it does not have a physical sense. One cannot be certain that the Signorini's law will be respected after the end of the time step. On the other hand, others methods consists in apply a movement to the nodes such that the constraints are totally satisfied at the end of the time step [Popescu and Compton, 2003; Galoppo et al., 2006]. It consists in adding a term in the equation 2.45:

$$\mathbb{M}\ddot{\boldsymbol{x}} + \mathbb{F}(\boldsymbol{x}, \dot{\boldsymbol{x}}) = \boldsymbol{f}_{\text{ext}} + \mathbb{H}^T\boldsymbol{\lambda} \tag{2.76}$$

where

1. $\mathbb{H} = \frac{\delta\psi}{\delta\boldsymbol{x}}$ with ψ representing the constraints. The matrix contains the constraint directions.
2. $\boldsymbol{\lambda}$ is the the Lagrange multipliers and contains the constraint force intensities.

Lagrange multipliers are a mathematical technique to find the minimum (or maximum) of a function under constraints. In the equation 2.76, the Lagrange multipliers $\boldsymbol{\lambda}$ are unknown and have to be computed.

When using the backward Euler time integration scheme (Section 2.1.3), the constraints term $\mathbb{H}^T\boldsymbol{\lambda}$ is added to the linear system 2.57 as follow:

$$\mathbb{A}\boldsymbol{x} = \boldsymbol{b} + \Delta t\ \mathbb{H}^T\boldsymbol{\lambda} \tag{2.77}$$

The solving process of $\boldsymbol{\lambda}$ from the equation 2.77 is performed in three steps. We summarize them very briefly, but more details are given in [Duriez et al., 2006].

Step 1: The equation is solved independently of the other objects by setting $\boldsymbol{\lambda}$ to 0. We obtain the *free motion* $\boldsymbol{x}^{\text{free}}$ of the object, as there is no interaction between objects.

Step 2: In the space of a contact α between colliding objects, we introduce the relative displacement δ_α and velocity $\dot{\delta}_\alpha$. The relative displacement depends on the contact α, the position $\boldsymbol{x}_1$ and $\boldsymbol{x}_2$ and time

t. The set of contacts are assembled into a global relative displacement vector $\boldsymbol{\delta}$. After a linearization of the relative displacement, we obtain:

$$\boldsymbol{\delta} = \boldsymbol{\delta}^{\text{free}} + \Delta t^2 \, \mathbb{H}\mathbb{A}^{-1}\mathbb{H}^T\boldsymbol{\lambda} = \boldsymbol{\delta}^{\text{free}} + \Delta t^2 \, \mathbb{W}\boldsymbol{\lambda} \tag{2.78}$$

where $\mathbb{W} = \mathbb{H}\mathbb{A}^{-1}\mathbb{H}^T$ is called the *compliance matrix*. This last equation is a linear complementary problem. If it is combined with Coulomb's law, it becomes a non-linear complementary problem. The value of $\boldsymbol{\lambda}$ is obtained using a Gauss-Seidel algorithm[3] dedicated to the non-linear complementary problem.

Step 3: $\boldsymbol{\lambda}$ is now available and a correction of the free motion can be applied. Finally, the new position is

$$\boldsymbol{x} = \boldsymbol{x}^{\text{free}} + \boldsymbol{dx} \tag{2.79}$$

such that

$$\mathbb{A}\,\boldsymbol{dx} = \mathbb{H}^T\boldsymbol{\lambda} \tag{2.80}$$

2.4.5 Reference State

Introduction

In normal conditions, the brain is contained inside the skull and is surrounded by CSF. The fluid acts on the brain with pressure forces. Moreover, on earth, the brain undergoes also the effects of gravity. Therefore, the brain is at any moment under the action of forces due to the CSF and gravity. Including during a CT scan or a MRI. When a surgeon visualizes an image of a patient, the patient's brain on the image undergoes forces. It is yet static, presenting no movement. The brain is at equilibrium with these forces.

The brain shift simulation is generated with patient images. For instance, the brain is segmented, then reconstructed. If it is used as it is in the simulation, forces are applied on it. The brain will deform until equilibrium. However, the reconstructed brain is known to be already at equilibrium. In these conditions, the simulation should apply the forces such that the equilibrium state corresponds to the image state. But this is the inverse goal of a simulation. Usually a simulation computes the resulting deformation of the structure under known conditions. Here, we already know the resulting deformation under the known conditions. But we can change the initial geometry of the brain, such that the brain deforms until the equilibrium state corresponding the the image. Such a geometry is the *reference state* or *reference configuration* or *rest shape* of an object. It is the state when no forces act on it. The geometry used at $t = 0$ in a simulation is called the *initial state*. In most of simulations, the initial state and the reference state are the same. In our case, we have seen it is crucial to dissociate both states.

To give a concrete example, let us consider the example of the figure 2.7. On the left, the cylinder (yellow and denoted $\Omega_1^{(0)}$) is horizontal, and the left base is fixed with fixed constraints (the displacement of the constrained nodes is null). The mass is heterogeneous in the object. It undergoes the gravity in the vertical direction. The cylinder is deformable, so that is bend in the direction of the gravity. The green shape $\Omega_1^{(eq)}$ is the result of the action of gravity on the cylinder. It is the final shape at equilibrium. On the right, the cylinder $\Omega_2^{(0)}$ is bend upward at rest and initially. We can observe that, with that rest shape, the final shape of the cylinder at equilibrium $\Omega_2^{(eq)}$ is a horizontal straight cylinder. In a third simulation, we set different shapes for the initial and the rest: $\Omega_2^{(0)}$ is the rest configuration, while $\Omega_1^{(0)}$ is the initial configuration. In that case, the cylinder does not move whereas forces are acting on it. The object is initially at equilibrium. The goal is to compute $\Omega_2^{(0)}$ for the brain.

[3] Iterative method to solve linear systems

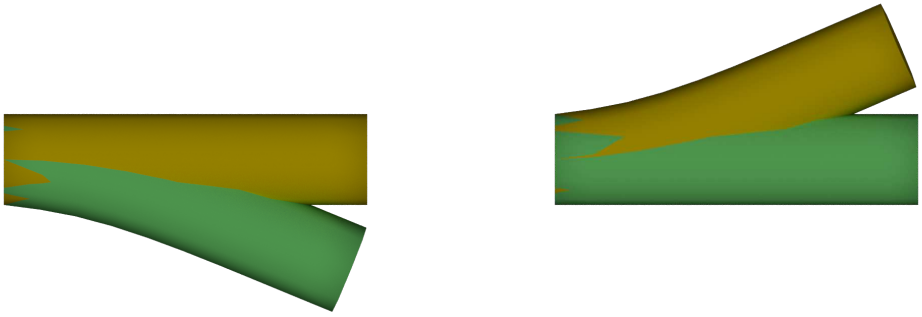

(a) Straight cylinder as initial shape (b) Deformed cylinder as initial shape

Figure 2.7 – *Two simulations of a deformable cylinder undergoing the effect of gravity. The yellow cylinder is the initial shape, while the green cylinder is the final shape, obtained at equilibrium.*

Reference State Computation

The computation of the reference state results from an inverse problem. Such problems have not been extensively studied as it requires, in direct computation, to inverse the governing equations. Moreover, it is often depending on the conditions of the problem. [Rajagopal et al., 2005, 2006; Rajagopal and Chung, 2007] proposed a direct calculation of the reference state of the breast. However, only a few details are given. [Ellabib and Nachaoui, 2008] introduces a complex iterative algorithm, but only valid for linear elasticity.

We first performed tests with an iterative geometric algorithm we have developed. We realized it was already published in [Sellier, 2011]. That is why we only describe the principles and the implementation and present some results. Proves of convergence are given in [Sellier, 2011] for a linear constitutive law. The method relies only on the geometry of the structure, and does not inverse the equations of motion. It iteratively computes a new shape of the structure until the equilibrium corresponds to the wanted shape.

Let us consider an object Ω discretized with n nodes. Let $X_i^{(0)}$ denote the initial position of the node i in the simulation of the object Ω, and $X_i^{(\text{def})}$ is the position of the node i at equilibrium, at the end of the simulation. The superscript stands for *deformed*. It corresponds to the position of the object in the patient image. In the algorithm, we set the rest position to be $X_i^{(0)}$. Intuitively, $X_i^{(\text{def})}$ depends on $X_i^{(0)}$. Finally, let $X_i^{(\text{ini})}$ denote only the position of the node i in the patient image, independently on the simulation. The goal of the algorithm is to iteratively compute a new $X_i^{(0)}$ such that $X_i^{(\text{def})} = X_i^{(\text{ini})}$, or minimizing $\|X_i^{(\text{def})} - X_i^{(\text{ini})}\|$. Here $X_i^{(\text{def})}$ is the position at equilibrium when the new $X_i^{(0)}$ is the initial and rest position. We add an index j to the initial position in the position ${}^jX_i^{(0)}$ to indicate the iteration j in the process.

On the first iteration, we set ${}^0X_i^{(0)} = X_i^{(\text{ini})}$ as a first guess. The simulation runs until equilibrium and results in a displacement ${}^0\Delta_i = X_i^{(\text{ini})} - {}^0X_i^{(\text{def})}$. For the next iterations ($j > 0$), we set ${}^jX_i^{(0)} = {}^{j-1}X_i^{(0)} - {}^{j-1}\Delta_i$. Another simulation runs with ${}^jX_i^{(0)}$ and result in a displacement ${}^j\Delta_i = X_i^{(\text{ini})} - {}^jX_i^{(\text{def})}$. The paper [Sellier, 2011] proves the convergence $\lim_{j\to\infty} \|{}^j\Delta_i\| = 0$.

In practice, we do not run j simulations. The framework SOFA allows to modify directly the reference

positions during a simulation. The equilibrium is then broken and the new deformed position is computed. Therefore, we iterate inside one unique simulation. Once we have computed the reference positions, SOFA allows to distinguish the reference position and the initial position by assigning them different values.

To evaluate the accuracy of the reference state computation, we can use the distance $\|^j\Delta_i\|$ as an error compared to our objective. More globally, the algorithm is defined to converge when

$$\frac{1}{n}\sum_{i=1}^{n}\|^j\Delta_i\| < \varepsilon_{\text{avg}} \tag{2.81}$$

The following convergence criteria can also be used:

$$\forall i \leq n,\ \|^j\Delta_i\| < \varepsilon_{\text{max}} \tag{2.82}$$

The final algorithm is sumarized in the algorithm 1.

Algorithm 1 Calculate the reference state

1: $^0X_i^{(0)} \leftarrow X_i^{(\text{ini})}$
2: run simulation 0 until equilibrium
3: $^0\Delta_i \leftarrow X_i^{(\text{ini})} - {}^0X_i^{(\text{def})}$
4: $j \leftarrow 0$
5: **while** $\frac{1}{n}\sum_{i=1}^{n}\|^j\Delta_i\| > \varepsilon_{\text{avg}}$ **do**
6: $\quad {}^jX_i^{(0)} \leftarrow {}^{j-1}X_i^{(0)} - {}^{j-1}\Delta_i$
7: $\quad$ run simulation j until equilibrium
8: $\quad {}^j\Delta_i \leftarrow X_i^{(\text{ini})} - {}^0X_i^{(\text{def})}$
9: $\quad j \leftarrow j+1$
10: **end while**

Implementation and Results

Before applying the method on a complex geometry such as the brain, we show some test results on a simple cylinder, similarly to the example in the figure 2.7. The cylinder is deformable, so that is bend in the direction of the gravity. The object is simulated in SOFA and different scenarios are tested. The different simulation scenarios are summarized in the table 2.2, with the results in error and number of iterations to converge. The results are illustrated in the figure 2.8.

		Mass density					
		500		1000		1500	
Young's modulus (kPa)	50	1.90E-004	5	9.65E-004	20	-	-
	100	2.12E-004	3	5.66E-004	5	8.15E-004	9
	200	1.45E-004	2	2.12E-004	3	3.11E-004	4

Table 2.2 – *The set of parameters (Young's modulus and the mass density) varying in our tests of the reference state algorithm. In a cell, the left value is the average distance between the initial shape and the equilibrium configuration when the current reference state is used (equation 2.81). The second value is the number of iterations required to converge with the criteria defined in the equation 2.82 with* $\varepsilon_{\text{max}} = 10^{-3}$.

In a second phase of tests, buoyancy is added to the cylinder, with the model of fluid interaction presented in Section 2.4.3. The density of the fluid is set to $\rho = 1000$, like water or CSF. The results are presented in the table 2.3 and the figure 2.9. These tests validate the algorithm with the forces due to gravity and a surrounding fluid, therefore, we can apply it on a brain geometry.

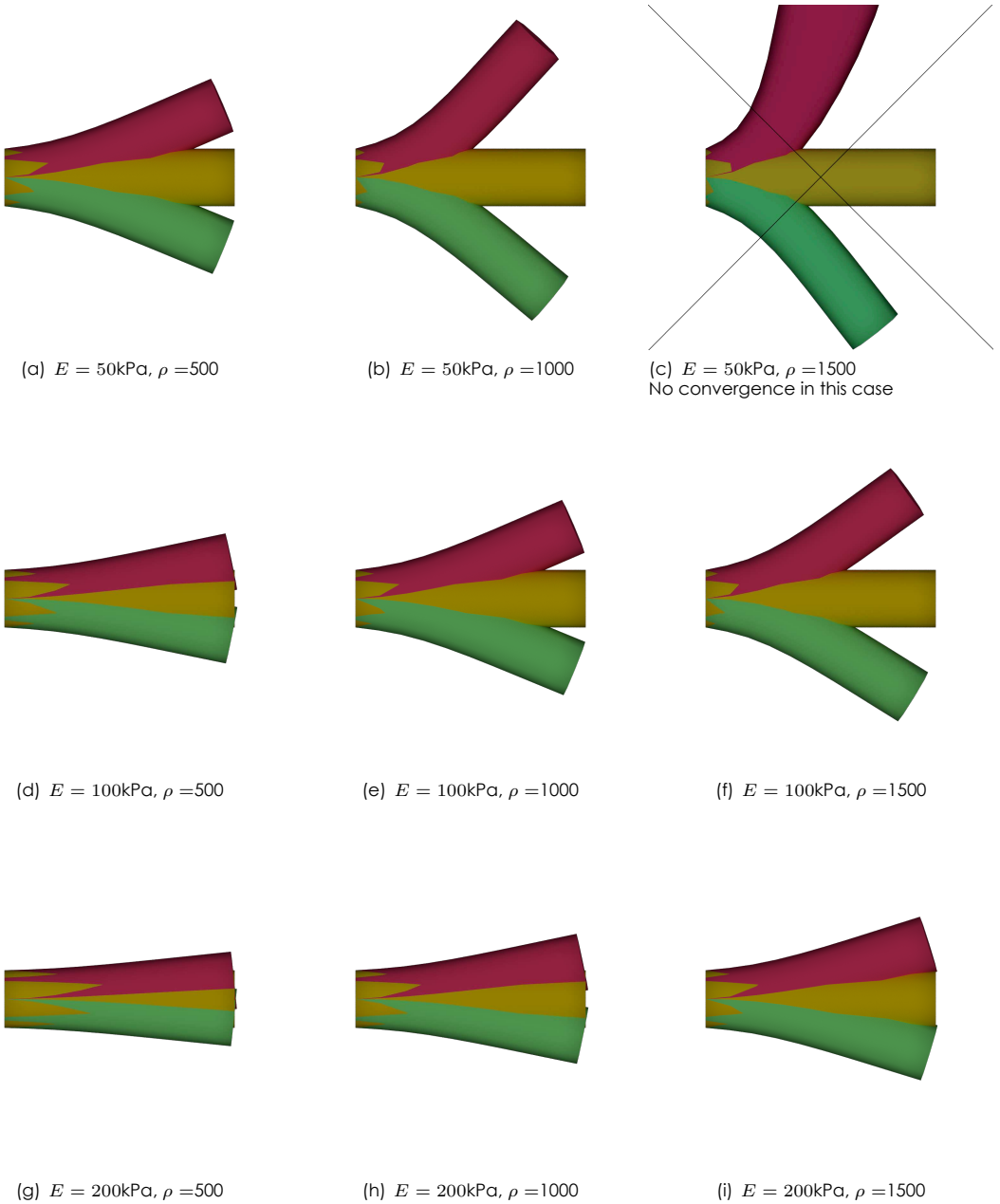

(a) $E = 50$kPa, ρ =500 (b) $E = 50$kPa, ρ =1000 (c) $E = 50$kPa, ρ =1500
No convergence in this case

(d) $E = 100$kPa, ρ =500 (e) $E = 100$kPa, ρ =1000 (f) $E = 100$kPa, ρ =1500

(g) $E = 200$kPa, ρ =500 (h) $E = 200$kPa, ρ =1000 (i) $E = 200$kPa, ρ =1500

Figure 2.8 – *Reference state computed for different sets of parameters. The Young´s modulus and the mass density vary. The initial shape of the cylinder is depicted in yellow, the equilibrium configuration (with a reference state equal to the initial state) is in green and the resulting reference state is in red.*

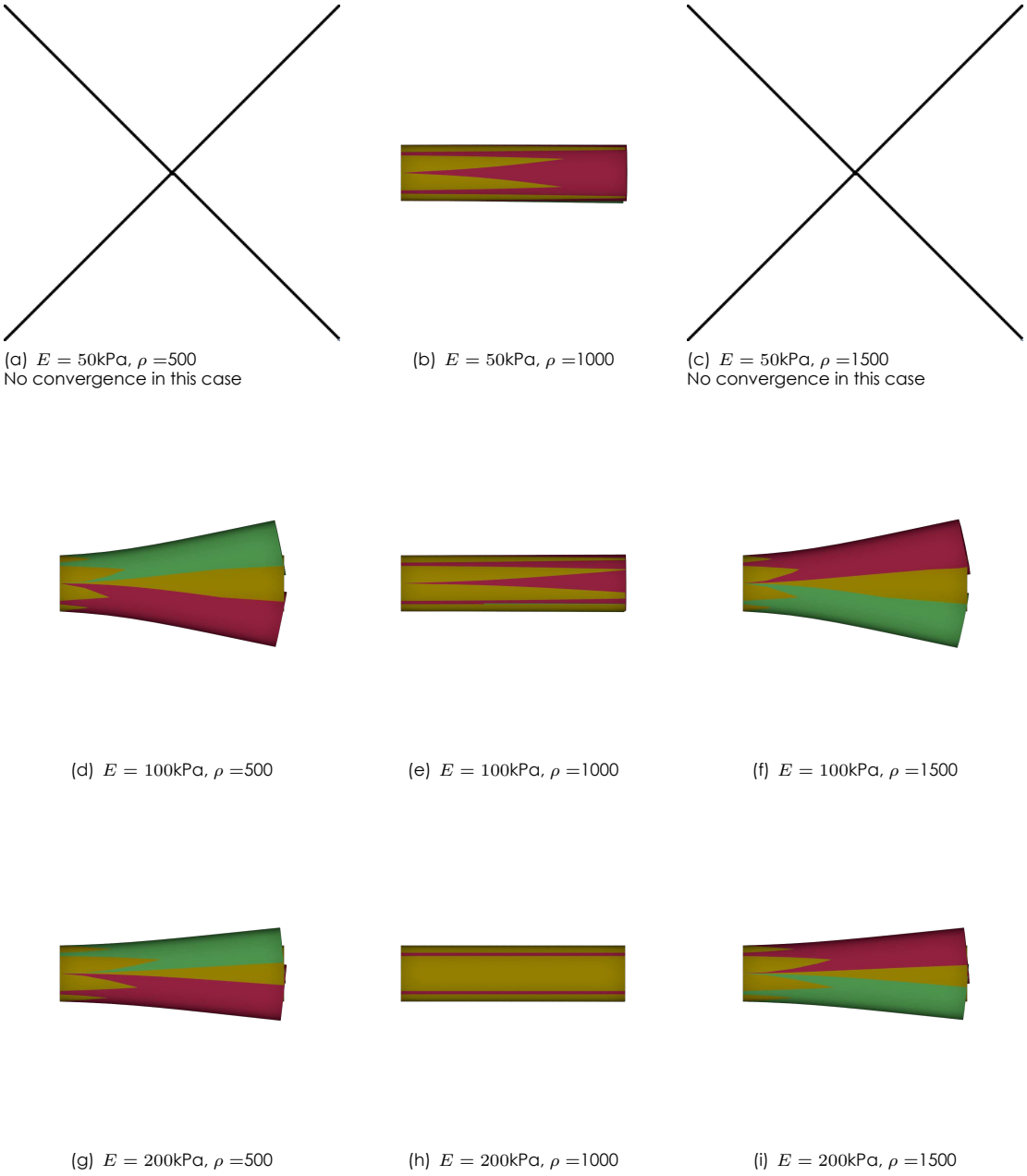

(a) $E = 50$kPa, ρ =500
No convergence in this case

(b) $E = 50$kPa, ρ =1000

(c) $E = 50$kPa, ρ =1500
No convergence in this case

(d) $E = 100$kPa, ρ =500

(e) $E = 100$kPa, ρ =1000

(f) $E = 100$kPa, ρ =1500

(g) $E = 200$kPa, ρ =500

(h) $E = 200$kPa, ρ =1000

(i) $E = 200$kPa, ρ =1500

Figure 2.9 – *Reference state computed for different sets of parameters. The Young´s modulus and the mass density vary. The initial shape of the cylinder is depicted in yellow, the equilibrium configuration is in green and the resulting reference state is in red. The experiment is similar to the figure 2.8, but with buoyancy (fluid density = 1000) in addition.*

		Mass density					
		500		1000		1500	
Young's modulus (kPa)	50	-	-	6.45E-005	2		10
	100	2.32E-004	4	2.50E-004	1	3.16E-004	4
	200	2.95E-004	2	3.50E-004	0	2.28E-004	2

Table 2.3 – *Same as the table 2.2, but with buoyancy in addition.*

2.4.6 Other boundary conditions

Because of its absence of motion during brain shift, the degrees of freedom in the vicinity of the tentorium cerebelli has been assigned to Dirichelet boundary condition. It imposes fixed positions to the nodes. Numerically, it null the row and the column corresponding to the node in the system to solve. In other conditions, it can be necessary to account for the interaction with the tentorium cerebelli, which is also dura mater, therefore the numerical model would be similar to the methods used with falx cerebri.

Brain hemispheres are modeled independently, but anatomically, the interhemispheric commissures connect the hemispheres. To mimic this anatomical feature, we add bilateral constraints[4] between both hemispheres, in the area of the corpsus callosum and fornix. This boundary condition is important in case of asymmetric brain shift: the deformation of an hemisphere due to brain shift will have an influence on the other hemisphere.

2.5 Global model

The following illustration (Figure 2.10) represents the physical components of our model. In the illustration, the patient is in the supine position, and the head orientation aligned with the horizontal plane. The brain is represented with triangles to indicate the model uses a mesh with tetrahedral elements to discretize the continuum of the brain in order to solve the equations governing the deformation. The Dirichlet boundary conditions are represented near the brainstem area. The CSF forces are represented by the surrounding fluid, between the brain and the skull, and in Figure 2.10(a) also by force vectors of some points distributed on the brain surface. The bilateral arrows indicates the potential contacts between the brain and the skull. Note that we also account for the contacts between the brain and the falx cerebri. In Figure 2.10(a), we represent the vectors of the two main forces acting on the brain: weight and CSF forces. At equilibrium, when the fluid surrounds fully the brain, the CSF balances the weight. However, when fluid is removed, the balance is broken (see Figure 2.10(b) where the vectors norms are not equal anymore and fluid is removed compared to Figure 2.10(a)). This leads to the brain deformation observed in Figure 2.10(b).

This model will be used in different contributions, presented in the following chapters. In order to facilitate the use of the model for a new patient, we developed a framework able to generate a simulation from patient-specific data.

2.5.1 Patient-specific simulation

The pipeline presented in [D'Albis et al., 2014], called pyDBS, provides the segmentation and the reconstruction of anatomical structures of interest. However, the use of them in a simulation is not straightforward. In this section, we present the steps to generate a patient-specific simulation from the output of the pyDBS pipeline. The process is managed with an application (screenshot in Figure 2.12) where the user can graphically run a patient-specific simulation from the pyDBS output.

[4] Equality constraints representing geometric connections

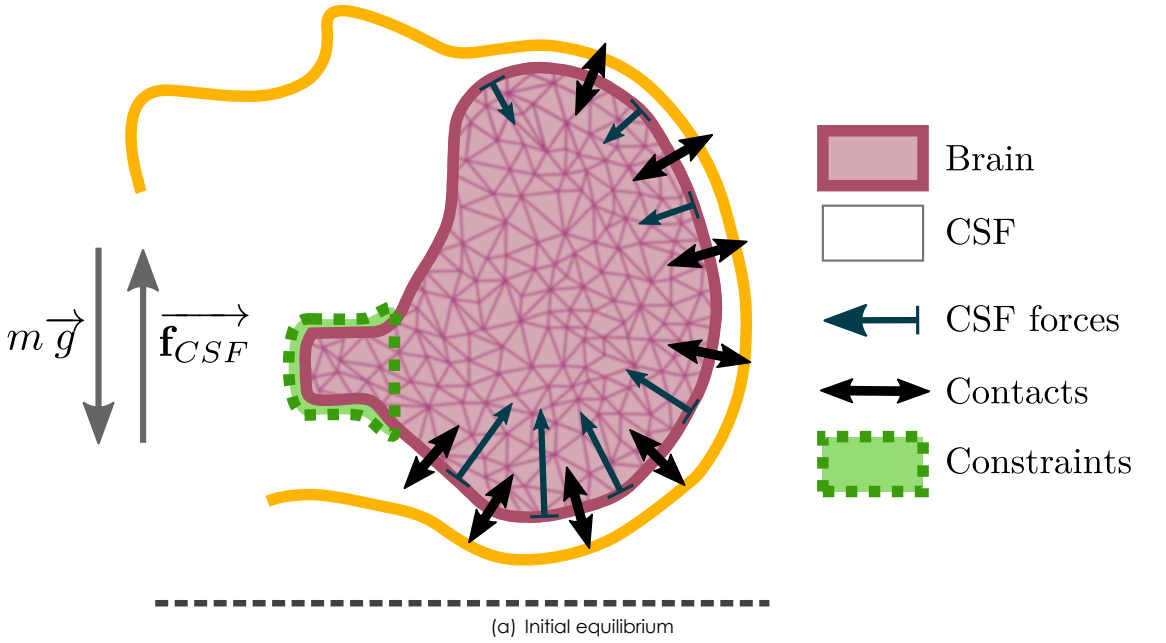

(a) Initial equilibrium

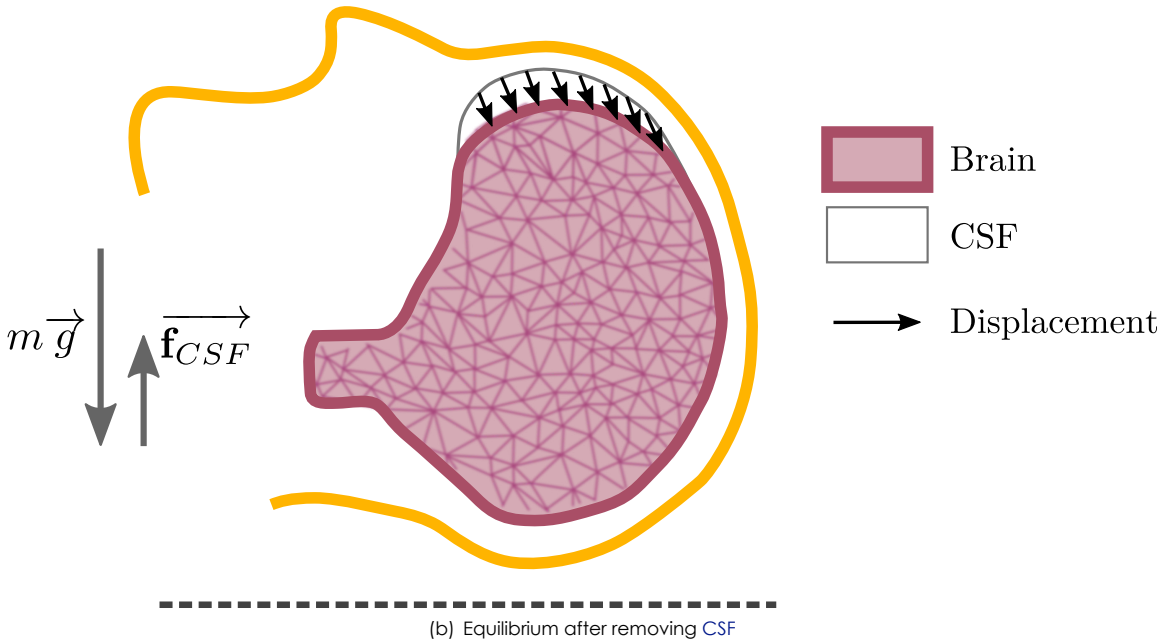

(b) Equilibrium after removing CSF

Figure 2.10 – *Global model representation*

Image processing

In some cases, some segmented structures are in intersection, sharing common voxels. We recall that it is crucial for the simulation not to start with intersections, otherwise contact forces would be created immediately. For instance, Figure 2.11 shows the intersection of the two brain hemispheres. Those intersections are usually small compared to the size of the objects. Waiting for appropriate segmentation methods, we propose to remove the common voxels, in order to reconstruct the models.

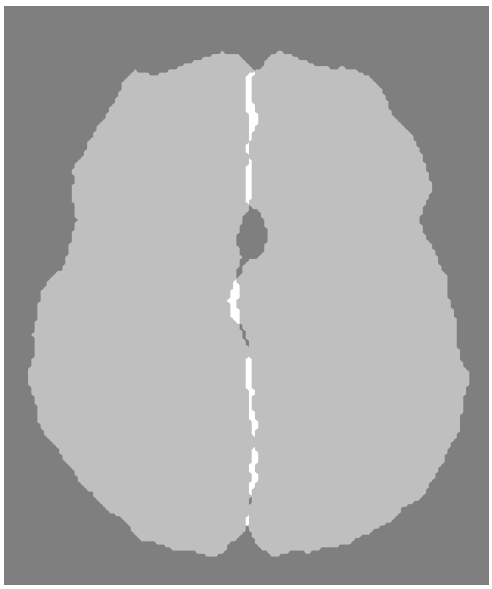

Figure 2.11 – *Visible intersection between the binary mask of the two hemispheres coming from an independent automatic segmentation.*

Mesh reconstruction

In order to generate the meshes required for the patient-specific simulation, we need two types of reconstructions. First, the deformable objects needs to be meshed in volume, i.e. with volumic elements such as tetrahedron or hexahedron. Such meshes are called *3d meshes*. Second, other structures, such as collision models or visual models, only need a *surface mesh*, made of surface elements. We will see how we use both methods and what are the parameters.

The generation of volumic meshes requires a bounded domain such as the brain in our case. Due to the complexity of the meshing process and the FEM algorithms, we rely on meshes made with only one type of elements. Moreover, again due to the complexity of the meshing process, we focus only on tetrahedral and hexahedral elements. Other types of elements or hybrid meshes require more time, more expertise and more control on the meshing process, which is not compatible with our goal to generate patient-specific simulation tools for surgeons.

To generate volumic meshes with tetrahedral elements, the library CGAL[CGAL, 2014] has been chosen for several reasons:

1. the ability to generate 3D meshes from a segmented 3D image
2. it allows to subdivide the mesh into several subdomains, particularly useful for heterogeneous models

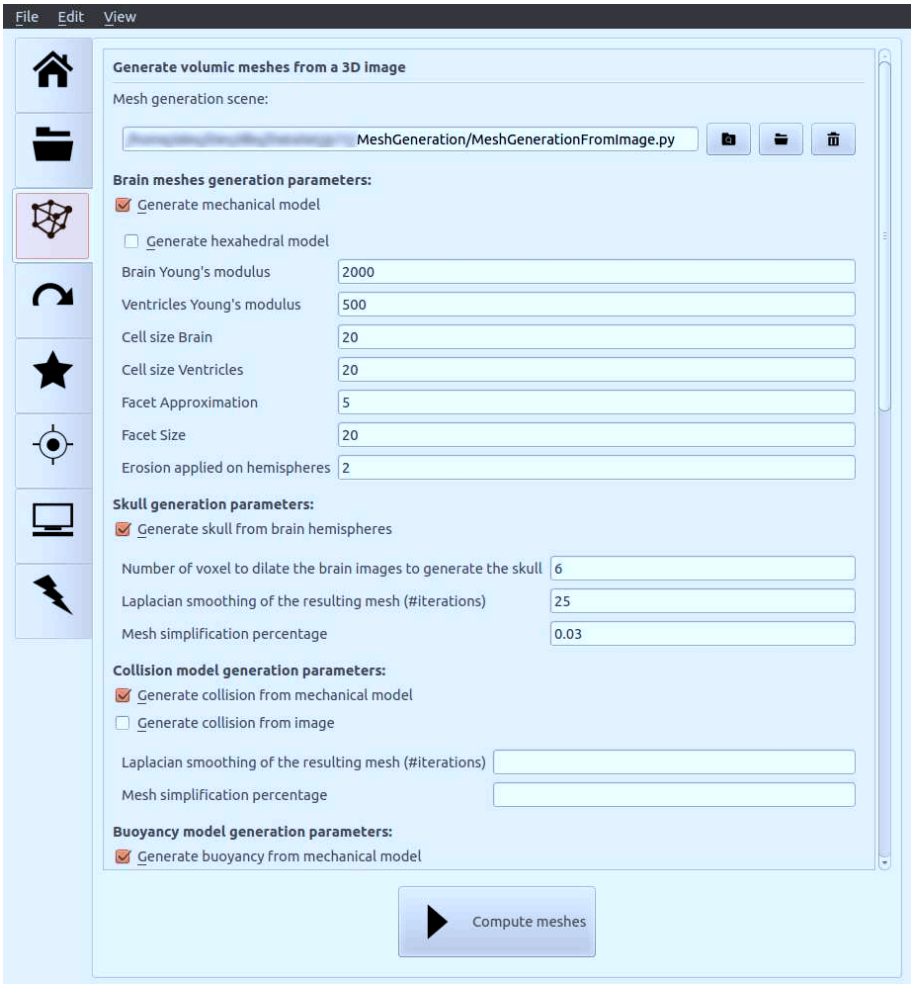

Figure 2.12 – *Screenshot of the application to compute the required meshes.*

3. the boundaries between the subdomains is respected: an element belongs to one and only one subdomain

Those properties are important for our simulation. For example, the lateral ventricles are large structures inside the brain, which are cisterns filled with CSF. Therefore, we need to distinguish this structure from the brain parenchyma. In a first phase, we decided to model the ventricles in the same mesh than the brain parenchyma, but with different mechanical parameters. It constraints us to use the same constitutive law. In the future, we can use a more advanced model for the CSF in the ventricles, and then distinguish both structures in two different objects. For the moment, in order to use the same mesh for the brain and the ventricles, we subdivide the brain mesh into two subdomains: one domain containing the ventricles and the rest, i.e the brain tissue. It is important here to respect the boundaries of the domains. One element belongs to only one subdomain in order to assign it only one mechanical property. To perform the meshing process with several subdomains, CGAL needs only one image, where the intensity of a pixel indicates the domain it belongs to. Therefore, another image processing is necessary in order to merge several segmented structures into one labeled image. Finally, CGAL allows to use different meshing parameters for every subdomains (see Figure 2.12). Note it is also possible to subdivide the brain tissue into two subdomains: the white matter and the grey matter. Unfortunately, mechanical parameters are not well

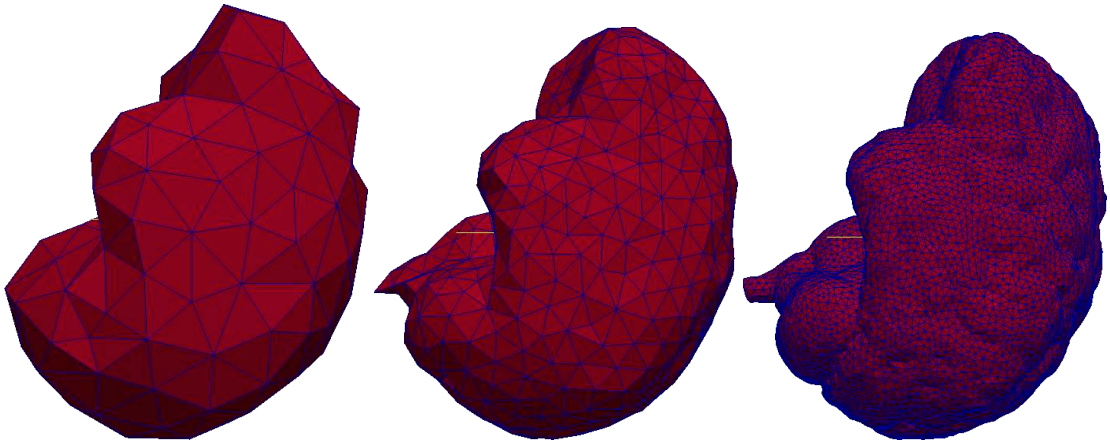

(a) 429 tetrahedra, 135 nodes (b) 5718 tetrahedra, 1188 nodes (c) 140,550 tetrahedra, 25,889 nodes

Figure 2.13 – *Meshes of a brain hemispheres with different meshing parameters, resulting in more or less geometrical accuracy.*

known and it would require a larger number of elements, which would lead to larger computation times. Briefly, the CGAL algorithm relies on a Delaunay refinement process, followed by an optimization phase. Figure 2.13 shows examples of different meshes for the same patient's brain, while Figure 2.14 emphasizes the meshing around the ventricles. In our interface, we let the user define the meshing parameters. With CGAL, the number of tetrahedra depends on the meshing parameters and the input geometry. Therefore, from one patient to another it is not possible to set the same number of tetrahedra, but the average size of the tetrahedra will be maintained. In our tests, we usually use meshes with 5,000 to 10,000 tetrahedra in order to keep fast computation.

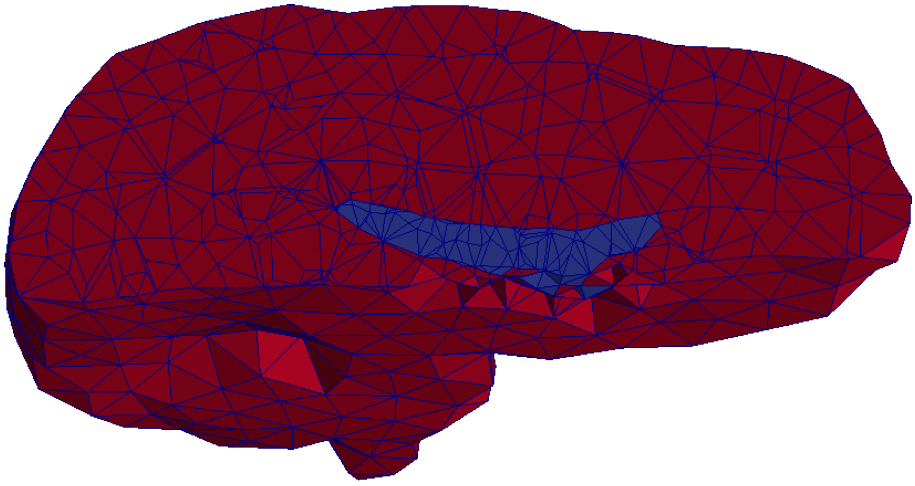

Figure 2.14 – *Clip of a heterogeneous mesh of the brain and ventricles. The colors indicate the Young's modulus*

Concerning hexahedral meshes, the meshing process is more complex than for tetrahedral meshes, and the development of automatic algorithms is still an open problem. We propose to approximate roughly the geometry of the brain by using a regular grid when generating a hexahedral mesh, in order to simplify the meshing. In [Bilger et al., 2014a], we take the advantage of the mapping system (presented in

Section 1.5.3) to improve the loss of accuracy due to the rough approximation of the geometry. Indeed, the hexahedral mesh is used only to compute the deformation, but we use other meshes for the mass, the collision and the buoyancy. An example of hexahedral mesh of the brain is shown in the figure 2.15.

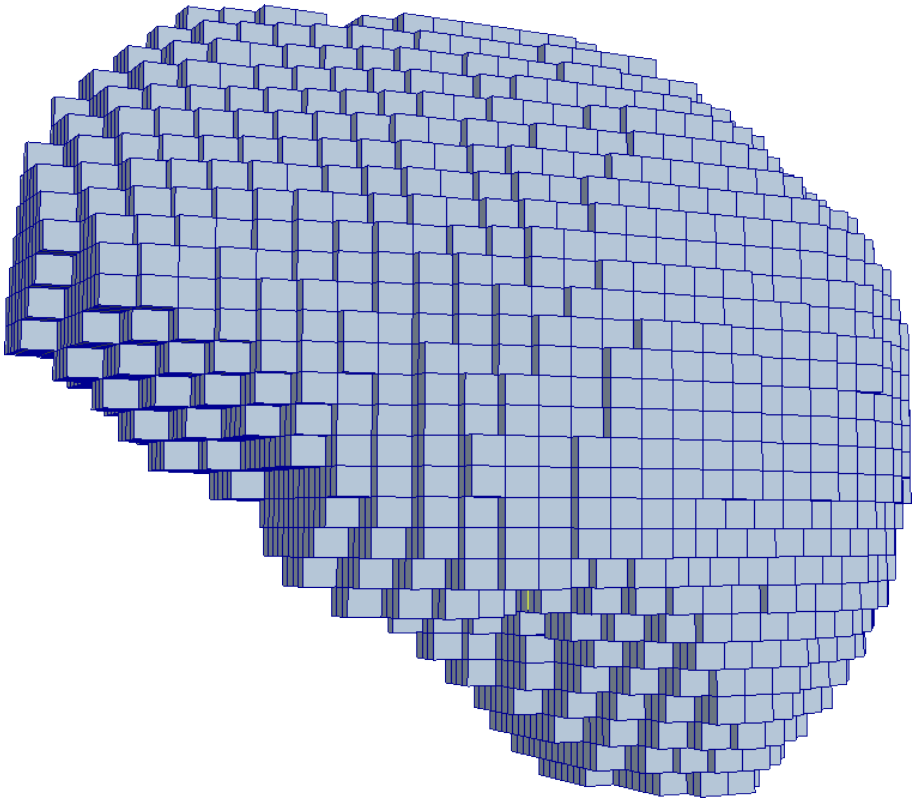

Figure 2.15 – *Hexahedral mesh of a brain hemisphere, approximated with a regular grid of 30x30x30, resulting in 12,004 hexahedron and 14,192 nodes.*

Transformation

Before starting steps related to the simulation, we propose to add a step to transform rigidly the meshes, in order to place them in the appropriate frame. We propose two rigid transformations. The first one is called *atlas to patient*, which allows to use an atlas instead of the patient-specific meshes. In practice, we do not use an atlas, so this transformation is often the identity. However, it can be useful in case of different frame orientation when collaborating with other teams. The second transformation is called *image to world* and transforms the meshes from the image space where units are voxels, to a world space, where units are meters. The transformation relies on the voxel size of the brain images. This step allows us to deal with meaningful physical units, which would not be the case with an image space.

Reference State

The goal of computing the reference state is explained in Section 2.4.5. This step is crucial before running the simulation. In the application, checkboxes allow the user to select what part of the simulation is loaded.

Simulation

A last tab in the application enables to run a brain shift simulation. The user can change the type of simulation by selecting a scene file and a controller for the loss of CSF. This controller can simply reduce the volume of CSF, or can control the simulation and compute multiple equilibrium states depending on the loss of CSF, which is used in Chapter 4 for example.

2.6 Conclusion

We have introduced the mathematical theory that allows the construction of our biomechanical model of brain shift. We also presented numerical methods in order to solve the equations of the model. In order to model the brain shift, we presented our model of the influence of CSF on the brain tissue, in addition to the weight. Due to the influence of the CSF during an imaging acquisition, we propose to compute the reference state of the brain with an iterative geometric approach. In addition to the brain deformation and the CSF, we also account for the collision of the brain with the skull and with the falx cerebri. Finally, the model is used for a patient-specific simulation, managed with a graphical interface.

Thanks to the presented model, we are able to use it for applications requiring to anticipate or estimate brain shift. In the following chapters, we present three phases of the DBS procedure (pre-operative, intra-operative and post-operative) where we use our model to solve problems due to brain shift.

2.6.1 Discussion

Brain model

The brain is a non-linear soft tissue [Bilston, 2011], but the co-rotational approach used in our model is a good trade-off between accuracy and computation time. To improve our model, we can easily replace the constitutive equation of the material in the simulation scene file, thanks to the modularity of our framework, and then replace the co-rotational approach with a non-linear constitutive equation. However, in this context, this new configuration has shown less stability than the co-rotational approach, mainly due to the large number of interactions with the skull and falx cerebri. Still, we continue to work at using a non-linear law. The last problem is to adjust the parameters of the materials (for example the parameters of the Mooney Rivlin model C_1 and C_2 presented in the equation 2.28). The literature has provided only few studies and has not converge to a unique value (nor a unique constitutive law for the same type of application). A last constraint for the non-linear law, is to be compatible with the computation of the reference state.

Reference State

The algorithm used to compute the reference state of an object undergoing external forces is presented in Section 2.4.5. We can notice in the experiences of Figures 2.8 and 2.9 that there are scenarios where the algorithm does not converge. Originally, the algorithm has been developed for linear materials, but no further study has been published on non-linear materials (or a co-rotational approach). We have seen the limit of the algorithm when the difference between the configuration at equilibrium and the initial configuration is important. We believe this algorithm is not suitable in all the situations, and investigations should be performed to find a better way to compute the reference state of the brain. Nevertheless, in the case of a linear constitutive law, the algorithm provided good results with the brain and buoyancy.

Collision

The first attempts of the brain shift model used the work of [Allard et al., 2010] to treat the collisions and take advantage of the Graphics Processing Unit (GPU) power. The method relies on the computation of an interpenetration volume. However, the small thickness of the falx cerebri leads to a too small interpenetration volume.

2.6.2 Last words

The presented limitations do not hinder the usability of the model in the applications described in the following chapters. In a first contribution, the model is used to account for the deformation pre-operatively.

Brain Shift Risk during Pre-operative Planning

Chapter 3

Abstract

This chapter focuses on the pre-operative steps involved in a Deep Brain Stimulation (DBS) procedure. We give details on the process to determine the targeted structure location as well as an electrode trajectory to reach it. A state of the art on the existing methods is presented. As the planning requires the highest precision, we present solutions to the problem of brain shift that can alter the accuracy of the electrode placement. In a first stage, we propose a method similar to the current technique employed by surgeons. Then, a method to compute automatically the electrode trajectory is presented. Both methods are based on a numerical model of deformation of the brain. The notion of risk of brain shift is introduced and necessary for both methods. The presented work has been published in [Bilger et al., 2012] and [Bilger et al., 2014c].

Contents

3.1 Pre-operative planning

The processes involved in the pre-operative DBS planning are briefly presented in Chapter Introduction, in Section 1.3.1. In this chapter, we detail the current techniques and establish a state of the art of the techniques still in research. We briefly recall that the main procedural steps of the pre-operative planning are:

1. Inclusion Magnetic resonance imaging (MRI) without stereotactic frame
2. Stereotactic frame placement
3. Pre-operative Computed Tomography (CT) with stereotactic frame
4. Target coordinates identification
5. Trajectory selection

We focus our research on the last two steps, with a particular interest on the selection of an safe trajectory.

3.1.1 Target Coordinates Determination

We assume that an MRI without the frame and a CT scan with the frame have been acquired. The objective is to determine the targeted structure location. This task is non-trivial because of the lack of visibility of the targeted structures in the images [D'Haese et al., 2005]. Indeed, the boundaries of some structures such as the Subthalamic Nucleus (STN) are not always visible.

To identify the target in the MRI, one can use one of the following methods:

1. Indirect targeting
2. Direct targeting
3. Atlas-based targeting

Indirect Targeting

The indirect targeting method is based on the position of the target in an atlas comprising the location of the structure among the whole brain. In the case of the STN, different studies proposed a simple formula to guide the identification of the structure, usually based on anatomical landmaks such as the Anterior Commissure (AC) and the Posterior Commissure (PC). For instance, [Starr et al., 2002] utilize the coordinates 12 mm lateral, 4 mm posterior (later adjusted to 3 mm) and 4 mm inferior to the midcommissural point. Often, the coordinates are based on an atlas, such as the Schaltenbrand-Wahren atlas [Schaltenbrand et al., 1977], or by adjusting the coordinates according to statistics on clinical scores.

Direct Targeting

The direct targeting method is based entirely on the visibility of the structures in the patient image. The task to locate the structure is assigned to the surgeon. To facilitate the identification of the STN, the surgeon can visualize neighbor structures, such as the red nucleus, the interpeduncular cistern and the substantia nigra [Starr et al., 2002].

However, most of the surgeons (79% according to [Abosch et al., 2013]) utilize a combination of indirect and direct targeting because of the difficulty to rely on the visibility of the targeted structures. [Starr et al., 2002] describes the process of fusing the solutions given by the indirect and direct method:

- if the distance between direct STN location and indirect STN location is less than 1 mm, the indirect coordinates are used.
- otherwise, the lateral and vertical indirect coordinates are adjusted by 0.5 to 1 mm (the anteroposterior axis being unreliable).

In their study, [Hamid et al., 2005] uses the coordinates 12 mm lateral, 3mm posterior and 4 mm inferior to the mid-point of the AC-PC line for indirect targeting, and adjust them with direct targeting to obtain a mean of the target of 11.5 mm lateral, 2.5 mm posterior and 4.1 mm inferior to the mid-point of the AC-PC line.

Although it is not widely used because of the high cost of the material, very high resolution MRI can help to identify the target thanks to an improved tissue contrast. In [Cho et al., 2010], the authors describe the improvement in the visualization of the targeted structure with 7-tesla MR imaging compared to 1.5- and 3-T MR imaging.

Atlas-based Targeting

In addition to indirect and direct (or a combination of both) targeting, one can identify brain structures with the registration of a digital atlas on the patient-specific pre-operative brain images. The figure 3.1 summarizes schematically the principles of an atlas-based segmentation in order to identify an invisible structure in the patient. This atlas must comprise the targeted structure as well as sufficient data to precisely register it on the patient image. Among the atlases used in stereotactic surgery, we can cite [Ganser et al., 2004], [D'Haese et al., 2005], [Lalys et al., 2010] and [Yelnik et al., 2007].The atlas from [Lalys et al., 2011] is currently in use in the Hôpital Ponchaillou in Rennes and is constructed by averaging 15 registered 3-T images. In the other hand, the atlas from [Yelnik et al., 2007] is in use in the Hôpital Pitié-Salpêtrière in Paris and is constructed by cryosection of a postmortem brain, resulting in 800 70μm thick slices. The method to locate brain structures used in this thesis is based on these two atlases. The technical details on the registration of the atlas on the pre-operative patient image is given in [D'Albis et al., 2014].

3.1.2 Electrodes Trajectory

A trajectory for a DBS electrode is defined geometrically as a 3D linear segment starting from an entry point located on the scalp of the patient to a targeted point located deep into the brain tissue, selected for its efficiency of treating symptoms by electrical stimulation. The microdrive will follow this trajectory to coincide the lead and the trajectory. At the end of the procedure, the lead is fixed to the entry point, and its extremity reaches the planned coordinates. This is exactly the definition of an electrode trajectory. Usually, the steps where the surgeon identifies the targeted point to stimulate and where he/she selects an optimal trajectory to reach the structure are dissociated. The later is done after the former.

The trajectory planning is not trivial, as it has to follow several constraints (listed by [Essert et al., 2011] and [Bériault et al., 2012]):

1. The tip of the electrode must be placed into the target. With this constraint, one extremity of the trajectory is fixed to the previously selected coordinates. The entry point remains to be determined.
2. The entry point has to be on the surface of the skin, in particular the upper surface for accessibility and aesthetic reasons. The surgeons can restrain more with entry points only within the frontal lobe and anterior to the primary motor cortex. This area is called *insertion zone*.
3. The trajectory must avoid (no intersection with) the midline. The constraint can be expressed as forbid entry points contralateral to the target.

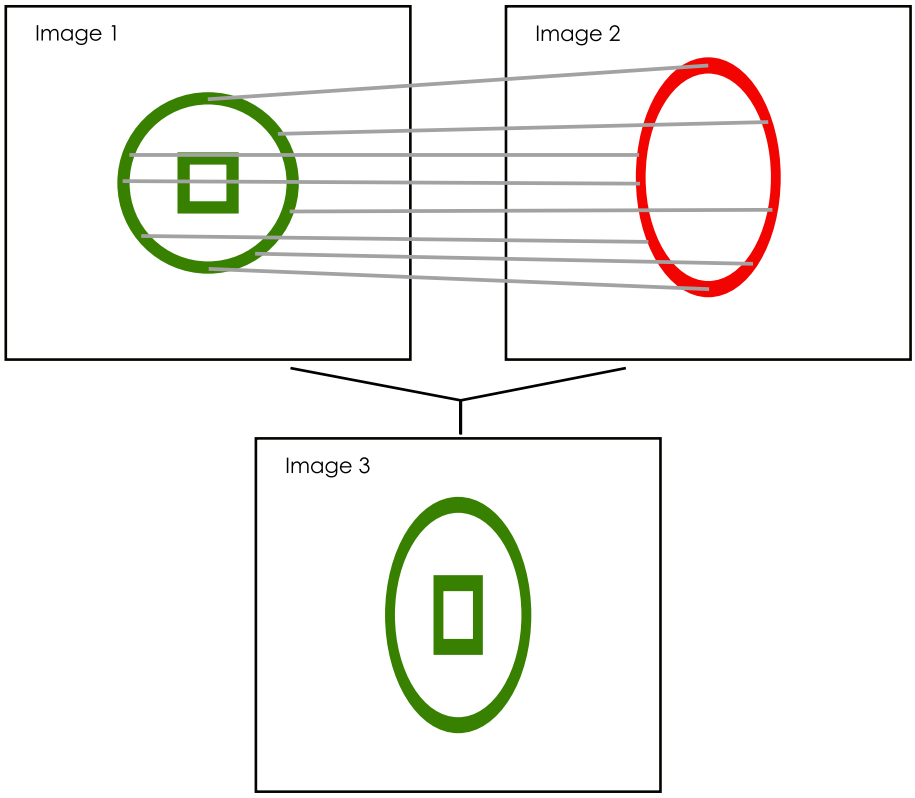

Figure 3.1 – *Principles of atlas-based segmentation. Let us consider two images (Image 1 and Image 2). Image 1 is an atlas image and Image 2 is a patient image. Both contain one common element: the green circle in Image 1 and the red ellipse in Image 2. This element could be the contour of the brain for example. Image 1 contains an element, the green square, not present in Image 2. This element (could be the STN for example) is present in the patient but not visible in the image. The atlas-based segmentation is a method that uses an atlas image to identify structures invisible in a patient. In simple words, the goal is to identify the square in Image 2. To do so, an algorithm finds the correspondence of every pixels of Image 1 in Image 2, based on the common elements. This displacement field (represented by grey lines between Image 1 and 2) is then used to transform Image 1 to Image 3 in order to match Image 2. This way, the element non-visible in Image 2 is obtained by this transformation as the vertically extended green rectangle in Image 3.*

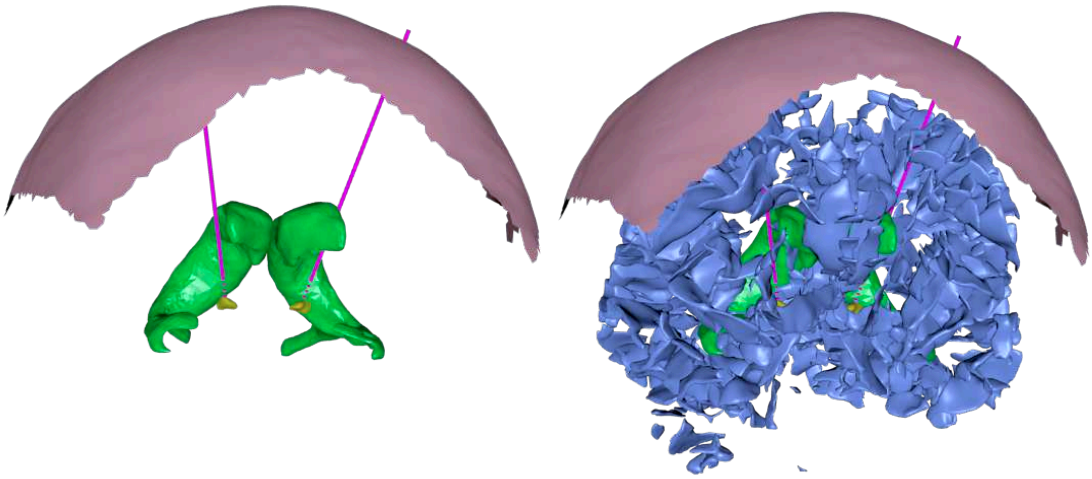

Figure 3.2 – *Example of DBS electrodes trajectory. The sulci are represented on the right picture (it is the only difference between both pictures). The following structures are represented:*
■ *Electrodes* ■ *Insertion zone* ■ *STN* ■ *Ventricles*

4. The trajectory must avoid (no intersection with) the blood vessels. An intersection with a blood vessel means that the electrode will cross it and damage it. Perforating a blood vessel leads to a hemorrhage. But blood vessels are very difficult to see in MRI (without contrast). It is difficult to segment them and the smallest are invisible. However, it is known that sulci contain blood vessels. The rule could be modified to avoid the sulci, instead of avoiding the vessels. The advantage is that the sulci are easy to see and to segment.
5. Depending on the choice of the surgeon, the trajectory must avoid the ventricles. This rule depends on the surgeon because the crossing of the ventricles does not necessarily damage it or lead to surgical complications. However, the results of [Zrinzo et al., 2009] show that avoiding the ventricles improves the accuracy of the targeting.

However, a trajectory can respect the previous conditions while being dangerous for the safety of the patient. For example, a trajectory could be not in intersection with a blood vessels at the time of the planning, but close enough to cause damages in case of brain shift. That is why surgeons also define the following rules:

1. Maximizing the distance of the trajectory with the blood vessels complex
2. Maximizing the distance of the trajectory with the ventricles
3. Minimizing the overlap of the trajectory with caudate would prevent symptoms of perioperative confusion [Bériault et al., 2012].
4. According to some surgeons, it is also preferable to minimize the trajectory length [Essert et al., 2011]. Anyway, the trajectory length is limited to 90 mm [Essert et al., 2011].
5. A maximum overlap of the trajectory with the targeted structure would allow the neurologist to test several stimulation location along the trajectory. This does not mean necessarily an alignment of the trajectory axis with the structure principal axis. Indeed, it is preferable to stimulate the sensorimotor territory of the STN (Section 1.2.10).

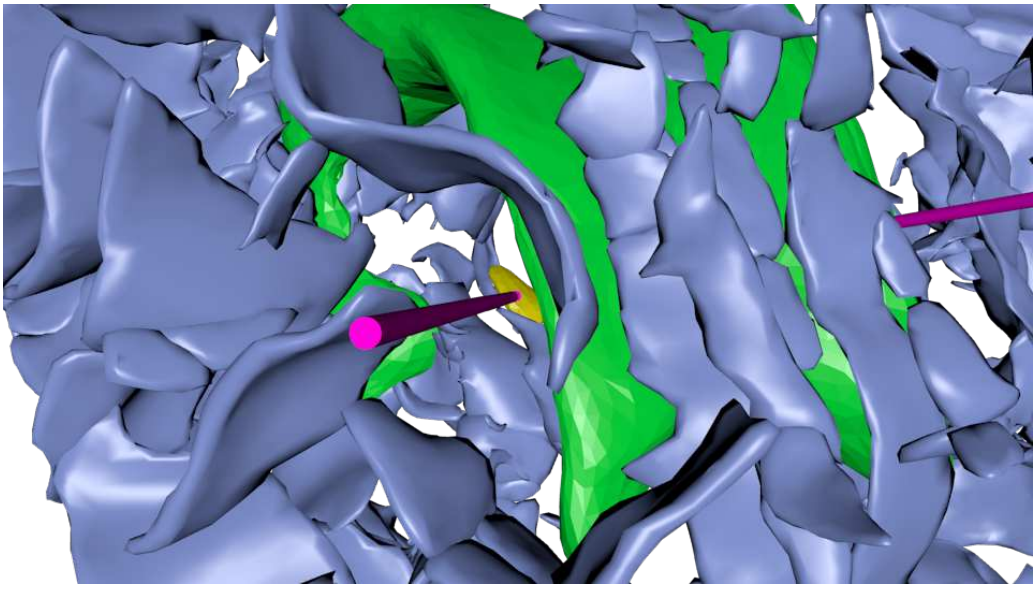

Figure 3.3 – *Electrode axis-aligned view in the same configuration as in the figure 3.2*
■ *Electrodes* ■ *Insertion zone* ■ *STN* ■ *Ventricles*

This set of constraints illustrates that DBS is not a standardized surgical procedure, and, as we have personally noticed, there are differences between the surgeons when planning the surgery.

Manuel planning

The conventional planning step following the identification of the target consists in a manual planning. The surgeon selects an entry point and verifies manually if the corresponding trajectory respects the constraints enumerated previously. The selection of the entry point is first based on the average of the trajectories that have been used in surgery in the center. For instance, in [Perozzo et al., 2001], the angle of the mean trajectory with the sagittal line in the coronal plane was 14-20°, while it is 58-63° with the intercommissural line in the parasagittal plane. In [Nakano et al., 2012], the authors refer to a shift: the burr hole is made 25-30 mm lateral to the midline of the skull and 20-30 mm anterior to the coronal suture. If the trajectory does not respect the conditions, mainly the safety, another trajectory is verified. The process is iterative until a trajectory respecting the conditions is found. The selection of a new trajectory after having ruled out the previous trajectory is based on the experience of the surgeon and the configuration of different structures (mainly the blood vessels network and sulci) of the patient.

Automatic planning

Manual planning requires experience of the surgeon and mostly time. That is why some groups ([Essert et al., 2011], [Bériault et al., 2012], [Shamir et al., 2010] and [Brunenberg et al., 2007]) have listed the constraints on a trajectory and formalized as geometric rules. A dedicated solver evaluates whether a trajectory respects the geometric rules or not. Some groups worked with meshes (e.g. [Essert et al., 2011]) and others with voxels [Shamir et al., 2010]. The evaluation of hundreds or thousands of trajectories is then possible. An optimization process search among the evaluation of trajectories to compute an optimal trajectory. In [Essert et al., 2011] and [Bériault et al., 2012] the different rules are weighted in a cost function. The weights define the relative importance of the criteria. The weight values have to be refined by an ex-

pert neurosurgeon, that is why this process is surgeon-dependent. An optimal trajectory is not absolutely optimal but surgeon-dependent.

Note that another group ([Guo et al., 2007]) computes automatically a trajectory based on probabilistic functional maps.

3.2 Problem

In this section, we focus on the problems due to brain shift in the previously described planning method.

3.2.1 Motivations

As it is insinuated in the planning method previously presented, the planning utilizes pre-operative data of the patient, mostly a MRI (the CT scan is only used to register the MRI in the stereotactic frame). This planning is based on the configuration of the brain and other structures at the moment the MRI was acquired. However, we know that the brain tissue is a deformable material. Normally, in daily life, the brain is not supposed to deform, but the surgery could lead to brain deformation. If the brain deforms between the pre-operative MRI and the moment to implant an electrode, the planning is obsolete and should be based on the deformed configuration. We call the methods described in the previous planning *rigid planning*, because it is assumed the brain would not deform, as it would be rigid. What are then the consequences of a brain shift if the surgeon trusts a rigid planning?

3.2.2 Target Displacement

Let us consider the planned target is located in $x^{\text{rigid}}_{\text{target}}$ in the configuration when the MRI was acquired, in the patient frame. The rigid planning results in an entry point located in $x^{\text{rigid}}_{\text{entry}}$. The trajectory is defined as the segment $\left[x^{\text{rigid}}_{\text{entry}}, x^{\text{rigid}}_{\text{target}}\right]$. The burr hole is drilled at the position $x^{\text{rigid}}_{\text{entry}}$, and the tip of the electrode will be placed in $x_{\text{elec}} = x^{\text{rigid}}_{\text{target}}$. However, the opening of the skull can lead to a brain shift. If the brain deforms, the position of the target will be $x^{\text{deformed}}_{\text{target}} \neq x^{\text{rigid}}_{\text{target}}$, therefore $x^{\text{deformed}}_{\text{target}} \neq x_{\text{elec}}$. This means that the tip of the electrode is not implanted where the target is located after deformation.

The electrical stimulation is not punctual, at the electrode location. There is a Volume of Tissue Activated (VTA) that is non-null [Butson et al., 2007]. The target coordinates are selected so that the VTA is centered on the electrode (x_{elec}) (Note this is a simplified situation, as there are actually four electrodes). The consequences of the difference between $x^{\text{deformed}}_{\text{target}}$ and x_{elec} depends on the inclusion of $x^{\text{deformed}}_{\text{target}}$ in the VTA. Usually, the brain shift does not affect a lot the deep tissue, such as the STN. If the target moves, the VTA is still larger than the target displacement and compensate the movement.

3.2.3 Blood Vessels Displacement

Similarly to the target displacement (3.2.2), the change of the brain configuration could have an impact on the surgery regarding to the blood vessels, and especially on the safety. Let us consider the trajectory is defined as the segment $\left[x^{\text{rigid}}_{\text{target}}, x^{\text{rigid}}_{\text{entry}}\right]$, with $x^{\text{rigid}}_{\text{target}}$ the position of the targeted point, and $x^{\text{rigid}}_{\text{entry}}$ the entry point, both selected with a rigid planning. The selection is based on the position of the blood vessels network at the time the MRI was acquired, to avoid the vessels and not to damage a vessel during the insertion of the electrode. With the brain shift (after opening the skull and dura mater, but before the electrode insertion), blood vessels may have moved. The surgery is not safe if a blood vessel shifts too close from the trajectory as the electrode implantation could damage the vessel. In the worst case, it could lead to a hemorrhage. The figure 3.4 shows three scenarios of brain shift (no brain shift, intermediary

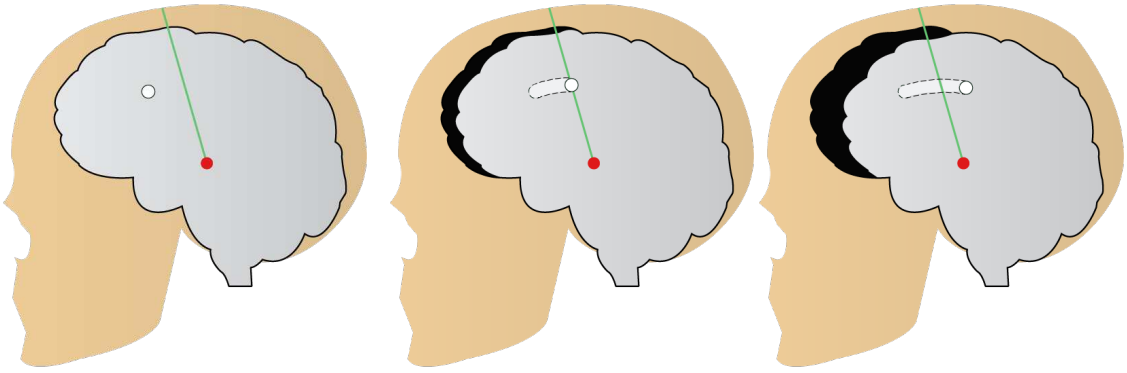

(a) No brain shift (b) Intermediary brain shift (c) Maximal brain shift

Figure 3.4 – *Sagittal projection of the brain for different possibilities of intensities of brain shift given an insertion point, from no brain shift (a) to a maximal brain shift (c). The trajectory is in green, from an insertion point on the scalp to the target in red. The area in black is the pneumocephalus. The white circle represents a vessel. In (a) the vessel lies in its initial position. In (b) and (c), we see its new position according to the brain shift, and the whole shape of its movement during the progression of the brain shift (light dotted shape).*

brain shift and important brain shift) where a vessel can shift onto the trajectory.

In order to avoid this to happen, the surgeon defines mentally what we call a *risk volume*, centered around the trajectory. A risk volume is a volume around the trajectory, where it is forbidden to have a risky structure such as the blood vessels. If a risky structure is inside, then it has chances to shift onto the trajectory and be damaged by the electrode insertion. With current techniques, the risk volume is a cylinder centered around the trajectory. This cylinder is actually defined when the surgeon verifies slide by slide in the trajectory view if a vessel is inside a certain *safety margin*. See an example in the figure 3.6. The safety margin corresponds to the radius of the cylinder. See figure 3.5 for a 3d representation of the risk volume as a cylinder. Although the risk volume shape is very simple for rigid planning (cylinder), it depends on the trajectory, i.e. on the entry point and target location. The segment $\left[x^{\text{rigid}}_{\text{target}}, x^{\text{rigid}}_{\text{entry}}\right]$ defines the orientation and the length of the cylinder, while the radius correspond to the safety margin defined by the surgeon.

Note that this risk volume can be used to avoid intersection with ventricles if it is a constraint decided by the surgeon.

3.2.4 Proposition

We have seen the brain shift could be a problem for the efficiency of the treatment (target displacement) and regarding to the safety of the patient (blood vessels displacement) with risks of hemorrhage. Therefore, it is necessary to take this phenomenon into account in order to ensure a safe surgery to the patient. The aim of the contributions presented in this chapter is to provide pre-operative tools based on a biomechanical model of the brain to prevent risks due to brain shift. We call a planning accounting for brain shift a *brain-shift aware planning* (in opposite to a rigid planning). We particularly focus on taking into account the risk of blood vessels displacement during the surgery.

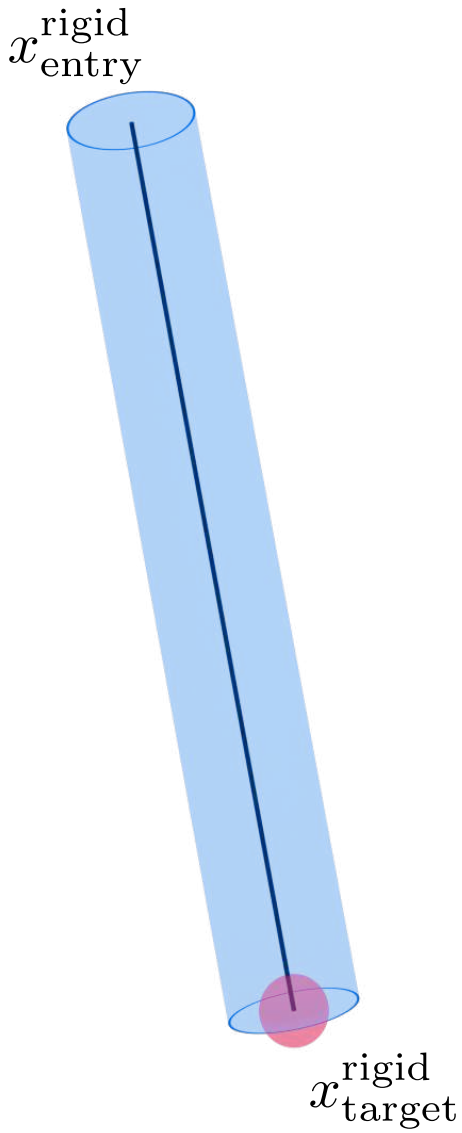

Figure 3.5 – *Risk volume: a cylinder centered around the trajectory. The radius of the cylinder corresponds to the safety margin defined by the surgeon.*

3.3 Working hypothesis

We describe the surgical conditions for the following of this chapter:

1. We are in the case where the surgical protocol could lead to a brain shift. It has chances to happen when the dura mater is opened for the electrode insertion. The contributions presented in this chapter can also be used if the patient does not present a brain shift, but it is equivalent to a rigid planning.
2. The methods described are applied pre-operatively, that is to say before the opening of the skull. At this moment, we cannot know in advance or anticipate the brain shift amount. Note that the computation time for a patient-specific brain-shift aware planning allows the surgeon to use the methods at the time of the planning: the simulation is fast enough but real-time is not required.
3. The data used in the methods presented in this chapter are only the pre-operative MRI, without the stereotactic frame. The pre-operative CT is used to register the MRI in the stereotactic frame and can provide more contrast on the bony structures.
4. The biomechanical model of brain shift is based on the model presented in Chapter Models of Brain Shift. It requires the segmentation of the following structures: two brain hemispheres, falx cerebri, endocranium, sulci or blood vessels network and Cerebro-Spinal Fluid (CSF).

3.4 Proposition

In the following sections, we present our two contributions for a brain shift aware pre-operative planning. First, Section 3.4.2 describes an approach similar to the actual clinical planning. Then, Section 3.4.3 presents the concept of risk map, and how we integer it in an automatic planning software to compute an optimal trajectory.

3.4.1 Problem: unknown CSF loss volume

The brain shift phenomenon leads to the displacement of structures, in particular the blood vessels. That is why the rigid planning is not always safe. If we can know in advance the position of the blood vessels after deformation, we could plan a brain-shift aware trajectory based on the deformed position. However this is not possible because brain shift depends on a large variety of factors, not necessarily known before the surgery.

If we would like to anticipate the displacement field with our biomechanical model, we would need to adjust the model with the CSF loss volume. This is precisely the parameter unknown pre-operatively. For this reason, we cannot develop method based on the anticipation of the displacement of the blood vessels. Instead, we propose methods based on the maximal risk of shift. For example, if our model must be adjusted with a CSF loss parameter, we estimate a maximal loss that could happen during the surgery. We will develop this idea later.

3.4.2 Risk volume

In classic pre-operative planning, the surgeon evaluates a candidate trajectory by checking slice by slice if the neighbor blood vessels are far enough for the trajectory to be safe. The surgeon defines a safety margin around the trajectory (a point in a slice) to avoid selecting a trajectory likely to damage a blood vessel. Moreover, this safety margin also includes errors due to the fusion and registration methods used during the planning. The safety margin in a slice is a circle (see figure 3.6). This geometric approach does not correctly describe the complexity of tissue motion during the brain shift. In particular, the brain shift

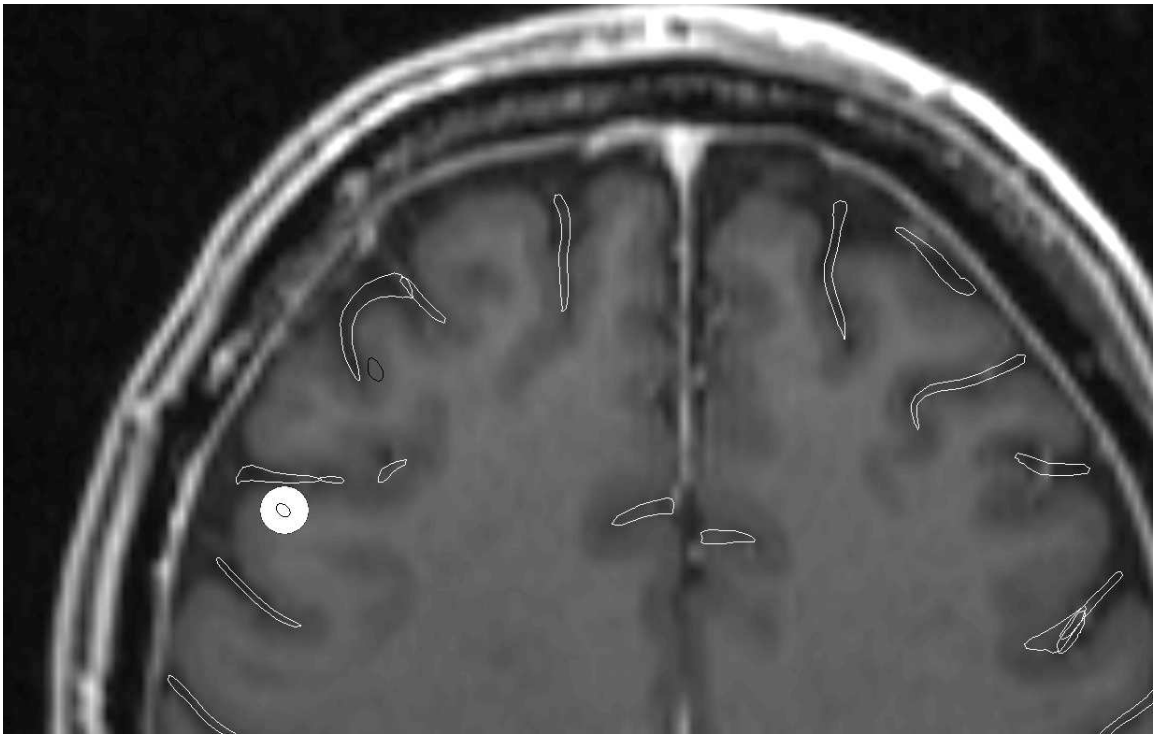

Figure 3.6 – *Considering a 5mm safety margin (in white) around an electrode path in classic pre-operative planning, the close blood vessel risks to be damaged if it shifts toward the trajectory.*

induces an anisotropic tissue motion, while describing the safety margin as a circle assumes an constant isotropic motion. Because the examined slices are orthogonal to the trajectory, the union of safety margins defines a cylinder (see figure 3.5). We call this cylinder a *risk volume*. In [Bilger et al., 2014c], we propose to define a brain shift aware risk volume which would be used exactly the same way by the surgeon. The brain shift aware risk volume is an advanced, more accurate method which better accounts for the complexity of the brain shift. The shape of the volume will include the anisotropy of the tissue motion, which is simulated with the model of the chapter 2.

Let x_t and x_e respectively the targeted point coordinates and the coordinates of a candidate insertion point. The rigid volume V_{rigid} could be defined with:

$$V_{\text{rigid}} = \left\{ x \in \mathbb{R}^3 \mid \|x - x_p\| \leq r, \forall x_p \in [x_t, x_e] \right\} \tag{3.1}$$

Note that this equation does not actually describe an exact cylinder. With this definition, the extremities of the cylinder-like shape are smoothed. This is not a problem as the implantation will not account for this phenomenon. We keep this definition, because the proposed brain shift aware risk volume will be similarly defined.

Brain Shift Aware Risk Volume

Definition To define the brain shift aware risk volume V, let us consider the initial brain configuration Ω_0. Let us assume the brain shifts to the configuration Ω. The displacement field ϕ maps the undeformed configuration Ω to the deformed configuration Ω. We now compute the points x_{p_0} such that

$$\forall x_p \in [x_t, x_e], \quad \phi(x_{p_0}) = x_p \tag{3.2}$$

and because ϕ is bijective

$$x_{p_0} = \phi^{-1}(x_p) \tag{3.3}$$

To compute p_0, we use the interpolation functions N_i^e of an element e, with $i \in [1,4]$ in case of linear tetrahedrons. Let us find the element e such that $P \in e$, then

$$x_{p_0} = \sum_{i=1}^{4} N_i^e(x_P)\, x_0^{e,i} \tag{3.4}$$

Here $\{x_0^{e,i} | i \in [1,4]\}$ is the coordinates of the nodes in the element e of the underformed brain. Finally, we define V as:

$$V = \left\{ x \in \mathbb{R}^3 \mid \|x - x_p\| \leq r,\ \forall x_p \in [p, \Phi^{-1}(p)],\ \forall p \in [x_t, x_e] \right\} \tag{3.5}$$

with r an error parameter handling the errors due to the model and the image processing uncertainties. A schematic 2D representation of the risk volume and the initial and deformed point is depicted in the figure 3.7.

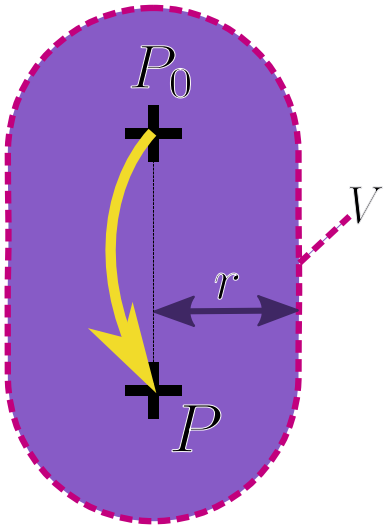

Figure 3.7 – *2D illustration showing an example of a point P on the trajectory, and its associated initial point $P_0 = \Phi^{-1}(P)$. V is represented depending on r.*

Interpretation Let us assume we run a simulation which deforms the brain configuration from Ω_0 to Ω. The set of points p_0 is the shape which will shift exactly on the trajectory with this particular simulation. It means that if a point of this shape is actually a point which belongs to a vessel, this vessel will shift onto the trajectory and will be damaged during the electrode implantation. However, it is impossible to anticipate precisely the brain deformation, mainly because the CSF loss volume is unknown pre-operatively (see section 3.4.1). Therefore, we cannot use only the p_0 without a precise anticipation of the shift. Instead, we define a simulation which will describe the potential maximal shift for this patient. Because we do not know what will be the shift between no shift and the maximal shift, we assume that all the p, such that $\forall x_p \in [x_t, x_e], \quad p \in [x_p, \phi^{-1}x_p]$, are points likely to shift onto the trajectory. These points constitute the risk volume of equation 3.5 with $r = 0$. The complete risk volume (with $r > 0$) is an extension accounting for the omnidirectional errors due to fusion and registration.

Note that if there is no brain shift,

$$\forall x_p \in [x_t, x_e], \quad x_{p_0} = x_p \tag{3.6}$$

In that case, the equation 3.5 becomes

$$V = \left\{ x \in \mathbb{R}^3 \mid \|x - x_p\| \leq r,\ \forall x_p \in [x_t, x_e] \right\}$$
$$= V_{\text{rigid}} \tag{3.7}$$

which is exactly the equation of the rigid risk volume, as expected.

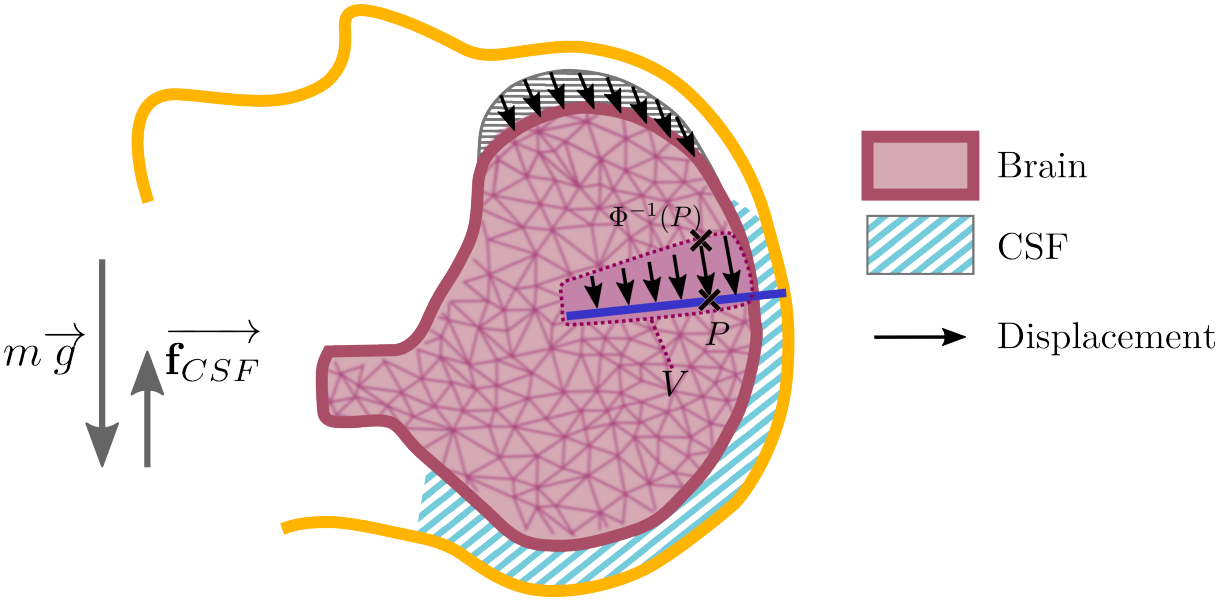

Figure 3.8 – *Because of a brain shift, the structures located in the vicinity of the electrode trajectory may move towards the electrode, increasing the risk of damaging vital structures. The risk volume V is represented with the associated displacement field ϕ.*

Implementation

Once the brain shift has been simulated, we discretize the trajectory segment into n_t points. For each of these points p, we identify the finite element e it belongs to. In this element, we apply the equation 3.4 to get the associated initial points p_0. We define the plane comprising the segment $[p, p_0]$ and orthogonal to the segment $[x_e, x_t]$. In this plane, we draw a semi-circle around p and another around p_0. The two semi-circles are oriented so that they can be linked together. See an example in the figure 3.9.

3.4.3 Brain-Shift aware Risk map

Again, any trajectory is defined as the segment between the target point and an entry point. The entry point has to be located on the scalp. Let us assume the target point has been identified and is fixed (or its displacement small enough to be negligible). The only variable parameter defining the trajectory is therefore the entry point location. To evaluate the degree of safety of a trajectory, we can assign it a relative score. To represent the trajectory scores, we assign the scores to the entry points, as a trajectory is defined only with one entry point. Therefore, a score is assign to every point located on the scalp. To visualize the score, we can use a color map. This process has been used in [Essert et al., 2011]. We call *risk*

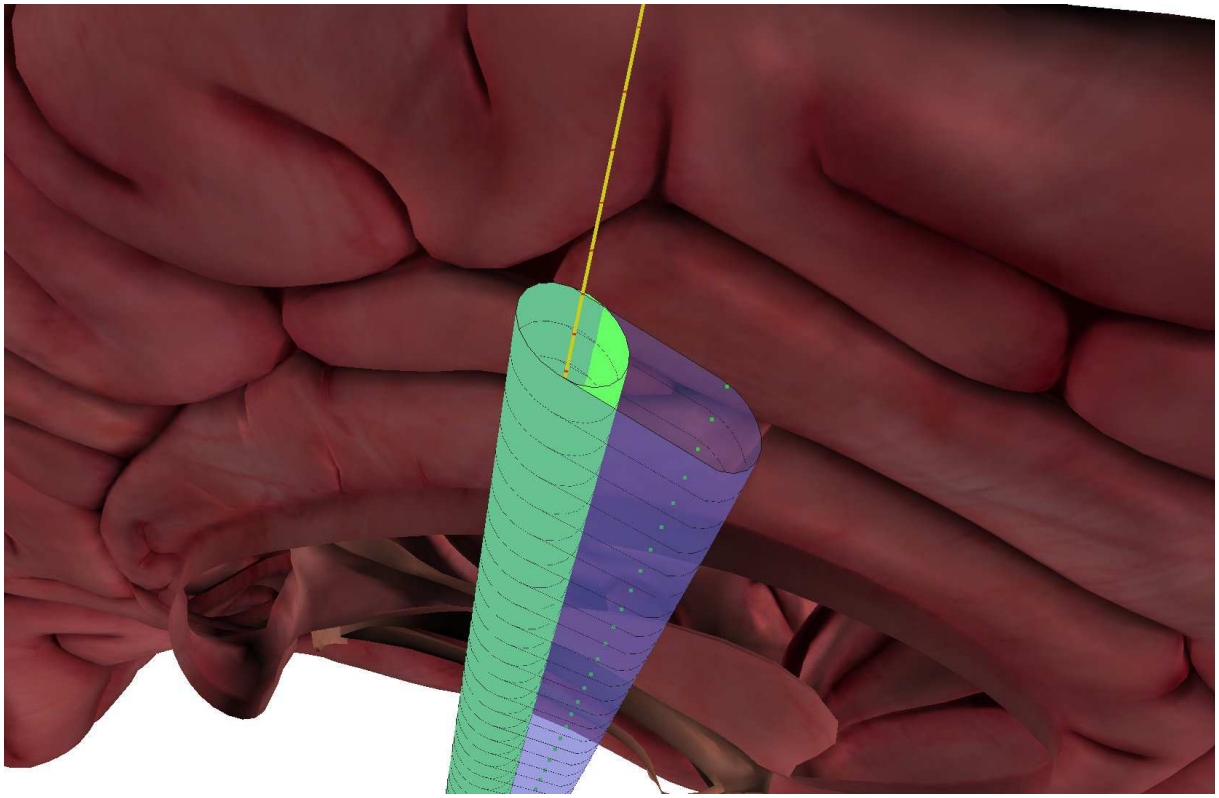

Figure 3.9 – *The risk volume associated with the trajectory in yellow. The brain shift aware risk volume is in purple, while the rigid one is in green.*

map the color map associated with a score, and corresponding to a risk to damage a blood vessel (see an example in the figure 3.10).

The contribution presented in this section is the development of a brain shift aware risk map. It has been presented in [Bilger et al., 2012]. Beyond the brain shift concerns during the pre-operative planning, the resulting brain shift aware risk map has been developed to be used easily in an automatic computation of optimal electrode trajectories, as an extension of [Essert et al., 2011]. In order to understand the concepts of the brain shift aware risk map, we present incrementally the different steps involved in the development of the method. Each step corresponds to a different risk map starting from the rigid risk map to the final brain shift aware risk map. The steps are illustrated with a 2D risk map as an example showing the main properties of the 3D risk maps. In the 2D examples, the 2D structure representing the vascular network is depicted in the figure 3.11(a).

Rigid risk map

The score in a rigid risk map is based on the distance d between the corresponding trajectory t and the blood vessels network:

$$R(t) = f\big(d(t, X_V)\big) \tag{3.8}$$

where R is the risk associated to the trajectory t which starts from the entry point x to the target point, f is any function (e.g. the identity or a normalization function), d is the distance between two objects. X_V is the pre-operative position of the blood vessels. This distance is defined as the distance between the trajectory (linear segment) and the closest point of the blood vessels network. The more the distance is

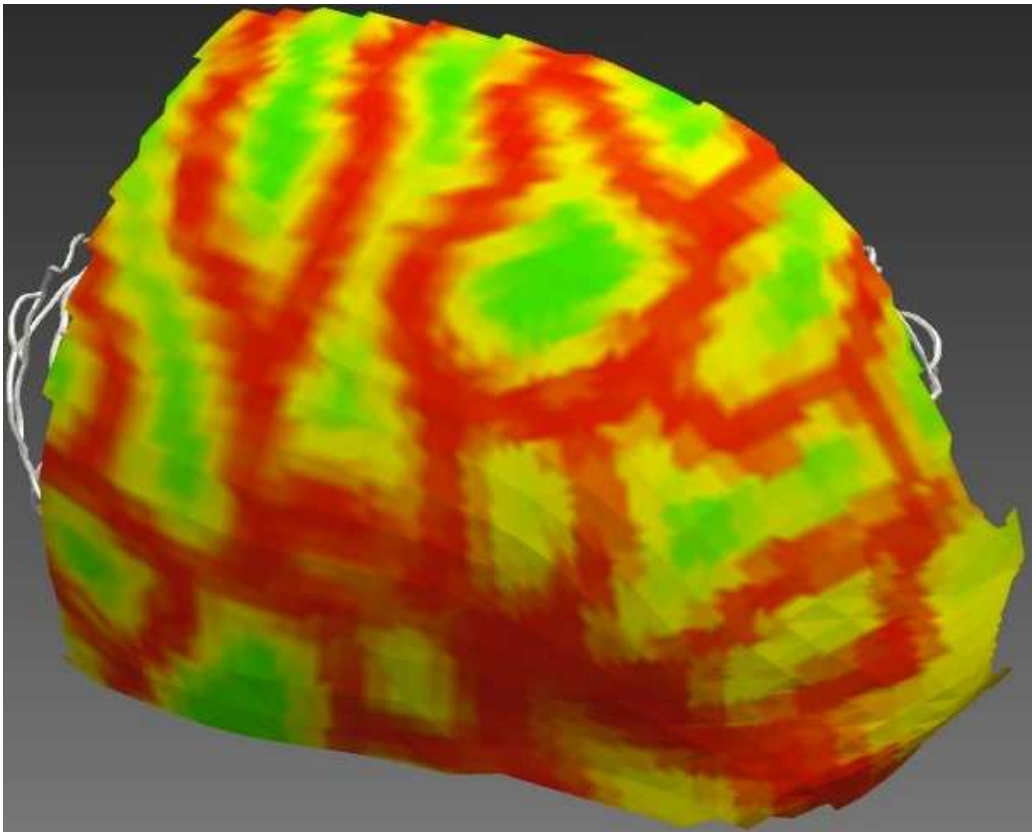

Figure 3.10 – *In this risk map, a color is assigned to every point of the scalp. The color corresponds to the degree of safety of the trajectory associated to the point regarding to the intersection of the trajectory with the blood vessels network. A red color corresponds to a risky trajectory (intersection with a blood vessel), while a green color corresponds to a safer trajectory.*

small, the more the trajectory is dangerous. The trajectory $t = t(x_e, x_t)$ is defined from an entry point x_e (variable) and a target point x_t (fixed). Therefore $t(x_e, x_t) = t(x_e)$ and

$$R(t) = R(x_e) = f\Big(d\big(t(x_e), X_V\big)\Big) \tag{3.9}$$

This risk map is used in [Essert et al., 2011] to compute an optimal electrode trajectory. However, this risk map is computed with the blood vessels network configuration at the time of the pre-operative MRI, under the assumption that the brain would not deform, as it is rigid. A 3D example of such a rigid risk map is depicted in the figure 3.10, while the figure 3.11(b) is the 2D rigid risk map corresponding to the network of the figure 3.11(a).

Updated risk map

After the opening of the skull and dura mater, and before the implantation of the electrode, brain deformes if there is a CSF leak. Blood vessels follow the motion of the brain tissue. To avoid any risks of damaging a blood vessels, the rigid risk map should be updated with the deformed configuration of the blood vessels. As well as the rigid risk map, the updated risk map based on the distance between the trajectory and the blood vessels network.

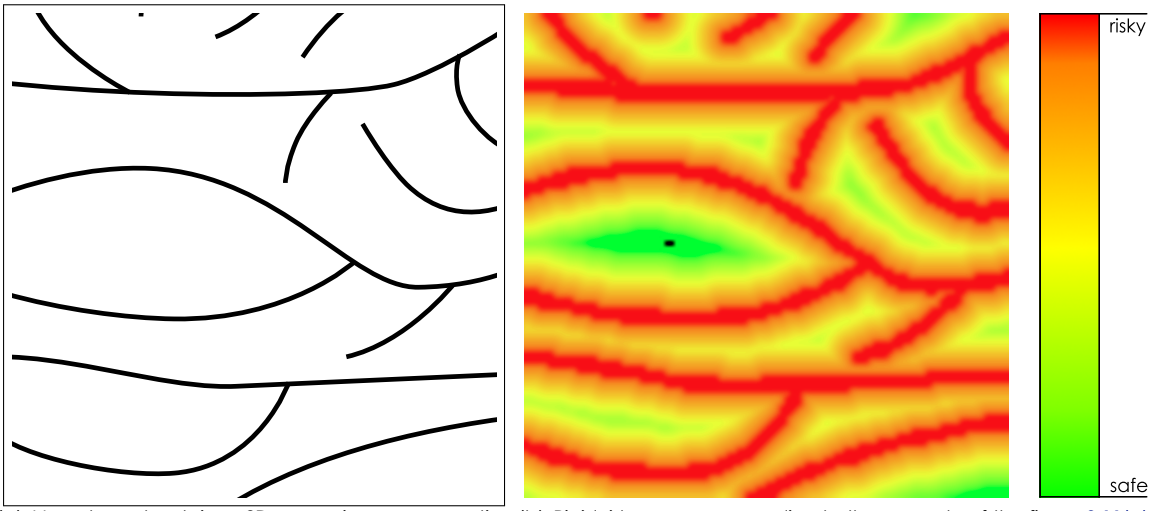

(a) Vascular network in a 2D space in a pre-operative configuration.

(b) Rigid risk map corresponding to the example of the figure 3.11(a). The pixel colors represent the distance of the pixel from the network, according to the scale in legend. A safe trajectory has to be selected in the area corresponding to a minimal distance, here in green. The black dot is the location of the optimal point, i.e. the point with the maximal distance to the blood vessels.

Figure 3.11 – *Rigid risk map in 2D from an example of a 2D vascular network.*

Several issues prevent us to use this risk map:

1. The deformed configuration of the blood vessels is difficult to acquire with intra-operative modalities. However, we propose a solution to this problem in Chapter Physics-Based Intra-operative Registration.
2. This risk map does not allow to update the planning as it would be computed after the opening of the skull and dura mater. A hole is already drilled for the trajectory selected with the rigid planning. An update of the planning could lead to another entry point, meaning probably another burr hole.
3. It is impossible to use it pre-operatively. Indeed, the brain shift occurs after the skull opening, meaning that a planning has already been performed. In order to use it pre-operatively, we could use an estimation of the deformed blood vessels configuration, but no model allows to predict the quantity of CSF loss. Consequently the brain shift amount cannot be anticipated, even with the most sophisticated models.

Worst case scenario risk map

We introduce a new risk map based on the distance between a trajectory and the blood vessels network deformed by a model (the biomechanical model presented in Chapter 2 for instance). But as it has already been said, there is no model to predict the CSF loss, and therefore the brain shift amount. Instead of trying to estimate the brain shift amount, we could base the risk score on a worst case scenario, i.e. a maximal brain shift amount. In this worst case scenario, our model is adjusted with high CSF losses values. The values could be:

- selected by the surgeon based on her/his experience, the patient particularities (e.g. brain atrophy), etc

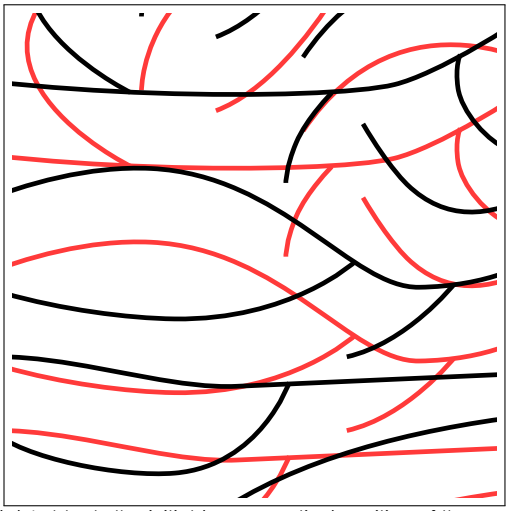

(a) In black, the initial (pre-operative) position of the vessels (figure 3.11(a)). In red, the same vessels shifted during the operation. The shift is vertical, from the top to the bottom.

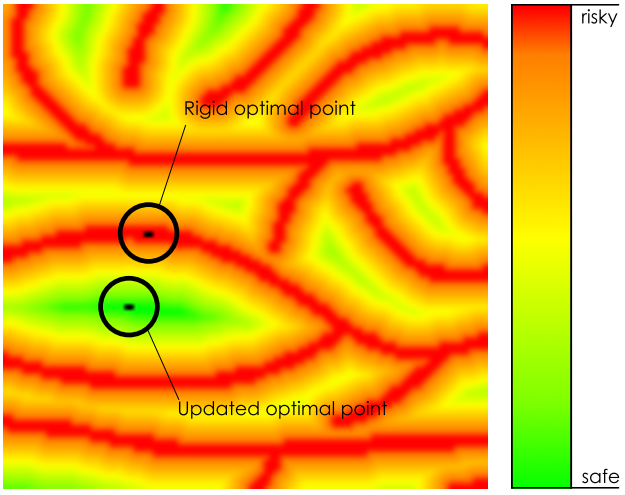

(b) Updated risk map, with a comparison of the optimal point of the rigid risk map (figure 3.11(b)) and the optimal point of the updated risk map. In this brain shift example, we notice that the entry point chosen from the rigid risk map is exactly in intersection with a shifted vessel. It would have been preferable to select the updated optimal point.

Figure 3.12 – *Updated risk map. The risk map is based on a shift of the vessels from the figure 3.11(a). The pixel colors represent the distance of the pixel from the network, according to the scale in legend. A safe trajectory has to be selected in the area corresponding to a minimal distance, here in green.*

- computed from the literature: some studies such as [Elias et al., 2007] measured the brain shift amount in a series of patient.

The issue with this risk map is that the planning would be based on the worst case scenario, which is more unlikely compared to a small brain shift that could be handled by a rigid planning. With this planning, we lost the initial undeformed configuration of the blood vessels. The planning with this risk map could lead to a trajectory located near an undeformed blood vessel.

Embedding surface risk map

None of the previously listed risk maps has been convincing to handle brain shift during pre-operative planning. The updated risk map has to be excluded because it is not possible to use it pre-operatively. The issue with the rigid risk map and the worst case scenario risk map is that it cannot anticipate accurately the blood vessels motion (or no motion at all). In this paragraph, we propose a combination of both risk maps: we forbid a trajectory to cross all intermediate positions of the vessels between its original position and its position in a brain shift scenario (could be the worst case scenario or an intermediary between no brain shift and worst case).

To build this risk map (in 3D) we developed an *embedded surface*. Let us consider the vessels occupies the volume X_V. In our model of brain shift, the amount of brain shift is controlled by the CSF loss volume v_{CSF}. It means that X_V depends on v_{CSF}: $X_V = X_V(v_{\text{CSF}})$. $X_V(0)$ corresponds to the initial (pre-operative) position of the vessels, while $X_V(v)$ is to the position of the vessels at equilibrium after a volume v of CSF loss during the surgery. We introduce the embedding surface S_V:

$$S_V(v_{\text{CSF}}) = X_V\big([0, v_{\text{CSF}}]\big) = \bigcup_{v=0}^{v_{\text{CSF}}} X_V(v) \tag{3.10}$$

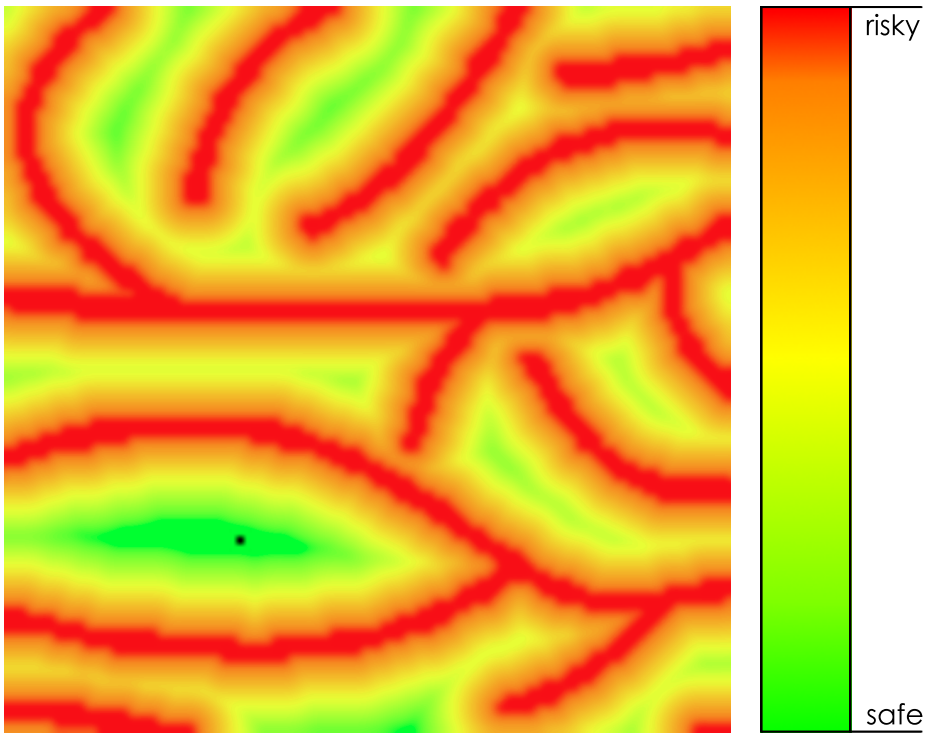

(a) Worst case scenario brain shift aware risk map. The black dot is the location of the optimal point, i.e. the point with the maximal distance to the blood vessels.

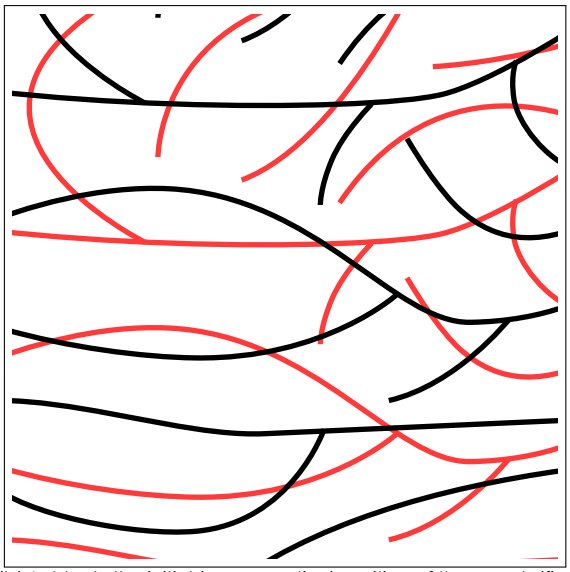

(b) In black, the initial (pre-operative) position of the vessels (figure 3.11(a)). In red, the same vessels shifted according to a worst case scenario. The shift is vertical, from the top to the bottom.

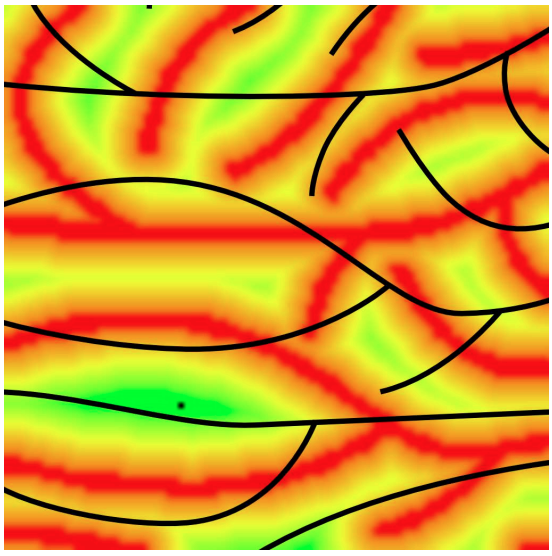

(c) Same as (a) in addition to the superimposition of the initial position of the vessels (figure 3.11(a)). We notice the optimal point is very close to the initial position of a vessel. In case of no brain shift, this risk map could be harmful.

Figure 3.13 – *Worst case scenario brain shift aware risk map. The risk map is based on a model of maximal shift of the vessels from the figure 3.11(a). The pixel colors represent the distance of the pixel from the network, according to the scale in legend. A safe trajectory has to be selected in the area corresponding to a minimal distance, here in green.*

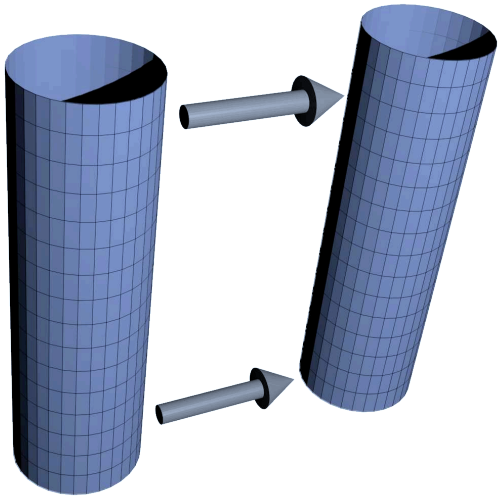

(a) Blood vessel motion. A blood vessel is represented by a cylinder. It is in its initial position on the left, and moves in its equilibrium position (right) during the surgery. The arrows indicate the motion from left to right.

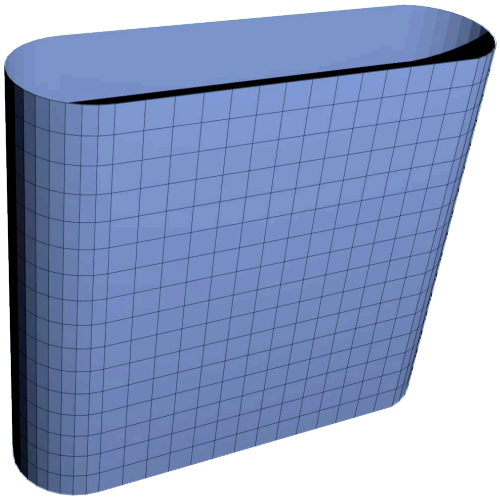

(b) Embedding surface. According to the motion in (a), the embedding surface embeds all the intermediate position of the vessel from its original position to its final position.

Figure 3.14 – *Embedding surface*

An example of the construction of such a surface is depicted in the figure 3.14. With this surface, we generate a risk map which the score is based on the distance to the embedding surface rather than a vessels position:

$$\begin{aligned} R(x_e) &= f\Big(d\Big(t(x_e), S_V\left(v_{\text{CSF}}\right)\Big)\Big) \\ &= f\left(d\left(t\left(x_e\right), \bigcup_{v=0}^{v_{\text{CSF}}} X_V(v)\right)\right) \end{aligned} \tag{3.11}$$

See an example in the figure 3.15.

The issue with this risk map is that it is too restrictive (see figure 3.15). Augmenting the surface of non-intersection reduces the area of safe entry point. In some cases, it is even possible the entire domain is covered by the embedding surface. The risk map would indicate only risky areas.

Final brain shift aware risk map

In the rigid risk map, safe areas could be revealed harmful because of the brain shift. That is why we want to remove this kind of "safe" areas. The embedding surface brain shift aware risk map allows to restrict the safe area compared to the rigid risk map. However, the restriction could be too much depending on the brain shift amount (or the parameter v_{CSF}).

According to the figure 3.16, we assume that the brain shift amount depends on the entry point location and the orientation of the patient head compared to the gravity direction. If the entry point is low, on the head of the patient (along the direction of the gravity), the risk of a large amount of CSF loss increases. This assumption is corroborated by the data coming from 9 patients from the Hôpital Pitié-Salpêtrière (see figure 3.17). We decided to integrate this property on the embedding surface risk map. We modify the embedding surface definition to take into account the entry point dependence. Let x_e be the entry point location (could be a point in 2D for the examples). The dependence of the CSF lost with the insertion point

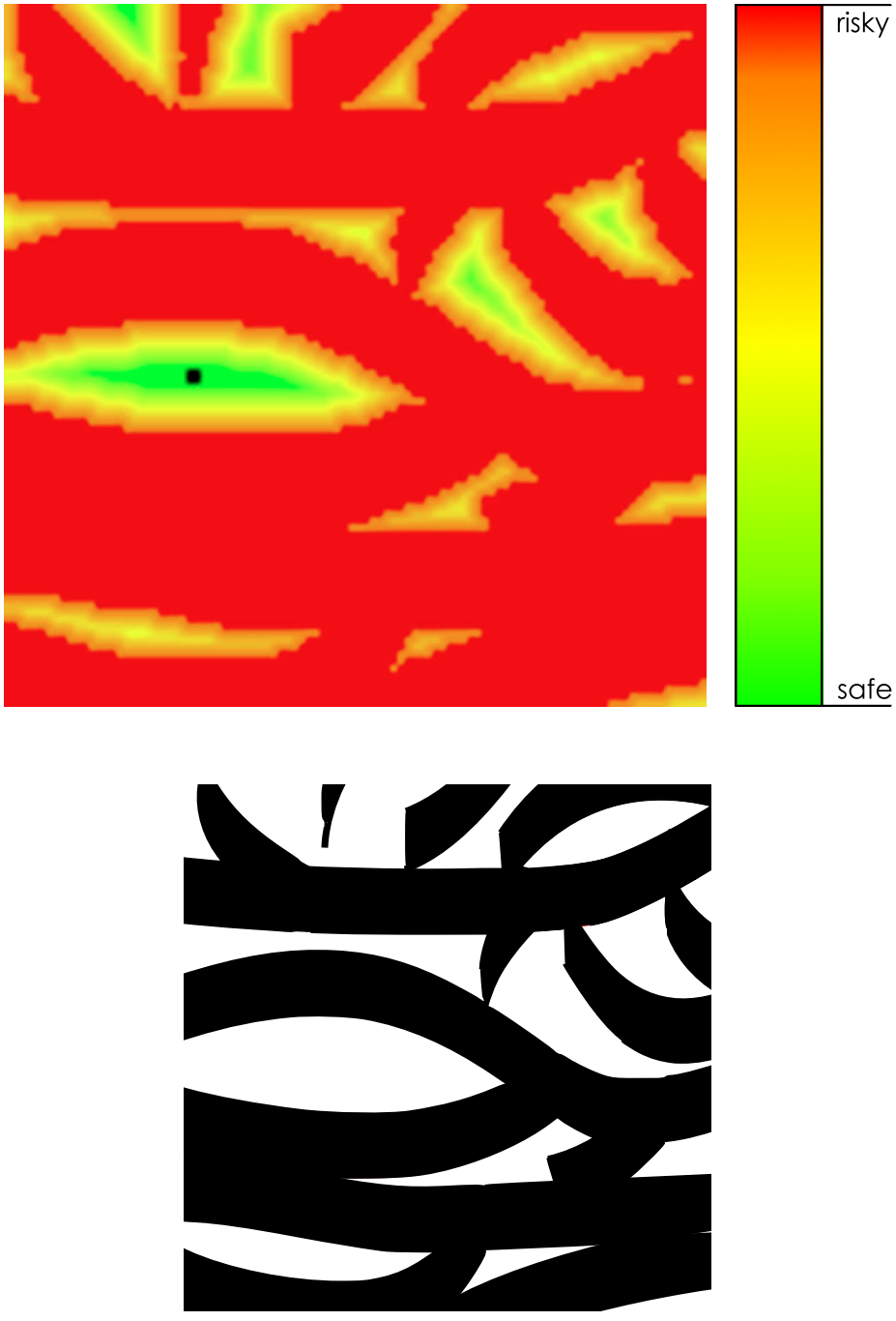

Figure 3.15 – *Embedded motion brain shift aware risk map corresponding to the example of the figure 3.11(a). The pixel colors represent the distance of the pixel from the network, according to the scale in legend. The trajectory has to be selected in the area corresponding to a minimal distance, here in green. The black dot is the location of the optimal point, i.e. the point with the maximal distance to the blood vessels.*

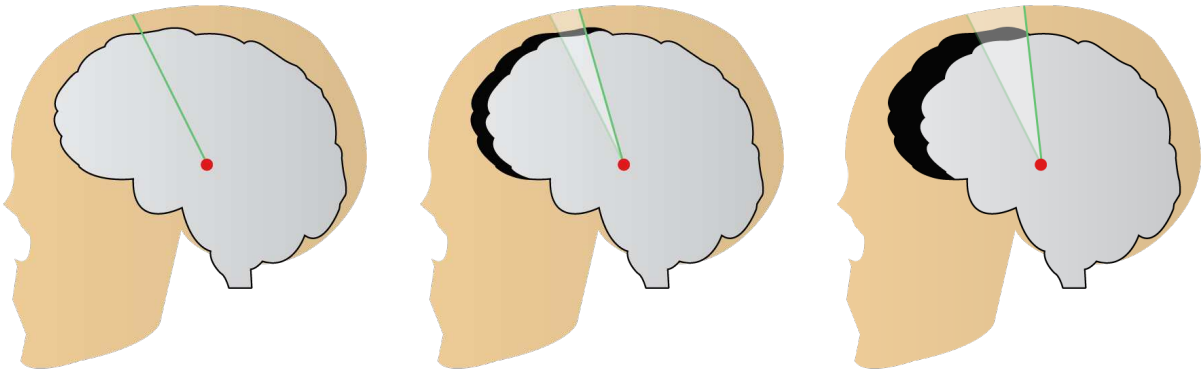

(a) Anterior trajectory (b) Intermediary trajectory (c) Posterior trajectory

Figure 3.16 – *Sagittal projection of the brain for 3 different trajectories. We assume that the brain shift depends on the location of the insertion point and on gravity. We depict here a patient in supine position. An anterior trajectory (a) causes a smaller brain shift than more posterior trajectories (b) and (c). Trajectories are in green and the target is in red. The area in black illustrates the maximum pneumocephalus that could occur in the worst case.*

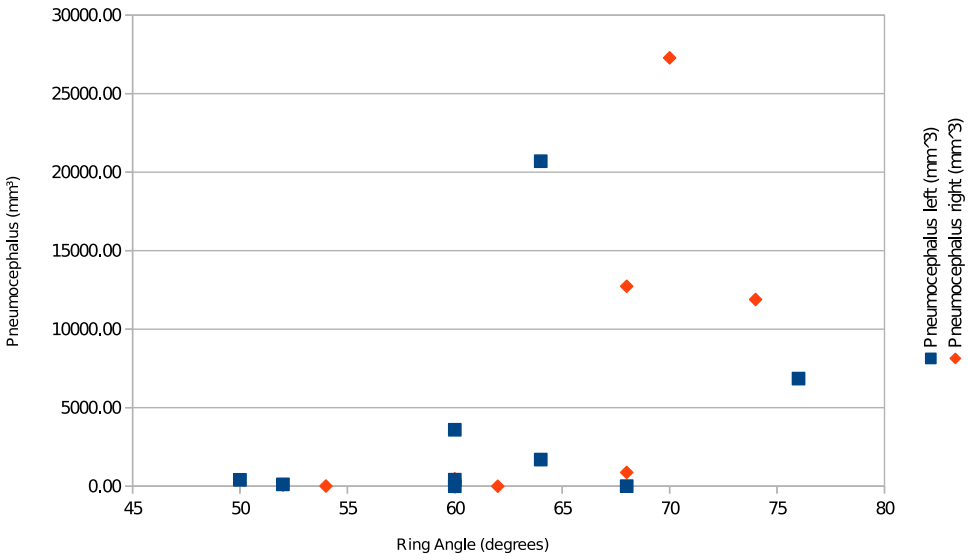

Figure 3.17 – *Pneumocephalus VS antero-posterior trajectory angle. The antero-posterior angle is depicted in the figure 3.16(a). We notice the growth of the pneumocephalus when the angle increase. Despite a low coefficient of determination, the positivity of the linear regression coefficient indicates also the growth. This confirms the assumption on the brain shift amount depending on the entry point location.*

is expressed by $v_{\text{CSF}} = v_{\text{CSF}}(x_e)$. The equation 3.10 becomes

$$S_V(x_e) = X_V\big([0, v_{\text{CSF}}(x_e)]\big) = \bigcup_{v=0}^{v_{\text{CSF}}(x_e)} X_V(v) \tag{3.12}$$

The embedding surface depends now on x_e, the insertion point. And the risk becomes:

$$\begin{aligned} R(x_e) &= f\Big(d\Big(t(x_e), S_V\big(v_{\text{CSF}}(x_e)\big)\Big)\Big) \\ &= f\Big(d\Big(t(x_e), \bigcup_{v=0}^{v_{\text{CSF}}(x_e)} X_V(v)\Big)\Big) \end{aligned} \tag{3.13}$$

Regarding the equation 3.12 and 3.13, the function v_{CSF} depending on the entry point x_e is unknown. According to our data (figure 3.17), the brain shift amount depends on the insertion point location: the more the entry point is low, the more CSF is lost, the more the brain shifts. Missing a reliable model of CSF loss depending on the entry point location, we assume a linear relation between them:

$$v_{\text{CSF}}(x_e) = \text{Lerp}\big(v_{\text{CSF}_{\text{min}}}, v_{\text{CSF}_{\text{max}}}, \text{proj}_g^{\perp}(x_e)\big) \tag{3.14}$$

The function $\text{Lerp}(a, b, x)$ is a linear interpolation of the variable x between a and b. $v_{\text{CSF}_{\text{min}}}$ and $v_{\text{CSF}_{\text{max}}}$ are two constants. The function $\text{proj}_g^{\perp}(x)$ is the orthogonal projection of the point x onto the axis g (here the gravity direction). Let $x_{e_{\text{min}}}$ (respectively $x_{e_{\text{max}}}$) the point(s) which are lowest (respectively highest) (compared to the gravity direction) in the entry point domain. Then, $v_{\text{CSF}_{\text{min}}}$ is the volume of CSF loss when the entry point is located in $x_{e_{\text{min}}}$. And similarly for $v_{\text{CSF}_{\text{max}}}$ and $x_{e_{\text{max}}}$.

$$\begin{cases} v_{\text{CSF}_{\text{min}}} = v_{\text{CSF}}(x_{e_{\text{min}}}) \\ v_{\text{CSF}_{\text{max}}} = v_{\text{CSF}}(x_{e_{\text{max}}}) \end{cases} \tag{3.15}$$

Because sometimes there is no brain shift at all, we can choose $v_{\text{CSF}_{\text{min}}} = 0$. It will act on the shift of the more frontal structures. The $v_{\text{CSF}_{\text{max}}}$ parameter is not trivial to define. Missing a real patient-specific (or surgeon-specific) personalization of this parameter, we propose the following method to define this parameter:

- Applying always the same constant parameter, defined from values taken in the literature. For example, [Elias et al., 2007] reported about 50 cm^3 of pneumocephalus, while [van den Munckhof et al., 2010] reported up to 88 cm^3.
- The surgeon can have the choice of a relative risk of shift. For example, we can define a scale of three values (small, intermediary and big) representing the amount of risk of brain shift. Depending on his/her experience, the surgeon can identify patients likely to present an important brain shift. It is based on some patient's properties, such as the brain atrophy.

Automatic Planning Software

In opposite to the risk volume (3.4.2), the brain shift aware risk map has been developed to be integrated in an automatic computation of electrodes trajectory. The planning software is an evolution of the framework presented in [Essert et al., 2011]. Originally, the computation of an optimal electrode trajectory is done by minimizing the following cost function:

$$f : t \longmapsto \sum_i \omega_i R_i(t) \tag{3.16}$$

where

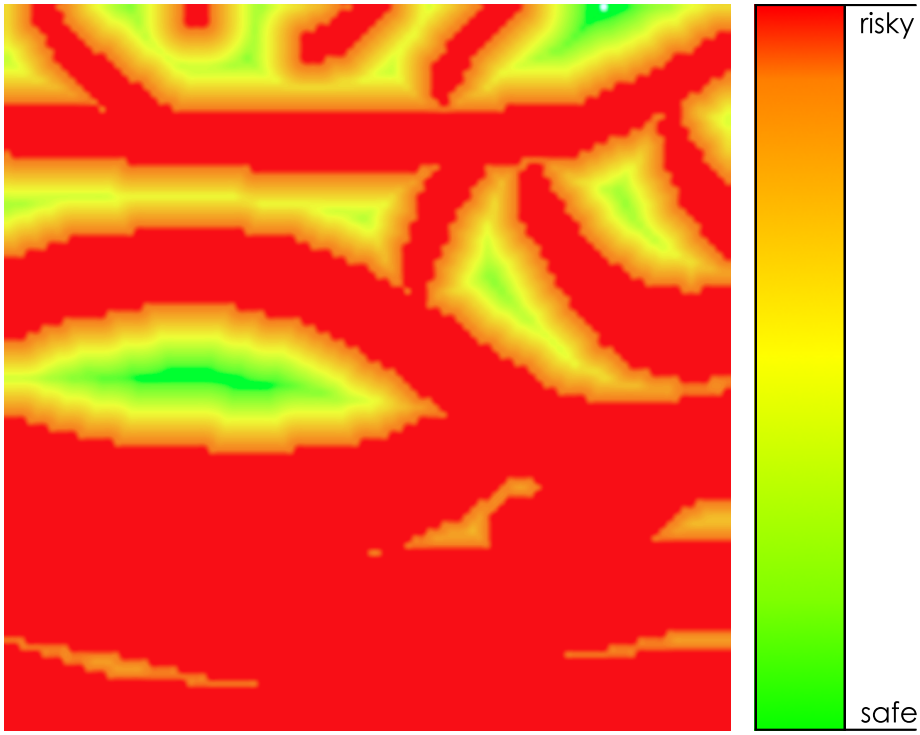

(a) Brain shift aware risk map. Notice that the red (harmful) areas are larger at the bottom than at the top.

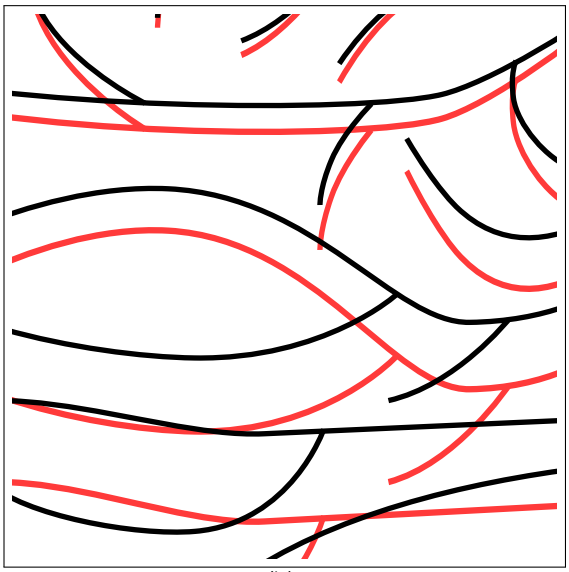

(b)

(c) .

Figure 3.18 – *Final brain shift aware risk map. The risk map is based on a simulated shift of the vessels from the figure 3.11(a). The pixel colors represent the distance of the pixel from the network, according to the scale in legend. A safe trajectory has to be selected in the area corresponding to a minimal distance, here in green.*

- f is the cost function to minimize
- the variable t is a trajectory to evaluate (or an entry point if the target has been fixed)
- R_i is a score associated to x. They are based on the constraints enumerated in Section 3.1.2. Each of the R_i output is in the range $[0, 1]$.
- ω_i are weights associated to each score R_i. The surgeon defines these weight to set the relative importance of the different scores. If $\omega_i \approx 0$, the score R_i will have a weak importance in the choice of the optimal trajectory. In opposite, with $\omega_i \approx 1$, the score R_i will be crucial.

The optimal trajectory t_{optim} associated with the cost function f of the equation 3.16 is:

$$t_{\text{optim}} = \min_t f(t) \tag{3.17}$$

In [Essert et al., 2011], one of the R_i was based on the distance of the trajectory to the sulci. It is actually the score of the equation 3.8. The proposition in the paper [Bilger et al., 2012] is to replace the rigid score (equation 3.8) by the brain shift aware score of the equation 3.13. By doing this, an optimal trajectory would be computed accounting for risks of brain shift.

3.5 Results

3.5.1 Risk Volume

We apply the brain shift aware risk volume method on the models presented in Section 2.4.1. We assume the target coordinates are already defined. First results are shown in the figures 3.9 and 3.19. In these tests, we compare the physics-based risk volume and the geometry-based risk volume. We notice the physics-based volume is larger,making the trajectory selection more restrictive (see Fig. 3.20 compared to Fig. 3.6). Moreover, we observe the restriction acts mainly in the direction of the brain shift. Finally, we notice that the dimension of the volume in the direction of the brain shift varies depending on the depth in the brain tissues (see figures 3.9 and 3.19). This is due to the fact that the tissues on the surface have a larger motion than the deep tissues.

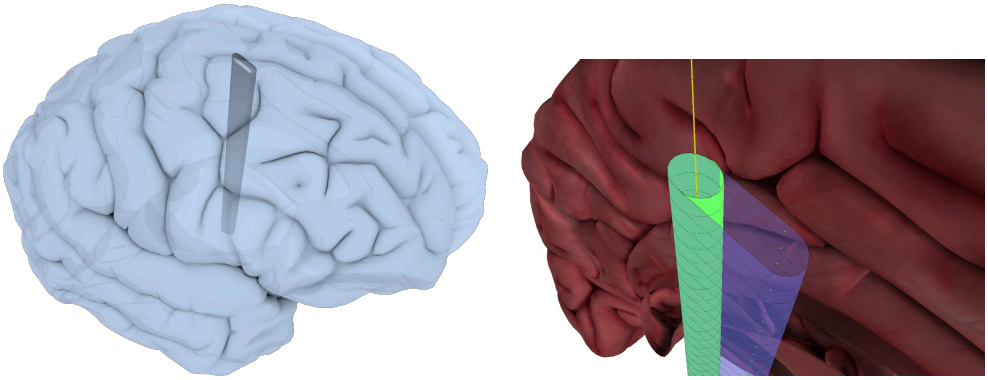

(a) 3D representation of the physics-based risk volume in the cerebral environment. The risk volume is computed for a trajectory of an electrode implanted in the right hemisphere, represented in transparent.

(b) Close-up in the 3D representation of the physics-based risk volume (purple shape), compared to the geometry-based safety margin (cylinder).

Figure 3.19 – *First results*

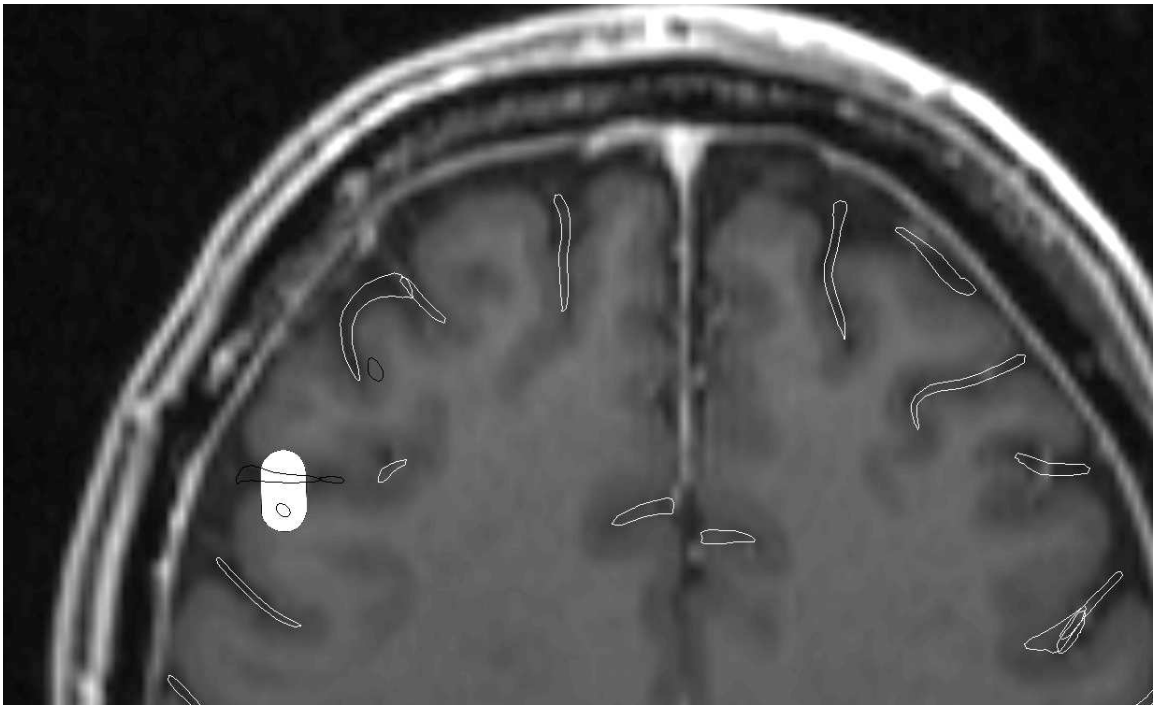

Figure 3.20 – *With our visualization of brain shift risk, vessels which can shift toward a trajectory are detected.*

Our method applies in the pre-operative planning step, when the CSF volume that will be lost during the surgery is unknown. Besides, there is no precise model to anticipate it. The CSF loss depends on many parameters: orientation of the patient's head, burr hole location, anatomy, pathology etc. For this reason, we ask the surgeon to select an amount of CSF loss, expressed in percentage from 0% (no CSF loss) to 100% (all the CSF of the intracranial cavity has leaked out). Different CSF losses have been tested, and are depicted in figure 3.21. It appears that the more the brain shift, the larger the risk volume, as expected. Although, the amount of CSF loss is difficult to evaluate, we have determined from the literature [Elias et al., 2007] that a realistic spectrum of percentage is between 0%-40% (knowing that 40% is a huge value that happens in some rare cases). Depending on the pathology and its known relationship with the amount of brain shift (e.g. atrophy of the brain), the surgeon can adjust the value of CSF loss to better estimate the intra-operative scenario. It is also known that the surgical technique has an impact on the CSF loss (e.g. dura mater opening). There is obviously a duality between the brain shift and the CSF loss volume, therefore we can also define a brain shift amplitude based on a displacement, rather than a CSF loss.

3.5.2 Risk Map

We compared the brain shift aware risk map with the regular distance map on the template. The result can be seen on Fig.3.22, which contains snapshots from the planning software. Two color maps corresponding to soft constraints are shown: (a) with regular distance computation (static vessels), and (b) the brain-shift aware risk map computed by the simulation. We can see that the green areas, corresponding to safe insertion points, are narrower and less numerous using our risk map. Only the areas that would be safe even with a brain shift are kept. However, sufficient number and surface of green areas are still present.

On Fig.3.23, the final result of the automatic optimal trajectory planning, including several constraints

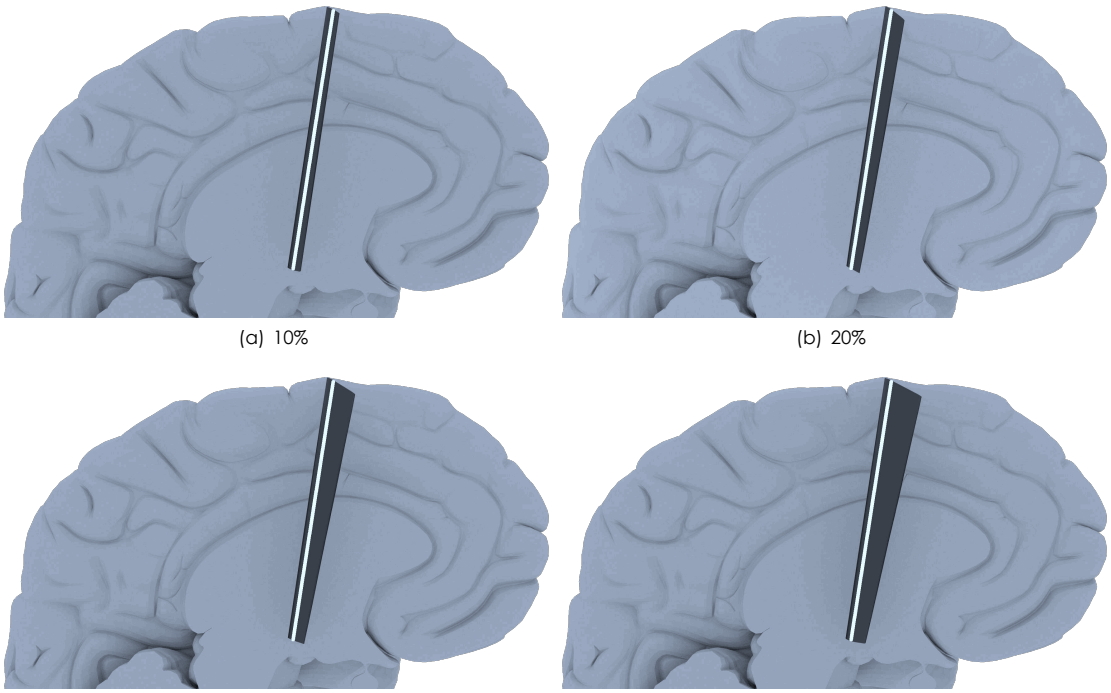

(a) 10% (b) 20%

(c) 30% (d) 4 0%

Figure 3.21 – *CSF variation. Considering a trajectory (the white line), we compare four brain shift aware risk volumes depending on the CSF loss amount, from 10% lost, to 40%.*

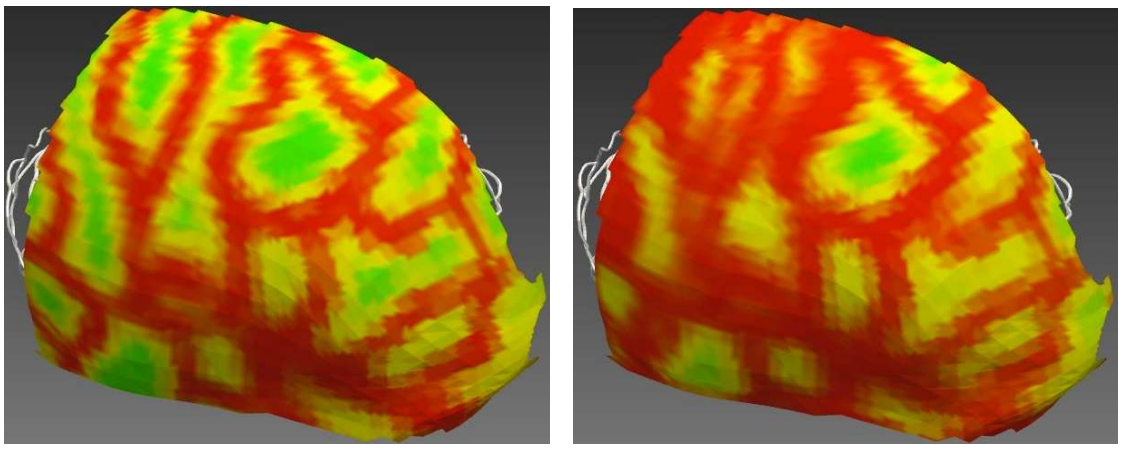

(a) Without brain shift (b) With brain shift

Figure 3.22 – *Color maps representing the risk in relation to the proximity of the vessels, computed without/with taking into account a possible brain shift. In green the safest zones, in red the zones to avoid.*

other than distance to the vessels, is shown for the template. We can notice that even with the restriction of the safe areas due to our risk map, an optimal trajectory can still be found within the range of the average angles relatively to AC/PC that are used as a basis in clinical routine (around 60° in antero-posterior and 30° latero-median axis).

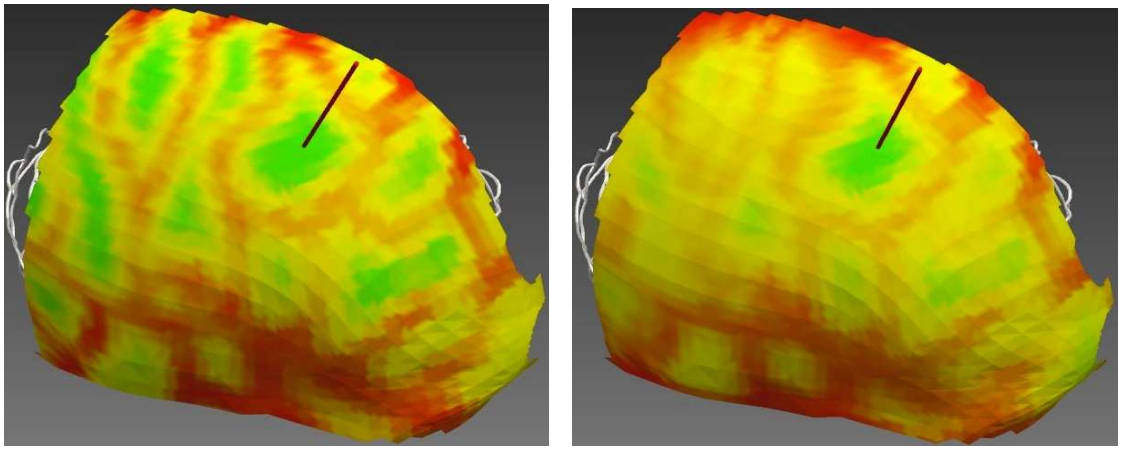

(a) Without brain shift (b) With brain shift

Figure 3.23 – *Optimal trajectory (red cylinder): trajectory satisfying at best the combination of soft constraints. In green the best zones, in red the zones to avoid.*

3.6 Conclusion

3.6.1 Brain Shift Aware Risk Volume

We propose a method to intuitively visualize a risk assessment in DBS planning. The computation is based on a physics-based brain shift simulation, handling the trajectory angle, the depth in the brain tissue, and the patient's head orientation. Morevoer, with a more advanced biomechanical model of the brain, we will be able to include more variations in the risk volume: heterogeneity and anisotropy of the brain tissue, interactions with the vascular network.

3.6.2 Brain Shift Aware Risk Map

We described a physics-based method for simulating deformations of cerebral structures and landmarks caused by the brain shift during deep brain stimulation surgery, according to a position of the burr hole and an estimation of the CSF loss. More particularly, we estimated the movement of the vessels which need to be avoided during the insertion of the electrode. We emphasize that our method does not pretend to provide an exact estimation of the brain deformation or vessel motion at the pre-operative planning step, as it is not possible to anticipate the exact CSF loss before the surgery, or other physiological parameters. To compensate for some uncertainties in the simulation (such as exact CSF loss), and to account for other possible errors (such as segmentation of the vessels and other structures on the patient data), we proposed to embed both vessel motion and estimated error into an advanced distance map. This map was used in a path planning software to produce optimal electrode placements.

The results of our experiments show the benefits of such a simulation, as it does not restrict too much the possible insertion areas but provides safer trajectories regarding the possibilities of brain shift. In the future,

we plan to better determine the influence of the CSF loss (as done in [Elias et al., 2007]) through additional studies.

3.6.3 Discussion

Although both methods (risk volume and risk map) seem different, we believe the common notion of risks makes them equivalent. The risk map has been developed to be used in an automatic computation of electrodes trajectory, while the risk volume targets directly the neurosurgeon for a manual verification. A close look on the common notions would allow us to unify both techniques.

We are aware the results presented in this chapter are not enough to validate completely the methods. We plan to apply the brain shift risk map on a larger series of patients. In addition, we need to investigate the usability of the method pre-operatively. A challenge would be to compute a trajectory in parallel, submit it to the surgeon, and compare it to the surgeon's trajectory. Moreover, we need to investigate the comparison of our brain shift aware optimal trajectory compared to the rigid optimal trajectory. Is the difference significant? Can the brain shift aware optimal entry point be located in a very different area? These questions have not been answered yet and will be addressed in future studies. The answers would prove the necessity of the method. Although the automatic computation of electrode trajectory could save time to the surgeon during the planning (but more importantly for the patient's confort), the simulation could be time consuming for a non-technician. That is why we need to evaluate the brain shift aware and the rigid methods in the goal of a clinical use.

3.6.4 Future Works

We have developed two pre-operative brain shift aware methods relying on the notion of risk of brain shift, especially the risk of CSF loss. Although we give hints on how to select the corresponding parameters, a better control of them would be required. We need pre-operative indicators of a brain shift. Does age, sex, symptoms duration, clinical scores, atrophy, burr hole location etc have an influence on the brain shift amount? Although some studies tries to find correlations, we think a more precise study with more parameters, which were not studied in previous works, is required. For instance, we think the surgeon's technique has an influence on the brain shift amount. The study needs to include patients from multiple centers. A better description of the surgical steps are necessary in the study: which side is open first? is the first implantation done after the first or the second skull opening? etc. Hopefully, we can find a correlation an better estimate the brain shift risk.

In addition, the problem encountered in Section 3.2.2, related to the target displacement, has not been treated in this chapter. This is due to the fact that the target displacement is considered negligible. However, an evolution of the framework presented in [Essert et al., 2011] is in development which would account for the target displacement. The method would automatically compute an optimal trajectory taking into account the target motion. The method would also be based on the simulations presented in this thesis, in particular the brain shift risks.

Physics-Based Intra-operative Registration

Chapter 4

Abstract

The brain shift affects the position of the internal structures during the surgery. This results in inaccuracy on the targeting and reduction of the safety regarding the blood vessels motion. Ideally, the surgeon would need a precise configuration of the brain during the operation, to update the pre-operative planning. We propose to use the pre-operative configuration of the brain and deform it with our brain shift model until it corresponds to the intra-operative configuration. The registration is based on physics. The presented work has been published in [Bilger et al., 2014a] and [Bilger et al., 2014b].

Contents

4.1 Context

4.1.1 Pre-operative planning

Section 3.1 describes in details the steps involved in the pre-operative planning. To summarize briefly, it consists in identifying the target and selecting a safe trajectory. We already mentioned the problem of brain shift that can alter the planning. The brain configuration changes intra-operatively, therefore the planning become obsolete.

4.1.2 The surgery

The procedural steps of the surgery are mentioned in Section 1.3.2. It starts by placing the stereotactic frame on the patient´s skull. When the surgeon makes the burr hole and open the dura mater, Cerebro-Spinal Fluid (CSF) can leak out. At this moment, due to the CSF loss, the brain can deform. Most of the deformation takes place during the first moments after the skull opening.

4.2 Intra-operative imaging

Due to the obsolescence of the planning after the skull opening, the surgeon may want an updated image of the brain configuration. For that, the surgeon can use an intra-operative imaging system such as the O-arm or an intra-operative Magnetic resonance imaging (MRI).

4.2.1 O-arm

The O-arm imaging system is presented in the paper [Lin et al., 2008]. This technology has been developed to acquire a Computed Tomography (CT) scan during a surgery. The advantage is the result of 3D images, compared to the 2D projected images of an X-ray traditionally used during a surgery. Similarly to a CT scanner, an O-arm system use the rotation of a X-ray emitter and uses the resulting 2D imaging to generate a 3D image. The novelty is the mobility of the system. Its size and the fact that the circle can be opened makes it easy to use in an operation room. A photograph of the system is in the figure 4.1.

Note that O-arm is not the only intra-operative CT scan (for instance C-arm and Artis Zeego).

4.2.2 Intra-operative MRI

Very similar to an MRI scanner, Intraoperative Magnetic Resonance Imaging (iMRI) is the use of an MRI scanner while the patient is undergoing surgery. It is mainly used for brain surgery, to detect risks of damaging or confirm a procedural step during the surgery. It has been used for the removal of brain tumors [Ginat et al., 2014; Senft et al., 2011; Schulder and Carmel, 2003], but it has been recently used for Deep Brain Stimulation (DBS). For instance, [Huston et al., 2011] use iMRI to evaluate acute hemorrhage, intracranial air, brain shift, and accuracy of lead placement. The ClearPoint system [1] uses iMRI to perform the planning during the surgery. In that case, the planning is always updated even in case of brain shift.

Despite a useful tool, iMRI has the following limitations:

- It requires more people to operate
- Longer anesthesia duration

[1] http://www.mriinterventions.com/clearpoint/clearpoint-overview

Figure 4.1 – *O-arm imaging system*

- Longer operation duration
- High cost of the system
- It requires dedicated operation room (MRI compatible tools)
- Poor image resolution
- In opposite to the O-arm system, iMRI is not mobile

Although the ClearPoint system seems to solve several problems, a very limited number of DBS centers are equipped with iMRI. The rest of the DBS centers still need methods to overcome the problems related to brain shift.

4.2.3 How can we use intra-operative imaging system?

Other imaging systems can be used intra-operatively, such as X-rays which can be used to verify the placement of the electrodes after implantation. But the two presented systems have the advantage to provide a 3D image of the head, with the brain and skull clearly visible, in opposite to X-rays. Despite this advantage, the images cannot be used to identify brain structures with precision, specially the target, due to poor contrast in the tissue. In addition, classic intensity-based registration techniques cannot be used when brain shift occurred due to the presence of air in the skull and the brain deformation. Nevertheless, an intra-operative CT can be registered rigidly [2] with the pre-operative CT scan, using the bones which did not deformed. In our contribution, we focus on the O-arm technology, which is available in the Hôpital Pitié-Salpêtrière.

Our goal is to provide to the surgeon the same level of details intra-operatively than the pre-operative image. In this chapter, we describe how we use intra-operative images in combination with pre-operative images to achieve this goal.

[2] 4×4 transformation

Related works

In the literature, intra-operative brain registration methods to estimate brain shift have been widely studied. We divide the different works into two categories: some groups used only images and intensity-based techniques to register the brain, while others used a biomechanical model of deformation. All the contributions need a source of intra-operative information to guide a model that will transform the pre-operative image.

Ultrasound is an attractive technology for an intra-operative use due to its low cost, and the few constraints to use it intra-operatively. [Gobbi, 2000] manually moves landmarks on the MRI to their new position in the reconstructed 3D ultrasound image. The brain is then warped according to the new landmarks position, using the Visualization Toolkit (VTK). [Pennec et al., 2005] first rigidly register the ultrasound image with the MRI when the dura mater is still closed to calibrate the ultrasound device location in the MRI space. [Farnia et al., 2014] propose a method based on the matching of the echogenic[3] structures such as sulci by optimizing the residual complexity[4] value in the wavelet domain between ultrasound image and MRI. [Reinertsen et al., 2007, 2014] use the blood vessels as a feature to register the two modalities, as it is relatively easy to detect the vascular tree in ultrasound images. The vascular tree is segmented and center lines are extracted to be registered with the segmented pre-operative center lines using a modified version of the iterative closest point algorithm[5]. They validated the usability of the method in the operating room, during surgery. However, for the moment, the method only transforms the brain with a rigid transformation. It is not adapted if the surgeon needs the new location of an internal structure. In the presented works on ultrasound registration, the challenge is to register two different modalities, but it is not focused on the deformation of the brain, in particular the resulting internal structures displacement and deformation

[Duay et al., 2003] used a laser-range scanning device as the intra-operative source of information. The input data are a picture and the 3D physical coordinates of objects within its field of view. The registration is serially solved with a Mutual Information-based algorithm. However the equipment is not standard and requires a large working space without occlusion, which is not the case in DBS procedures. [Berkels et al., 2014] rely on a simple photograph of the brain surface, but is not adapted to DBS because of the large field of view required. [Hastreiter, 2000] propose two registration methods based on intra-operative MRI.

In the other hand, some groups have studied the intra-operative registration of the brain based on a biomechanical model. [Castellano-Smith et al., 2001] introduced a Finite Element Method (FEM) model generated from an atlas mesh. They measure the change of volume of the lateral ventricles between pre- and post-operative MRI, then they apply a load to the model so that the resulting deformation leads to the same change of volume. In our opinion, the information guiding the model is not enough for an accurate deformation. [Skrinjar et al., 2002] presented a method to deform pre-operative data according to a partial intra-operative brain surface, captured by a stereo camera, while [Chen et al., 2011] and [Audette et al., 2003] used a laser range scanner. The work of [Wittek et al., 2007] is very similar to [Skrinjar et al., 2002] but they used intra-operative MRI to guide the deformable model and took extra care on the complex model of the brain tissue deformation. However [Skrinjar et al., 2002] and [Wittek et al., 2007] do not model physically the brain shift phenomenon, because they include artificial forces by adding virtual springs or constraints between pre- and intra-operative control points. Similarly, [Vigneron et al., 2012] presented a serial intra-operative method, where they apply a displacement to some brain surface landmarks. In this work, it is interesting to register the brain with a sequence of intra-operative images. It would hep us to understand the dynamic of brain shift. None of the presented methods accounts for the effects of gravity, influence of CSF and brain tissue and loss of CSF. On the contrary, Chen et al. [Chen et al., 2011] used a computational model which accounts for CSF loss and gravity. They pre-operatively built a statistical atlas of deformation to solve the inverse problem intra-operatively.

[3] Ability to bounce an echo
[4] Introduced in [Myronenko and Song, 2010], residual complexity is a similarity measure between two images
[5] Algorithm to minimize the difference between two point clouds

Motivation

Our objective is to propose a method relying on a biomechanical model. In our opinion, this is the best direction to explore as brain shift is a physical phenomenon, and despite its difficulty to model it now, we think the correct physical model will lead to the best results. Of course, a lot of problems remain to solve before proposing the best accuracy possible (see the perspectives in Section 4.6). To summarize, the objective is to reproduce the brain shift phenomenon by simulation so that the resulting deformation corresponds to the intra-operative observation.

From the related works in the literature, we have learned that a lot of contributions use a biomechanical model without any physical sense. It is used as a regularization energy for the registration, often based on the displacement of some landmarks. We list here the choices made in the models of the literature, that we think are not physical, or an obstacle to the accuracy:

1. Applying a displacement between a node of the mesh a its intra-operative location so that the rest of the brain deforms accordingly. This process adds artificial forces between corresponding control points. These forces do not exist in reality.
2. Not accounting for gravity and CSF influence. This is precisely the main causes of brain shift that need to be included in the model (see Section 1.4). The models which does not account for these influences do not model brain shift but only the brain deformation, which has to be guided by something that is not the real cause.
3. When accounting for gravity and/or CSF forces, none of the contributions mentioned the computation of the reference state (see Section 2.4.5), which is crucial in our opinion.

For practical reasons, we also need the following constraints in our method:

1. The intra-operative time to apply the method (including the computation time) should be very short. It is not an option to add more discomfort to the patient who already undergoes up to eight hours of brain surgery.
2. The intra-operative modality we use is CT, therefore landmarks are not visible in the brain tissue. We need a more simple intra-operative observation but with enough information to correctly guide the model

To conclude, the following will present our contribution based on the previous observation: our objective is to model brain shift and its causes (and not only brain deformation) in order to match the intra-operative configuration. Our model will be guided by an intra-operative CT scan.

4.3 Working hypothesis

1. We are in the case where the surgical protocol could lead to a brain shift. It has chances to happen when the dura mater is opened for the electrode insertion. The contributions presented in this chapter can also be used if the patient does not present a brain shift, but the interest is limited. The registration will lead to null displacements.
2. Two moments of the procedure are involved in the described methods. First, a pre-computation is performed before the surgery. Then, an intra-operative imaging system is necessary and an estimation process runs for the registration from the provided data. The methods have been developed to be used in a real procedure, in minimizing the time to perform the registration.
3. The data used in the methods presented in this chapter are the pre-operative MRI, without the stereotactic frame and an intra-operative CT scan. We insist that the method could also be used with an

intra-operative MRI instead of a intra-operative CT scan. The use of ultrasounds would require an additional method to register the data on pre-operative MRI.

4. The biomechanical model of brain shift is based on the model presented in Chapter Models of Brain Shift. It requires the segmentation of the following structures: two brain hemispheres, falx cerebri, endocranium, sulci or blood vessels network, CSF and the other structures of interest such as the target. Note that our approach is not dependent on our brain shift model.

4.4 Proposition

To update the pre-operative brain configuration to the intra-operative configuration, we propose to use our physics-based deformation model (Chapter 2). The goal is to estimate the parameters of the model leading to the intra-operative configuration via an inverse problem.

4.4.1 Overall pipeline

The proposed method relies on the pipeline in the figure 4.2. The following sections detail each of the steps we add to the procedural steps (figure 1.18), i.e the highlighted steps in the figure 4.2.

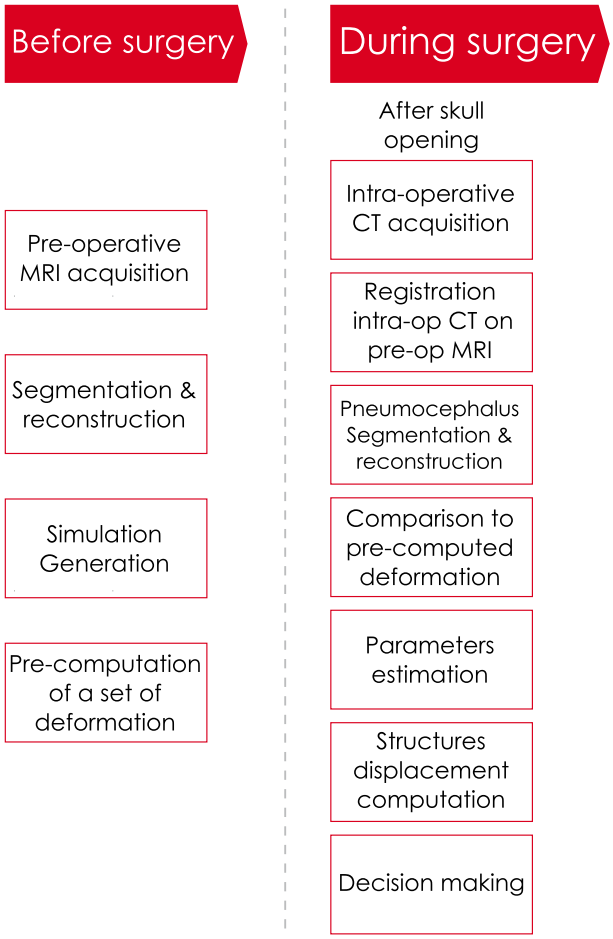

Figure 4.2 – *Overall pipeline to register the pre-operative brain configuration on the intra-operative configuration.*

4.4.2 Simulation Generation

Once the segmentation and the reconstruction of structures has been done from the pre-operative MRI scan using pyDBS [D'Albis et al., 2014], we generate a brain shift simulation specific to the patient. The process is detailed in Chapter Models of Brain Shift.

Parameters to estimate

As explained in Chapter 2, the brain shift model depends on the following parameters: patient's head orientation compared to gravity direction, patient variability (geometry), mechanical properties of the tissue and the amount of CSF lost during the procedure. The two first parameters are known: we can measure the orientation of the patient's head and the geometry is acquired by the segmentation of patient images. The mechanical parameters of the brain tissue have been estimated by several groups using different techniques, but there is no consensus and there is no direct measurement technique personalized for a patient. Although it would be interesting to add the mechanical properties to the parameters to estimate, the deformation is also controlled by the CSF volume lost, meaning that these two parameters cannot be dissociated. That is why the mechanical properties are fixed. Moreover, the mechanical parameters are not the main physical cause of the brain shift phenomenon, in opposite the loss of CSF pressure on the brain. We will show that an acceptable error in the mechanical parameters does affect the parameter estimation, but not the output of our algorithm. Finally, only the CSF volume lost is estimated. As we model both hemispheres independently, two quantities have to be estimated.

4.4.3 Pre-computation of a set of deformation

We have seen that only the CSF volume parameter is estimated. This parameter (actually two for both hemispheres) ranges from $V_{\text{min}} = 0$ (no brain shift) to V_{max}. Let us consider the parameter $v_{\text{CSF}}^{\text{left}}$ of the model is the CSF volume lost in the left hemisphere, and $v_{\text{CSF}}^{\text{right}}$ for the right hemisphere. The pre-operative configuration of the brain is denoted Ω_0. It is deformed into the configuration Ω through the mapping function ϕ. Ω is the configuration of the brain at equilibrium. ϕ depends on $v_{\text{CSF}}^{\text{left}}$ and $v_{\text{CSF}}^{\text{right}}$ among other parameters. Therefore Ω depends also on $v_{\text{CSF}}^{\text{left}}$ and $v_{\text{CSF}}^{\text{right}}$. We discretize the interval $[V_{\text{min}}, V_{\text{max}}]$ with the step h_v resulting in n_v values, so that we have the following set of parameters couple $\left\{v_{\text{CSF}}^{\text{right}(i)}, v_{\text{CSF}}^{\text{right}(j)}\right\}$, $\forall\ 0 \leq i, j < n_v$. One couple leads to a different configuration. For the following of the method, we compute the $n_v \times n_v$ equilibrium configurations corresponding to the $n_v \times n_v$ different parameters.

4.4.4 Intra-operative acquisition

In order to estimate the parameters of the brain shift simulation leading to a brain configuration close to the intra-operative state, we need intra-operative information to guide the estimation. We need an imaging method able to provide (more or less) information about the deformation of the brain. The O-arm system is an CT imaging technique allowing to acquire a 3D image, where the brain, the skull and air are easily distinguishable. An example of an O-arm image showing brain shift is depicted in Figure 4.3. We decided to focus on this technology but other imaging system can be used with our method. In this work, we describe the steps of the pipeline with an O-arm system. Only few steps have to be modified if we change the imaging modality. Similarly to [Ferrant et al., 2001] or[Wittek et al., 2007], it is also possible to use an intra-operative MRI, or ultrasound [Bucki et al., 2007].

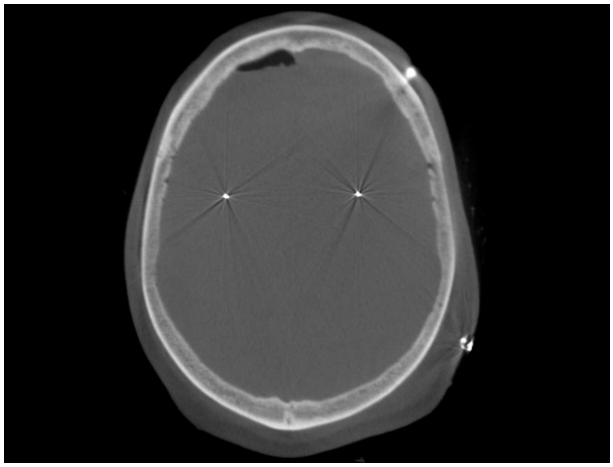

Figure 4.3 – *Example of O-arm intra-operative image showing brain shift. This image has been acquired after the procedure (the artifacts due to the electrodes are visible). We can observe the absence of contrast inside the brain tissue.*

4.4.5 Registration intra-op CT on pre-op MRI

The intra-operative CT scan is rigidly registered on the pre-operative MRI scan using FLIRT[6]. It is a tool for linear intra- and inter-modal brain image registration, based on the work of [Jenkinson and Smith, 2001] and [Jenkinson et al., 2002].

4.4.6 Pneumocephalus segmentation and reconstruction

The pneumocephalus is the presence of air or gas within the cranial cavity. During a stereotactic procedure, air is located in the frontal part. It compresses the frontal lobes, resulting in a Mount Fuji sign [Ishiwata et al., 1988], a tented appearance of the brain in a cross sectional imaging. In CT or MRI, air appear as a black homogeneous area. Therefore, it is quite easy to segment it.

In our pipeline, we use a snake evolution based semi-automatic segmentation method. Basically, a snake is a spline deformed by image forces and external constraint forces until it match the contour of a structure in the image. The algorithm consists in a the minimization of an internal and an external energy. The internal energy ensures the smoothness of the contour. The external energy guides the snake towards strong edges or contours. A third term can be added to ensure the homogeneity of the sampling along the contour. The process is explained in [Kass et al., 1988]. We use the implementation of the method proposed by ITK-SNAP [ITK-SNAP, 2014].

4.4.7 Comparison to pre-computed deformation

We introduce a measure of similarity, to compare the final deformed geometry of the brain, obtained at equilibrium after applying a CSF loss in a simulation, and the visible surface of the brain, extracted from an intra-operative modality. The similarity between these two objects is defined with a least-squares approach:

$$d(S, M) = \sum_{x_S \in S} \|x_S - p(x_S, M)\|^2 \tag{4.1}$$

[6] http://fsl.fmrib.ox.ac.uk/fsl/fslwiki/FLIRT

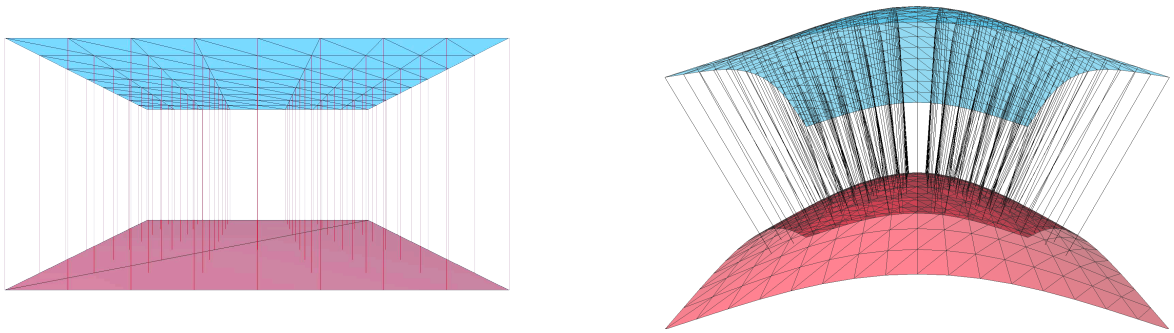

(a) Example showing the projection of a simple plane surface on the same plane, but with a different resolution

(b) Example with curved planes

Figure 4.4 – *Mesh projection. Two examples showing the projection of a mesh onto another. The lines between the meshes represent the projection of a vertices onto the target surface.*

with x_S a point on the surface S of the intra-operative brain, $p(x_S, M)$ is the projection of the point x_S on the surface M of the simulated brain. To compute the projection of a point P on a triangular mesh, we first find the closest point of the surface. P is projected on every triangles around the closest point. We consider only the projections that are inside the corresponding triangle and take the one with minimal distance. The measure is normalized by dividing by the number of points in S, and represents the average distance between both surfaces. Figure 4.5 shows a representation of such a projection in image space, and Figure 4.4 in 3D space.

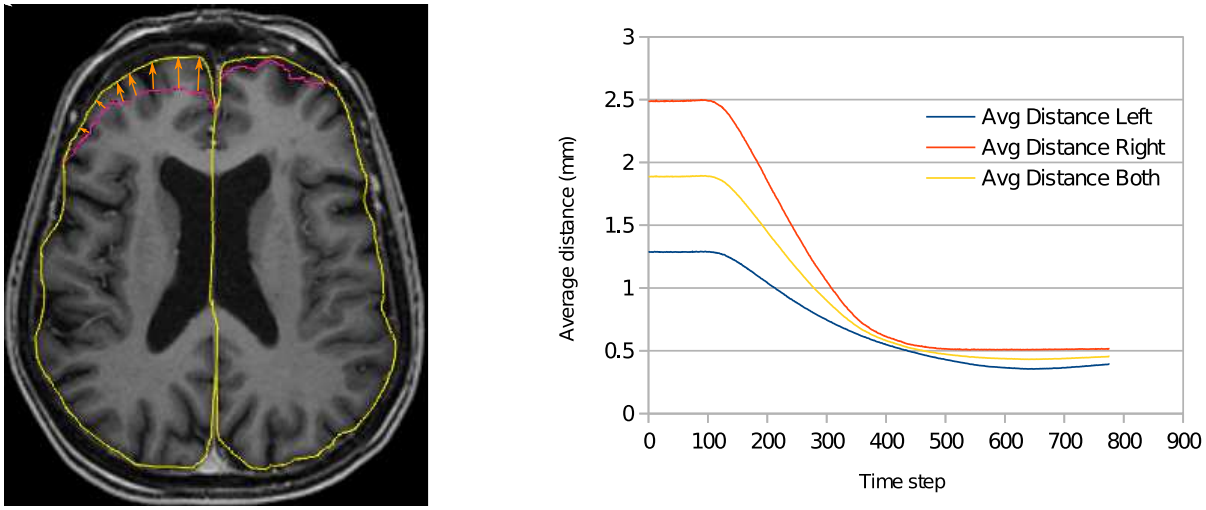

(a) Measure of similarity: the intra-operative triangular surface (pink) is projected on the simulated brain surface (yellow). The measure is the average distance of projection.

(b) At each time step of a simulation, the average distance between the simulated brain and the intra-operative data is measured. In this example, the simulation is parameterized with the same values used to generate the intra-operative data, that is why the distance converges to a small value.

Figure 4.5 – *Mesure of similarity between the simulated brain state and intra-operative data.*

4.4.8 Parameters estimation

The section 4.4.2 presents the parameters of the brain shift simulation to estimate in order to compute a brain configuration matching the observation in the intra-operative data. To estimate the parameters, we need to evaluate the influence of them on the simulation. Do the parameters result in a brain configuration close to the intra-operative data? We compare the simulated brain configuration and the intra-operative data with the method presented in Section 4.4.7. The comparison provides a scalar (a score or an evaluation of the function) which enables to compare the score of different set of parameters. With a least-square approach, like in the equation 4.1, the goal is to compute the set of parameters resulting into a minimal score. This "quest" is an optimization problem, consisting into minimizing a real function. In our case, the real function is the result of a simulation, that is why we do not have access to an analytic form.

Different types of algorithms exist to solve such problems:

- Gradient or Hessian-dependent methods
- Gradient-free methods
- Stochastic optimization methods

Gradient or Hessian-dependent methods The gradient and Hessian-dependent methods require the evaluation of the gradient or the Hessian. Obviously it requires the function to be $\mathcal{C}^1$ to use the gradient, and $\mathcal{C}^2$ to use the Hessian. The algorithms are iterative: they evaluates the function (and its derivatives) iteratively until convergence. The most famous gradient and Hessian-dependent methods are the gradient descent, the conjugate gradient [Hestenes and Stiefel, 1952], the Newton's method etc. Because we do not have the analytic form of the function to minimize, the gradient (or the Hessian) could only be estimated numerically. The gradient evaluation costs several estimations of the function.

Gradient-free methods Unlike gradient dependent methods, the gradient-free methods do not require to evaluate the derivative of the function. These methods are useful when the gradient is not available (like in our case). The Nelder-Mead method [Nelder and Mead, 1965] computes multiple evaluations of the function on the vertices of a simplex. The iterations deform the simplex until convergence. [Powell, 1964] introduces another method using directions and adjusting them over the iterations.

Stochastic optimization methods Stochastic methods involves the use of random variables. The most famous algorithm is the Monte Carlo method [Metropolis and Ulam, 1949]. It computes a large number of random samples to estimate the distribution of the function.

What method to choose? To evaluate a set of parameters, we need to run a simulation with the parameters until it reaches the equilibrium of the brain, then compare it with the targeted data with the function 4.1 to minimize. This process requires approximately five minutes to compute in our tests, but the computation time could vary depending on the model parameters (if we increase the number of nodes, the computation time also increases) or with the constitutive model. More generally, a range of one to twenty minutes has to be considered. To clarify, it means the evaluation of a set of parameters requires one to twenty minutes to compute.

First, stochastic optimization methods are not interesting in our case. They require a large number of evaluations, which has to be multiplied by the duration of a simulation of brain shift to estimate the total duration of the optimization. Despite their faster convergence compared to the gradient-free methods, the gradient dependent methods do not require less function evaluations (in our case) because the gradient needs several function evaluations to be estimated numerically, . Tests have been performed with the following methods: Nelder-Mead, Powell, Conjugate gradient, BFGS and Newton-CG. However, it results in several tens of evaluations until convergence. Any optimization method would require at least

several hours before estimating the brain shift parameters. It is a problem if we want to apply one of these methods intra-operatively.

Instead of using an optimization method, we propose to compute a set of pre-computed brain configurations. The pre-computation is based on a regular discretization of the parameters domain. Each sample picked in the parameters domain leads to a different brain configuration. The computation is performed pre-operatively, when time is not crucial. During the operation, we only compare the different configurations to the intra-operative data. This process takes less than a second to compute, which is more than compatible for a clinical use. The estimated parameters are the parameters leading to the pre-computed configuration with a minimal score. The disadvantage of this method is the dependence on the discretization step of the parameters domain. A high discretization would require more brain configuration to compute, but would lead to a better precision to match the intra-operative observation. Therefore, the discretization is limited by the time separating the pre-operative planning and the surgery, which is maximum one day.

4.4.9 Structures displacement computation

The goal of our method is to compute the displacement of brain structures after the skull opening. We have particular interest in the blood vessels (or sulci) and the ventricles not to damage them, or the tracking of the target (Subthalamic Nucleus (STN), Ventrointermediate nucleus (VIM) etc) displacement.

The structures displacement is computed with the mapping system described in Section 1.5.3.It uses the displacement of the brain mechanical mesh (composed of volume elements) and propagate the displacement to the internal structures via the barycentric coordinates.

The estimated parameters are the input of a particular simulation, leading to a deformed brain configuration. The mechanical model of this simulation propagates the displacement to the considered structures.

4.4.10 Decision making

As we already discussed in Chapter Brain Shift Risk during pre-operative Planning, a trajectory is defined as a linear segment between the target point and an entry point. The target point belongs to a structure targeted to be stimulated. This structure can be registered with our method. The registered structure may have moved and deformed. In classical procedures, as the structure is located in the deep tissue, the motion can be neglected and the surgeon can continue the surgery with the same target point. However, our method provides a quantified information on the motion of the target to the surgeon. The surgeon can rely on this information to decide if the target point selected during the pre-operative planning is still a right spot for a stimulation. Similarly, the blood vessels may have shift following the brain motion. The surgeon can rely on the result of the registration to know the actual position of the blood vessels. She/he can decide if the trajectory is still safe, i.e. it does not damage a blood vessel.

4.5 Results

The registration method needs to be validated in order to prove the results are close enough from the reality. We first demonstrate the method is numerically sound. Then, the method is applied on one patient. We illustrate the registration is usable and it provides good results.

4.5.1 Numerical Validation

Before applying our registration method on patients, we show that it is numerically sound by applying it on a template containing high-fidelity models of the brain, skull, skin, ventricles and blood vessels (see 2.4.1). In our tests, both hemispheres are meshed with approximately 10,000 tetrahedrons. The Young's modulus E is set to 3000 Pa and Poisson's ratio to 0.45 according to [Ferrant et al., 2002].

A virtual brain shift, obtained with fixed chosen parameters, is applied on the template. The obtained configuration will be used as a synthetic of 3D intra-operative data. These data are then used in the parameters estimation process to prove the consistency of the method: the estimated parameters are compared to the parameters used to generate the data.

Finally, we also made a sensitivity analysis on the Young's modulus: we show that if it differs slightly from the mechanical parameters used to generate the synthetic intra-operative mesh, our algorithm still register the intra-operative brain with a minimal error.

Data Generation

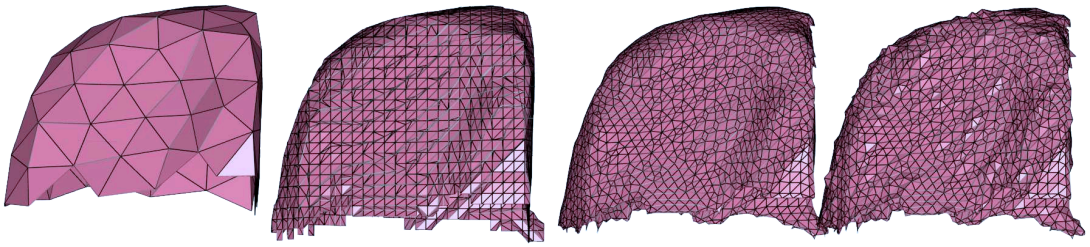

Figure 4.6 – *Remeshing of simulated intra-operative data. From left to right: simulated brain from the mechanical model, uniform remeshing, laplacian smoothing, noise along normals*

With given input parameters V_L and V_R (CSF loss volume for both sides), a deformation is computed with the brain shift simulation: the pre-operative configuration undergoes a CSF leak leading to a brain shift. After the brain shift, when the deformed brain is at equilibrium, the surface in contact with air is extracted, i.e. the same data we extract from intra-operative patient data (see the pink line in Fig. 4.7). The surface is uniformly remeshed with a marching cube algorithm to mimic data coming from 3D images, and noise is added (See figure 4.6) , to meet as much as possible the intra-operative conditions. Finally, the parameters leading to this surface are estimated.

Validation protocol

Multiple intra-operative data were generated in order to validate different scenarios: symmetric brain shift(#1), asymmetric brain shift (#2), unknown mechanical parameters for both symmetric (#3) and asymmetric brain shifts (#4). The parameters (CSF loss volumes and Young's modulus) of each scenario are summarized in the table 4.1.

Error measurement

For each scenario, a set of deformation is computed, and compared to the synthetic intra-operative model, in order to find the minimum distance. The figure 4.8 shows the average distance between data generated with the scenario #2 and the simulated brain shifts, with CSF losses varying between 0 and

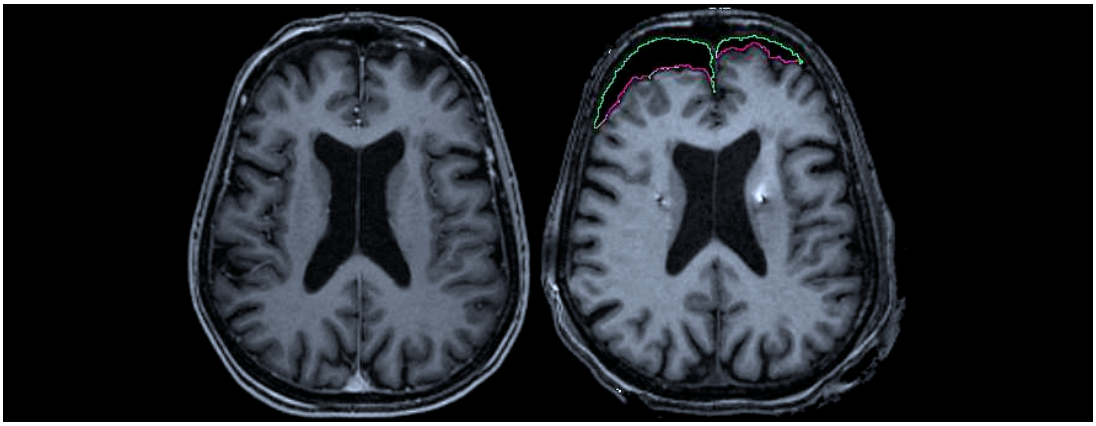

Figure 4.7 – *Pre-operative (left) MR image without brain shift, and post-operative (right) MRI showing asymmetric brain shift. The green and pink contours is a segmentation of the pneumocephalus (air inside skull). The pink line represents the surface of the brain in contact with air.*

30cm^3.

Table 4.1 summarizes the error between the values used to generate the synthetic intra-operative model, and the values estimated by the minimization process. These values are comparable only if the mechanical parameters used for generation and optimization process. To measure errors if the mechanical parameters are different, we compare directly the brain geometry with the measure of similarity presented in Section 4.4.7.

The data in Table 4.1 show that, in the scenarios #1 and #2, the volume parameters are the same in input and output (the error in the measure of similarity comes from the remeshing and noise in the intra-operative data). In scenarios #3 and #4, where the brain is stiffer in the parameters estimation, the volumes estimated are greater, as expected, but the brain deformed with these parameters still matches the intra-operative data. We conclude that a small variation of the Young's modulus does not have an effect on the registration output. The sensitivity of this parameter (which is difficult to estimate for each patient) on our method is low.

The figure 4.9 shows an example of the difference between the pre-operative configuration of the brain and the deformed brain fitting the intra-operative data. With our method, we are able to estimate the CSF volume lost, which gives a registration of the brain if used in the brain shift model. The entire process

Scenario	Input parameters				Optimization output			
	Volume (cm³)		Young's modulus (Pa)		Volume (cm³)		Average distance (mm)	
	Left	Right	Data	Simulation	Left	Right	Left	Right
#1	30	30	3000	3000	30	30	0.4	0.4
#2	10	20	3000	3000	10	20	0.5	0.5
#3	30	30	3000	4000	40	40	0.4	0.4
#4	10	20	3000	4000	15	25	0.6	0.5

Table 4.1 – *Different scenarios of brain shift used to validate the method. The scenarios #2 and #4 mimic an asymmetric brain shift. #3 and #4 use data generated with mechanical parameters different from the minimization process.*

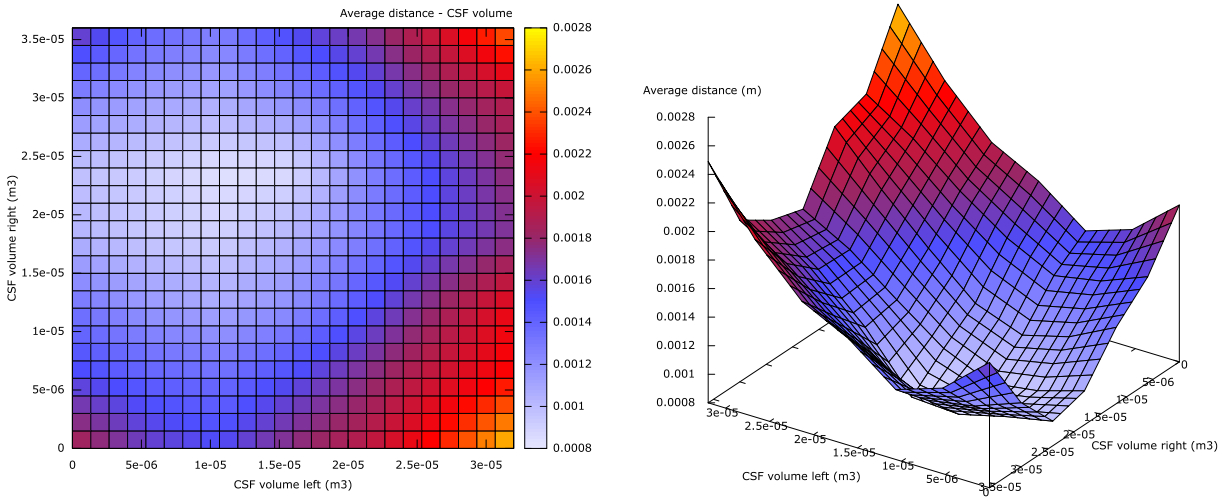

Figure 4.8 – *The CSF loss volume are varying (X and Y axis). The colors represents the average distance between the equilibrium state of the deformed brain caused by a CSF loss (x,y) and the intra-operative brain surface (Equation 4.1). The minimum is located at* $(1 \times 10^{-5}, 2 \times 10^{-5})$*, which is the set of parameters used to generate the intra-operative data (scenario #2).*

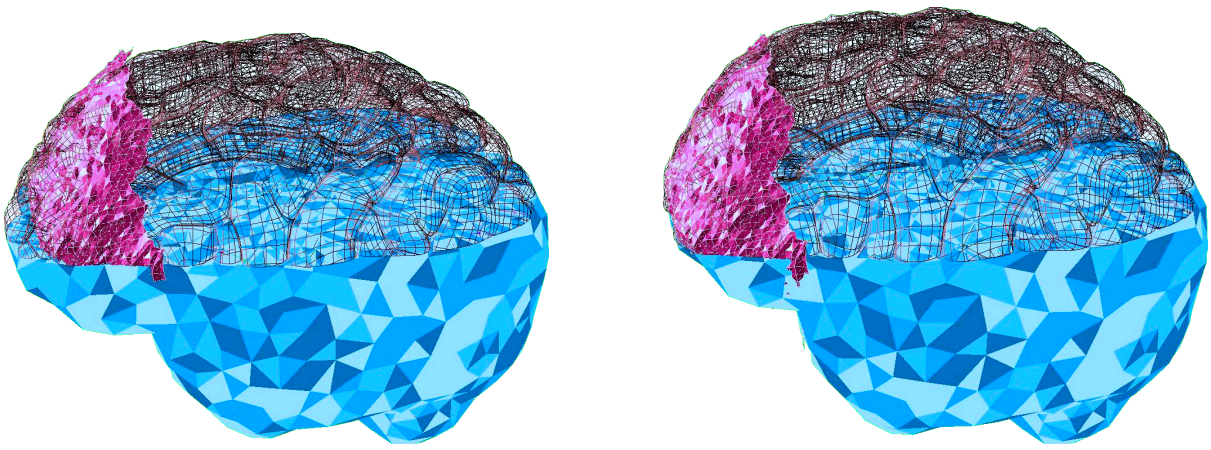

Figure 4.9 – *3D view of the mechanical model of the brain (in blue, only cut for visualization purpose). In pink, the mesh corresponding to intra-operative data. Left: the mechanical model is in its pre-operative configuration. Right: The brain fits the intra-operative data after a deformation*

is based on a physical model, and no artificial forces are needed. The registration algorithm also provides the deformation and displacement of brain structures thanks to the displacement field.

4.5.2 Patient Validation

In this section, we compare the result of our registration method to the pre-operative configuration, through a comparison of the blood vessels network. However, the quality of an intra-operative image does not allow to extract a ground truth. To get around this issue, we consider using a post-operative image

instead. In the days following the procedure, intracranial air is replaced by the CSF produced and brain tissue shift back to its original configuration. We can consider the displacement has not yet started just after the operation. That is why, we chose, for the validation of our method, to use a post-operative MR image of the patient, where we can segment the structures of interest and compare them with the registered structures. We assume the intra-operative configuration to register and the post-operative configuration of the brain are equivalent.

With this assumption, in this section, the intra-operative data of our method are taken from the post-operative image: we only extract air from the image, in the same way as in the intra-operative image. Our method, presented to be applied on CT scans, does not differ with an MRI because air appears as a volume with no intensity in both imaging modalities CT and MRI. In both cases, the pneumocephalus is segmented semi-automatically with an active contour model. Other details from the post-operative image, and not visible in the intra-operative image, are not taken into account in the registration process. However, some structures of interest are segmented in the post-operative image for a comparison purpose (not used during the registration process): the post-operative data follow the same preprocessing pipeline that the preoperative one and is registered on the pre-operative space by a rigid method (FLIRT 6 DoF).

In this study, the Young's modulus E is set to 6 kPa and Poisson's ratio to 0.45. Note that we showed previously that the Young's modulus has a weak influence on the result, that is why we chose a value leading to more stable simulations, compared to the value 3000 Pa usually used.

To estimate the parameters of the model, i.e the volumes of CSF lost resulting to the intra-operative deformation, a set of 169 brain configurations is pre-computed, with parameters varying from 0 cm^3 to 24 cm^3. A higher number of configurations would result in more precision, but given the computation time, 169 configurations (on a laptop i7-4800MQ CPU) is a maximum for a global time compatible with a clinical use (about 14 hours). We believe we can increase this number by optimizing our method, but for now the number of brain configurations we can pre-compute is obtained by dividing the duration between the pre-operative CT scan and the surgery by the duration of one brain shift simulation. The different configurations are then compared to the intra-operative data, i.e. the brain surface in contact with intracranial air. A score of similarity is computed for each configuration according to the measure described in section 4.4.7. The minimum score corresponds to the parameters to estimate. The corresponding configuration is a registration of the whole brain. The comparison process on the complete set is almost instantaneous and does not requires any optimization.

The patient used for the validation of the method presents an asymmetric brain shift (See Fig. 4.7). We notice the right hemisphere has shifted more than the left. This phenomenon is found in the estimated parameters: we estimated that the right hemisphere needed a CSF loss of **18 cm^3** to deform and match the intra-operative data, whereas the left hemisphere needed **12 cm^3**. The average distance computed with these parameters is **2.5 mm** for the right hemisphere and **1.8 mm** for the left. The following results are based on these estimated parameters.

The displacement field and the shape functions of the FEM model is used to compute the displacement and deformation of internal brain structures. Most of the blood vessels are located in the sulci and if a blood vessel shifts on the trajectory of a stimulating electrode during a DBS procedure, it could lead to an hemorrhage. For this reason, we focus the tests of our method on the sulci.

To compare the different configurations, we use the following measure:

$$d(X,Y) = \max\left[\frac{1}{|X|}\sum_{x\in X}\inf_{y\in Y} d(x,y), \frac{1}{|Y|}\sum_{y\in Y}\inf_{x\in X} d(x,y)\right] \tag{4.2}$$

for two meshes X and Y and d the euclidean distance between two vertices. A smaller distance indicates more similarity. The distance between sulci in pre-operative configuration and post-operative configuration is **2.7 mm**. The distance between sulci in the registered configuration and post-operative configuration is **1.3 mm**. This preliminary result shows that our method is promising as it gives a better estimation of the sulci location than using the pre-operative data. This is encouraging to continue to investigate in this direction, and to validate the method on more patients.

4.6 Conclusion

In some cases, the planning could become invalid because of brain deformation occurring during the surgery. The structures of interest, such as the targeted structure or the vital structures, follow the brain deformation and may have moved at the time the electrode is inserted. We propose to update the position of the structures of interest after brain shift has occurred. Our method relies on a brain shift model, including brain deformation model and CSF interaction model, and the corresponding input parameters are estimated from information extracted from an intra-operative image. The method has been tested for its numerical soundness with an anatomical template, and then we illustrate its usability on one patient. With the information provided by our algorithm, the surgeon would have access to an estimation of the new location of the structures. This way, (s)he could decide if the procedure can continue or not, because of a risk to dissect a blood vessel or because of a too large displacement of the targeted structure.

As we mentioned, the method has been tested only on one patient, which is obviously not enough to prove the correctness and accuracy of the method. With that in mind, we plan to test and validate our method on more patients. This future study would follow the method described in Section 4.5.2. However, we face difficulties regarding the described validation method. As we mentioned, there is no ground truth to compare our results to, that is why we rely on a post-operative MRI. But this approach has several limitations.

First, we assume the post-operative configuration is similar enough to the intra-operative configuration so that we can test our method and compare the results with post-operative images. This could be addressed with an intra-operative MRI but the quality of the image will be the source of more inaccuracy in the segmentation method. If we keep working with a post-operative image, a post-operative CT scan is generally preferred, rather than a MRI, because of strong recommendations for safety during MRI acquisition. The data need to present signs of brain shift, a large enough variability in the brain shift effects (asymmetry, shape etc) and enough patient number in order to statistically validate the approach. These constraints on the data are very restrictive, hence the difficulty to obtain reliable data. The third limitation is the approach used to compare the structures. In our method, we compare to atlas-based segmentation of the structures in the post-operative MRI. It relies strongly on the assumption that the segmentation is the ground truth, but atlas-based segmentation is not exempt of inaccuracy. If there are errors (how to detect them?), there is no sense to compare our results to the results of the segmentation. Because of the exposed reasons, we think we need to develop another strategy to validate rigorously our method. Although it is still an open question, we can maybe combine the current validation with the use of the micro-electrode records, which can locate the structures crossed by the electrode, despite its incapacity to analyze the whole brain (only one 1D segment).

Then, we think that a better characterization of the tissue (patient-specific?) or a better model of interaction of the fluid will lead to better results, assuming we can compare to some relying data. The ideas to improve the model are described in Section 2.6.1.

Finally, the following chapter presents algorithms to simulate physically the insertion of the electrode in the brain tissue. In this way, we are able to simulate the whole surgical protocol. One aspect that motivated the modeling of the insertion of the electrode is related to the post-operative deformation (or curvature) of the electrode. In our opinion, the models of insertion of the electrode could be helpful in the validation of the intra-operative registration. Indeed, electrodes are simple to segment in post-operative modalities [Pollo et al., 2004; Hemm et al., 2009]. If we can simulate the electrode curvature so that it corresponds to the segmented post-operative electrode curvature, it will strengthen the validation of our method as well as our trust in our complete framework. The analysis of the electrode deformation would be based on the work of [Lalys et al., 2013]. This aspect will be addressed in the future studies.

Post-operative Electrode Curvature

Chapter 5

Abstract

After a Deep Brain Stimulation (DBS) procedure where the patient underwent a brain shift, Cerebro-Spinal Fluid (CSF) continues to be produced and replace progressively intracranial air. After that, brain shifts back to its original position, whereas the electrode has been implanted. Due to the mechanical properties of the electrode compared to the brain, the electrode follows the brain deformation, leading to a curvature of the lead. It can even cause a migration of the tip of the electrode. In order to address this problem, we propose a model of electrode/brain interaction and reproduce the brain shift, the implantation and the inverse brain shift to compute the curvature of the electrode after the procedure, once air has resolved. This work has been presented in [Bilger et al., 2011].

Contents

5.1 Context

In a DBS procedure, the placement of the electrode(s) is crucial to maximize outcomes and to prevent adverse effects. The placement is achieved in two main stages: first, pre-operative medical images of the patient are combined with the use of a stereotactic frame (and sometimes an atlas of the brain) to determine the target coordinates and optimal trajectory for the electrode(s) (Chapter 3). Second, the patient is taken to the operating room where a macro-electrode attached to a thin wire is inserted into the brain according to the planned trajectory. However, a combination of brain shift and a certain inaccuracy in the exact location of the target area require to test the area next to the planned target (micro-electrode recording) to optimize the placement of the electrode. This test is performed by recording the brain activity using the macro-electrode. This entire process takes several hours, and once the appropriate area has been identified the final (micro) electrode will be left in place and secured to the skull. The electrode is highly flexible to be compatible with the softness of the brain. However, due to this flexibility it cannot be implanted directly inside the tissue. To have a precise insertion, a guide, made of a stiffer material is necessary. This guide is a tube called *cannula*. After implantation of the cannula, the electrode can be inserted inside the tube to obtain a precise placement. Then the cannula is removed and the electrode remains.

5.2 Post-operative electrode curvature

During the process, two major problems arise: first, the planning stage does not account for the brain shift that takes place during surgery. This has been addressed in Chapter 3. Another method is provided in Chapter 4 to update the planning from intra-operative data guiding a simulation of brain shift. The second problem, also linked to the amplitude of the brain shift, takes place several days or weeks after the surgery. As reported in [van den Munckhof et al., 2010] a post-operative electrode displacement and deformation may appear as the brain returns to its initial position when the subdural air introduced during surgery has resolved (see Fig.5.1). This hinders the efficiency of the procedure because upward migration of the electrode may fail to correctly stimulate the subthalamic area. In the rest of the chapter, this phenomenon will be named *inverse brain shift*.

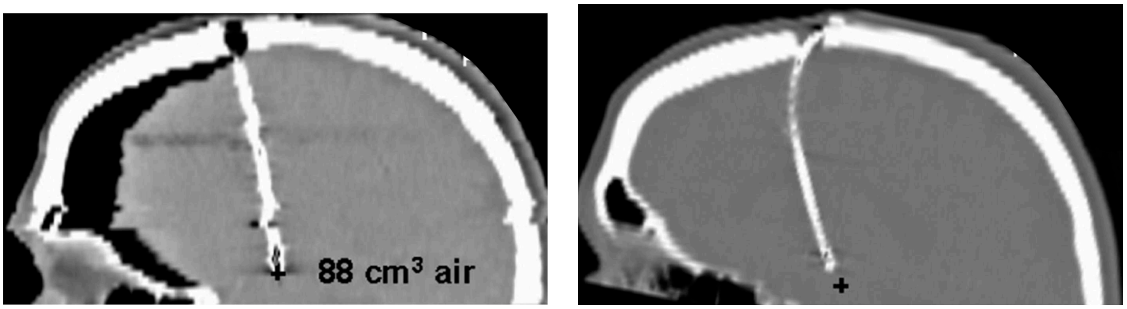

Figure 5.1 – *Post-operative (left) and follow-up (right) CT scans. The post-operative scan illustrates the brain shift at the end of the procedure. The follow-up scan emphasizes the deformation of the electrode due to the inverse brain shift, leading to an upward migration of the electrode away from its initial location after the craniotomy (black cross). For large brain shifts, the electrode can move of up to 5 mm. Courtesy of [van den Munckhof et al., 2010].*

5.3 Working hypothesis

1. We are in the case where the surgical protocol could lead to a brain shift. It has chances to happen when the dura matter is opened for the electrode insertion. The contributions presented in this chapter can also be used if the patient does not present a brain shift, but the interest is limited. The simulation will lead to null displacements of the electrode(s).
2. In this chapter, two moments of the procedure are adressed. First, during the surgery, the electrode is inserted after the brain has shifted. Second, during the days following the surgery, the brain shift back to its initial configuration. Both of these phases are simulated within the same simulation.
3. The biomechanical model of brain shift is based on the model presented in Chapter Models of Brain Shift. It requires the segmentation of the following structures: two brain hemispheres, falx cerebri, endocranium, CSF and the other structures of interest such as the target.
4. In this chapter, no additional data than the data used for the construction of the patient-specific simulation are required. However, the definition of the trajectory is necessary for the simulation of the electrode insertion.

5.4 Model of the Electrode Insertion and its Interaction with the Brain

5.4.1 Electrode model

Similarly to the brain, the electrode is simulated with the Finite Element Method (FEM). This numerical method allows us to simulate deformable objects relying on the continuum mechanics. The FEM has been introduced in Chapter 2, as well as how the brain is modeled. In this section, we will describe how the electrode is modeled, before describing the interactions between the electrode and the brain.

We have seen that the brain geometry is approximated with a tetrahedral or hexahedral finite elements mesh, in order to fill the space occupied by the tissue. Although an electrode is a 3D volume structure similarly to the brain, the same meshing process could not be applied on the electrode. Indeed, an electrode is a wire-like structure where only one dimension is predominant: the length of the object is much greater than the width or depth. A meshing of the electrode with volume elements, such as tetrahedra or hexahedra, would lead to very small elements (compared to the brain) and more importantly to a too large number of them. That is why the models of wire-like structures propose to approximate only the predominant dimension of the object.

5.4.2 Wire-like models in the literature

Two different approaches have been proposed in the literature: continuous models or discrete models. For instance, [Lenoir et al., 2002] modeled a thread as a spline, providing a continuous representation, but this model does not incorporate torsional energy terms. On the other hand, [Nowinski and Chui, 2001] proposed a virtual catheter model, based on linear elasticity, using a set of beam elements. Beam elements are a particular type of element, composed of two nodes connected by a linear segment, and each node has six degrees of freedom, i.e. three for the translation and three for the rotation (see Figure 5.2). Such models allow to account for torsion, tension and compression of the object.

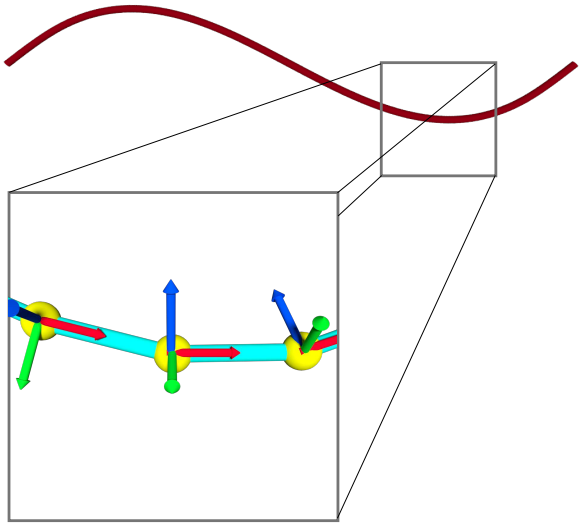

Figure 5.2 – *A wire-like structure is modeled with 1D beam elements. Each node, represented by a yellow sphere, has six degrees of freedom, represented by a RVB frame.*

5.4.3 Our model

The model used in our simulation has been proposed in [Duriez et al., 2005] (extended in [Duriez and Cotin, 2006]) and is based on beam theory [Przemieniecki, 1985]. The main issue with the beam elements model of [Nowinski and Chui, 2001] is that it does not handle large geometric non-linearities. In [Duriez et al., 2005; Duriez and Cotin, 2006], the authors propose to fix this issue with a co-rotational approach, that has already been presented for the brain (Section 2.4.2). In linear elasticity, the stiffness matrix for beam elements is a 12×12 symmetric matrix $\mathbb{K}_e$ (the matrix is described in detail in [Duriez et al., 2005]). Thus, the force $\boldsymbol{f_e}$ at the level of the element is equal to:

$$\boldsymbol{f_e} = \mathbb{K}_e(\boldsymbol{u} - \boldsymbol{u_0}) \tag{5.1}$$

where $\boldsymbol{u}$ (respectively $\boldsymbol{u_0}$) is the current (respectively initial) configuration of the beam. However, the stiffness matrix is computed in local coordinates. Therefore, it is necessary to introduce a transformation matrix Λ changing the frame from a local to a global coordinate system, and then:

$$\boldsymbol{f_e}^{\text{global}} = \Lambda^T \boldsymbol{f_e} \tag{5.2}$$

The global matrix system, consisting in summing the contribution of each element, becomes:

$$\boldsymbol{df} = \mathbb{K}\, \boldsymbol{dx} \tag{5.3}$$

where $\mathbb{K}$ is the global stiffness matrix, which is actually a block-tri-diagonal matrix due to the serial structure of the model, and $\boldsymbol{dx}$ is a variation around the current position. The block-tri-diagonal property of the stiffness matrix enables to use a linear solver adapted for it (Thomas algorithm for example [Conte and Boor, 1980]), and more efficient than a generic linear solver. The complexity of solving the equation 5.3 remains linear with a block-tri-diagonal solver.

5.4.4 Electrode Insertion

The geometrical model of the electrode consists in creating N nodes along a linear segment defined between the tip of the electrode and another point of the electrode, such that the distance to the tip is

greater than the distance between the target and the skull. The nodes are used to create serial beam elements. This geometrical model is then placed and oriented according to the pre-operative planning, which is a phase aiming at selecting a candidate trajectory for the electrode. The virtual electrode is placed outside the skull, and a controller moves it linearly until reaching the target, and always according the the planned trajectory. The movement is linear and is defined in an external file.

5.4.5 Interaction between Electrode and Brain tissue

Our problem of the insertion of the cannula is similar to the insertion of needle in soft tissue. The first publications concerning this problem were [DiMaio and Salcudean, 2005] and [Alterovitz et al., 2005]. Later, a survey [Abolhassani et al., 2007] summarized the advances in needle insertion modeling. Our model of interaction between the electrode and the brain tissue is based on [Duriez et al., 2009]. The model relies on the resolution of constraints and no remeshing process is needed.

When the electrode is inserted in the brain, constraint points are created along the inserted part of the electrode. The constraint points are equally spaced. Constraint points are created as long as the electrode is not fully inserted, i.e. when the tip of the electrode has reached the targeted structure. A constraint points is shared between an electrode beam element and a tetrahedron of the brain (see Figure 5.3(a)). The goal is to satisfy the following conditions:

1. When the tetrahedron containing the constraint point is deformed and/or moved, the constraint point moves accordingly, and distribute the displacement and forces to the electrode beam elements.
2. When the beam element containing the constraint point is deformed and/or moved, the constraint point moves accordingly, and distribute the displacement and forces to the tetrahedron of the brain.

These two conditions can be satisfied with a mapping, such as in Figures 5.3(b) and 5.3(c). If we call P_b the constraint point in the tetrahedron, and P_c the same point in the beam element, the displacement $\boldsymbol{u_b}$ of P_b, and the displacement $\boldsymbol{u_c}$ of P_c can be obtained with the displacement of the nodes of the elements, $\boldsymbol{\Delta q_b}$ for the tetrahedron and $\boldsymbol{\Delta q_c}$ for the beam element:

$$\begin{cases} \boldsymbol{u_b} = \mathbb{J}_b \boldsymbol{\Delta q_b} \\ \boldsymbol{u_c} = \mathbb{J}_c \boldsymbol{\Delta q_c} \end{cases} \tag{5.4}$$

where $\mathbb{J}_b$ (respectively $\mathbb{J}_c$) is a matrix made with barycentric coordinates of P_b (respectively P_c). In our case, the subscript b (respectively c) stands for brain (respectively cannula).

Now, if δ is a measure of the distance between P_b and P_c, the goal is to nullify this distance in the orthogonal directions to the beam (the beam must be able to be inserted along its axis). However, the nullity of the distance is a too strong constraint that would not allow the electrode to be inserted. To fix this issue, the constraint is not solved in the direction of the beam, so that the beam can slide in its direction. If we measure δ along a defined constraint direction $\boldsymbol{n}$, the variation $\Delta\delta$ of δ can be mapped on the displacement $\boldsymbol{\Delta q_b}$ and $\boldsymbol{\Delta q_c}$:

$$\Delta\delta = \boldsymbol{n}^T(\boldsymbol{u_b} - \boldsymbol{u_c}) = \boldsymbol{n}^T(\mathbb{J}_b \boldsymbol{\Delta q_b} - \boldsymbol{\Delta q_c}) = \mathbb{H}_b \boldsymbol{\Delta q_b} + \mathbb{H}_c \boldsymbol{\Delta q_c} \tag{5.5}$$

Let us denote $\boldsymbol{\lambda}$ the force used to solve the constraint. From the virtual work principle, we have:

$$\boldsymbol{\lambda}\, \Delta\delta = \boldsymbol{f_b} \boldsymbol{\Delta q_b} + \boldsymbol{f_c} \boldsymbol{\Delta q_c} \tag{5.6}$$

Finally, we obtain:

$$\begin{cases} \boldsymbol{f_b} = \mathbb{H}_b^T \boldsymbol{\lambda} \\ \boldsymbol{f_c} = \mathbb{H}_c^T \boldsymbol{\lambda} \end{cases} \tag{5.7}$$

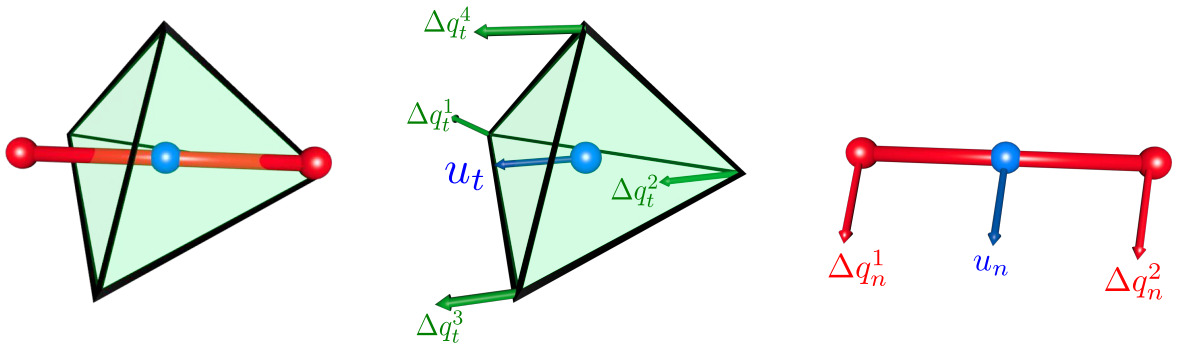

(a) A constraint point (blue) is shared by the beam element (red) and the tetrahedron (green)

(b) The displacement of the tetrahedron nodes is applied on the constraint point

(c) The displacement of the beam nodes is applied on the constraint point

Figure 5.3 – *Example of mapping for a constraint point.*

For the resistance during insertion, friction is added.

To solve the constraint, we recall, from Equation 2.76, that we have to solve the following equations for both the brain and the electrode:

$$\begin{cases} \mathbb{M}_t \ddot{\boldsymbol{x}}_{\boldsymbol{b}} + \mathbb{F}_b(\boldsymbol{x}_{\boldsymbol{b}}, \dot{\boldsymbol{x}}_{\boldsymbol{b}}) = \boldsymbol{f}_{\text{ext}_b} + \mathbb{H}_b^T \boldsymbol{\lambda} \\ \mathbb{M}_n \ddot{\boldsymbol{x}}_{\boldsymbol{c}} + \mathbb{F}_c(\boldsymbol{x}_{\boldsymbol{c}}, \dot{\boldsymbol{x}}_{\boldsymbol{c}}) = \boldsymbol{f}_{\text{ext}_c} + \mathbb{H}_c^T \boldsymbol{\lambda} \end{cases} \tag{5.8}$$

where the subscript b (respectively c) indicates the brain (respectively the cannula).

We use an optimization method to compute the value of $\boldsymbol{\lambda}$ such that the displacement δ is null in the normal direction of the electrode. In addition, we can also model friction in the direction of the electrode. The resulting value of $\boldsymbol{\lambda}$ enables to solve the equation 5.8 by solving a mixed complementary problem (see [Duriez et al., 2009]).

5.4.6 Operating Protocol

With the model of electrode insertion presented previously, we are able to insert the electrode into the brain tissue, then it remains an interaction between both objects. The model remains valid of the insertion of the cannula. Only the mechanical parameters of the cannula are different from the electrode model. With that in mind, we will present in the following section the complete simulation of the operating protocol.

5.5 Results

In this section we present a series of results for the main steps of the procedure described in section 5.4. The conditions and parameters used in the simulation reproduce as closely as possible the conditions and parameters reported in the literature to facilitate comparisons, i.e : the patient lies in the supine position; the craniotomy is performed first on the right side of the skull; a first brain shift takes place before the cannula is inserted through the right hemisphere; the electrode and wire are then inserted through the cannula; the cannula is removed and the electrode remains in the brain but is slightly shifted due to secondary brain shift; the CSF is restored and the air is removed to simulate post-operative conditions several weeks after the surgery. The same process is repeated for the left side of the brain. Figure 5.4 illustrates the simulation of the asymmetric brain shift.

During the surgery and even after the loss of CSF, the brain shifts continuously because of the pressure due to air invasion. However, the rigid material of the cannula prevents the brain motion. That is why,

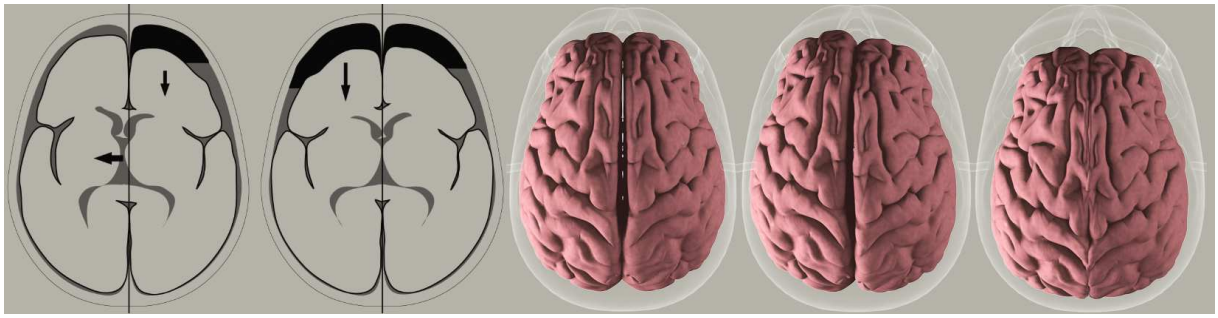

Figure 5.4 – *Asymmetrical brain shift simulation: the brain shift is more important on the side where the craniotomy first takes place, as illustrated in the left most images (courtesy of [Lurig et al., 1999]). The rightmost images show the evolution of brain shift during our simulation: (a) no brain shift; (b) after a right craniotomy; and (c) after both craniotomies.*

the removal of the cannula causes a second but minor brain shift. This effect involves an anteroposterior deformation of the implanted wire, as depicted in figure 5.5. Several days after surgery no more air is in the cranial space and the CSF has been restored. We simulate this effect by modifying the CSF level. The resulting deformations of the brain are computed using our FEM approach. As the electrode and its wire are constrained within the brain (only sliding is possible) and the wire is secured on the skull surface, this results in a relative motion of the electrode with respect to its intra-operative location. This leads to a posteroanterior curvature, as illustrate in figure 5.5 which correlates very well with data from figure 5.1.

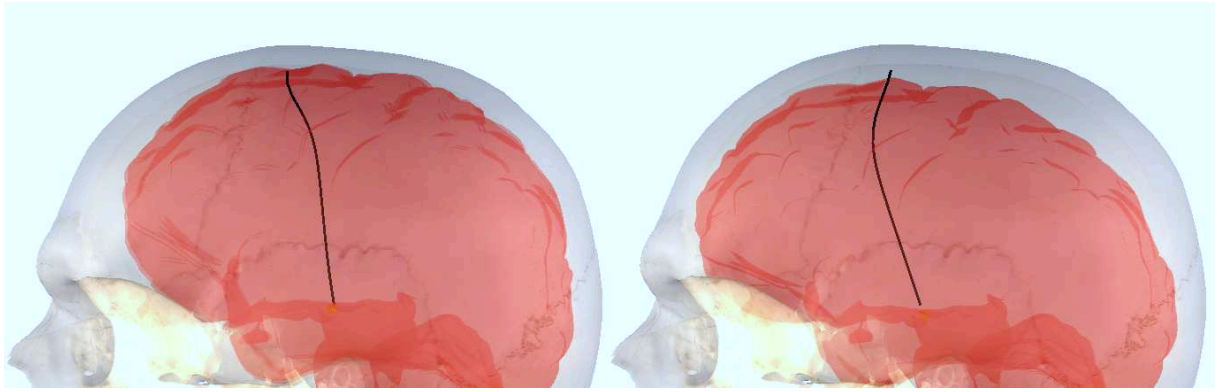

Figure 5.5 – *Screenshot showing the deflection of the right electrode after the cannula removal (left) and after CSF recovery (right).*

We also quantitatively compared our results (amplitude of electrode migration) with data reported in [van den Munckhof et al., 2010]. In their study, a correlation between the volume of subdural air and upward electrode displacement along its trajectory was determined. The relationship between the displacement D (in mm) and subdural air volume V (in cm^3) can be empirically described as $D = 2 + 0.08 * V$. We simulated two relatively different amounts of CSF loss, and computed the corresponding values of V (as the difference between the volume of the brain before and after brain shift) and D. We found that for $V = 22$ cm^3 a displacement $D = 3$ mm is computed, compared to 3.7 mm± 2 mm according to the experimental data [van den Munckhof et al., 2010]. Similarly, for $V = 62$ cm^3 a displacement $D = 6.8$ mm is computed, compared to $D = 6.96$ mm ± 2.5 mm according to the experimental law above. This

strong correlation between our results and published data illustrates the potential of our method. It is also important to note that the entire simulation of the combined models (from pre- to post-operative stages) only requires a few minutes to be computed.

5.6 Conclusion

This chapter presents a model of interaction between the brain tissue and the electrode. It has been used in addition to a the brain shift model in order to reproduce an operating protocol:

1. Brain shift occurs
2. Cannula and electrode insertion
3. Cannula removal
4. Inverse brain shift

After the simulation, which corresponds to the moment when the brain has recover its original configuration, we have observed a curvature of the electrode in accordance with the observation of [van den Munckhof et al., 2010].

5.6.1 Perspectives

Further validation must be performed. In particular, we can have access to the data from [Lalys et al., 2013] that could be useful for the comparison with our simulated electrode deformation. As mentioned in Chapter 4, we could use this data to validate the intra-operative registration that has been presented in the same chapter. To go further, with both validated approaches we could be able to predict intra-operatively the future post-operative curvature of the electrode, as well as the displacement of the tip of the electrode. This information could be useful to the surgeon and neurologist to decide to adjust the position of the electrode.

Conclusion and Perspectives

Chapter 6

Discussing with neurosurgeons about DBS teaches us that the brain shift is still a problem 25 years after the first DBS surgery. With the advances in numerical computation of physical deformation, the objective of our research is to propose solutions in order to solve the brain shift issues.

We spent time to assemble the amount of information around the DBS procedure. That is why, in Chapter 1 we propose a complete and clear description of DBS, necessary to understand the problems involved in the following. It encompasses the description of the DBS system and its therapeutic outcomes. Then, a detailed description of the operating protocol is provided. The heart of the problem is introduced, namely the brain shift, a deformation of the brain occurring during the neurosurgery. A brief description of the physical phenomenons leading to brain shift is given. It is the base of our work to model numerically the brain shift.

Chapter 2 (Models of Brain Shift) introduces the mathematical background necessary to understand our model of deformation. Then, we provide a state of the art of the methods to model the brain deformation presented in the literature. We present our proposition of brain shift model: the deformation relies on the FEM and the inclusion of brain weight and the CSF forces. A loss of CSF will decrease the forces so that the balance between the weight and the fluid action is broken. Because of the presence of external forces in our model, we need a method to calculate the reference state of the brain. The chosen algorithm, based on a geometric iterative method, works well for the small deformation involved in the application of the external forces. Finally, the chapter ends with a description of our framework to generate a simulation dedicated to a patient, through the processing of the associated medical images. This chapter presents the model that will be used in the following contributions.

Chapter 3 (Brain Shift Risk during pre-operative Planning) is dedicated to the use of our model before the surgery. The goal is to anticipate the risk of brain shift when the targeted structure is identified and

the optimal and safest trajectory is selected. We introduced two methods. The first relies on the same technique used currently by the neurosurgeon. The selection is made manually by defining a safety margin around the potential trajectory. We propose an extension of the geometrical approach with a more physical approach, based on our brain shift model. In a second contribution, we present the development of a brain shift aware risk map. The aim of this development is, first, to provide information to the surgeon on the safety of the trajectories while taking into account the brain shift, and second, to use this risk map in an automatic optimal trajectory computation software. With these techniques we aim at improving the safety of the procedure, while not adding strong constraints to the surgeon. Our next step is to include the displacement of the target into the optimization process.

Chapter 4 (Physics-Based Intra-operative Registration) provides propositions to use intra-operatively. One issue of brain shift is that it cannot be anticipated. Here, we propose to get information from medical images after the brain shift has taken place. The intra-operative information is used to guide and estimate parameters of our model in order to compute the modified location of structures of interest. Early results are encouraging, but we need to improve the model accuracy as well as the pre-operative structures segmentation precision. We also need novel methods to validate the approach, for example using the contribution presented in the next chapter, related to the electrode curvature.

Chapter 5 (Post-operative Electrode Curvature) is our last contribution and is related to the post-operative curvature of the electrode due to the inverse brain shift. We propose a framework to simulate brain shift, insertion of electrodes and inverse brain shift, while accounting for the interaction between the electrode and the brain tissue. In our experiments, we can observe that the tip of the electrode can shift from the target during its migration. One application of this work can be combined with the intra-operative registration, presented in Chapter 4. We have data that can be used to validate the approach. We believe that this tool can be used intra-operatively to anticipate the electrode curvature and migration.

The presented work is a set of investigations to better understand the circumstances of the brain shift phenomenon. The objective is to provide tools to surgeons with patients undergoing brain shift during surgery. We investigated pre-operative methods for planning the surgery while taking brain shift into account. This type of methods suffers for a major problem: how to prove that our tool leads to a better choice on the placement of the electrode? In our opinion, we presented a logical method, but dealing with unknown parameters. If we are not able to anticipate parameters of our model in advance with precision, we are constrained to work with assumptions or probability. Therefore, after having studied pre-operative planning methods to account for brain shift, we conclude that brain shift is a problem that should preferably be addressed intra-operatively and could not be anticipated pre-operatively without a clear understanding of the dynamic and the physical causes of the phenomenon.

That is why, we also investigated intra-operative estimation of brain shift through our model. In our opinion, this is the key idea to explore in the future. We think a better model, not only of deformation but also on the CSF influence and its leak, will improve the quality of the registration. Several groups have showed registration methods relying on a biomechanical model, but we think the method should rely also on the physical causes of brain shift: influence of CSF and gravity. Our philosophy is to reproduce the reality with physics-based model rather than dealing with artificial forces or constraints, although it is necessary to perform a comparison of the accuracy of both methods. Apart from the model improvement, the developed methods can help to provide new tools. For instance, the combination of the intra-operative registration with the model of electrode insertion can be used to estimate the final electrode curvature. However, during our investigation, we felt necessary to develop new segmentation methods to provide quality meshes for a simulation. Indeed, the constraints to meet on the input of numerical simulations are numerous, and are not always satisfied by classical segmentation methods. Addressing the limitations of the validation of the intra-operative registration, we also need a new strategy to avoid to compare our results to the output of a segmentation algorithm. Finally, we also need to improve the usability of the simulations. Indeed, surgeons are supposed to use the tools we develop, and our application must be

robust, fast and simple.

This work has been involved in a national project, funded by the French national research agency. The participants of the project were: INSERM, University of Rennes 1, CRICM (Centre de Recherche de l'Institut du Cerveau et de la Moelle) – UPMC / INSERM UMR S975 / CNRS UMR 7225 Hôpital de la Pitié-Salpêtrière Paris, University of Strasbourg - Team IGG of the laboratory ICube and Inria - Team Shacra Lille and VR4i Rennes. The project results in three different frameworks: pyDBS, the automatic computation of optimal electrode trajectory and our work on the deformation. When our application will be ready to be used in clinical conditions, a connection between the frameworks will be required. We will be able to evaluate our work for a clinical use.

The common project was to propose models for computer assisted surgical planning for DBS. Perspectives for the following of the project are very various and cannot all be listed here. We present here the next ideas to explore in our opinion, and the ideas relative to our work on brain deformation. Volume of Tissue Activated (VTA) can be included in the optimization process when computing the optimal trajectory. Regarding to the atlases, it would be interesting for us to develop an atlas including the anatomical constraints (intersection, relative position, connection etc) that could be used in a new registration method. During the surgery, a software could assist the neurologist when the micro-electrode records electrical activity. We could imagine a connection with the pre-operative images (or with our updated image) and an automatic process to identify the recorded structure. That would necessitate the construction of an electrophysiological atlas. Finally, it is maybe necessary to construct new histological atlas for other disease than Parkinson's Decease (PD).

During this project, we also discovered the difficulty to have a generic framework for every DBS center. pyDBS was initially developed for Hôpital Ponchaillou in Rennes. Then, a lot of modifications have to be made in order to apply it according to the operating protocol in Hôpital Pitié-Salpêtrière in Paris. In addition, more modifications were necessary when we used post-operative Magnetic resonance imaging (MRI) in the validation of our physics-based registration. It is due to the variability in the operating protocol which can deal with various image modalities or atlases. Moreover, our methods based on the biomechanical model should also be adapted according to the protocol. For now, the physics-based registration relies on an O-arm imaging system. It has to be adapted if we would like to use ultrasounds or intra-operative MRI. Finally, the order of the procedural steps could be different in other centers, so the simulation of electrode insertion should be adapted accordingly.

As a conclusion for this work, we have shown that a biomechanical model can be used to provide useful information before, during and after a Deep Brain Stimulation procedure. Although generating "automatically" a reliable patient-specific simulation remains a challenge, we believe it can provide a significant addition to the pre-operative planning currently used by neuro-surgeons.

Bibliography

Abolhassani, N., Patel, R., and Moallem, M. (2007). Needle insertion into soft tissue: a survey. *Medical engineering & physics*, 29(4):413--31.

[Cited on page 136.]

Abosch, A., Timmermann, L., Bartley, S., Rietkerk, H. G., Whiting, D., Connolly, P. J., Lanctin, D., and Hariz, M. (2013). An international survey of deep brain stimulation procedural steps. *Stereotactic and functional neurosurgery*, 91(1):1--11.

[Cited on pages 16, 17, 32, and 85.]

Allard, J., Faure, F., Courtecuisse, H., Falipou, F., Duriez, C., and Kry, P. G. (2010). Volume contact constraints at arbitrary resolution. *Transactions on Graphics (Proceedings of SIGGRAPH 2010)*, 29(4):1--10.

[Cited on page 81.]

Alterovitz, R., Goldberg, K., and Okamura, A. (2005). Planning for steerable bevel-tip needle insertion through 2D soft tissue with obstacles. In *Robotics and Automation, 2005. ICRA 2005. Proceedings of the 2005 IEEE International Conference on*, number April, pages 1640--1645. IEEE.

[Cited on page 136.]

Anderson, R. J., Frye, M. a., Abulseoud, O. a., Lee, K. H., McGillivray, J. a., Berk, M., and Tye, S. J. (2012). Deep brain stimulation for treatment-resistant depression: efficacy, safety and mechanisms of action. *Neuroscience and biobehavioral reviews*, 36(8):1920--33.

[Cited on page 17.]

Appleby, B. S., Duggan, P. S., Regenberg, A., and Rabins, P. V. (2007). Psychiatric and neuropsychiatric adverse events associated with deep brain stimulation: A meta-analysis of ten years' experience. *Movement disorders : official journal of the Movement Disorder Society*, 22(12):1722--8.

[Cited on page 38.]

Arruda, E. and Boyce, M. (1993). A three-dimensional constitutive model for the large stretch behavior of rubber elastic materials. *Journal of the Mechanics and Physics of Solids*.

[Cited on page 50.]

Audette, M. a., Siddiqi, K., Ferrie, F. P., and Peters, T. M. (2003). An integrated range-sensing, segmentation and registration framework for the characterization of intra-surgical brain deformations in image-guided surgery. *Computer Vision and Image Understanding*, 89(2-3):226--251.

[Cited on page 117.]

Baltuch, G. H. and Stern, M. B. (2007). *Deep Brain Stimulation for Parkinson's Disease*. Neurological Disease and Therapy. Taylor & Francis.

[Cited on page 26.]

Bayly, P. V., Clayton, E. H., and Genin, G. M. (2012). Quantitative imaging methods for the development and validation of brain biomechanics models. *Annual review of biomedical engineering*, 14:369--96.
[Cited on page 57.]

Benabid, A.-L., Pollak, P., Louveau, A., Henry, S., and De Rougemont, J. (1987). Combined (thalamotomy and stimulation) stereotactic surgery of the VIM thalamic nucleus for bilateral Parkinson disease. *Stereotactic and Functional Neurosurgery*, 50(1-6):344--346.
[Cited on page 15.]

Benzley, S., Perry, E., Merkley, K., and Clark, B. (1995). A comparison of all hexagonal and all tetrahedral finite element meshes for elastic and elasto-plastic analysis. *International Meshing*.
[Cited on page 65.]

Bériault, S., Subaie, F. A., Collins, D. L., Sadikot, A. F., and Pike, G. B. (2012). A multi-modal approach to computer-assisted deep brain stimulation trajectory planning. *International journal of computer assisted radiology and surgery*, 7(5):687--704.
[Cited on pages 86, 88, and 89.]

Berkels, B., Cabrilo, I., Haller, S., Rumpf, M., and Schaller, K. (2014). Co-registration of intra-operative brain surface photographs and pre-operative MR images. *International journal of computer assisted radiology and surgery*, 9(3):387--400.
[Cited on page 117.]

Bilger, A., Bardinet, E., Fernandez-Vidal, S., Duriez, C., Jannin, P., and Cotin, S. (2014a). Intra-operative Registration for Deep Brain Stimulation Procedures based on a Full Physics Head Model. In *MICCAI 2014 Workshop on Deep Brain Stimulation Methodological Challenges-2nd edition*, Boston, USA.
[Cited on pages 65, 78, and 113.]

Bilger, A., Bardinet, E., Fernandez-Vidal, S., Duriez, C., Jannin, P., and Cotin, S. (2014b). Intra-operative Registration for Stereotactic Procedures driven by a combined Biomechanical Brain and CSF Model. In *ISBMS-International Symposium on Biomedical Simulation*, Strasbourg, France.
[Cited on page 113.]

Bilger, A., Dequidt, J., Duriez, C., and Cotin, S. (2011). Biomechanical simulation of electrode migration for deep brain stimulation. *Proc. Medical Image Computing and Computer-Assisted Intervention (2011)*, 14(1):339--346.
[Cited on page 131.]

Bilger, A., Duriez, C., and Cotin, S. (2014c). Computation and visualization of risk assessment in deep brain stimulation planning. *Studies in health technology and informatics*, 196:29--35.
[Cited on pages 83 and 94.]

Bilger, A., Essert, C., Duriez, C., and Cotin, S. (2012). Brain-shift aware risk map for Deep Brain Stimulation Planning. In *DBSMC - MICCAI 2012 Workshop on Deep Brain Stimulation Methodological Challenges*, Nice, France.
[Cited on pages 83, 97, and 107.]

Bilston, L. E. (1997). Linear viscoelastic properties of bovine brain tissue in shear. *Biorheology*, 34(6):377--385.
[Cited on page 58.]

Bilston, L. E. (2011). Brain tissue mechanical properties. In *Biomechanics of the brain*, pages 69--89. Springer.
[Cited on pages 24, 57, 58, and 80.]

Boris, P., Bundgaard, F., and Olsen, A. (1987). The CT (Hounsfield unit) number of brain tissue in healthy infants. *Child's Nervous System*, pages 175--177.
[Cited on page 20.]

Breit, S., Schulz, J. B., and Benabid, A.-L. (2004). Deep brain stimulation. *Cell and tissue research*, 318(1):275--88.

[Cited on page 39.]

Brunenberg, E. J. L., Vilanova, A., Visser-Vandewalle, V., Temel, Y., Ackermans, L., Platel, B., and ter Haar Romeny, B. M. (2007). Automatic trajectory planning for deep brain stimulation: a feasibility study. In *Medical Image Computing and Computer-Assisted Intervention--MICCAI 2007*, volume 10, pages 584--92. Springer.

[Cited on page 89.]

Bucki, M., Lobos, C., and Payan, Y. (2007). Framework for a low-cost intra-operative image-guided neuronavigator including brain shift compensation. *Engineering in Medicine and*, 11(4):872--875.

[Cited on page 120.]

Butson, C. R., Cooper, S. E., Henderson, J. M., and McIntyre, C. C. (2007). Patient-specific analysis of the volume of tissue activated during deep brain stimulation. *NeuroImage*, 34(2):661--70.

[Cited on page 90.]

Castellano-Smith, A., Hartkens, T., and Schnabel, J. (2001). Constructing patient specific models for correcting intraoperative brain deformation. *Image Computing and*, pages 1091--1098.

[Cited on pages 59, 60, and 117.]

CGAL (2014). CGAL. http://www.cgal.org/.

[Cited on page 76.]

Chatelin, S., Constantinesco, A., and Willinger, R. (2010). Fifty years of brain tissue mechanical testing: from in vitro to in vivo investigations. *Biorheology*, 47(5-6):255--76.

[Cited on page 57.]

Chen, I., Coffey, A. M., Ding, S., Dumpuri, P., Dawant, B. M., Thompson, R. C., and Miga, M. I. (2011). Intraoperative brain shift compensation: accounting for dural septa. *IEEE transactions on bio-medical engineering*, 58(3):499--508.

[Cited on pages 60 and 117.]

Cho, Z.-H., Min, H.-K., Oh, S.-H., Han, J.-Y., Park, C.-W., Chi, J.-G., Kim, Y.-B., Paek, S. H., Lozano, A. M., and Lee, K. H. (2010). Direct visualization of deep brain stimulation targets in Parkinson disease with the use of 7-tesla magnetic resonance imaging. *Journal of neurosurgery*, 113(3):639--647.

[Cited on page 86.]

Clarke, D. B., D'Arcy, R. C. N., Delorme, S., Laroche, D., Godin, G., Ghosh Hajra, S., Brooks, R., and Diraddo, R. (2012). Virtual Reality Simulator: Demonstrated Use in Neurosurgical Oncology. *Surgical innovation*.

[Cited on page 39.]

Clatz, O., Delingette, H., Bardinet, E., and Dormont, D. (2004). Building a Specific Biomechanical Model of the Brain from Medical Image Analysis and Its Application to the Planning. *Methods*.

[Cited on page 59.]

Clatz, O., Delingette, H., Bardinet, E., Dormont, D., and Ayache, N. (2003). Patient-specific biomechanical model of the brain: application to Parkinson's disease procedure. *Proceedings of the 2003 international conference on Surgery simulation and soft tissue modeling*, pages 321--331.

[Cited on pages 59 and 60.]

Cloots, R. J. H., Gervaise, H. M. T., van Dommelen, J. a. W., and Geers, M. G. D. (2008). Biomechanics of traumatic brain injury: influences of the morphologic heterogeneities of the cerebral cortex. *Annals of biomedical engineering*, 36(7):1203--15.

[Cited on page 61.]

Conte, S. D. and Boor, C. W. D. (1980). *Elementary numerical analysis: an algorithmic approach*. McGraw-Hill Higher Education.

[Cited on page 135.]

Cooper, J. B. and Taqueti, V. R. (2008). A brief history of the development of mannequin simulators for clinical education and training. *Postgraduate medical journal*, 84(997):563--70.

[Cited on page 39.]

Courtecuisse, H., Allard, J., Duriez, C., and Cotin, S. (2010). Asynchronous preconditioners for efficient solving of non-linear deformations. *VRIPHYS-Virtual Reality Interaction and Physical Simulation*, pages 59----68.

[Cited on pages 57 and 65.]

D'Albis, T., Haegelen, C., Essert, C., Fernandez-Vidal, S., Lalys, F., and Jannin, P. (2014). PyDBS : An automated image-processing workflow for planning and postoperative assessment of deep brain stimulation. *International Journal of Computer Assisted Radiology and Surgery*.

[Cited on pages 74, 86, and 120.]

Debono, D. J., Hoeksema, L. J., and Hobbs, R. D. (2013). Caring for patients with chronic pain: pearls and pitfalls. *The Journal of the American Osteopathic Association*, 113(8):620--7.

[Cited on page 17.]

Denson, J. S. and Abrahamson, S. (1969). A computer-controlled patient simulator. *Jama*, 208:504----508.

[Cited on page 39.]

D'Haese, P.-F., Cetinkaya, E., Konrad, P. E., Kao, C., and Dawant, B. M. (2005). Computer-aided placement of deep brain stimulators: from planning to intraoperative guidance. *IEEE transactions on medical imaging*, 24(11):1469--78.

[Cited on pages 85 and 86.]

DiMaio, S. S. P. and Salcudean, S. E. (2005). Needle steering and motion planning in soft tissues. *IEEE transactions on bio-medical engineering*, 52(6):965--974.

[Cited on page 136.]

Dormont, D., Seidenwurm, D., Galanaud, D., Cornu, P., Yelnik, J., and Bardinet, E. (2010). Neuroimaging and deep brain stimulation. *American Journal of Neuroradiology*, pages 15--23.

[Cited on page 33.]

Duay, V., Sinha, T. K., Miga, M. I., and Dawant, B. M. (2003). Non-rigid Registration of Serial Intra-operative Images for Automatic Brain Shift Estimation. *Most*, pages 61--70.

[Cited on page 117.]

Duriez, C. and Cotin, S. (2006). New approaches to catheter navigation for interventional radiology simulation. *Computer Aided Surgery*, 11(October 2005):300--308.

[Cited on page 135.]

Duriez, C., Cotin, S., Lenoir, J., Neumann, P., and Dawson, S. (2005). New approaches to catheter navigation for interventional radiology simulation. In *Medical Image Computing and Computer-Assisted Intervention--MICCAI 2005*, pages 534--542.

[Cited on page 135.]

Duriez, C., Dubois, F., Kheddar, A., and Andriot, C. (2006). Realistic haptic rendering of interacting deformable objects in virtual environments. *Visualization and Computer Graphics, IEEE Transactions on*, 12(1):1--12.

[Cited on page 68.]

Duriez, C., Guébert, C., Marchal, M., Cotin, S., and Grisoni, L. (2009). Interactive simulation of flexible needle insertions based on constraint models. In *Medical Image Computing and Computer-Assisted Intervention--MICCAI 2009*, volume 12, pages 291--9. Springer.

[Cited on pages 136 and 137.]

Duvernoy, H. M., Delon, S., and Vannson, J. L. (1981). Cortical blood vessels of the human brain. *Brain research bulletin*, 7(5):519--79.

[Cited on page 24.]

Echegaray, G., Herrera, I., Aguinaga, I., Buchart, C., and Borro, D. (2014). A Brain Surgery Simulator. *Computer Graphics and Applications, IEEE*, 34(June):12----18.

[Cited on page 60.]

Elias, W. J., Fu, K.-M., and Frysinger, R. C. (2007). Cortical and subcortical brain shift during stereotactic procedures. *Journal of neurosurgery*, 107(5):983--8.

[Cited on pages 100, 105, 108, and 111.]

Ellabib, a. and Nachaoui, a. (2008). An iterative approach to the solution of an inverse problem in linear elasticity. *Mathematics and Computers in Simulation*, 77(2-3):189--201.

[Cited on page 70.]

Essert, C., Haegelen, C., Lalys, F., Abadie, A., and Jannin, P. (2011). Automatic computation of electrode trajectories for Deep Brain Stimulation: a hybrid symbolic and numerical approach. *International journal of computer assisted radiology and surgery*.

[Cited on pages 34, 86, 88, 89, 96, 97, 98, 105, 107, and 111.]

Farnia, P., Ahmadian, A., Shabanian, T., Serej, N. D., and Alirezaie, J. (2014). Brain-shift compensation by non-rigid registration of intra-operative ultrasound images with preoperative MR images based on residual complexity. *International journal of computer assisted radiology and surgery*.

[Cited on page 117.]

Faure, F., Duriez, C., Delingette, H., Allard, J., Gilles, B., Marchesseau, S., Talbot, H., Courtecuisse, H., Bousquet, G., Peterlik, I., and Cotin, S. (2012). Sofa: A multi-model framework for interactive physical simulation. In Payan, Y., editor, *Soft Tissue Biomechanical Modeling for Computer Assisted Surgery*, volume 11, pages 1--39. Springer.

[Cited on page 39.]

Fava, M. (2003). Diagnosis and definition of treatment-resistant depression. *Biological Psychiatry*, 53(8):649--659.

[Cited on page 17.]

Felippa, C. and Haugen, B. (2005). A unified formulation of small-strain corotational finite elements: I. Theory. *Computer Methods in Applied Mechanics and Engineering*, 194(21-24):2285--2335.

[Cited on page 64.]

Fernandes, M., Pavithra, M., and Jatti, A. (2013). ESTIMATION OF BRAIN SHIFT CAUSED BY MENINGIOMA. *International Journal*, 1(5):490--498.

[Cited on page 60.]

Ferrant, M., Nabavi, A., Macq, B., Black, P. M., Jolesz, F. a., Kikinis, R., and Warfield, S. K. (2002). Serial registration of intraoperative MR images of the brain. *Medical image analysis*, 6(4):337--59.

[Cited on pages 58, 60, and 125.]

Ferrant, M., Nabavi, A., Macq, B., Jolesz, F. a., Kikinis, R., and Warfield, S. K. (2001). Registration of 3-D intraoperative MR images of the brain using a finite-element biomechanical model. *IEEE transactions on medical imaging*, 20(12):1384--97.

[Cited on pages 60 and 120.]

Galoppo, N., Otaduy, M. A., Mecklenburg, P., Gross, M., and Lin, M. C. (2006). Fast simulation of deformable models in contact using dynamic deformation textures. *Proceedings of the 2006 ACM SIGGRAPH/Eurographics symposium on Computer animation*, pages 73--83.

[Cited on page 68.]

Ganser, K. a., Dickhaus, H., Metzner, R., and Wirtz, C. R. (2004). A deformable digital brain atlas system according to Talairach and Tournoux. *Medical Image Analysis*, 8(1):3--22.

[Cited on page 86.]

Ginat, D. T., Swearingen, B., Curry, W., Cahill, D., Madsen, J., and Schaefer, P. W. (2014). 3 Tesla intraoperative MRI for brain tumor surgery. *Journal of Magnetic Resonance Imaging*, 39(6):1357--1365.

[Cited on page 115.]

Gobbi, D. G. (2000). Correlation of pre-operative MRI and intra-operative 3D ultrasound to measure brain tissue shift. *Proceedings of SPIE*, 3982:77--84.

[Cited on page 117.]

Gordon, M. S. (1974). Development of an Animated Manikin to Teach Cardiovascular. *The American journal of cardiology*, 34(September):350----355.

[Cited on page 39.]

Grant, R., Condon, B., Hart, I., and Teasdale, G. (1991). Changes in intracranial CSF volume after lumbar puncture and their relationship to post-LP headache. *Journal of Neurology, Neurosurgery & Psychiatry*, pages 440--443.

[Cited on page 37.]

Gross, R. E., Krack, P., Rodriguez-Oroz, M. C., Rezai, A. R., and Benabid, A.-L. (2006). Electrophysiological mapping for the implantation of deep brain stimulators for Parkinson's disease and tremor. *Movement disorders : official journal of the Movement Disorder Society*, 21 Suppl 1:S259--83.

[Cited on page 35.]

Guo, T., Parrent, A. G., and Peters, T. M. (2007). Automatic target and trajectory identification for deep brain stimulation (DBS) procedures. In *Medical Image Computing and Computer-Assisted Intervention--MICCAI 2007*, volume 10, pages 483--90. Springer.

[Cited on page 90.]

Hagemann, A., Rohr, K., Stiehl, H. S., Spetzger, U., and Gilsbach, J. M. (1999). Biomechanical modeling of the human head for physically based, nonrigid image registration. *IEEE transactions on medical imaging*, 18(10):875--84.

[Cited on page 59.]

Hamid, N. a., Mitchell, R. D., Mocroft, P., Westby, G. W. M., Milner, J., and Pall, H. (2005). Targeting the subthalamic nucleus for deep brain stimulation: technical approach and fusion of pre- and postoperative MR images to define accuracy of lead placement. *Journal of neurology, neurosurgery, and psychiatry*, 76(3):409--14.

[Cited on pages 36 and 86.]

Hamidian, H., Soltanian-Zadeh, H., Faraji-Dana, R., and Gity, M. (2008). Estimating Brain Deformation During Surgery Using Finite Element Method: Optimization and Comparison of Two Linear Models. *Journal of Signal Processing Systems*, 55(1-3):157--167.

[Cited on page 60.]

Hardy, W. N., Foster, C. D., Mason, M. J., Yang, K. H., King, A. I., and Tashman, S. (2001). Investigation of head injury mechanisms using neutral density technology and high-speed biplanar X-ray. Technical report, SAE Technical Paper.

[Cited on page 57.]

Hastreiter, P. (2000). Registration techniques for the analysis of the brain shift in neurosurgery. *Computers & Graphics*, 24(3):385--389.

[Cited on page 117.]

Hemm, S., Coste, J., Gabrillargues, J., Ouchchane, L., Sarry, L., Caire, F., Vassal, F., Nuti, C., Derost, P., Durif, F., and Lemaire, J.-J. (2009). Contact position analysis of deep brain stimulation electrodes on post-operative CT images. *Acta neurochirurgica*, 151(7):823--9; discussion 829.

[Cited on pages 36 and 129.]

Hestenes, M. and Stiefel, E. (1952). Methods of conjugate gradients for solving linear systems. *Journal cf Research of the National Bureau of Standards Vol*, 49(6):81--85.

[Cited on pages 57 and 123.]

Hirtz, D., Thurman, D. J., Gwinn-Hardy, K., Mohamed, M., Chaudhuri, a. R., and Zalutsky, R. (2007). How common are the "common" neurologic disorders? *Neurology*, 68(5):326--37.

[Cited on page 17.]

Hrapko, M., van Dommelen, J. a. W., Peters, G. W. M., and Wismans, J. S. H. M. (2008). The influence of test conditions on characterization of the mechanical properties of brain tissue. *Journal of biomechanical engineering*, 130(3):031003.

[Cited on page 57.]

Hu, J., Jin, X., Lee, J. B., Zhang, L., Chaudhary, V., Guthikonda, M., Yang, K. H., and King, A. I. (2007). Intraoperative brain shift prediction using a 3D inhomogeneous patient-specific finite element model. *Journal of neurosurgery*, 106(1):164--9.

[Cited on page 58.]

Huston, O. O., Watson, R. E., Bernstein, M. A., McGee, K. P., Stead, S. M., Gorman, D. A., Lee, K. H., and Huston III, J. (2011). Intraoperative magnetic resonance imaging findings during deep brain stimulation surgery. *Journal of neurosurgery*, 115(4):852--857.

[Cited on page 115.]

Ishiwata, Y., Fujitsu, K., Sekino, T., Fujino, H., Kubokura, T., Tsubone, K., and Kuwabara, T. (1988). Subdural tension pneumocephalus following surgery for chronic subdural hematoma. *Journal of neurosurgery*, 68(1):58--61.

[Cited on page 121.]

ITK-SNAP (2014). ITK-SNAP. http://www.itksnap.org/.

[Cited on page 121.]

Jenkinson, M., Bannister, P., Brady, M., and Smith, S. (2002). Improved Optimization for the Robust and Accurate Linear Registration and Motion Correction of Brain Images. *NeuroImage*, 17(2):825--841.

[Cited on page 121.]

Jenkinson, M. and Smith, S. (2001). A global optimisation method for robust affine registration of brain images. *Medical image analysis*, 5:143--156.

[Cited on page 121.]

Karachi, C., François, C., Parain, K., Bardinet, E., Tandé, D., Hirsch, E., and Yelnik, J. (2002). Three□dimensional cartography of functional territories in the human striatopallidal complex by using calbindin immunoreactivity. *Journal of Comparative Neurology*.

[Cited on pages 26 and 31.]

Kass, M., Witkin, A., and Terzopoulos, D. (1988). Snakes: Active contour models. *International journal of computer vision*, 331:321--331.

[Cited on page 121.]

Kaster, T., Sack, I., and Samani, a. (2011). Measurement of the hyperelastic properties of ex vivo brain tissue slices. *Journal of biomechanics*, 44(6):1158--63.

[Cited on pages 24 and 57.]

Kohn, L., Corrigan, J., and Donaldson, M. (2000). *To Err Is Human:: Building a Safer Health System*, volume 627. National Academies Press.

[Cited on page 39.]

Kruse, S. a., Rose, G. H., Glaser, K. J., Manduca, A., Felmlee, J. P., Jack, C. R., and Ehman, R. L. (2008). Magnetic resonance elastography of the brain. *NeuroImage*, 39(1):231--7.

[Cited on page 24.]

Kumar, R., Lozano, A. M., Kim, Y. J., Hutchison, W. D., Sime, E., Halket, E., and Lang, A. E. (1998). Double-blind evaluation of subthalamic nucleus deep brain stimulation in advanced Parkinson's disease. *Neurology*, 51(3):850--855.

[Cited on page 16.]

Laksari, K., Shafieian, M., and Darvish, K. (2012). Constitutive model for brain tissue under finite compression. *Journal of biomechanics*, 45(4):642--6.

[Cited on page 57.]

Lalys, F., Haegelen, C., D'albis, T., and Jannin, P. (2013). Analysis of electrode deformations in deep brain stimulation surgery. *International journal of computer assisted radiology and surgery*.

[Cited on pages 129 and 139.]

Lalys, F., Haegelen, C., Ferre, J.-C., El-Ganaoui, O., and Jannin, P. (2010). Construction and assessment of a 3-T MRI brain template. *NeuroImage*, 49(1):345--54.

[Cited on page 86.]

Lalys, F., Maumet, C., Haegelen, C., and Jannin, P. (2011). Analysis of Electrode placement and deformation in deep brain stimulation from medical images. *Brain*, pages 3--6.

[Cited on page 86.]

Larsson, T. and Akenine-Möller, T. (2001). Collision detection for continuously deforming bodies. In *Eurographics*, pages 325----333. Citeseer.

[Cited on page 67.]

Lenoir, J., Meseure, P., Grisoni, L., and Chaillou, C. (2002). Surgical thread simulation. *ESAIM: Proceedings*, 12(November 2002):102--107.

[Cited on page 134.]

Limousin, P. and Krack, P. (1998). Electrical stimulation of the subthalamic nucleus in advanced Parkinson's disease. *The New England Journal of Medicine*, pages 1105--1111.

[Cited on page 15.]

Limousin, P., Pollak, P., and Benazzouz, A. (1995). Effect on parkinsonian signs and symptoms of bilateral subthalamic nucleus stimulation. *The Lancet*, pages 91--95.

[Cited on page 15.]

Lin, E. L., Park, D. K., Whang, P. G., An, H. S., and Phillips, F. M. (2008). O-Arm Surgical Imaging System. *Seminars in Spine Surgery*, 20(3):209--213.

[Cited on page 115.]

Lippert, S. A., Rang, E. M., and Grimm, M. J. (2004). The high frequency properties of brain tissue. *Biorheology*, 41(6):681--691.

[Cited on page 57.]

Lurig, C., Hastreiter, P., Nimsky, C., and Ertl, T. (1999). Analysis and Visualization of the Brain Shift Phenomenon in Neurosurgery. *TCVG Symposium on Visualization (VisSym)*, pages 285--290.
[Cited on page 138.]

Marescaux, J., Clément, J. M., Tassetti, V., Koehl, C., Cotin, S., Russier, Y., Mutter, D., Delingette, H., and Ayache, N. (1998). Virtual reality applied to hepatic surgery simulation: the next revolution. *Annals of surgery*, 228(5):627--34.
[Cited on page 39.]

Mayberg, H. S., Lozano, A. M., Voon, V., McNeely, H. E., Seminowicz, D., Hamani, C., Schwalb, J. M., and Kennedy, S. H. (2005). Deep brain stimulation for treatment-resistant depression. *Neuron*, 45(5):651--60.
[Cited on page 17.]

Mehdizadeh, S., Khoshgoftar, M., Najarian, S., Farmanzad, F., and Ahmadi, S. A. (2008). Comparison between Brain Tissue Gray and White Matters in Tension Including Necking Phenomenon. *American Journal of Applied Sciences*, 5(424):1701--1706.
[Cited on page 24.]

Metropolis, N. and Ulam, S. (1949). The monte carlo method. *Journal of the American statistical association*, 44(247):335--341.
[Cited on page 123.]

Miga, M. I., Paulsen, K. D., Hoopes, P. J., Kennedy, F. E., Hartov, a., and Roberts, D. W. (2000a). In vivo quantification of a homogeneous brain deformation model for updating preoperative images during surgery. *IEEE transactions on bio-medical engineering*, 47(2):266--73.
[Cited on pages 58 and 59.]

Miga, M. I., Paulsen, K. D., Hoopes, P. J., Kennedy Jr, F. E., Hartov, A., and Roberts, D. W. (2000b). In vivo quantification of a homogeneous brain deformation model for updating preoperative images during surgery. *Biomedical Engineering*, 47(2):266--273.
[Cited on page 60.]

Miga, M. I., Paulsen, K. D., Lemery, J. M., Eisner, S. D., Hartov, a., Kennedy, F. E., and Roberts, D. W. (1999). Model-updated image guidance: initial clinical experiences with gravity-induced brain deformation. *IEEE transactions on medical imaging*, 18(10):866--74.
[Cited on page 59.]

Miller, K. and Chinzei, K. (2002). Mechanical properties of brain tissue in tension. *Journal of biomechanics*, 35:483--490.
[Cited on pages 57 and 59.]

Miller, K., Horton, a., Joldes, G. R., and Wittek, a. (2012). Beyond finite elements: A comprehensive, patient-specific neurosurgical simulation utilizing a meshless method. *Journal of biomechanics*, 45(15):2698--701.
[Cited on page 65.]

Miller, K. and Lu, J. (2013). On the prospect of patient-specific biomechanics without patient-specific properties of tissues. *Journal of the Mechanical Behavior of Biomedical Materials*.
[Cited on pages 58, 59, and 62.]

Miller, K., Wittek, A., and Joldes, G. (2002). Biomechanics of the brain for computer-integrated surgery. Publishing House of Warsaw University of Technology.
[Cited on page 60.]

Miller, K., Wittek, A., and Joldes, G. (2011). Biomechanical modeling of the brain for computer-assisted neurosurgery. In *Biomechanics of the Brain*, pages 111--136. Springer.
[Cited on pages 59 and 65.]

Mooney, M. (1940). A Theory of Large Elastic Deformation. *Journal of Applied Physics*, 11(9):582.
[Cited on page 50.]

Muthupillai, R., Lomas, D. J., Rossman, P. J., Greenleaf, J. F., Manduca, A., and Ehman, R. L. (1995). Magnetic resonance elastography by direct visualization of propagating acoustic strain waves. *Science*, 269(5232):1854--1857.
[Cited on page 57.]

Myronenko, A. and Song, X. (2010). Intensity-based image registration by minimizing residual complexity. *Medical Imaging, IEEE Transactions on*, 29(11):1882--1891.
[Cited on page 117.]

Nakano, N., Taneda, M., Watanabe, A., and Kato, A. (2012). Computed three-dimensional atlas of subthalamic nucleus and its adjacent structures for deep brain stimulation in Parkinson's disease. *ISRN neurology*, 2012:592678.
[Cited on page 89.]

Nazzaro, J. M., Lyons, K. E., Honea, R. a., Mayo, M. S., Cook-Wiens, G., Harsha, A., Burns, J. M., and Pahwa, R. (2010). Head positioning and risk of pneumocephalus, air embolism, and hemorrhage during subthalamic deep brain stimulation surgery. *Acta neurochirurgica*, 152(12):2047--52.
[Cited on page 38.]

Nelder, J. A. and Mead, R. (1965). The downhill simplex method. *Computer Journal*, 7(308-310):5.
[Cited on page 123.]

Noort, R. V., Black, M., Martin, T., and Meanley, S. (1981). A study of the uniaxial mechanical properties of human dura mater preserved in glycerol. *Biomaterials*, 2.
[Cited on page 24.]

Nowinski, W. L. and Chui, C.-K. (2001). Simulation of interventional neuroradiology procedures. *Medical Imaging and Augmented Reality, 2001. Proceedings. International Workshop on*, pages 87--94.
[Cited on pages 134 and 135.]

Ogden, R. (1972). Large deformation isotropic elasticity-on the correlation of theory and experiment for incompressible rubberlike solids. *Proceedings of the Royal Society of London. A. Mathematical and Physical Sciences*, 326(1567):565--584.
[Cited on page 50.]

Ommaya, A. (1968). Mechanical properties of tissues of the nervous system. *Journal of Biomechanics*, I(September 1967):127--138.
[Cited on pages 57 and 60.]

PAOLIS, L., MAURO, A., Raczkowsky, J., and Aloisio, G. (2009). Virtual model of the human brain for neurosurgical simulation. *Studies in health technology and informatics*, pages 811--815.
[Cited on page 58.]

Paulsen, K. D., Miga, M. I., Kennedy, F. E., Hoopes, P. J., Hartov, a., and Roberts, D. W. (1999). A computational model for tracking subsurface tissue deformation during stereotactic neurosurgery. *IEEE transactions on bio-medical engineering*, 46(2):213--25.
[Cited on pages 58, 59, and 60.]

Pennec, X., Ayache, N., Roche, a., and Cachier, P. (2005). Non-rigid MR/US registration for tracking brain deformations. *Proceedings International Workshop on Medical Imaging and Augmented Reality*, pages 79--86.
[Cited on page 117.]

Perozzo, P., Rizzone, M., Bergamasco, B., Castelli, L., Lanotte, M., Tavella, A., Torre, E., and Lopiano, L. (2001). Deep brain stimulation of the subthalamic nucleus in Parkinson's disease: comparison of pre- and postoperative neuropsychological evaluation. *Journal of the Neurological Sciences*, 192(1-2):9--15.

[Cited on page 89.]

Peterlík, I., Duriez, C., and Cotin, S. (2012). Modeling and real-time simulation of a vascularized liver tissue. In *Medical Image Computing and Computer-Assisted Intervention--MICCAI 2012*, volume 15, pages 50--7. Springer.

[Cited on page 61.]

Pollak, P., Benabid, A.-L., Gross, C., Gao, D. M., Laurent, A., Benazzouz, A., Hoffmann, D., Gentil, M., and Perret, J. (1992). Effects of the stimulation of the subthalamic nucleus in Parkinson disease. *Revue neurologique*, 149(3):175--176.

[Cited on pages 15 and 17.]

Pollo, C., Villemure, J.-G., Vingerhoets, F., Ghika, J., Maeder, P., and Meuli, R. (2004). Magnetic resonance artifact induced by the electrode Activa 3389: an in vitro and in vivo study. *Acta neurochirurgica*, 146(2):161--4.

[Cited on pages 36 and 129.]

Ponce, F. a. and Lozano, A. M. (2014). Erratum: Highly cited works in neurosurgery. Part II: the citation classics. *Journal of neurosurgery*, 120(5):1252--7.

[Cited on page 18.]

Popescu, D. C. and Compton, M. (2003). A model for efficient and accurate interaction with elastic objects in haptic virtual environments. In *Proceedings of the 1st international conference on Computer graphics and interactive techniques in Australasia and South East Asia*, pages 245--250. ACM.

[Cited on page 68.]

Powell, M. (1964). An efficient method for finding the minimum of a function of several variables without calculating derivatives. *The computer journal*.

[Cited on page 123.]

Przemieniecki, J. S. (1985). *Theory of matrix structural analysis*. Courier Dover Publications.

[Cited on page 135.]

Pudenz, R. H. and Shelden, C. H. (1946). The Lucite Calvarium-A Method for Direct Observation of the Brain: II. Cranial Trauma and Brain Movement*. *Journal of neurosurgery*, 3(6):487--505.

[Cited on page 57.]

Raghupathi, L., Grisoni, L., Faure, F., Marchall, D., Cani, M.-P., and Chaillou, C. (2004). An intestinal surgery simulator: Real-time collision processing and visualization. In IEEE, editor, *IEEE Transactions on Visualization and Computer Graphics*, pages 708----718.

[Cited on page 39.]

Rajagopal, V. and Chung, J.-H. C. (2007). Determining the finite elasticity reference state from a loaded configuration. *International Journal for Numerical Methods in Engineering*, 72(March):1434--1451.

[Cited on page 70.]

Rajagopal, V., Chung, J.-H. C., Nielsen, P. M. F., and Nash, M. P. (2005). Finite Element Modelling of Breast Biomechanics: Finding a Reference aState. In *Engineering in Medicine and Biology Society, 2005. IEEE-EMBS 2005. 27th Annual International Conference of the*, volume 3, pages 3268--71. IEEE.

[Cited on page 70.]

Rajagopal, V., Chung, J.-H. C., Nielsen, P. M. F., and Nash, M. P. (2006). Finite element modelling of breast biomechanics: directly calculating the reference state. In *Engineering in Medicine and Biology Society, 2006. EMBS'06. 28th Annual International Conference of the IEEE*, volume 1, pages 420--3. IEEE.
[Cited on page 70.]

Rasche, D., Rinaldi, P., Young, R., and Tronnier, V. (2006). Deep brain stimulation for the treatment of various chronic pain syndromes. *Neurosurgical focus*, 21(6):1--8.
[Cited on page 17.]

Reddy, J. (2007). *An introduction to continuum mechanics*. Cambridge University Press.
[Cited on page 45.]

Reinertsen, I., Descoteaux, M., Siddiqi, K., and Collins, D. L. (2007). Validation of vessel-based registration for correction of brain shift. *Medical image analysis*, 11(4):374--88.
[Cited on page 117.]

Reinertsen, I., Lindseth, F., Askeland, C., Iversen, D. H. y., and Unsgå rd, G. (2014). Intra-operative correction of brain-shift. *Acta neurochirurgica*.
[Cited on page 117.]

Rivlin, R. S. (1948). Large elastic deformations of isotropic materials. I. Fundamental concepts. *Philosophical Transactions of the Royal Society of London. Series A, Mathematical and Physical Sciences*, 240(822):459--490.
[Cited on page 50.]

Schaltenbrand, G., Wahren, W., and Hassler, R. (1977). *Atlas for Stereotaxy of the Human Brain*. Thieme Publishers Series. Thieme.
[Cited on page 85.]

Schiavone, P., Chassat, F., Boudou, T., Promayon, E., Valdivia, F., and Payan, Y. (2009). In vivo measurement of human brain elasticity using a light aspiration device. *Medical image analysis*, 13(4):673--8.
[Cited on page 59.]

Schulder, M. and Carmel, P. W. (2003). Intraoperative magnetic resonance imaging: impact on brain tumor surgery. *Cancer control : journal of the Moffitt Cancer Center*, 10(2):115--24.
[Cited on page 115.]

Sellier, M. (2011). An iterative method for the inverse elasto-static problem. *Journal of Fluids and Structures*, 27(8):1461--1470.
[Cited on page 70.]

Senft, C., Bink, A., Franz, K., Vatter, H., Gasser, T., and Seifert, V. (2011). Intraoperative MRI guidance and extent of resection in glioma surgery: a randomised, controlled trial. *The lancet oncology*, 12(11):997--1003.
[Cited on page 115.]

Shamir, R. R., Tamir, I., Dabool, E., Joskowicz, L., and Shoshan, Y. (2010). A method for planning safe trajectories in image-guided keyhole neurosurgery. *Medical Image Computing and Computer-Assisted Intervention--MICCAI 2010*, pages 1--8.
[Cited on page 89.]

Skrinjar, O., Nabavi, A., and Duncan, J. S. (2002). Model-driven brain shift compensation. *Medical image analysis*, 6(4):361--73.
[Cited on page 117.]

Slotty, P. J., Kamp, M. a., Wille, C., Kinfe, T. M., Steiger, H. J., and Vesper, J. (2012). The impact of brain shift in deep brain stimulation surgery: observation and obviation. *Acta neurochirurgica*, 154(11):2063--8.
[Cited on page 37.]

Sofa (2014). SOFA. http://www.sofa-framework.org/.
[Cited on page 39.]

Starr, P. A., Christine, C. W., Theodosopoulos, P. V., Lindsey, N., Byrd, D., Mosley, A., and Marks Jr, W. J. (2002). Implantation of deep brain stimulators into subthalmic nucleus: technical approach and magnetic imaging-verified electrode locations. *Journal of neurosurgery*.
[Cited on page 85.]

Takizawa, H. and Sugiura, K. (1994). Analysis of intracerebral hematoma shapes by numerical computer simulation using the finite element method. *Neurologia medico-chirurgica*.
[Cited on page 60.]

Talairach, J. and Tournoux, P. (1988). Co-planar stereotaxic atlas of the human brain. 3-Dimensional proportional system: an approach to cerebral imaging.
[Cited on page 24.]

Talbot, H., Spadoni, F., Duriez, C., Sermesant, M., Cotin, S., and Delingette, H. (2014). Interactive Training System for Interventional Electrocardiology Procedures. In *Biomedical Simulation*. Springer.
[Cited on page 39.]

Tang, M., Curtis, S., Yoon, S.-E., and Manocha, D. (2009). ICCD: interactive continuous collision detection between deformable models using connectivity-based culling. *IEEE transactions on visualization and computer graphics*, 15(4):544--57.
[Cited on page 67.]

Thines, L., Lemarchand, F., and Francke, J. (2008). *Atlas interactif de neuroanatomie clinique: Atlas photographique*. Elsevier Masson.
[Cited on pages 18 and 19.]

Tong, F., Ramirez-Zamora, A., Gee, L., and Pilitsis, J. (2014). Unusual complications of deep brain stimulation. *Neurosurgical review*.
[Cited on page 38.]

Toro, R., Perron, M., Pike, B., Richer, L., Veillette, S., Pausova, Z., and Paus, T. (2008). Brain size and folding of the human cerebral cortex. *Cerebral cortex (New York, N.Y. : 1991)*, 18(10):2352--7.
[Cited on page 23.]

Valencia, A., Blas, B., and Ortega, J. H. (2012). Modeling of Brain Shift Phenomenon for Different Craniotomies and Solid Models. *Journal of Applied Mathematics*, 2012:1--20.
[Cited on pages 59, 64, and 66.]

van den Munckhof, P., Contarino, M. F., Bour, L. J., Speelman, J. D., de Bie, R. M. a., and Schuurman, P. R. (2010). Postoperative curving and upward displacement of deep brain stimulation electrodes caused by brain shift. *Neurosurgery*, 67(1):49--53; discussion 53--4.
[Cited on pages 38, 105, 133, 138, and 139.]

van Essen, N. L., Anderson, I. a., Hunter, P. J., Carman, J., Clarke, R. D., and Pullan, a. J. (2005). Anatomically based modelling of the human skull and jaw. *Cells, tissues, organs*, 180(1):44--53.
[Cited on page 20.]

Viceconti, M. and Taddei, F. (2003). Automatic generation of finite element meshes from computed tomography data. *Critical Reviews™ in Biomedical Engineering*, 31(1&2).
[Cited on page 65.]

Vigneron, L. M., Noels, L., Warfield, S. K., Verly, J. G., and Robe, P. a. (2012). Serial FEM/XFEM-Based Update of Preoperative Brain Images Using Intraoperative MRI. *International journal of biomedical imaging*, 2012:872783.

[Cited on pages 60 and 117.]

Visser-Vandewalle, V., Huys, D., Neuner, I., Zrinzo, L., Okun, M. S., and Kuhn, J. (2014). Deep Brain Stimulation for Tourette syndrome: The Current State of the Field. *Journal of Obsessive-Compulsive and Related Disorders*, pages 1--6.

[Cited on page 18.]

Škrinjar, O., Spencer, D., and Duncan, J. S. (1998). Brain shift modeling for use in neurosurgery. *Medical Image Computing and Computer-Assisted Intervention — MICCAI'98*.

[Cited on pages 58 and 62.]

Wang, D., Shi, L., Chu, W. C. W., Cheng, J. C. Y., and Heng, P. A. (2009). Segmentation of human skull in MRI using statistical shape information from CT data. *Journal of magnetic resonance imaging : JMRI*, 30(3):490--8.

[Cited on page 20.]

Wang, E., Nelson, T., and Rauch, R. (2004). Back to elements-tetrahedra vs. hexahedra. In *Proceedings of the 2004 International ANSYS Conference*.

[Cited on page 65.]

Wang, P., Becker, a. a., Jones, I. a., Glover, a. T., Benford, S. D., Greenhalgh, C. M., and Vloeberghs, M. (2006). A virtual reality surgery simulation of cutting and retraction in neurosurgery with force-feedback. *Computer methods and programs in biomedicine*, 84(1):11--8.

[Cited on page 39.]

Winchell, S. W. and Safar, P. (1966). Teachin and Testing Lay and Paramedical Personnel in Cardiopulmonary Resuscitation. *Anesthesia & Analgesia*, 45:441----449.

[Cited on page 39.]

Wittek, A., Joldes, G., and Miller, K. (2011). Algorithms for computational biomechanics of the brain. In *Biomechanics of the Brain*, pages 189--219. Springer.

[Cited on page 59.]

Wittek, A., Miller, K., Kikinis, R., and Warfield, S. K. (2007). Patient-specific model of brain deformation: application to medical image registration. *Journal of biomechanics*, 40(4):919--29.

[Cited on pages 65, 117, and 120.]

Yelnik, J., Bardinet, E., Dormont, D., Malandain, G., Ourselin, S., Tandé, D., Karachi, C., Ayache, N., Cornu, P., and Agid, Y. (2007). A three-dimensional, histological and deformable atlas of the human basal ganglia. I. Atlas construction based on immunohistochemical and MRI data. *NeuroImage*, 34(2):618--38.

[Cited on pages 31, 34, and 86.]

Yousefi, H., Ahmadian, A., and Khodadad, D. (2013). An optimised linear mechanical model for estimating brain shift caused by meningioma tumours. *article.sciencepublishinggroup.com*, 1(1):1--9.

[Cited on page 60.]

Zhang, C., Wang, M., and Song, Z. (2011). A brain-deformation framework based on a linear elastic model and evaluation using clinical data. *IEEE transactions on bio-medical engineering*, 58(1):191--9.

[Cited on page 59.]

Zrinzo, L., van Hulzen, A. L. J., Gorgulho, A. a., Limousin, P., Staal, M. J., De Salles, A. a. F., and Hariz, M. (2009). Avoiding the ventricle: a simple step to improve accuracy of anatomical targeting during deep

brain stimulation. *Journal of neurosurgery*, 110(6):1283--90.

[Cited on page 88.]